

**Geochemical constraints on the development of
Archaean greenstone belts: New insights from the
Stolzburg Complex, Barberton Greenstone Belt,
South Africa**

WITS
UNIVERSITY



Merrily Tau (student no: 736057)

Supervisor: Prof. Robert Bolhar

Co-supervisors: Prof. Sebastian Tappe

Prof. Carl Anhaeusser

MSc. dissertation

June 2021

Dedication

I dedicate this dissertation to my family as they have made it possible for me to pursue postgraduate studies without any pressure to go look for a job after my first degree.

I also dedicate this work to the Love-Peace-Happiness family and to each and every disadvantaged and unprivileged black child, particularly those who would have loved to continue with their studies but they could not as the odds are against them.

Declaration

I declare that this dissertation is my own, unaided work. It is being submitted for the Master of Sciences degree at the University of the Witwatersrand, Johannesburg. It has not been submitted before for any degree or examination in any other University.



Date: 30 June 2021

Merrily Mathume Tau

School of Geosciences,

University of the Witwatersrand,

Johannesburg

Acknowledgments

I would like to acknowledge invaluable guidance by Prof Robert Bolhar and Prof Sebastian Tappe throughout the course of this study. I would also like to acknowledge Prof Carl Anhaeusser who allowed me to use his samples and other resources for this study. Support from friends and colleagues, particularly Mbili Tshiningayamwe, is acknowledged. Mr. Marlin Patchappa and Prof Allan Wilson are recognized for conducting the XRF and ICP-MS analyses. Mr Caiphus Majola and Sam Tshabalala are acknowledged for preparing the polished thin sections. Katlego Matlou, Sarah Glynn, and Mbili Tshiningayamwe are acknowledged for sample preparation training. Dr. Kirsten Youlton is recognized for training me to use the new Olympus BX53M/DP74 petrographic microscope.

Financial support from DSI-NRF CIMERA is highly appreciated.

Moral and financial support from my family is highly appreciated as well. Support from the Love-Peace-Happiness family is acknowledged.

I recognize God, the Creator and Enabler.

Table of contents

Dedication	i
Declaration	ii
Acknowledgements	iii
Table of contents	iv
List of figure	vi
List of tables	viii
Abstract	x
1 Introduction	1
2 Aims and objectives	2
3 Geology of the Barberton Granitoid-Greenstone Terrane	3
3.1 Barberton Greenstone Belt (BGB)	3
3.2 Granitoids	4
3.3 Deformation and structures	5
3.4 What do the ultramafic-mafic complexes represent?	8
3.4.1 Subvolcanic sill model	8
3.4.2 Poned lavas model	9
3.4.3 Alpine-type tectonites model	9
3.5 Metamorphism and alteration	10
4 Geographic locations of the Barberton layered complexes	12
4.1 Schist belts and layered complexes clusters	13
4.2 Spatial positioning and attitude of the layered complexes	16
4.2.1 Pioneer, Saw Mill, and Emmenes complexes	16
4.2.2 Handsup, Mundt's Concession, Hillside, and Kaapsehoop complexes	18
4.2.3 Ship Hill, Budd, and Koedoe complexes	19
4.2.4 Stolzburg, Sterkspruit, and Morgenson complexes	20
4.2.5 Kalkkloof Complex	23
4.2.6 Core Zone and Richmond complexes	24

4.2.7 Sugden Siding (Bon Accord) Complex	24
4.2.8 Summary of finding and implications	24
5 Archaean geodynamics	25
5.1 Plate tectonics and suture zones in the Barberton greenstone belt	27
6 Samples and methods	35
7 Geology of the Stolzberg Complex	36
7.1 General geology	36
7.2 Petrography	40
7.3 Shallow-level sills vs ponded lavas	54
7.4 What do the rodingites represent?	61
8 Assessing the effect of alteration on primary geochemistry	62
9 Primary geochemistry.....	84
9.1.Major elements	84
9.2.Trace elements	84
10. Petrogenesis	88
10.1 Fractional crystallization	88
10.3 Mode of melting (part 1)	90
10.4 Mantle source characterization	92
10.4 Comparison between the geochemistry of the Stolzberg Complex, the surrounding rocks, and other Barberton layered complexes.	96
10.5 Evaluation of crustal contamination	98
10.6 Geodynamic setting of the Stolzberg Complex	101
10.6.1 Normalized multi-element diagrams	102
10.6.2 Tectonic discrimination diagrams	104
10.6.3 Summary and interpretations	115
10.7 An alternative model for the origin of the Barberton greenstone belt	120
10.7.1 Influx of impactors on Earth in the Archaean	120
10.7.2 Bolide impact-based models for the origin of Archaean greenstone belts ...	122
10.7.3 Impact-related melt generation mechanism(s)	122
10.7.4 Evidence for the occurrence of impact events in the vicinity of the area now called Barberton	123

10.7.5 Melting conditions for Al-undepleted melts	126
10.8 Temporal relations between spatially intimate but compositionally distinct magmatic units	129
10.9 Coupled origin of Archaean greenstone belts, SCLM, and TTG suites	133
11 Conclusions	136
12 References	138
13 Appendices	170

List of figures

Fig. 1A: Geological map of the Barberton Greenstone Belt and the surrounding TTG plutons.	4
Fig. 1B: Structural map of the Barberton Greenstone Belt showing the attitude of fabric and structures that characterize the terrane.	7
Fig. 2A: A map of the Barberton Mountain Land showing locations of the schist belts that makes up the northern domain of the BGB.	15
Fig. 2B: A map illustrating the structure of the Nelshoogte Schist Belt as well as relationship with the enveloping granitoids.	21
Fig. 3: Magnetic map of the southwestern portion of the Barberton Mountain Land showing the continuation of the highly positive magnetic anomaly of the southwestern tip of the Nelshoogte Schist Belt (location F) in a broad arc (location D) towards the Kalkkloof Schist Belt.	32
Fig. 4: Simplified geological map of the Stolzberg Complex showing the cyclically repetitive, sub-vertically dipping, differentiated sequence.	37
Fig. 5.1: Micrographs of Stolzberg Complex meta-dunitites.	41
Fig. 5.2: Micrographs of Stolzberg Complex meta-harzburgites.	44
Fig. 5.3: Micrographs of Stolzberg Complex meta-peridotites.	46
Fig. 5.4: Micrographs of orthopyroxenites of the Stolzberg Complex.	48
Fig. 5.5: Micrographs of gabbro-norites of the Stolzberg Complex.	51

Fig. 5.6: Olivine-Orthopyroxene-Plagioclase and Orthopyroxene-Clinopyroxene-Plagioclase classification diagrams of ultramafic-mafic rocks based on estimated modal abundances.	53
Fig. 6.1.1: Plots of generally immobile trace elements (Zr, TiO ₂ , Al ₂ O ₃ , Yb, Y, La, Nb, Ta, Eu, Th) against Hf.	68
Fig. 6.1.2: Correlation diagrams between elements with very similar bulk partition coefficients (i.e., Ta vs Nb and U vs Th).	71
Fig. 6.1.3: Plots of generally mobile trace elements (Rb, Sr, Cs, Ba, U, Pb) against Hf.	72
Fig. 6.1.4: Plots of major oxides against Hf.	74
Fig. 6.1.5: Plots of compatible trace elements against Hf.	76
Fig. 6.1.6: Plot of Al ₂ O ₃ against TiO ₂ .	78
Fig. 6.1.7A: Plot of Nb/Ta and Th/U against Zr/Hf showing groupings of the Stolzburg Complex rocks based on degree of preservation.	81
Fig. 6.1.7B: Plot of La/Hf and Yb/Hf against Zr/Hf showing groupings of the Stolzburg Complex rocks based on degree of preservation.	82
Fig. 6.1.7C: Correlation diagrams for Stolzburg Complex data. Plot of Ta against Nb (left). Plot of U against Th (right). Samples are distinguished by the defined rock groups.	83
Fig. 6.1.7D: Plots of Al ₂ O ₃ /TiO ₂ against Zr/Hf showing the relationship between the Al ₂ O ₃ /TiO ₂ ratio and rocks type and degree of primary geochemistry preservation.	83
Fig. 6.2.1A: Primitive mantle – normalized trace element patterns for the best preserved rocks of the Stolzburg Complex (group 1).	85
Fig. 6.2.1B: Primitive mantle – normalized trace element patterns for group 2 rocks of Stolzburg Complex.	85
Fig. 6.2.1C: Primitive mantle – normalized trace element patterns for group 3 rocks of Stolzburg Complex.	86
Fig. 6.2.1D: Primitive mantle – normalized trace element patterns for group 4 rocks of Stolzburg Complex.	86

Fig. 6.2.1E: Primitive mantle – normalized trace element patterns for group 5 rocks of Stolzberg Complex.	87
Fig. 6.2.2A: Plot of $(La/Nd)_{PM}$ against Al_2O_3/TiO_2 showing LREE enrichment in rocks of the Stolzberg Complex with an average $(La/Nd)_{PM}$ value of 1.38.	87
Fig. 6.2.2B: Plot of $(Gd/Yb)_{PM}$ against Al_2O_3/TiO_2 showing the flat HREE pattern displayed by rocks of the Stolzberg Complex with an average $(Gd/Yb)_{PM}$ value of 0.98.	88
Fig. 6.3.1: Demonstration of distinction in the Al_2O_3/TiO_2 ratio between the Stolzberg Complex and Nelshoogte greenstones.	97
Fig. 6.3.2: Plot of Nb against La/Yb demonstrating the lack of crustal contamination signatures in the Stolzberg Complex.	100
Fig. 6.4: PM-normalized diagram comparing incompatible elements patterns of the Stolzberg Complex, Pioneer Complex, Komati Formation, Gorgona Island komatiites; Mariana arc, Ontong Java oceanic plateau, N-MORB, and OIB.	103
Fig. 6.5.1: Th/Yb vs. Nb/Yb tectonic discrimination diagram (after Pearce, 2008).	108
Fig. 6.5.2: Nb/Th vs. La/Nb tectonic discrimination diagram (after Zhang et al., 2012).	110
Fig. 6.5.3: $(Hf/Sm)_{PM}$ vs $(Ta/La)_{PM}$ tectonic discrimination diagram (after La Flèche et al., 1998).	112
Fig. 6.5.4: Zr/Nb vs. Nb/Th tectonic discrimination diagram (after Condie, 2005).	114
Fig. 6.5.5: Nb/Y vs. Zr/Y tectonic discrimination diagram (after Fitton et al., 1997, 2003).	115
Fig. A1: Plot of Cr (ppm) obtained by ICP-MS method against Cr_2O_3 (wt. %) determined by XRF analysis.	178
Fig. A2: Plots of inter-element ratios of samples from the Stolzberg Complex, where samples are discriminated in terms of lithology.	179

List of tables

Table 1: Summary of petrography of the rocks of the Stolzberg Complex.	52
Table 2: Inter-element ratios in the Stolzberg Complex rocks.	95
Table A1: Primary modal abundances of rocks of the Stolzberg Complex.	170
Table A2: Certified Reference Materials (CRMs) data from XRF analysis.	171
Table A3: Certified Reference Materials (CRMs) data from ICP-MS analysis.	172
Table A4: XRF major elements and quadrupole ICP-MS trace elements data of samples from the Stolzberg Complex.	173
Table A5: Groups of samples from the Stolzberg Complex according to degree of preservation of primary geochemistry.	178

Abstract

Ultramafic-mafic layered complexes are an important but poorly-studied component of Archaean granitoid-greenstone terranes. In the vicinity of the Barberton greenstone belt, at least 27 such complexes occur intimately with the supracrustal succession. The petrogenesis of one of these layered bodies, namely Stolzberg Complex (SC), is explored together with its relationship to the surrounding Barberton volcanic succession.

In contrast to published models for the development of Barberton layered complexes (namely subvolcanic sills, ponded lavas, and alpine-type tectonites), the present work is most consistent with the emplacement as sheeted sills into the country rocks. Unlike the subvolcanic sills model, whereby each complex grew through repetitive magma injection and differentiation in a single chamber, the preferred model regards each magmatic unit in the complexes as a discrete sill. Using major and trace element geochemistry, the Lower and Upper divisions of the Stolzberg Complex are inferred to be petrogenetically related, but compositionally distinct from the enveloping Nelshoogte volcanic rocks.

On the basis of certain geochemical indicators (the low $(La/Yb)_{PM} \sim 1.47$ and high $Zr/Th \sim 135$), the SC is shown to be free of crustal contamination, consistent with development in an oceanic setting. The chemistry of the magmatic source appears to be similar to that of the Primitive Mantle, except that it was enriched in LREE. Furthermore, trace element systematics (lack of heavy REE depletion, chondritic Zr/Y and Al_2O_3/TiO_2 ratios) suggest that the parental magma was generated through partial melting of a mantle source with no garnet in the restite. In contrast to the general belief that Al-undepleted melts were generated in the spinel stability field, it is proposed that the SC parental magma was produced through very high degree partial melting of an undepleted mantle source, where garnet was completely consumed. It is speculated that an unknown high pressure phase remained in the restite, consequently retaining Nb and Ta in the residual solid.

None of the modern geodynamic environments appear to provide a suitable framework to explain the geochemical aspects of the SC. Consequently, a preferred model is presented, whereby SC parental magmas formed as impact-generated melts. The development of Archaean greenstone belts is, correspondingly, attributed to bolide impact events in the early Earth. Accordingly, the origin of cratonic roots and TTG suites are ascribed to the above processes and not endogenic processes as proposed in previously published studies.

1. Introduction

Archaean rocks provide a record of geological activities that took place during the early stages of the development of the Earth. By studying these rocks, insights on Archaean surface processes can be gained (Condie, 1981; De Wit and Ashwal, 1986; Glikson, 2014). Much of what is known about the Archaean environment comes from granitoid-greenstone terranes (Anhaeusser, 2014). The granitoid-greenstone terranes are characterized by supracrustal successions composed dominantly of subaqueously-erupted basalts, with lesser ultramafic and felsic extrusives and marine sedimentary rocks all metamorphosed to greenschist to amphibolite facies (Anhaeusser, 1985; De Wit and Ashwal, 1995, 1996; Condie, 1981). These successions are typically surrounded by granitoid domes (Anhaeusser, 1973a, 1992a; Glikson, 2014). In addition to the voluminous volcanic rocks, differentiated ultramafic-mafic complexes often occur in intimate association with the supracrustal succession and are normally restricted to the volcanic pile (Anhaeusser, 2001, 2014). The intrusions may also be present as inliers within the gneissic granitoids. These ultramafic-mafic complexes are an important but poorly understood component of Archaean granitoid-greenstone terranes (Anhaeusser, 2004, 2006). In the vicinity of the Barberton Greenstone Belt, at least 27 Archaean complexes of ultramafic to mafic compositions have been identified in the supracrustal successions (Anhaeusser 1985, 1986).

The fact that these layered ultramafic-mafic complexes are common in greenstone belts suggests that the formation of these bodies constitutes an important phase in the genesis of greenstone belts. Specifically, the close relation between the volcanic pile (which is considered the earliest component of greenstone belts (Anhaeusser, 1973a; De Wit and Ahwal, 1986, 1995, 1996) and the ultramafic-mafic bodies suggests that these layered complexes were emplaced during the early stages of development of the greenstone belts (Anhaeusser, 1985). For these reasons, important information about the genesis and evolution of greenstone belts may be acquired through thorough study of the ultramafic-mafic complexes (Anhaeusser, 1985, 2001).

This project is aimed at studying one of the best-preserved layered ultramafic bodies, namely, the Stolzberg Complex, which is hosted in the Barberton Greenstone Belt, South Africa. The focus is on constraining igneous processes that lead to the formation and differentiation of the ultramafic-mafic complex and their geodynamic setting and an assessment of the petrogenetic relation

between the intrusion and the spatially-associated ultramafic-mafic extrusives. Other important aspects include the evaluation of secondary alteration and the assessment the role of crystal accumulation processes in the layering within the complex.

2. Aims and objectives

- Use petrography to classify the samples from the Stolzberg Complex in terms of mineralogy; assess secondary processes (alteration); and also determine whether the rocks are cumulates or products of in situ crystallization.
- Use major and trace elements geochemistry to assess the rocks for possible incompatible elements mobilization as a result of rock-fluid interaction.
- Classify rocks of the Stolzberg Complex in terms of their major and trace elements compositions.
- Use of whole-rock major and trace elements geochemistry to reconstruct or constrain (1) the nature and composition of the source rock (mantle reservoir) from which the Stolzberg melt(s) were derived as well as (2) the modes of partial melting that generated the melt. Crustal and source contamination will also be examined.
- Evaluate the possible geodynamic settings for the Stolzberg Complex emplacement.
- Compare the trace element geochemistry of the Stolzberg Complex with that of other Barberton greenstones.

3. Geology of Barberton Mountain Land

3.1. Barberton Greenstone Belt (BGB)

The Barberton Greenstone Belt (BGB) is a granitoid-greenstone terrane, which comprises a unique sequence of some of the best-preserved, first-formed lithologies on the planet; it is among some of the oldest greenstone belts currently known in the world (Brandl et al., 2006). The BGB is situated south and southeast of a town in Eastern Mpumalanga called Nelspruit and is a strongly folded, ENE-trending, mid-Archaean (3600-3100 Ma) volcano-sedimentary remnant, entirely surrounded by a variety of granitoids of the Kaapvaal Craton (fig. 1A) (Anhaeusser et al., 1981).

Rocks of the BGB have been grouped stratigraphically into the Barberton Supergroup, which comprise three major lithostratigraphic units, namely, from the base upwards, (1) the Onverwacht Group (3.5 - 3.26 Ga), (2) the Fig Tree Group (3.26 - 3.22 Ga), and (3) the Moodies Group (3.23 - 3.21 Ga) (Brandl et al., 2006; Lowe, 1991; Lowe and Byerly, 1999). The Onverwacht Group consists largely of submarine mafic to ultramafic volcanic rocks, locally showing pillow lava features, which indicate extrusion into a large body of water (possibly an Archaean ocean) (Viljoen and Viljoen, 1969a).

Previously, the composition of the lavas was believed to transition from komatiitic at the bottom, through komatiitic basalts, to basaltic lavas at the top (De Wit and Ashwal, 1986, 1995). Recent studies demonstrated that lavas of different compositions are complexly interstratified (Lowe and Byerly, 1999)

Twenty-seven layered ultramafic-mafic complexes have been identified in the Onverwacht Group (fig. 2A) (Anhaeusser, 2001, 2006a). Most of these entities occur as sill-like bodies or complexes showing pronounced igneous layering (Anhaeusser, 1985, 2001; Rodel, 1993). Many complexes show cyclically repeated layered units, consisting dominantly of dunite, orthopyroxenite and harzburgite, and lesser clinopyroxenite, gabbro and anorthositic gabbro-norite rocks.

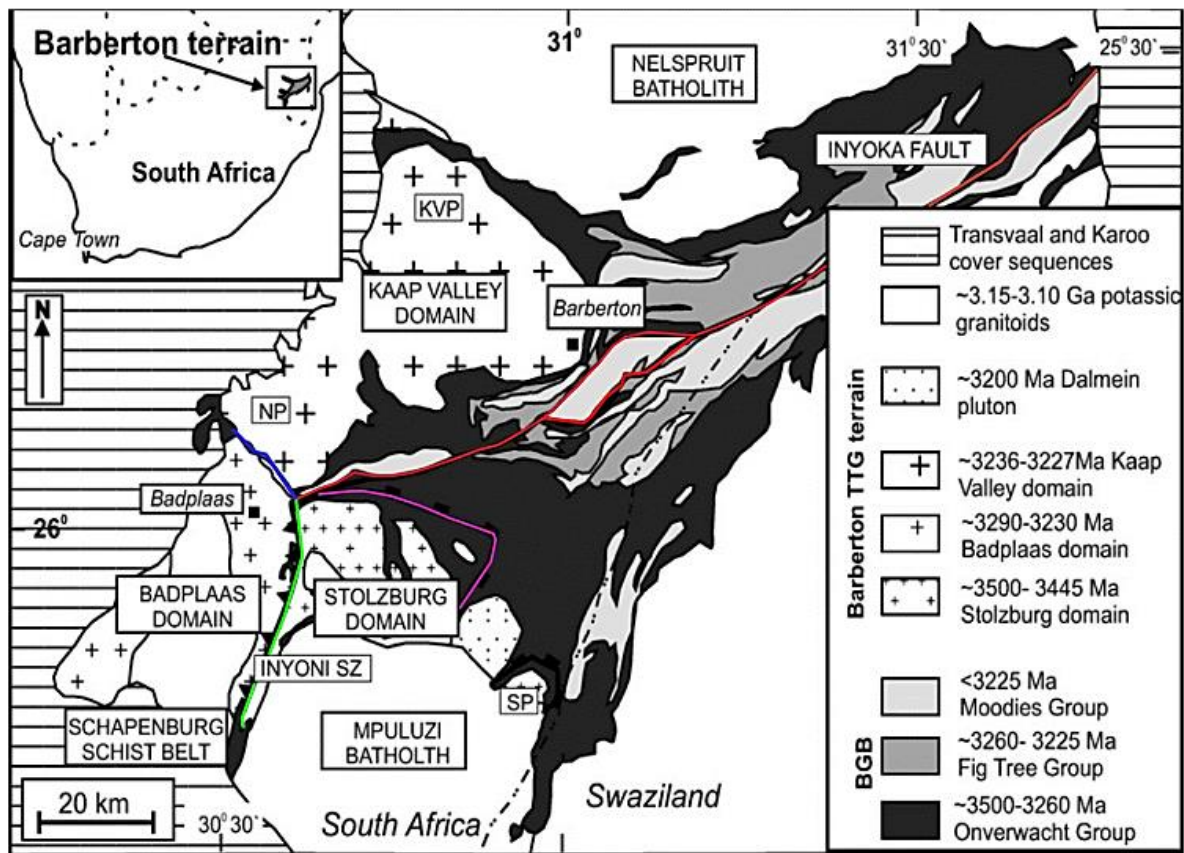


Figure 1A: Geological map of the Barberton Greenstone Belt and the surrounding TTG plutons. Inset: Location of the map area in South Africa (Kisters et al., 2010). Red = Inyoka-Saddleback Fault; green = Inyoni Shear Zone; pink = Komati Fault; blue = boundary between Nelshoogte and Badplaas plutons.

3.2. Granitoids

The Barberton Greenstone Belt is entirely surrounded by Archaean granitoids (Anhaeusser and Robb, 1981). The granitoids occur as two types. One type is a suite of felsic plutons of the Tonalite-Trondhjemite-Granodiorite (TTG) class, which are essentially limited to Archaean terranes. These granitoids are distinguished by their marked depletion of potassic feldspars. Two age groups, both of which are restricted to the Palaeoarchaeon Era, have been recognized for this suite. An older group is dated around 3.4 Ga and predominantly occurs along the southern margin of the greenstone belt whereas the younger group is dated around 3.2 Ga and typically occurs along the

northwestern margin of the greenstone belt (Anhaeusser, 1984). The ca. 3.4 Ga TTG granitoids include the Stolzburg, Theespruit and Doornhoek Plutons (Kisters and Anhaeusser, 1995a, b) while the ca. 3.2 Ga granitoids include the Nelshoogte, Badplaas, Kaap Valley and Stentor Plutons (Kisters et al., 2010). The second type of granitoids is essentially constituted by potassic granitoids with ages around 3.1 Ga (Wang et al., 2018). These late granitoids commonly occur as batholiths around the northeastern, southern and southeastern margins of the Barberton Greenstone Belt. Examples include the Nelspruit, Piggs Peak, and Mpuluzi Batholiths (Anhaeusser, 2019).

3.3. Deformation and structures

Although the Barberton Greenstone Belt is, by Archaean standards, spectacularly preserved, it was affected by multiple episodes of deformation. The earliest apparent phase of deformation, commonly referred to as D_1 , is evident in the southern portion of the greenstone belt (de Ronde and de Wit, 1994). This deformation event has been shown to coincide with the ca. 3.4 Ga felsic magmatic event manifested by TTG plutonism in the southern portion of the belt as well as felsic volcanism of the same age occurring with the predominantly mafic lavas in the upper Onverwacht Group. The D_1 deformational event has been dated between 3445 Ma and 3416 Ma (de Ronde and de Wit, 1994).

In addition to the D_1 event, a more regional deformation event is apparent throughout the entire greenstone belt (de Wit, 1982; Lowe, 1991). This deformation is manifested by the NE-SW regional trend of the greenstone belt as well as the NE-SW- to E-W-trending major isoclinal folds developed throughout the greenstone belt (fig. 1B) (Anhaeusser, 2019; Brandl et al., 2006; Tomkinson and King, 1991). This event has been shown to coincide with the ca. 3.2 Ga felsic magmatism represented by the TTG plutons along the northwestern margin of the greenstone belt as well as felsic volcanism in the lower Fig Tree Group (de Ronde and Kamo, 2000). The event has been dated between 3230 Ma and 3225 Ma (de Ronde and Kamo, 2000). However, it undoubtedly continues post-3225 Ma but up to 3110 Ma (Heubeck and Lowe, 1994; Lowe and Byerly, 2007) as rocks of the Moodies Group have also been affected by this deformation event. The lower time bound for this event is poorly constrained but the undeformed Dalmein pluton, which has been dated at ca. 3216 Ma, provides a minimum age (de Ronde and Kamo, 2000).

Moreover, the coarse clastic rocks of the Moodies Group are generally believed to have developed during this event (de Ronde and de Wit, 1994).

In the southern and central portions of the Barberton Greenstone Belt, the D_2 event led to the development of NE-SW- to E-W-trending, generally upright, isoclinal folds (F2) which plunges steeply to the northeast (de Wit, 1982). These folds are commonly bounded by major and minor steeply-dipping longitudinal faults which are believed to have accompanied the deformation event (Anhaeusser, 1984, 2019). The vertical to subvertical supracrustal units of the Onverwacht Group crops out in a series of these F2 folds, including the Onverwacht and Steynsdorp anticlines and Kromberg Syncline (Cloete, 1994; Lowe, 1991; Lowe and Byerly, 2007). Some of the major longitudinal faults that dissect the southern and central portion of the Barberton Greenstone Belt include the Kromberg, Granville Grove, and Auber Villiers Faults (Lowe, 1999).

In a similar fashion, the northern portion of the Barberton Greenstone Belt consists of major and minor NE-SW- to E-W-trending, upright to overthrust, isoclinal folds (F2) (i.e., bedding has been rotated to vertical or subvertical dips), which have been attributed to the D_2 deformation event (Tomkinson and King, 1991, Heubeck and Lowe, 1994). Evidently, the region is dominated by well-developed NE-SW-trending synclinal structures as exemplified by the Eureka, Ulundi, Lily, Saddleback, Stolzburg, and Weltevreden Synclines, which are bounded by steeply south-dipping longitudinal faults including the Moodies, Belvue, Sheba, Lily, Barbrook Faults (Anhaeusser, 1976a, 1984, 2019; de Ronde and Kamo, 2000). Sheared and attenuated antiformal septa of the Onverwacht rocks occur in between the synclines (Anhaeusser, 1984; Lowe and Byerly, 1999). In essence, the northern portion of the Barberton greenstone belt is constituted by a series of well-developed synclinal structures of mainly Moodies Group and Fig Tree Group rocks which are separated by highly attenuated antiformal structures of Onverwacht Group rocks. This means that rocks of the lower stratigraphic levels are exposed along the anticlinal structures. The steeply dipping longitudinal faults typically mark the structural contacts between the synclinal and anticlinal structures. Typically, the longitudinal faults and the axial planes of the isoclinal folds verge to the northwest (Lowe and Byerly, 1999; Tomkinson and King, 1991). The regional NE-SW-striking Inyoka-Saddleback fault system (fig. 1A) is commonly regarded as a divide between the southern and northern domains (occurring south and north of the fault, respectively) of the Barberton Greenstone Belt (de Ronde and de Wit, 1994; de Ronde and Kamo, 2000; Kisters et al.,

2010; de Wit et al., 2018). Late deformation events have disrupted some of the generally NE-SW trending structures as displayed by the inflection of the Eureka and Ulundi Synclines (Anhaeusser, 1976).



Figure 1B: *Structural map of the Barberton Greenstone Belt (after Anhaeusser et al., 1968) showing the attitude of fabric and structures that characterize the terrane. Notice the general NE-SW trending structures as well as the by arcuate foliation in the enveloping granitoids.*

Despite over 60 years of describing and documenting the regional deformation and structures that characterize the Barberton Greenstone Belt, the mechanism(s) responsible for the development of these features remains highly controversial (Anhaeusser, 2014). This is a critical topic because it has tight links to the nature of Archaean geodynamics that dominated the Barberton terrane. There are two main competing models; one which attributes the deformation to convergent margins in a plate tectonic regime and the other which envisage vertical tectonism – a process restricted to the infant Earth (Anhaeusser, 2019). Advocates of vertical tectonism, as the principal mechanism

responsible for the D_2 deformation, ascribe the development of the isoclinal folds and the accompanying longitudinal faults to diapiric emplacement of the granitoids that encloses the greenstone belt (Anhaeusser, 1984, 2010; Kirsters and Anhaeusser, 1995a, 1995b; Minnitt and Anhaeusser, 1992; Van Kranendonk et al., 2004, 2007, 2014, 2021). In contrast, proponents of horizontal tectonic processes advance the operation of Phanerozoic-style plate tectonics in the Mesoarchaean Era. These workers envisage the occurrence of subduction zone environments at ca. 3.2 Ga; one along the present-day northwestern margin and the other along the southeastern margin of the Barberton Greenstone Belt (Anhaeusser, 2006a; de Wit, 1982; de Wit et al., 2018; MacLennan, 2012; de Ronde and Kamo, 2000; de Ronde and de Wit, 1994; Moyen et al., 2006; Lowe, 1994; Furnes et al., 2012). In this model, the regionally extensive, NE-SW-striking, Inyoka-Saddleback fault system (fig. 1A) along the northwestern portion of the belt and the Manhaar Fault along the southeastern margin are regarded as suture zones along which different terranes amalgamated.

Initially, compressive stresses led to the development of NE-SW-trending folds. Further compression resulted in the juxtaposition of the synclinal structures, in the process attenuating the intervening anticlines. This was enabled by the development of the steeply-dipping longitudinal faults. The faults are interpreted as thrust planes (Heubeck et al., 2013; de Wit, 1982) or gravitational slip planes (Anhaeusser, 1984a; Van Kranendonk, 2021).

3.4. What do the ultramafic-mafic complexes represent?

The origin of layered ultramafic complexes, which are common in Archaran greenstone belts, constitutes a highly debated topic today. Several models have been proposed in an attempt to put this mystery to rest. These models are briefly reviewed below.

3.4.1. Subvolcanic sill model

The oldest model proposes that these layered bodies were emplaced as shallow sills, either penecontemporaneously into the developing succession of mafic to ultramafic lavas or shortly thereafter (Anhaeusser, 1976, 1979, 1985; Jolly, 1977; Naldrett and Turner, 1977; Rodel, 1993; Viljoen and Viljoen, 1970; Williams and Hallberg, 1973). Furthermore, the model suggests that

these sill-like bodies acted as staging chambers which fed the enveloping mafic volcanism (Anhaeusser, 1985). Essentially, this model envisages a comagmatic origin for the complexes and the adjacent metavolcanic successions. Parental magmas with ultramafic compositions evolved in the magma chambers through crystal fractionation, resulting in the basaltic differentiates, which erupted to form the Onverwacht basaltic lavas, leaving behind high-Mg cumulates composed mainly of olivine and orthopyroxene. These cumulates formed the ultramafic rocks of the Barberton ultramafic complexes. The residual and fractionated melt in the chamber crystallized under slow cooling conditions to form the upper units of the complexes with more differentiated compositions. The komatiitic lavas are considered to be a result of rare cases where the ultramafic parental magma reached the surface of the earth without undergoing differentiation in a shallow level staging chamber.

3.4.2. Ponded lavas model

The complexes were later re-interpreted by some workers as products of thick and voluminous komatiitic lava rivers and/or lakes that ponded in some pre-existed topographical features (Cooper, 2008; Huber and Byerly, 2018; Rodel, 1993; Thompson-Stiegler, 2012). Such a model was first put forth by Donaldson et al. (1986), Hill et al. (1989) and Barnes et al. (1988) for the origin of ultramafic complexes found in the Eastern Goldfields Province of the Yilgarn Block, western Australia. These large lava flows are thought to have resulted from prolonged eruptions. Over time, the lavas solidified in such a way that the slow-cooled lower portion of the thick dammed lava crystallized to form the cumulate rocks and the fast-cooled upper portion of the lava formed the fine-grained and spinifex-textured volcanics. The model was put forth in attempts to explain the origin of the Stolzberg (Rodel, 1993), Pioneer (Cooper, 2008; Thompson-Stiegler et al., 2012), and Saw Mill (Huber and Byerly, 2018) complexes.

3.4.3. Alpine-type tectonites model

Attempts were made to associate the Barberton Greenstone Belt with ophiolites (de Wit, 1983; 1986; 1991; de Wit and Tredoux, 1988; de Wit and Hart, 1993). For instance, de Wit et al. (1987) suggested the entire succession of the Barberton Greenstone Belt represent a pseudostratigraphy of an Archaean ophiolite. In their reconstruction, these workers regarded the Stolzberg Complex (and other Barberton layered ultramafic bodies) as exhumed basal peridotitic section of an oceanic

lithosphere (i.e., the topmost upper mantle section that forms part of oceanic lithospheres (de Wit and Tredoux, 1988)) similar to the ones that are encountered in Phanerozoic ophiolites. The model has significant implications as it proposes that the Barberton Greenstone Belt represents an Archaean oceanic lithosphere, which was generated at a spreading centre. Moreover, it was suggested that the supposed upper mantle was exhumed through obduction in subduction zone settings.

More recently, Anhaeusser (2006) put forth a similar model whereby the Barberton layered complexes were regarded as fragments of peridotitic cumulate section found at the base of Phanerozoic ophiolites. The model suggests that the area in which these bodies are found marks an Archaean suture zone where the northern and southern domains of the Barberton Greenstone Belt collided in a subduction zone environment.

3.5. Metamorphism and alteration

As in other Palaeoarchaean greenstone belts, rocks of the Barberton greenstone belt show pervasive low temperature and low pressure alteration, which is thought to have occurred very early in the development of the greenstone belt, perhaps nearly contemporaneous with volcanism (Anhaeusser et al., 1969; Cloete, 1999). Metasomatic processes recognized range from H₂O-dominated, similar to those observed at present-day spreading ridges (hydration of newly formed oceanic crust through large-scale convection of heated seawater), to CO₂-dominated, such as those that are inferred to occur in the deep crust and upper mantle (Cloete, 1994, 1999; de Wit et al., 1987). It is proposed that different fluid activity occurred at different times during the evolution of the greenstone belt, with the water-dominated processes occurring early, and then followed by the CO₂-dominated processes (Cloete, 1999).

The most common type of metasomatic alteration involves silicification, with virtually all rock types being affected by this process (Hofmann and Harris, 2008). Essentially, this process involves the addition of silica. Hofmann and Harris (2008) showed that silicification is prevalent in sections several tens of metres thick at the top of Onverwacht Group volcanic sequences that are capped by sedimentary chert horizons.

It has been known since the mid-1800s that a variety of green secondary minerals, namely serpentine, chlorite, epidote, actinolite, and hornblende constitute at least 80% of mafic-ultramafic rocks of greenstone belts (Ashwal and De Wit, 1996). This pervasive replacement of primary minerals (olivine, pyroxene and plagioclase) by these secondary alteration products is attributed to low-temperature and low-pressure (typically 300–450 °C and 1–4 kilobars) alteration processes including serpentinization, chloritization, uralitization, steatization, saussuritization and epidotization (Cloete, 1999; Ficq et al., 2018; Kareem, 2005).

Serpentinization is the principal alteration process affecting ultramafic rocks (de Wit et al., 1987; Viljoen and Viljoen, 1969). This process essentially involves the transformation, through the addition of water under greenschist facies temperature-pressure conditions, of the Mg-Fe-silicates such as olivine, pyroxene, or amphiboles contained in ultramafic rocks into serpentine group minerals. The formation of serpentine minerals is accompanied by the release of the iron, which was incorporated in the primary minerals since it cannot be accommodated in the serpentine crystal structure. Consequently, serpentinization is normally accompanied by the formation of magnetite from the released iron. Other commonly recognized alteration processes affecting ultramafic rocks include carbonation and steatization (Hess, 1933; Viljoen and Viljoen, 1969). Carbonation involves reactions between Mg-Fe-silicates in the ultramafic rocks with CO₂-bearing fluids. This process is normally manifested by the occurrence of secondary carbonate minerals (commonly calcite and dolomite) as well as the magnesian carbonate mineral magnesite (Toulkeridis et al., 2010). Steatization involves the transformation of Mg-Fe-silicates such as pyroxene and olivine into talc. This process essentially entails the addition of water and silica to the primary minerals. Secondary minerals such as serpentines can also be replaced by talc through the addition of only silica. Steatization is not restricted to ultramafic rocks, it also common in mafic rocks.

Mafic rocks are primarily constituted by pyroxene and plagioclase. Having been subjected to greenschist facies metamorphism as well, this class of rocks in Archaean greenstone belts has suffered pervasive alteration. Commonly encountered indicators involve the replacement of plagioclase by an assemblage of epidote + zoisite + chlorite or just epidote as a result of alteration processes known as saussuritization and epidotization, respectively (Ashwal and de Wit, 1995; Cloete, 1999; Rodel, 1993). The plagioclase, which originally occurs in the anorthite form, can undergo albitization where the calcium cation is replaced by sodium cations. Multiple alteration

paths of the pyroxenes have been recognized. The pyroxenes can be altered to actinolite-tremolite, chlorite, or talc as a consequence of processes, respectively, referred to as uralitization, chloritization and steatization. Chloritization is also common in ultramafic rocks. Mafic rocks exposed to greenschist facies metamorphism are therefore characterized by the assemblage actinolite + epidote + chlorite + albite \pm calcite \pm quartz \pm pyrite.

It has been established that most Archaean greenstone belts, including the Barberton greenstone belt, have been exposed to regional, static, greenschist facies metamorphism where rocks display preservation of primary textures, absence of tectonic fabric and occasional preservation of primary minerals (Anhaeusser, 1969; Cloete, 1991, 1994, 1999; Viljoen and Viljoen, 1969). Various mechanisms have been proposed to explain the origin of the pervasive greenschist facies metamorphism. One of the proposed possibilities involves autometasomatism, whereby the fluids exsolved from the evolved magma were re-introduced into the system and interacted with the early crystallized phases (Anhaeusser, 2006b, 2014). It has also been proposed that fluids exsolved from the surrounding granitoid plutons could have interacted with the crystallizing rocks in the early stages of the greenstone belts (Viljoen and Viljoen, 1969). Metamorphic studies on the lower Onverwacht rocks have highlighted that the regional metamorphism that affected the Barberton greenstone belt and the associated ultramafic-mafic intrusions may be a result of sea floor alteration and the subsequent burial metamorphism (Cloete, 1991, 1999; Ficq et al., 2018; Kareem, 2005). More recently, Bolhar et al. (2021) reaffirmed the sea floor alteration option using secondary geochemical signatures displayed by the Stolzberg Complex.

4. Geographical locations of the Barberton layered complexes

The main aim of this section is to determine whether the layered complexes are an integral part of the Barberton greenstone belt or they were emplaced tectonically later during a deformation phase of the belt. This is done through assessing the relationship between the major structures of the belt as well as the granitoids that surround the belt and the positioning of the layered bodies. Although the current study is mainly focused on the Stolzberg Complex, for regional context, other Barberton layered complexes are also reviewed.

It has been highlighted that many of the reported Barberton layered complexes (twenty out of twenty-seven) occur linearly along the northern margin of the of the greenstone belt (Anhaeusser, 1969, 2002, 2006; de Wit et al., 2018). In addition, at least four of the remainder occur along the southeastern margin of the belt (Anhaeusser, 1985; MacLennan, 2012). The remaining three complexes occur in the central portion of the belt. This distribution of the layered complexes led Anhaeusser (2006b) to suggest that these bodies mark a suture zone along the northwestern margin of the belt and possibly another one along the southeastern margin. Anhaeusser (2006b) proposed that the layered complexes in the northern domain may have initially formed part of a continuous, NE-SW-trending, sheet-like intrusion, or a series of related but disconnected sills aligned and traceable at least over the entire present-day extent of the northern boundary of the greenstone belt. This arrangement of the bodies was then disrupted by later deformation events, possibly one that accompanied the magmatic emplacement of the Kaap Valley Pluton. These, supposedly allochthonous, layered bodies are envisaged to have been emplaced tectonically into the Onverwacht Group volcanic succession (Anhaeusser, 2006b; de Wit et al., 1987; 2018; MacLennan, 2012). Anhaeusser (2006b) went on to suggest that the aligned layered complexes represented the true suture zone along which the northern and southern domains of the BGB were merged.

4.1. Schist belts and layered complexes clusters

Historically, the greenstone terrains situated north of the Inyoka-Saddleback fault system were studied as separate sections or partitions, referred to as schist belts, as opposed to more regional considerations. This approach /was mainly based on the nature of their geographical distribution and seeming discontinuities amongst them, but not presumed contrasting origins. Exploration for mineral resources and mining greatly influenced the choice of areas of interest. Figure 2A shows the locations of these schist belts (together with the layered complexes they host) that make up the northern domain of the Barberton Greenstone Belt. Based on geographical location alone, the layered complexes seem to occur in clusters.

On the extreme northeastern portion of the BGB lies the Kaapmuiden-Malelane schist belt, which hosts the Ship Hill, Budd, Koedoe, Central, and Magnesite-Canal complexes (Viljoen and Viljoen,

1970; Anhaeusser, 2019). To the southwest of this area, there is a greenstone terrain, which stretches towards the northwest, nearly perpendicular to the regional northeast-southwest-trend of the BGB, referred to as the Jamestown schist belt (Anhaeusser, 1972, 1976). This schist belt hosts the Handsup, Mundt's Concession, Hillside, and Kaapsehoop complexes (Anhaeusser, 1969; 1972). Further northwest to the area where the Jamestown schist belt disappear below the Proterozoic cover rocks, the Elandshoek Complex occurs adjacent to the exposed Archaean granitoids. The Barclay Vale schist belt, which is completely detached from the Barberton greenstone main land, occurs immediately north of this area (Robb, 1977). This schist belt hosts the Core Zone and Richmond complexes. The thin stretch of greenstone terrain that connects the Kaapmuiden-Malelane schist belt with the Jamestown schist belt hosts the Sugden Siding (Bon Accord) Complex (Tredoux et al., 1989). The Oorschot-Weltevreden schist belt, which hosts the Pioneer, Saw Mill, and Emmenes complexes, is situated to the southwest of the area where the Jamestown schist belt is attached to the BGB main land (Wuth, 1980). Further southwestwards, the Nelshoogte schist belt hosts the Stolzburg, Sterkspruit and Morgenson complexes (Anhaeusser, 2001; de Ronde and Kamo, 2000; Wuth, 1980). The Kalkkloof schist belt, which is also completely detached from the Barberton greenstone belt main land, occurs west of the Nelshoogte schist belt, hosting the Kalkkloof Complex (Menell et al., 1981). In addition to the layered complexes situated in the northern domain, ultramafic bodies that have been reported in the region south of the Inyoka-Saddleback fault system, include the Rosentuin, Granville Grove, Msauli, Havelock, Motjane, Dunbar, Josefsdal, and Forbes Reef complexes (Anhaeusser, 2006a).

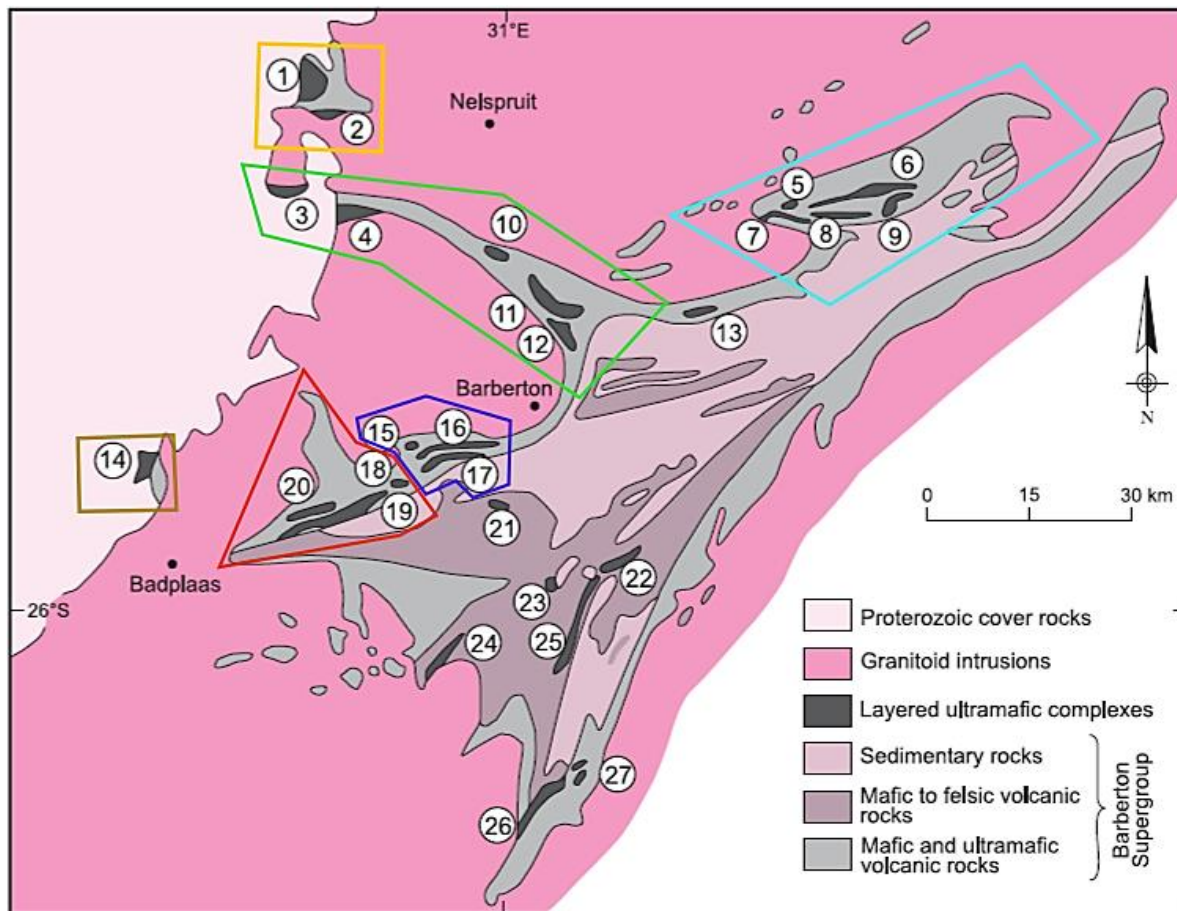


Figure 2A: A map of the Barberton Mountain Land showing locations of the schist belts that makes up the northern domain of the BGB (Anhaeusser, 2006a): Nelshoogte schist belt (red polygon); Oorschot-Weltevreden schist belt (navy blue); Jamestown schist belt (green polygon); Kaapmuiden-Malelane schist belt (sky blue); Barclays schist belt (orange polygon); Kalkkloof schist belt (brown polygon). The locations of the layered complexes are also shown: 1. Core Zone; 2. Richmond; 3. Elandshoek; 4. Kaapsehoop; 5. Ship Hill; 6. Magnesite-Canal; 7. Budd; 8. Central; 9. Koedoe; 10. Hillside; 11. Mundt's Concession; 12. Handsup; 13. Sugden Siding, Bon Accord; 14. Kalkkloof; 15. Emmenes; 16. Sawmill; 17. Pioneer; 18. Morgenson; 19. Stolzburg; 20. Sterkspruit; 21. Granville Grove; 22. Havelock; 23. Dunbar and Josefsdal; 24. Rozentuin; 25. Msauli; 26. Motjane; 27. Forbes Reef.

4.2. Spatial positioning and attitude of the layered complexes

In this section, the positioning and attitude (dip and younging direction) of the layered complexes relative to each other and their surroundings are reviewed. The focus is on the complexes that are situated north of the Inyoka-Saddleback fault system. The main goal is to attempt to determine whether the complexes were magmatically or tectonically emplaced into the Onverwacht supracrustal succession.

Some complexes are situated near the greenstone-granitoid contacts whereas other are located considerably further away from the contacts. It is found that there is regularity between the position of the complex relative to the greenstone-granitoid contacts and the attitude of the complex. Those that occur near the contacts, without exception, face towards the interior of the greenstone belt (i.e., the younging direction points away from the adjacent pluton), whereas those that are situated further away from the contacts occur in antiformal structures located away from the greenstone-granitoid contacts. Selected complexes (based on the availability of information) are examined below.

4.2.1. Pioneer, Saw Mill, and Emmenes complexes

Detailed geological studies on the Pioneer, Saw Mill and Emmenes complexes were conducted earlier by Wuth (1980) and more recently by Cooper (2008), Thompson-Stiegler et al. (2012) and Huber and Byerly (2018). In addition, a review was provided by Anhaeusser (2006a). As mentioned above, these complexes are hosted by the Oorschet-Weltevreden Schist Belt. The northern boundary of the schist belt is marked by an intrusive contact with the Kaap Valley Pluton whereas the southern boundary is a tectonic contact marked by the Moodies Fault.

The Emmenes Complex is the northernmost of the three complexes and it is situated near the contact between the Oorschet-Weltevreden Schist Belt in the south and the Kaap Valley Pluton in the north. Using differentiation cycles in the complex, Wuth (1980) was able to establish that the complex is younging to the south. Some considerable distance to the south of the Emmenes Complex, the Saw Mill Complex is encountered. A short distance (about 400 m, Huber and Byerly, 2018) further south the Pioneer Complex is encountered. Ultramafic lithologies of the Pioneer and

Saw Mill complexes are interstratified with ultramafic tuffs (Thompson-Stiegler et al., 2008, 2011, 2012) which were initially interpreted as sheared or slaty rocks of the complexes. Cooper (2008) and Thompson-Stiegler. (2012) used preserved cross-bedding in the tuffs as well the differentiation cycles to demonstrate that the Pioneer complex is younging to the south. Using the same methods, Huber and Byerly (2018) were able to show that the Saw Mill Complex is facing to the north.

The Pioneer complex extends across the entire NE-SW length of the Oorschot-Weltevreden Schist Belt and its NE-SW-striking southern boundary is marked in the east by the Moodies Fault and in the west by the Oorschot-Weltevreden Fault (de Ronde and Kamo, 2000; Thompson-Stiegler et al., 2012; Wuth, 1980). Between the Oorschot-Weltevreden and the Moodies Faults in the west, a narrow succession of the Onverwacht Group supracrustal rocks exists. The northern boundary of the Pioneer complex is marked by the NE-SW-striking Pioneer Fault. The southern boundary of the Saw Mill Complex may be tectonic, but it is not clear whether or not the northern boundary is intrusive or it is marked by a fault.

Wuth (1980), Cooper (2008), Thomson-Stiegler et al. (2012) and Huber and Byerly (2018) noticed the remarkable similarities in the lithologies that constitute the Pioneer, Saw Mill and Emmenes complexes and suggested that these bodies may be structural repetitions of the same, once-extensive, isoclinally folded, layered complex. This proposition is consistent with (and supported by) the spatial and structural arrangement of these bodies as revealed above. I concur with this submission and further suggest that the Pioneer and the Saw Mill complexes occur along an antiformal structure. Moreover, the considerable distance between the Saw Mill and the Emmenes complexes probably represent a synclinal structure.

The contacts between the granitoids and the greenstones have been shown to dip steeply away from the plutons (Minnitt and Anhaeusser, 1992; Kirsters and Anhaeusser, 1995a, b; Anhaeusser, 2010; Van Kranendonk, 2004). The supracrustal successions along the margins of the greenstone belt display the same orientation, where the oldest (and initially deepest) rocks occur closest to the contact and young away from the pluton. These features may be attributed to diapiric emplacement of the granitoids, where the greenstone succession was forcibly and steeply tilted away from the diapir. It is, therefore, concluded that the Emmenes Complex forms part of the succession of the Onverwacht Group that was steeply tilted away from the Kaap Valley Pluton (hence the southward younging direction) during diapiric emplacement.

4.2.2. Handsup, Mundt's Concession, Hillside, and Kaapsehoop complexes

The Handsup, Mundt's Concession, Hillside, and Kaapsehoop complexes are hosted by the Jamestown schist belt. This schist belt constitutes a linear limb or 'branch' of the Barberton Greenstone Belt which projects in a northwesterly direction, almost perpendicularly to the regional NE-SW trend of the BGB. It is a developed synclinal structure which is sandwiched between the Kaap Valley Pluton in the southwest and the Stentor Pluton as well as the Nelspruit Batholith in the northeast. The greatest thickness of the Jamestown schist belt is attained in its southeastern end, where it is attached to the Barberton Greenstone Belt mainland, and generally thins out in the northwestern direction before disappearing below the Proterozoic cover rocks. The Handsup and Mundt's Concession complexes occur to the southeastern end of the belt. Moving in the northwestern direction, the Hillside complex is encountered approximately halfway between the two ends of the schist belt. A farther distance to the northwest, the Kaapsehoop complex is encountered at or near the northwestern end of the belt. The Elandshoek Complex, which occurs further northwest in a 'window' into Archaean rocks, is considered to be the northwestern extension of the Kaapsehoop Complex.

Layered complexes hosted by the Jamestown Schist Belt were documented in detail by Anhaeusser (1969, 1972, 1976; 1986). The Handsup Complex is situated near the intrusive contact between the schist belt in the northeast and the Kaap Valley Pluton to the southwest. The complex constitutes an anticlinal structure which plunges steeply towards the northeast (Anhaeusser, 1972). It is apparent that this anticlinal structure represents drag folding as a result of sinistral movement along the NW-SE-striking Albion Fault, which marks the southwestern boundary of the anticline. To the southwest of the anticline and the Albion Fault, there are unfolded stratigraphically lower units of the complex. This indicates that initially, the complex was simply a linear body with NW-SE trend and facing towards the interior of the schist belt (i.e., to the northeast). A short distance to the north of the Handsup layered body, the Mundt's Concession Complex is encountered. This body represents another anticlinal structure (Ramsey, 1963; Anhaeusser, 1972) but one with general NW-SE-trend, nearly parallel to the regional trend of the Jamestown schist belt. A valley occurs between the Handsup and Mundt's Concession anticlines, which is believed to mark a syncline separating the two bodies (Anhaeusser, 1972). It is thus believed that the two complexes

represent parts of the same sill-like body which has undergone deformation. This suggestion is supported by the lithological equivalence displayed by the two complexes.

Another body, named the Hillside Complex, which resembles the Handsup and Mundt's Concession complexes, occurs approximately halfway through the Jamestown schist belt in the northwest direction. Similar to the Handsup Complex, the Hillside layered body constitutes a drag anticlinal fold but one which is situated near the northeastern greenstone-granitoid contact and steeply plunging to the southwest. A NW-SE-striking sinistrial fault marks the northern boundary of the Hillside Anticline. It is therefore evident that the Hillside Complex initially formed a NW-SE-trending (parallel to the regional trend of the schist belt), linear body with younging direction towards the southwest (i.e., facing the interior of the Jamestown Schist Belt).

The Kaapsehoop Complex is situated at the northwestern end of the Jamestown schist belt and mainly on the southwestern side of the belt. The body constitutes a synclinal structure, parallel to the trend of the schist belt, with a well-developed, northward younging, southern limb and a highly disrupted northern limb (Anhaeusser, 1976). The Kaapsehoop Complex is interpreted as being part of the older greenstone succession of the Jamestown Schist Belt, which was exhumed during the diapiric emplacement of the Kaap Valley Pluton along the southwestern side of the belt, where the succession was steeply tilted towards the northeast.

4.2.3. Ship Hill, Budd, and Koedoe complexes

Layered bodies hosted in the Kaapmuiden-Malelane area include, but are not limited to, Ship Hill, Budd, and Koedoe complexes. These layered bodies are well-documented in Viljoen and Viljoen (1970) and in later reviews by Anhaeusser (1985, 2006a, 2019). Lithologically, all three complexes comprise a peridotitic chill zone at the base, followed by dunitic zone, which is in turn overlain, in stratigraphic order, by orthopyroxenite, websterite, and anorthositic gabbro units. These units constitute one complete differentiation sequence, which is overlain by an upper dunitic zone. An upper peridotitic chill zone is not uncommon. The differentiation sequence is very useful in determining the younging direction. There is no (or very little) doubt that these bodies represent intrusives into the host meta-tholeiites of the Kaapmuiden-Malelane Schist Belt (Viljoen and Viljoen, 1970).

The Koedoe layered body constitutes an asymmetrical synclinal structure, with a well-developed northern limb and a poorly-developed southern limb, whose origin is ascribed to sinistral movement along the Stentor Fault. This fault marks the southern boundary of the Koedoe Syncline and it facilitated westward translation of the Koedoe Complex. Similarly, the Ship Hill complex forms an asymmetric synclinal structure, which is also a result of movement along a bounding fault. However, in this case, the movement along the fault is dextral, implying that the layered body was pushed towards the east. In contrast, the Budd complex only displays a minor bent in its central section, as opposed to drag folding.

Reconstruction of these bodies shows that all three were initially younging to the south. It is therefore concluded that these three complexes initially formed one continuous sill which was disrupted by late deformation events. The spatial and petrogenetic relationship to the other complexes (namely, Central, Magnesite, Canal bodies) occurring in the area is not clear due to lack of information.

4.2.4. Stolzberg, Sterkspruit, and Morgenson Complexes

The Nelshoogte Schist Belt forms a triangular, funnel-shaped, synclinal structure (fig. 2B) whose origin is ascribed to gravitational collapse of the Onverwacht Group succession between diapirically emplaced Nelshoogte Pluton in the west and the Kaap Valley Pluton in the north, with buttressing effect of the adjacent greenstone sequence in the southeast (Anhaeusser, 1984, 2001). This structure is essentially constituted by three synclines, which plunge towards a central location (i.e., the core of the structure).

The Stolzberg Complex is amongst the most studied layered complexes in the Barberton Mountain Land (Anhaeusser, 1976, 1986, 1985, 2001; de Wit et al, 1987, 2018; MacLennan, 2012; Rodel, 1993; Bolhar et al., 2021). The complex is situated considerably far from the contact between the Nelshoogte Schist Belt and the granitoids (Nelshoogte and Kaap Valley Plutons). The Southern boundary of the Stolzberg Complex is marked by the Belvue Fault. A narrow Onverwacht Group succession is sandwiched between the southern boundary (Belvue Fault) of the Stolzberg Complex and the northern boundary (Moodies Fault?) of the Stolzberg Syncline in the eastern section (de

Wit et al., 1987). The Moodies and Belvue faults probably merge on the southeastern side of the Stolzberg Complex (Anhaeusser, 2001). The Stolzberg Syncline, situated to the south, is juxtaposed against the Stolzberg Complex along the Belvue Fault. The northwest boundary of the Stolzberg Complex is obscured, making it difficult to determine whether the contact is tectonic or intrusive (see later). While the Stolzberg Complex is dipping (Van Biljon, 1964) and younging to the southeast, supracrustal rocks of the Nelshoogte Schist Belt, which lie to the north of the complex, have been shown to face in the opposite direction- to the northwest (Anhaeusser, 2001).

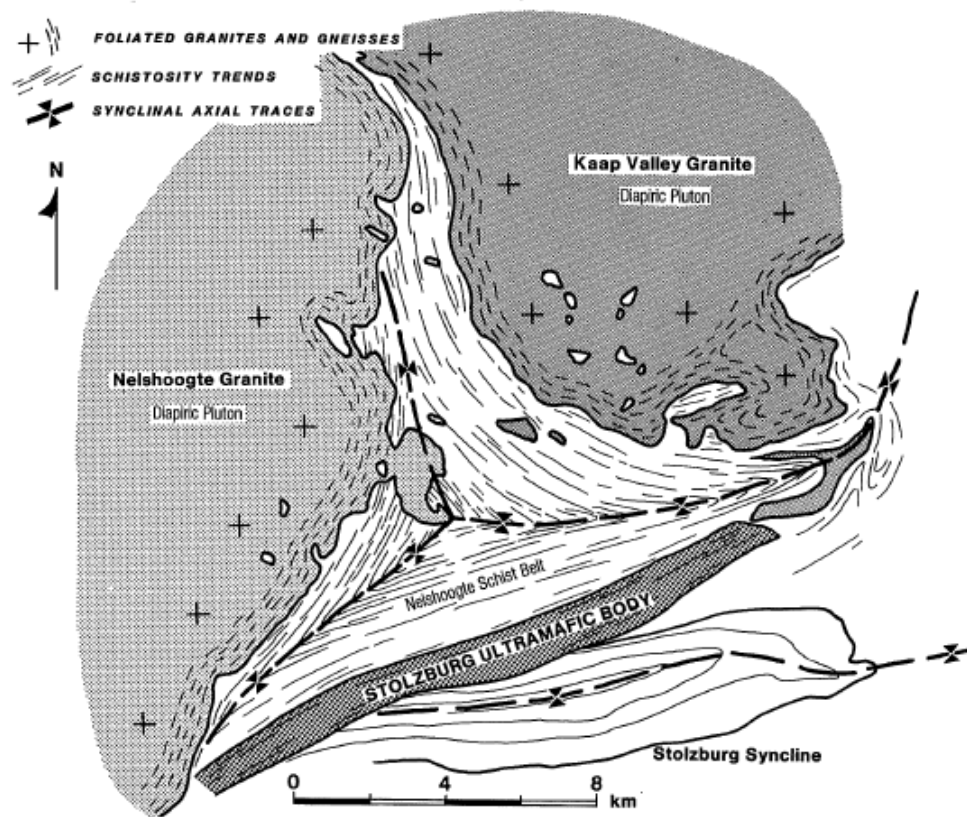


Figure 2B: A map illustrating the structure of the Nelshoogte Schist Belt as well as its relationship with the enveloping granitoids (after Anhaeusser, 1983). Notice that the Stolzberg Complex is wedged between the Stolzberg Syncline in the South and the Nelshoogte Synclinorium in the north.

Immediately north of the Stolzberg Complex lies a differentiated body known as the Sterkspruit Gabbro. The Sterkspruit body (Anhaeusser, 2001; Conway, 1997) is unique from all the other

Barberton complexes in that its bulk composition is mafic as opposed to ultramafic. The complex has been interpreted to have a younging direction towards the South together with the Stolzburg Complex (Conway, 1997). Here, I contest this suggestion and propose that the body is actually younging to the north together with the enveloping succession of the Nelshoogte Schist Belt. Conway (1997) arrived at this conclusion based on the fact that: of the four lithological zones of the Sterkspruit Gabbro, the only unit that display cumulate textures occurs to the north, interpreted as the oldest layer. In addition, a quartz-rich gabbro unit (south-most zone) and quartz diorite layer occur to the South. Interestingly, the quartz diorite unit, interpreted as a “late stage differentiate”, occurs north of the quartz-rich gabbro. The author also reported the occurrence of northerly-dipping, fine, rhythmic layering in the north-lying cumulate zone. This feature suggests that the Sterkspruit body is either younging to the north or it was overturned. The latter case is unlikely given that the Stolzburg Complex, situated a short distance to the south, does not appear to be overturned. Another piece of evidence that suggests northerly younging direction is that the MgO content in the cumulate zone increases to the South. This feature suggests that the most primitive phases were accumulated in the southern portion of the unit. This demonstrates that the Sterkspruit Gabbro is younging to the north. Provided that the Sterkspruit Gabbroic Body was emplaced into the supracrustal succession of the Nelshoogte Schist Belt before deformation by the diapiric emplacement of the Nelshoogte and Kaap Valley Plutons, the suggested southward younging direction for the body implies that the lavas “sandwiched” between the Stolzburg Complex and the Sterkpruit Gabbro are also younging to the South. This in turn insinuates the presence of a tectonic contact between the northern side of the Sterkspruit Gabbro and the northerly dipping lava in the north. Such a contact does not exist, in fact, Conway (1997) reported a rather continuous non-tectonic contact between the northern portion of the Sterkpruit Gabbro and the Nelshoogte Schist Belt lavas. It is, therefore, suggested that the “sandwiched” lavas are also younging to the north, together with the Sterkspruit Gabbro and the supracrustal succession to the north. This remains to be confirmed.

Based on the spatial configurations between the supracrustal rocks of the Nelshoogte Schist Belt, the Stolzburg Complex and the Sterkspruit Gabbro, together with the established younging directions, it is concluded that the Stolzburg Complex marks an anticlinal structure between the Stolzburg Syncline in the south and the syncline of the Nelshoogte Schist Belt that lie to the north of the complex.

The Morgenson Complex is situated near the intrusive contact between the Kaap Valley Pluton and the eastern portion of the Nelshoogte Schist Belt (de Ronde and Kamo, 2000; Wuth, 1980). Information about the attitude of this complex is not available but the body is most probably younging to the south, representing an exhumed older succession of the Onverwacht Group stratigraphy.

4.2.5. Kalkkloof Complex

The Kalkkloof schist belt, which hosts the Kalkkloof Complex, is situated west of the Nelshoogte Schist Belt. Studies on this entity have been conducted by Menell et al. (1981). The Kalkkloof Complex has been demonstrated to young in a westerly direction; gabbroic units occur on the western side of the westerly-dipping complex. The complex disappears below younger Proterozoic cover rocks, meaning its western margin is marked by this contact.

The resemblance of the Stolzberg layered body displayed by the Kalkkloof Complex led Anhaeusser (2006b) to suggest that the latter was prized-off of a once continuous layered body, which is today represented by the Stolzberg Complex. Geophysics show connectivity between the southwestern tip of the Nelshoogte Schist Belt and the Kalkkloof Schist Belt (MacLennan, 2012; de Wit et al., 2018). This connection is manifested by the detection of magnetic greenstone lithologies along the contact between Nelshoogte and Badplaas Plutons (see below). The greenstone lithologies, which trace out the linkage between the two schist belts, have been observed along the contact between the two plutons (Kirsters et al., 2010). This apparent connectivity between the Nelshoogte and Kalkkloof Schist Belts, together with the remarkable similarities between the Stolzberg Complex lithologies and those of the Kalkkloof Complex, are consistent with the suggestion that these two layered bodies were once part of one continuous sill-like complex, which was disrupted by later deformation event(s), particularly the magmatic emplacement of the Nelshoogte Pluton. This would suggest that the Kalkkloof Complex, like the Stolzberg Complex, was initially facing to the southeast.

4.2.6. Core Zone and Richmond Complexes

Robb (1977) demonstrated that the Barclays Schist Belt forms a synformal structure, where the margins dip towards the centre of the belt. In addition, based mainly on geochemical trends, the author was able to show that the Core Zone and Richmond complexes, hosted by this schist belt, also young away from the margins of the belt.

4.2.7. Sugden Siding (Bon Accord) Complex

South of the Stentor Pluton occurs the Sugden Siding ultramafic Complex, which is known for its peculiar, both mineralogically and chemically, Ni-Fe oxides deposit (now mined out), termed the Bon Accord body. Detailed studies on the Sugden Siding body were conducted early by Tredoux et al. (1989) and more recently by Chabangu (2015). This complex comprises coarse-grained serpentinized peridotites with minor (ortho?)pyroxenites. The northern and southern boundaries of the layered body are southerly dipping (away from the BGB-Stentor Pluton contact) thrusts. The complex also dips to the south. The younging direction of this body is not known but, given its position, it is likely to be to the south as well. Tredoux et al. (1989) interpreted the complex as an Alpine-type tectonite, representing a remnant of an Archaean mantle.

4.2.8. Summary of findings and implications

The study finds that there are two relative geological positions where the layered complexes occur. Complexes that occur near the margins of the greenstone belt are steeply dipping and younging in a direction away from the adjacent pluton. These layered bodies are interpreted as being part of older Onverwacht Group rocks, which were exhumed as a result of the diapiric emplacement of the adjacent plutons. These diapirs forceful and steeply tilted the Onverwacht succession away from the intruding body. In contrast, complexes that are situated a considerable distance away from the margins of the greenstone belt occur along attenuated anticlinal structures, which are usually positioned adjacent to well-developed synclines, and separated by steeply-dipping, generally NE-SW-striking, longitudinal faults. Along these faults, older rocks of the Onverwacht Group are juxtaposed against the younger sedimentary successions. Complexes that occur along the anticlinal

structures are therefore interpreted as being part of the older Onverwacht Group lithologies that are exposed along the cores of the anticlines. This reconstruction, therefore, implies that the Barberton ultramafic-mafic layered complexes are autochthons, contrast to the belief by some workers that these bodies represent tectonically-emplaced, Alpine-type tectonites into the supracrustal succession of the Barberton Greenstone Belt. The conformable nature between the layering of the complexes and that of the surrounding metavolcanics support this suggestion.

5. Archaean geodynamics

In a quest for feasible geodynamic settings for the origin of Archaean ultramafic-mafic complexes, it is imperative to assess the validity of the notion that plate tectonics operated in the early Archaean. The logic employed is that: if there was no plate tectonics in the Kaapvaal area at the time of formation of the Stolzberg Complex, then plate tectonic settings cannot be considered as possible environments from which this layered body originated. If plate tectonic settings are found to be infeasible, non-uniformitarian settings should instead be considered.

Despite decades of research into Archaean tectonics, the geodynamic setting for Archaean terranes remains highly controversial (Bédard, 2006, 2017; Condie and Kröner, 2008; Glikson, 2014; Smithies et al., 2018; Van Kranendonk, 2007). It remains unclear whether or not modern-style plate tectonics operated in the Archaean. There are two schools of thought on this topic. One group advocates for uniformitarianism, invoking modern-day plate tectonic settings for Archaean terranes (e.g. de Wit et al., 2018), while the other group rejects the operation of plate tectonics in the Archaean and proposes unfamiliar non-plate tectonic geodynamic settings for the origin of Archaean terranes instead (Bédard, 2006, 2017; Francois et al., 2014; Van Kranendonk et al., 2003). This divergence in views relating to the role of plate tectonics in shaping the Archaean rock record is rooted on disagreements around the timing of onset of this mechanism. Many workers are in support of the onset of plate tectonics only towards the late Archaean (Bédard, 2017; Bédard et al., 2012; Bolhar et al., 2017; Condie, 2018; Cawood et al., 2018; Hansen, 2015; Harris and Bédard, 2014a; Hickman and Van Kranendonk, 2012; Kamber, 2015; Laurent et al., 2014; McCall, 2003; O'Neal et al., 2013, 2016; Smithies et al., 2018; Stern et al., 2017; Van Hunen and Van den Berg, 2007; Van Kranendonk, 2007; Van Kranendonk et al., 2014, 2015; Wiemer et al., 2016,

2018), whereas others are convinced that the process may have operated throughout much of the geological time, perhaps as early as during the Eoarchaeon, or even in the Hadean (De Wit & Ashwal, 1996; Harrison et al., 2008; Reimink et al., 2018; Smart et al., 2016; Sotiriou et al., 2018; Wyman, 2013, 2017). Condie and Kröner (2008) and Gerya (2014) suggested that plate tectonics began locally and became progressively more widespread across the planet from the early to the late Archaean, as opposed to it starting as a single global “event” at a distinct time. There is growing consensus that plate tectonic processes in the Archaean, if they existed at all, were not the same as those we are familiar with on modern Earth (Bleeker, 2002; Van Kranendonk, 2007). For example, unlike the modern-style high-angle subduction, shallow subduction or underthrusting is envisaged during the early Archaean (Hastie et al., 2016).

Significant changes in the geological and geochemical rock record are evident towards the late Archaean (Condie, 2018; Cawood et al., 2018; Van Kranendonk, 2007). Some of these changes include the replacement of the dome-and-keel structures in granitoid-greenstone terranes by linear thrust imbricated belts (Cawood et al., 2018; Hansen, 2015; Wiemer et al., 2018); diversification in both the nature and petrogenesis of granitoids in Archaean cratons (Condie, 2018; Gerya, 2014); increasing proportion of basalts with “arc-like” geochemical signatures (Condie, 2018); and appearance of eclogitic inclusions in diamonds (Condie, 2018). Evidence of significant lateral movements (such as palaeomagnetic data; Cawood et al., 2018) and the occurrence of ductile mylonite-bounded geological terranes (Nutmans et al., 2002; Van Kranendonk, 2007) become common after this period. These changes in the rock record are interpreted to be a result of changes in the geodynamic behavior of the Earth, involving steady transition from a non-plate tectonic regime to the plate tectonic-dominated regime (i.e., the onset of plate tectonics), during this period (Condie, 2018; Cawood et al., 2018). There is notable absence of convincing ophiolites, blueschist facies metamorphic rocks, and Phanerozoic-type accretionary prisms from the Archaean rock record (Bédard, 2012, 2017; Condie, 2018; Furnes et al., 2007; Gerya, 2014; McCall, 2003; Stern, 2005). These features are thought to be products of seafloor spreading and subduction settings, respectively, hence their absence or scarcity from Archaean terranes is regarded as an indication that there was no seafloor spreading or subduction in the Archaean Eon (Bédard, 2017; Furnes et al., 2007). McCall (2003) suggests that the absence of these features in the Archaean terranes may not necessarily preclude the existence of plate tectonics in the Archaean Eon, but that the form or nature of plate interaction was possibly different then. Other workers propose that the scarcity of

true ophiolites and blueschist facies metamorphic rocks is, respectively, a result of preferential preservation of only the upper basaltic units of oceanic crusts and a reflection of steeper subduction geotherms and slower rates of exhumation during the Archaean (Condie and Kröner, 2008).

Advocates of uniformitarianism base their argument on the common recognition of Archaean contractional deformation fabrics; the not-uncommon identification of accreted Archaean terranes, and the existence of the “arc-like” trace element signatures (i.e., depletion of Nb, Ta and Ti relative to Th and LREE (Polat et al., 2011)) exhibited by some Archaean rocks (Bédard et al., 2012; Johnson et al., 2016). These arguments are motivated by the fact that in the modern Earth, accretion of terranes, the generation of magmas (from the hydrated and enriched mantle wedge) with the “arc-like” geochemical signatures, and terranes exhibiting fabrics formed by bulk shortening are confined to convergent margins (Bédard, 2017; Furnes et al., 2007; Johnson et al., 2016). Opponents of the uniformitarian models have, however, proposed alternative explanations for these features that are ascribed to plate tectonics. McCall (2003) has warned that similar petrotectonic assemblages and geochemical signatures should not necessarily be regarded as an indication of similar geodynamic environments. In addition, it has been argued that the “arc-like” geochemical signatures displayed by some Archaean rocks are not necessarily unique to subduction environments but may as well be products of other mechanisms (such as delamination, sagduction, and/or contamination) of enriched mantle sources (Bédard, 2006; Johnson et al., 2016; McCuaig et al., 1994; Xie et al., 1993). Many workers believe that unfamiliar mechanisms are more plausible at the higher temperatures and geothermal gradients that would have characterized the Archaean (Johnson et al., 2016). In the following section, the geological features of the BGB are carefully analysed and alternative interpretations are offered where needed.

5.1. Plate tectonics and suture zone(s) in the Barberton Greenstone Belt

Based mainly on available sedimentological, geochronological and structural data, the BGB is regarded by some workers as an assembly of multiple exotic domains with contrasting origins. While most of these workers consider the greenstone belt as two distinct terranes (namely, southern and northern domains) which were amalgamated along the Inyoka-Saddleback fault system (fig. 1A) (de Ronde and de Wit, 1994; de Ronde and Kamo, 2000; de Wit et al., 1992, 2018; Kröner et al., 1996; Schoene et al., 2008), Lowe (1994, 1999) and Lowe and Byerly (2007) regard it as a collection of tectono-stratigraphic blocks which were largely accreted magmatically, possibly

along rifted margins of the older domains, as opposed to tectonic accretion of exotic terranes along convergent plate margins. The structures that are regarded as boundaries to the tectono-stratigraphic blocks in Lowe (1994, 1999) and Lowe and Byerly (2007) actually represent the longitudinal faults of the D_2 deformation event. Lowe and Byerly (2007) envisage plume and rift settings for the origin of the ultramafic-mafic rocks of the Onverwacht Group as opposed to intra-oceanic arc environments suggested by the other workers. Workers who regard the Inyoka-Saddleback fault system as a suture zone between the southern and northern domains envisage a collisional event at about 3230 Ma along this structure. According to them, the collisional event was preceded by closure of an ocean, following subduction of a southern oceanic terrane below a northern oceanic terrane which eventually led to the collision of the two cratonic blocks believed to represent island arcs. The regional NE-SW trend of the BGB and the regional-scale, generally NE-SW-trending, isoclinal folds and longitudinal faults have been attributed to this event. However, these deformation and structural features of the Barberton Greenstone Belt have alternatively been ascribed to partial convective overturn and diapiric emplacement of the granitoid plutons in the northwest of the belt (Anhaeusser, 1975, 1984; Van Kranendonk, 2021; Van Kranendonk et al., 2004, 2011, 2014).

The northern domain of the Barberton Greenstone Belt is generally regarded (by the proponents of the accreted exotic terranes model) as a younger block than the southern domain (de Wit et al., 2011, 2018; Lowe and Byerly, 2007). This suggestion is at odds with the occurrence of a ca. 3.4 Ga dioritic body immediately east of the Barclay Vale Schist Belt (i.e., north of the northwestern tip of the Jamestown Schist Belt) (Wang et al., 2018). In addition, granitic pebbles and boulders, believed to have been derived from the north (Anhaeusser, 1969, 1976), and dated at 3570 – 3518 Ma (Kröner and Compston, 1988; Sanchez-Garrido et al., 2011), have been reported in the Moodies Group rocks of the Eureka Syncline. The above observations suggest that the northern domain is actually much older than present suggestions.

The notable similarities between the northern and southern facies of the pre-collisional Fig Tree Group suggest that these rocks may have been deposited in different parts of a one large sedimentary basin (Lowe and Byerly, 1999, 2007; Zeh et al., 2013). There are notable Fig Tree Group facies variations within the southern domain as well (Lowe and Byerly, 1999), supporting contemporaneous deposition in multiple sub-basins.

Previous attempts to regard the Barberton Greenstone Belt (and other Archaean greenstone belts) as an ophiolite have been invalidated (Dann, 2000; Hamilton, 1998, 2003; McCall, 2003). de Wit et al. (1987) and de Wit (2004) interpreted the entire Onverwacht Group as an intact ophiolite sequence, where the Komati Formation was interpreted as a sheeted dyke complex and the Stolzberg Complex was interpreted as the ultramafic base of the oceanic lithosphere (that is, an uppermost oceanic lithospheric mantle). It was later shown that the Komati Formation actually represents a subvertically-rotated sequence (Cloete, 1991; Dann, 2000). Additionally, Rodel (1993), in contrast to the claim made by de Wit et al. (1987), showed that the Stolzberg Complex does not exhibit a V-shaped REE pattern which is characteristic of alpine-type peridotites. This finding is reaffirmed in the present study (fig. 6.2.1A). Thus, it is concluded that the Stolzberg Complex (and possibly other Barberton layered bodies) do not represent alpine-type peridotites.

More recently, some workers (e.g., de Wit et al., 2011, 2018; Furnes et al., 2013; Lowe and Byerly, 1999, 2007) challenged the “layer-cake” stratigraphy of the Onverwacht Group (Viljoen and Viljoen, 1969) and re-interpreted the entity as a collage of tectonically-stacked oceanic slabs, which were formed in spreading centre or intra-oceanic arc environments. These workers nevertheless acknowledged the complete absence of sheeted dyke complexes in these rock packages. Additionally, the Komati Fault (fig. 1A), which is regarded by these workers as a tectonic boundary along which the Komati Formation of the Onverwacht Group was thrust (in a southwesterly direction) over the older domain constituted by the Theespruit and Sandspruit formations, has been shown to display an extensional sense of movement (i.e., normal faulting) (Anhaeusser, 2010; Kisters et al., 2003). The notable scarcity of ca. 3.4 Ga generation felsic rocks in the Komati Formation further argues against the suggestion that this sequence once constituted an overriding plate. Other workers suggest that Archaean greenstone belts represents partly preserved fragments of oceanic lithosphere (Dewey, 2003; Sengör and Natal'in, 2004). This would imply that the complete absence of sheeted dyke complexes in all Archaean greenstone belts is a result of preferential elimination of this section of ophiolites, but leaving behind the top section comprised of pillowed lavas. There is no conceivable process that can be deemed capable of developing such geological entities. It is, therefore, very unlikely that such a process occurred. The layered complexes are also regarded as basal components (compared to the peridotitic section of ophiolites) of the northern oceanic terrane which was obducted over the southern terrane along the envisaged northerly-directed subduction zone (de Wit et al., 2018; MacLennan, 2012). However,

despite the fact that the deposition of the Fig Tree Group started at ca. 3260 Ma (Byerly et al., 1996) and the envisaged collisional event occurred at ca. 3230 Ma (de Ronde and Kamo, 2000), about 30 million years later, none of the layered complexes are hosted in the Fig Tree Group, which should have been the topmost sequence at the time of collision. Instead, all of the complexes display conformable relationships with the host Onverwacht Group metavolcanic succession (Anhaeusser, 1985, 2006b). It is therefore inferred that geodynamic environments, such as spreading centre and MOR settings, from which Phanerozoic-type oceanic crust originate, did not exist at least in Palaeoarchaeon times.

There are other features which have been considered to represent surviving vestiges of subduction zone processes at ca. 3.2 Ga in the region presently referred to as Barberton Mountain Land (or Barberton Granitoid-Greenstone Terrane). These include the presence of high pressure and moderate temperature metamorphic rocks in the southwestern portion of the BGB (Moyen et al., 2006) and the apparent alignment of the layered complexes along the northwestern margin of the belt (Anhaeusser, 2006a).

Further south of the southwestern tip of the BGB, a regional, NNE-SSW-trending, subvertical, linear, structural feature, named Inyoni Shear Zone, exists, which marks a contact between the ca. 3.4 Ga Stolzburg Pluton on the eastern side and the ca. 3.2 Ga Badplaas Pluton to the west (fig. 1A) (Kirsters et al., 2010; Moyen et al., 2006). This structure has been interpreted by these authors as a southward extension of the Inyoka-Saddleback Shear Zone, marking a continuation of the suture along which the northern and southern domains of the BGB amalgamated at ca. 3.23 Ga (Diener et al., 2005). Stevens et al. (2002, 2007) and Moyen et al. (2006) reported the existence of garnet-bearing high pressure and moderate temperature metamorphic assemblages in high strain mafic-ultramafic lithologies in the northern portion of the Inyoni Shear Zone. These workers interpreted the high-pressure metamorphic assemblages as traces of a ca. 3.23 Ga palaeosubduction zone, along which the eastern terrane was subducted below the western terrane. While Moyen et al. (2006) claimed that the high-pressure metamorphic assemblages were formed under a low geothermal gradient of 12 – 15 °C/ km, comparable to modern-day subduction zone conditions, subsequent studies in the same lithologies showed that the geothermal gradient at which these rocks were formed was actually much higher (17 – 22 °C/ km), contrasting with metamorphic conditions reported in vestiges of Phanerozoic subduction zones (Cutts et al., 2014;

Nédélec et al., 2012). Additionally, the garnet-bearing high-pressure metamorphic assemblages have been shown to be restricted to the northern portion of the Inyoni Shear Zone. The central and southern part of the shear zone (e.g. Schapenburg schist belt) display amphibolite-grade metamorphic facies and lower strains (Stevens et al., 2002; Van Kranendonk et al., 2014). Rocks of the southwestern tip of the BGB, situated immediate north of the Inyoni Shear Zone, show an amphibolite-grade contact metamorphic character along the intrusive margins with the surrounding granitoids (Nelshoogte and Stolzberg Plutons to the north and south, respectively), which transition into greenschist facies grade at the core of the body (Kirsters et al., 2003). These notable inconsistencies between features characterizing the Inyoni Shear Zone and those that typify modern subduction zones, combined with detailed structural and kinetic analysis of the high strain northern part of the shear zone, led Brown (2015), Van Kranendonk et al. (2014) and Wang et al. (2018) to provide an alternate model for the origin of the high-pressure metamorphic assemblages. This model proposes that the Inyoni Shear Zone represents a greenstone keel or drip, which was formed during a partial convective overturn episode.

In contrast to the suggestion by Moyon et al. (2006) and Kirsters et al. (2010) that the Inyoni Shear Zone represents a southerly extension of the Inyoka-Saddleback Shear Zone, de Wit et al. (2018) and MacLennan (2012) inferred, based on high-resolution aeromagnetic data, that the Inyoka-Saddleback Shear Zone continues to the west and then northwest in a broad arc that trends towards the Kalkkloof Schist Belt, west of the Nelshoogte Schist Belt (see fig. 1A: the boundary between the Nelshoogte and Badplaas plutons). These authors showed that the high positive magnetic anomalies displayed by the southwestern portion of the Nelshoogte (or Stolzberg) Schist Belt continues along the broad arc towards the northwest (fig. 3). This broad arc actually marks the contact between the Nelshoogte Pluton in the east and the Badplaas Pluton to the west. The maps (Figs. 2 & 3) in Kirsters et al. (2010) show the presence of mafic-ultramafic lithologies along this contact. Results of the aeromagnetic survey show no magnetic anomalies along the Inyoni Shear Zone. It was, therefore, concluded that the broad arc together with the Inyoka-Saddleback Shear Zone traces out a suture, marking a north-directed palaeosubduction zone. This notion suggests that the ca. 3.2 Ga Badplaas Pluton formed part of the supposedly older southern domain, which was underthrust below the northern domain. While the occurrence of the 3.2 Ga generation TTG plutons in the northern domain is consistent with north-directed subduction zone, the predominantly northwesterly vergence of the regional scale NE-SW-trending structures in the

northern domain is at odds with this model; such subduction zone configuration would have resulted in southeasterly verging structures. Furthermore, the occurrence of the Baplaas Pluton (which has a similar age as the envisaged collisional event) in the supposed subducted plate is inconceivable. Alternatively, I propose that the mafic-ultramafic lithologies observed and imaged along the contact between the Nelshoogte and Badplaas Plutons represent wedged greenstones between diapirically emplaced granitoids.

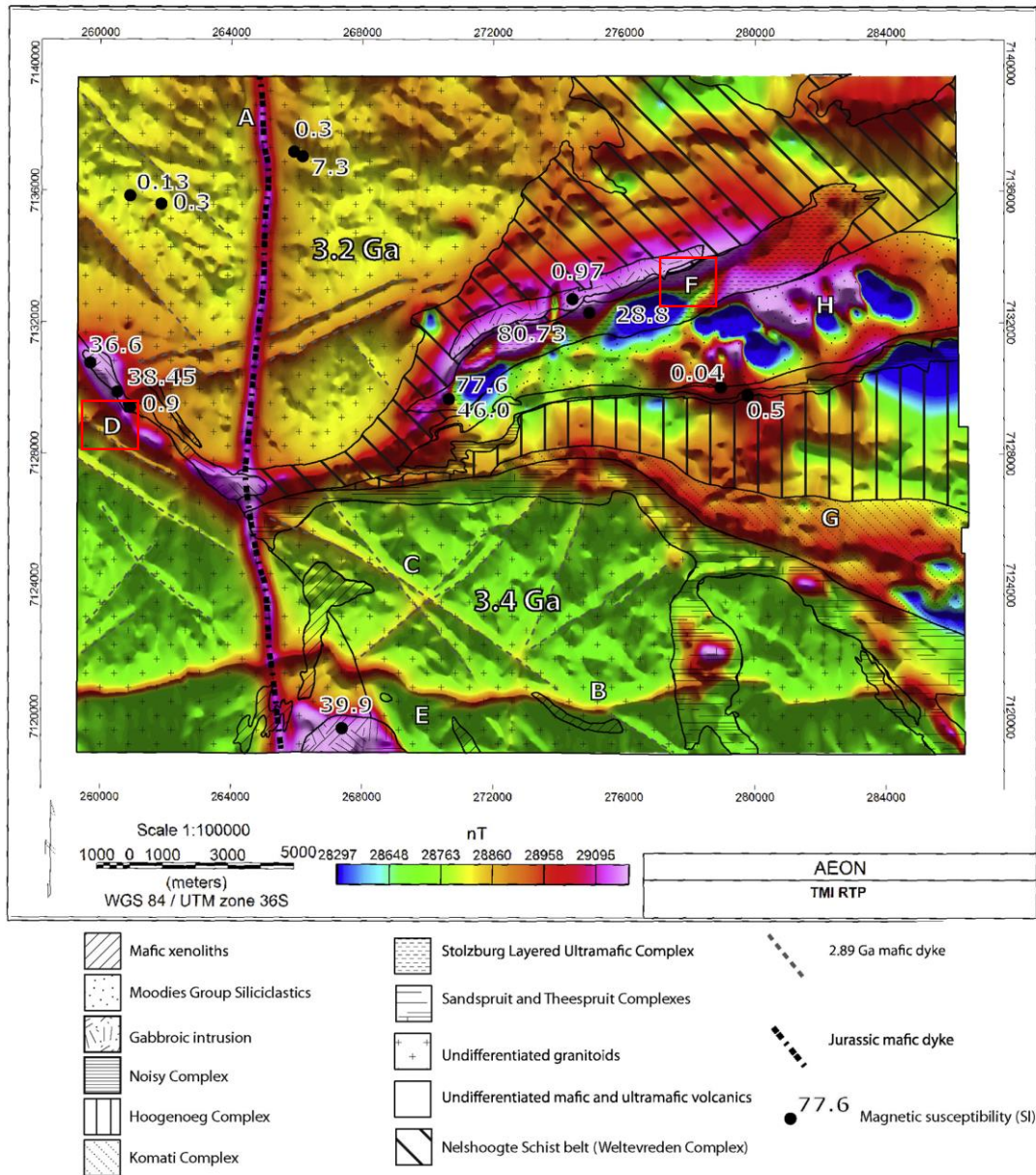


Figure 3: *Magnetic map of the southwestern portion of the Barberton Mountain Land showing the continuation of the highly positive magnetic anomaly of the southwestern tip of the Nelshoogte Schist Belt (location F) in a broad arc (location D) towards the Kalkkloof Schist Belt.*

The absence of regional, uniaxial, foliation in the Barberton Greenstone Belt, particularly on either sides of the Inyoni Shear Zone, as displayed by modern orogenic belts, is noteworthy. Distinctively, this Archaean terrane is characterized by arcuate foliations, parallel to the contacts between the greenstones and the granitoids. This fabric character has been attributed to compressional stresses accompanying the diapiric emplacement of the plutons. This style of plutonism led to the development of the lobe-cusp folding of the adjacent greenstones, resulting in the dome-and-keel structural pattern that characterizes Archaean terranes (Anhaeusser, 1975, 1984; Van Kranendonk, 2011).

The suture zone envisaged by Anhaeusser (2006b) does not overlap with the Inyoka-Saddleback Shear Zone, implying that large parts of the southern portion of the northern domain actually belong to the southern domain. This revelation is rather interesting. Furthermore, the model presented by Anhaeusser (2006b), in contrast to the submissions of de Wit et al. (2018), Kirsters et al. (2010) and Schoene et al. (2008), suggest that the envisaged subduction zone was directed (in the present-day Barberton region) to the southeast. Unlike models which suggest that the postulated ophiolite represents an oceanic northern domain which was obducted onto the southern domain (e.g., de Wit et al., 2018), Anhaeusser (2006) proposed that the northern domain represents preserved fragments of an oceanic crust which was underthrust beneath the southern domain. While the southward-directed subduction is consistent with the reported attitude (i.e., northwesterly vergence) of the structures, it is at odds with the fact that the ca. 3.2 Ga generation TTG granitoids (which were supposedly derived from partial melting of the subducted slab) are situated behind the hypothesized suture zone. The model is also at odds with the paucity of the ca. 3.2 Ga TTG suites in the supposed overriding southern domain. The demonstrated autochthonous character of the ultramafic complexes (Cooper, 2008; Huber and Byerly, 2018; Rodel (1993); Thompson-Stiegler et al., 2012; Viljoen and Viljoen, 1970; this study) argues against the presumed allochthonous identity of these layered bodies, therefore, irreconcilable with the environment envisaged by Anhaeusser (2006b).

Most of the layered complexes, indeed, show a general NE-SW trend. A striking deviation is presented by the (NW-SW) trend of the complexes hosted by the Jamestown Schist Belt. Of importance is the fact that this trend is approximately perpendicular to the general NE-SW strike of the other complexes. Anhaeusser (1969, 2006a, 2019) attributed this discordance to the tearing off and subsequent northeastwards rotation of a northwestern portion of the (generally NE-SW-trending) BGB mainland which today constitutes the Jamestown Schist Belt. This event is ascribed to the diapiric emplacement of the Kaap Valley Pluton. Such a reconstruction requires that the entire length of the Jamestown Schist Belt fit in the area between the Nelshoogte Schist Belt in the southwest and the Jamestown hills area in the northeast. As the Elandshoek Complex is regarded as a northwesterly extension of the Kaapsehoop Complex, this means that the Jamestown Schist Belt continues northwestwards below the Proterozoic cover sequence. It is difficult to conceive fitting such a lengthy linear structure in the relatively smaller suggested space. There are no reports of the existence of prominent NE-SW-trending tensional and compressional structures, respectively, along the southwestern and northwestern sections of the Jamestown Schist Belt, especially at its southeastern end where most of the rotation would have happened. In fact, the Jamestown Schist Belt is geometrically and structurally comparable to the Nelshoogte Schist Belt whose form or shape has been ascribed to the wedging of greenstones in between diapirically emplaced granitoids (Nelshoogte and Kaap Valley Plutons in the west and east, respectively) (Anhaeusser, 1984, 2001). Similarly, I propose that the Jamestown Schist Belt did not undergo any considerable rotation, instead, this entity represents greenstones sandwiched between TTG diapirs which pierced through a regionally continuous ultramafic-mafic crust at ca. 3.2 Ga. The Jamestown Schist Belt is also similar in structure and surroundings to the Tjakastad Schist Belt in the southern portion of the BGB, where greenstones are wedged between the Stolzburg and Theespruit Plutons (Anhaeusser, 2010).

The lack of uncontested physical manifestation of plate tectonic processes together with the predominance of dome-and-keel structural patterns (unique to Archaean terranes), instead of the Phanerozoic orogenic belt, in the Barberton Mountain Land, strongly argues against the operation of Phanerozoic-style plate tectonics in the Archaean. The origin of this terrane is, instead, attributed to a geodynamic environment (dominated by vertical tectonics), which was unique to the Archaean Earth (see later).

6. Samples and methods

6.1. Samples

Samples used in this study were obtained from Prof Carl Anhaeusser's collection of rocks of the Stolzburg Complex. Fifty samples were selected for polished thin sections as well as major and trace elements analyses. Samples were selected in such a way that different lithologies of the Stolzburg Complex are represented, while targeting those that appeared better preserved. Samples locations are indicated on the "geological map of a portion of the Nelshoogte Schist Belt and the Stolzburg Layered Ultramafic Complex, Barberton Mountain Land", published by Anhaeusser (1971). See table A4 for sample names.

6.2. Methods

Polished thin sections were prepared by Mr Caiphus Majola and Mr Sam Tshabalala at the thin sections and ore blocks laboratory, Geosciences building, University of the Witwatersrand, Johannesburg. Petrographical studies were conducted using the Olympus BX53M/DP74 microscope situated at the same building.

Prior to chemical analysis, samples were cleaned to remove any weathered material or potential sources of contamination using a cutting saw. Samples were crushed using a slash hammer while covered in two layers of thick plastic and then milled using a carbon case-hardened pure iron rotary mill. Thirty of the fifty major and trace elements analyses were conducted (using XRF and quadrupole ICP-MS instruments, respectively) by Mr Marlin Patchappa and Prof Allan Wilson at the EarthLab, Bernard Price Building, University of the Witwatersrand, Johannesburg, as described in Wilson (2012). The other twenty analyses were done at the University of Johannesburg by Prof Sebastian Tappe. See table A2 and A3 for the certified reference materials (CRMs) used in the XRF major oxides and ICP-MS trace elements analyses, respectively.

7. Geology of the Stolzburg Complex

7.1. General geology

The Stolzburg Complex is one of the best-preserved Archaean layered ultramafic complexes in the world (Anhaeusser, 1976, 1985, 2001; De Wit et al., 1987; Rodel, 1993). The body is situated in the extreme southwestern portion of the Barberton Greenstone Belt, in a section referred to as the Nelshoogte Schist Belt, geographically located (approximately 15 km) northeast of Badplaas town and southwest of the Barberton town. Along strike, it extends for at least 14 km and has an approximate N-S extent (thickness?) of 1.2 km. To the extreme northeast, the complex is covered by dense plantations of the Nelshoogte Forestry Reserve (Anhaeusser, 2001; de Wit et al., 1987; Rodel, 1993).

The Stolzburg Complex shows pronounced progressive magmatic differentiation stratigraphically upwards and common development of conspicuous macro-rhythmic igneous layering (fig. 4) (Anhaeusser, 2001). It has been subdivided into a Lower Division comprising cyclic repetition of dunite and orthopyroxenite units and an Upper Division displaying cyclicity between harzburgitic and gabbroic rock layers (Anhaeusser, 2001; Rodel, 1993). Abrupt contacts have been observed between the dunite and orthopyroxenite units in the Lower Division (Anhaeusser, 2001). The two Divisions are separated by a zone of Ca-metasomatised gabbros and associated rodingite dykes (Anhaeusser, 1979; MacLennan, 2012; Rodel, 1993). Some workers have proposed that the Lower and the Upper Divisions constitute two unrelated geological entities as opposed to being one stratigraphically continuous body (de Wit et al., 1987, 2018; MacLennan, 2012). At least thirteen cycles (five and eight in the Lower and Upper Divisions, respectively) exist in the complex (Anhaeusser, 1971, 1979; Rodel, 1993). The units of the Lower Division are generally much thicker (up to 480 m and 120 m for dunitic and orthopyroxenitic layers, respectively) than those of the Upper Division. Furthermore, the gabbroic components are minor (up to a thickness of 50 m) relative to the peridotitic complements (with maximum thickness of 100 m) in the Upper Division.

In the field, the orthopyroxenite layers form more prominent, regionally continuous units than the less weathering-resistant dunitic layers. On weathered outcrop surfaces, the dunites display yellowish-green or grey colours whereas the orthopyroxenite rocks show a reddish-brown colour.

In contrast, dunites (which have effectively undergone complete alteration) display green-black or black colours on unweathered surfaces while orthopyroxenites show dark waxy greenish colour and dark blue-green colour on unaltered and altered parts, respectively. In the Upper Division, the gabbroic layers weather negatively and constitutes intervening valleys between ridges comprised of the more resistant peridotitic layers. Orthopyroxene phenocrysts in the harzburgitic layers tend to weather positively.

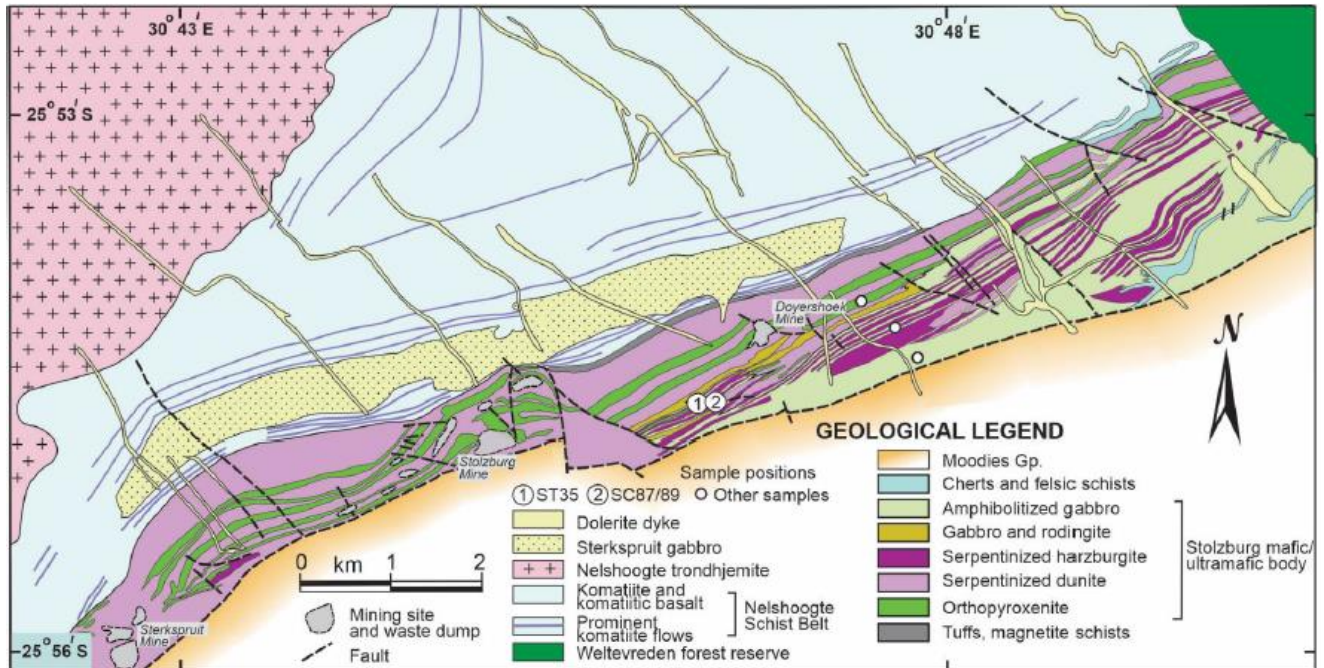


Figure 4: Simplified geological map of the Stolzburg Complex showing the cyclically repetitive, sub-vertically dipping, differentiated sequence (Anhaeusser, 2001 and Bolhar et al., 2021). The sequence youngs to the southeast. The Sterkspruit gabbroic intrusion, which is not genetically related to the Stolzburg Complex, is situated northwest of the Stolzburg Complex.

Similar to the Onverwacht Group mafic-ultramafic volcanics, rocks of the Stolzburg Complex have also suffered an intense alteration, with primary phases being barely preserved. Original lithologies comprised olivine, orthopyroxene, clinopyroxene, and plagioclase in different combinations and varying proportions. Consequently, the secondary (and current) mineralogy of these rocks is as simple, with ultramafic rocks mainly comprising serpentine, talc, chlorite and magnetite and mafic components constituted by actinolite, epidote, chlorite and albite. Although in most cases the rocks have been totally altered, original names are used. The alteration occurred

in such a way that the secondary minerals pseudomorphed after the primary phases. In this way, the primary igneous textures were preserved in spite of the intense alteration. Even though well textural preservations can be observed even in cases of total alteration, in some rocks, textures have been completely destroyed.

Generally, rocks of the Lower Division are coarse-grained whereas those of the Upper Division are medium-grained. The altered dunites and orthopyroxenites of the Lower Division are virtually monomineralic and they display clear cumulate textures as manifested by the predominance of subhedral to euhedral crystals that are in contact with each other without interstitial material. These cumulate textures are not as clear in the harzburgitic and gabbro-noritic units (which are, by definition, not monomineralic) of the Upper Division. These features have critical implications for the history of the igneous layering in the Stolzburg Complex and the origin of the body itself.

As in the counterpart Barberton layered bodies, the Stolzburg Complex has a similar (if not the same) strike as the volcanic succession of the Nelshoogte Schist Belt. However, the relationship between the two entities is complex as the Stolzburg layered body is subvertically dipping and younging to the southeast whereas the adjacent (alongside the northwestern boundary) metavolcanics of the Nelshoogte Schist Belt are facing in the opposite direction (i.e., northwestwards). While the southeastern boundary of the Stolzburg Complex is clearly marked by the Belvue Fault (where the body is juxtaposed against the Stolzburg Syncline to the southeast), the northwestern boundary is obscured. The boundary was interpreted by some workers as a fault contact (Anhaeusser, 1976, 1979; MacLennan, 2012; de Wit et al., 2018) while others envisage an intrusive contact (de Wit et al., 1987; Rodel, 1993).

Although the strike of the layering in the Stolzburg Complex is generally consistent with that of the bedding in the supracrustal rocks of the Nelshoogte Schist Belt, an apparent discordance has been noted in the extreme western section of the complex, in the area north of the Sterkspruit asbestos mine (Anhaeusser, 2001; de Wit et al., 1987, 2018; MacLennan, 2012). Despite it evidently being localized, this feature has been regarded as an indication that the entire northwestern boundary of the Stolzburg Complex is tectonic in nature (MacLennan, 2012; de Wit et al., 2018). These workers further utilized high-resolution aeromagnetic survey data to infer a structural break between the supracrustal rocks of the Nelshoogte Schist Belt and the Stolzburg Complex. In their interpretation, they assign a region of very low magnetization (likely

representing a dipolar effect) (south of location F in fig. 3) to the Stolzberg Complex (a body enriched in magnetite). This interpretation is obviously flawed and inaccurate as it is inconsistent with the clearly ubiquitous magnetic material (magnetite) in the Stolzberg Complex.

North of the Sterkspruit asbestos mine, in the vicinity of the area where layering discordance was noted, de Wit et al. (1987) observed chert units that display brecciation and assimilation features similar to those that have been observed in the Onverwacht Anticline, in the southern domain of the Barberton Greenstone Belt. Moreover, Rodel (1993) reported, in the vicinity of the Stolzberg asbestos mine, a sharp igneous contact between a basal dunite layer of the Stolzberg Complex and metavolcanics of the Nelshoogte Schist Belt. As a result, this author interpreted the northwestern boundary of the Stolzberg Complex to be an intrusive contact. The notable absence of shearing along this boundary (de Wit et al., 1987; Anhaeusser, 2001) together with the general strike consistency everywhere else supports this interpretation.

The deformation of the Nelshoogte Schist Belt has been attributed to the emplacement of the Nelshoogte (dated ca. 3236 Ma; de Ronde and Kamo, 2000) and Kaap Valley (dated ca. 3227 Ma; Kamo and Davis, 1994) plutons on the western and eastern borders of the belt, respectively (Anhaeusser, 1984, 2001). This places the minimum age of the supracrustal rocks of the Nelshoogte Schist Belt at ca. 3236 Ma. Because the Stolzberg Complex seems to have endured the same deformation, this minimum age may also be assigned to the layered body. U-Pb titanite ages ranging from 3236 and 3270 Ma have been obtained from the gabbroic units of the Stolzberg Complex (Ficq et al., 2018). The agreement between the minimum relative age constrained by the intruded Nelshoogte pluton and the lower bound of the obtained radiometric date of the gabbroic units of the Stolzberg Complex is striking. Unfortunately, there are no direct ages obtained from the supracrustal succession of the Nelshoogte Schist Belt to allow comparison with these ages of the Stolzberg Complex. Such a task would shed some light on the relationship between the supracrustal rocks and the complex, allowing further constraints to be placed on the origin of the layered body. Since the Belvue Fault in the south also affected the Moodies Group rocks of the Stolzberg Syncline, it may be inferred that the structure developed in post-Moodies times (< 3225 Ma (minimum age of the Fig Tree Group); Byerly et al., 1996). If this is correct, it would imply that the Stolzberg Complex was juxtaposed against the Stolzberg Syncline only after 3225 Ma. A review of models proposed for the origin of the Stolzberg Complex and its relationship

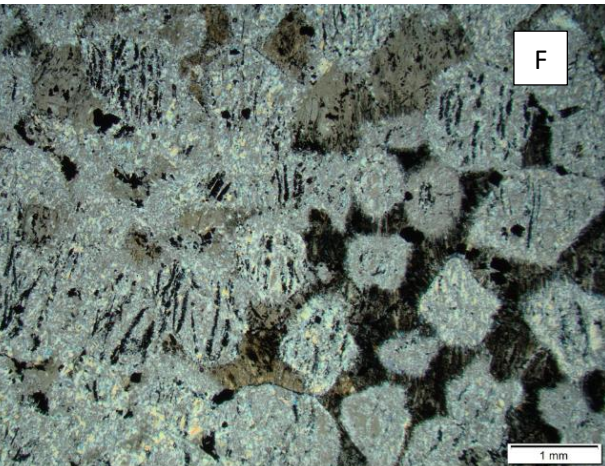
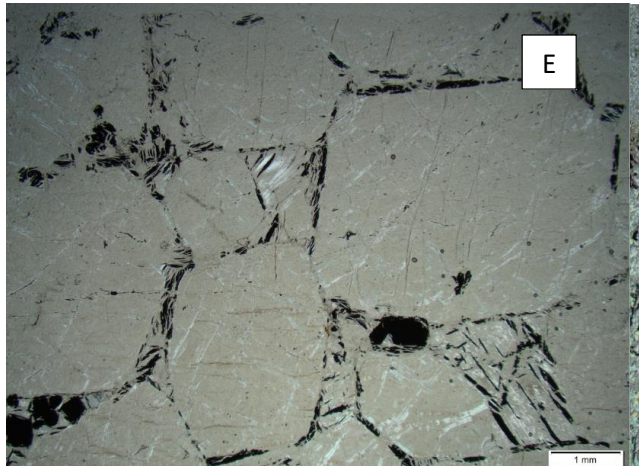
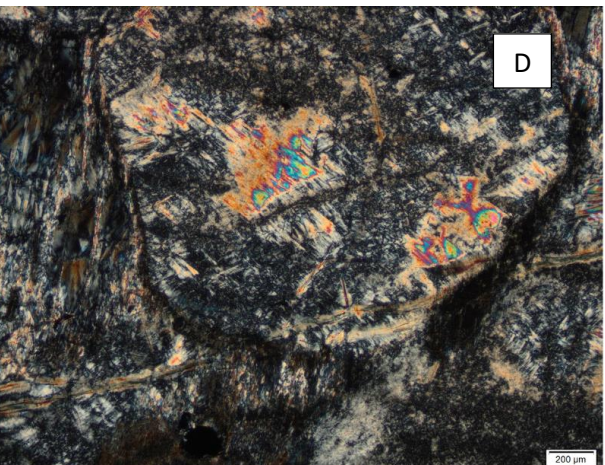
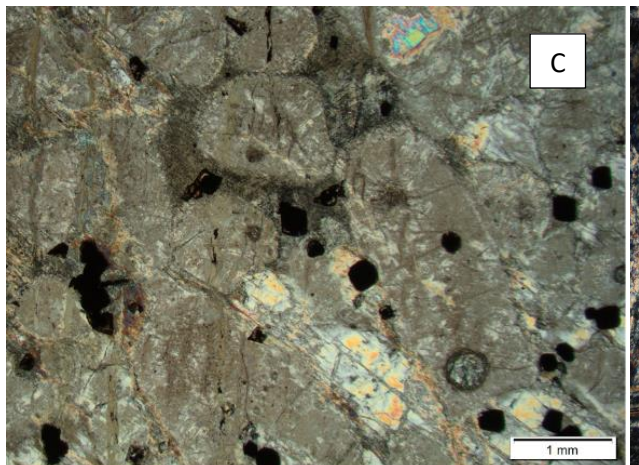
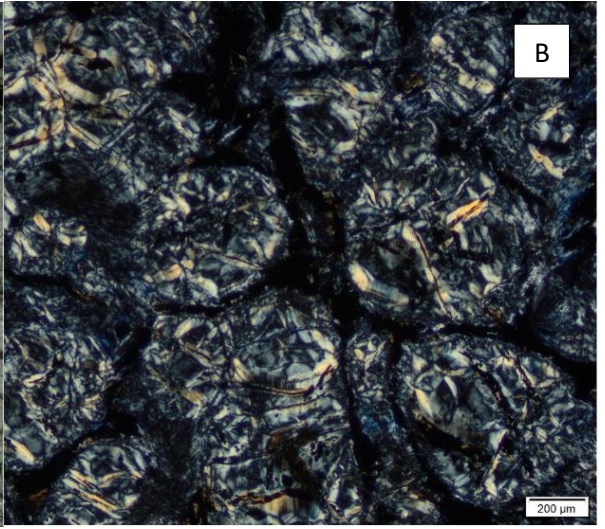
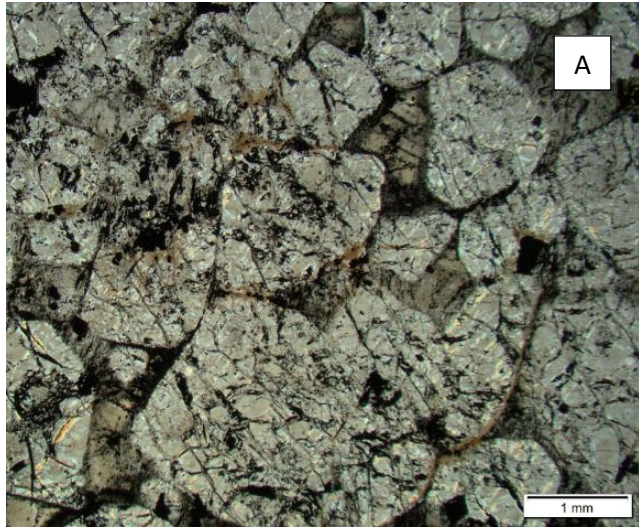
with the adjacent metavolcanic rocks of the Nelshoogte Schist Belt has been provided in earlier sections of this thesis.

7.2. Petrography

Meta-dunites (Serpentinites)

Originally, Stolzburg Complex dunites generally comprised over 80% olivine and minor orthopyroxene and euhedral chromite (see fig. 5.6A). These rocks have been affected by extreme serpentinization, to an extent where all of the primary olivine crystals have been completely replaced by serpentine minerals, i.e. there is no residual olivine. However, in some instances, iddingsite replaced olivine instead (e.g., DH59: fig. 5.1H). Tertiary talc can be observed replacing serpentine (e.g., SM2: fig. 5.1C & D). This is accompanied by the occurrence of thin and irregular talc veinlets (e.g., DH59 & NF6: fig. 5.1G & I, respectively). The intercumulus orthopyroxene is generally altered to talc or bastite (e.g., GV1: fig. 5.1A).

In most cases, the secondary alteration occurred in such a way that the serpentine minerals pseudomorphs the olivine crystals, allowing preservation of primary textures (e.g., GV1 & SM4: fig. 5.1A & B, respectively). Secondary magnetite, which accompanied serpentinization, tends to rim the serpentine minerals, in this way, tracing out the original shapes of the replaced olivine crystals (e.g., DH65: fig. 5.1E). Similarly, altered intercumulus orthopyroxene promoted the preservation of the original crystal shapes and textures (e.g., NF3: fig. 5.1F). Sub-parallel magnetite veinlets in serpentine grains, which presumably trace out fractures along which olivine alteration advanced, can be observed in some samples (e.g., NF3: fig. 5.1F). Where primary textures are preserved, equant and subhedral to euhedral serpentine pseudomorphs are apparent. These features reveal the original cumulus nature of the replaced olivine crystals. Granular textures are apparent, where crystal sizes range from 1 mm to 4 mm with an average of 2 mm. In cases where textures have been destroyed completely, the rocks (under microscope) appear like a mass of microcrystalline serpentine flakes with fine and speckly magnetite (e.g., NF20: fig. 5.1J).



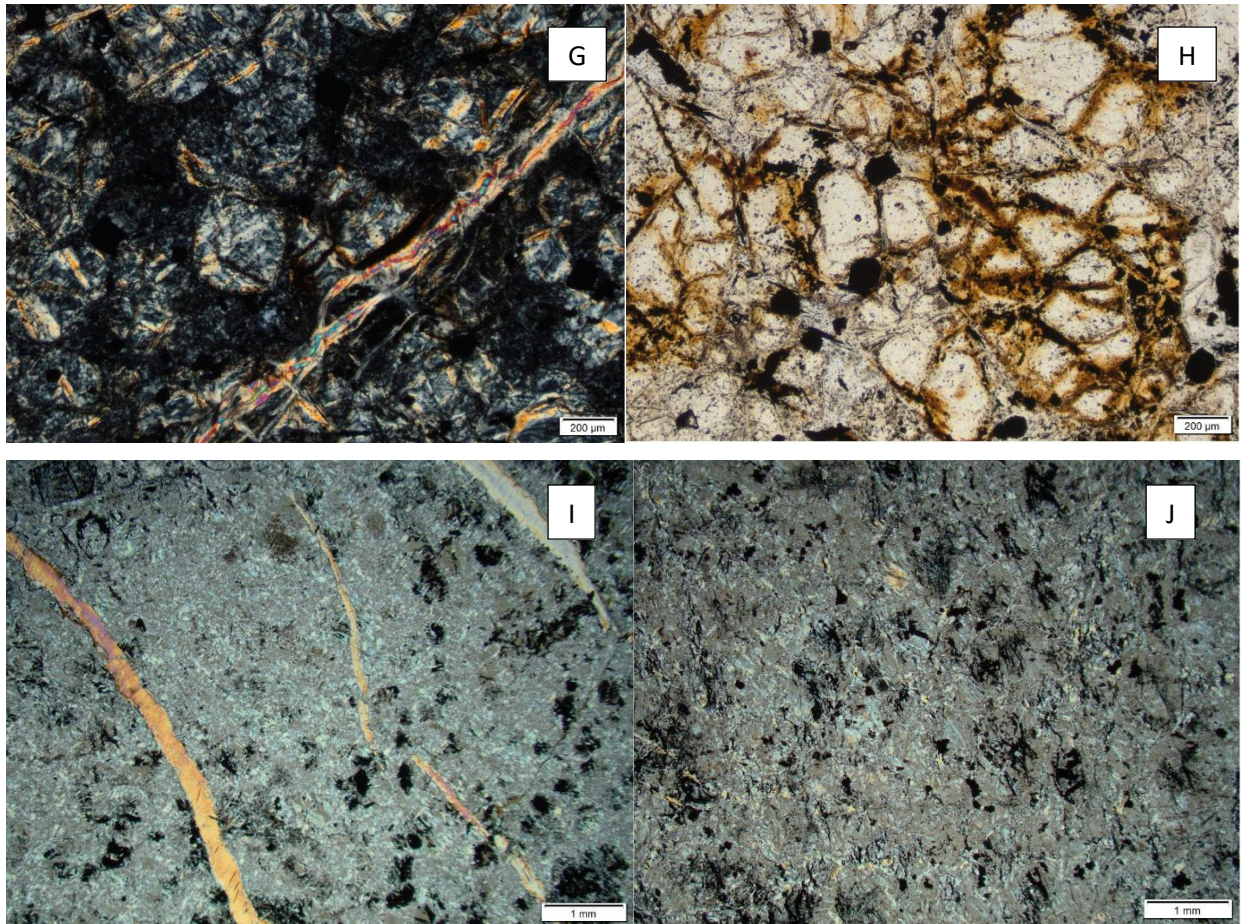


Figure 5.1: Micrographs of Stolzburg Complex meta-dunites. (A) GVI (1.25x; XPL) and (B) SM4 (4x; XPL) showing preserved primary textures and pseudomorph of serpentine after olivine. (C) SM2 (1.25x; XPL) and (D) SM2 (4x; XPL) showing the replacement of serpentine by talc. (E) DH65 (1.25x; XPL) showing large olivine crystal sizes and fine magnetite grains tracing out grain boundaries. (F) NF3 (1.25x; XPL) showing magnetite stringers inside the serpentine pseudomorphs as well as intercumulus orthopyroxene which promoted texture preservation. (G) DH59 (4x; XPL) & (H) DH59 (4x; XPL) showing talc veins and olivine replacement by iddingsite. (I) NF6 (1.25x; XPL) exhibiting talc vein and eradication of primary textures in Stolzburg Complex meta-dunite sample. (J) NF20 (1.25x; XPL) showing complete destruction of primary textures in serpentinized dunite sample.

Meta-harzburgites:

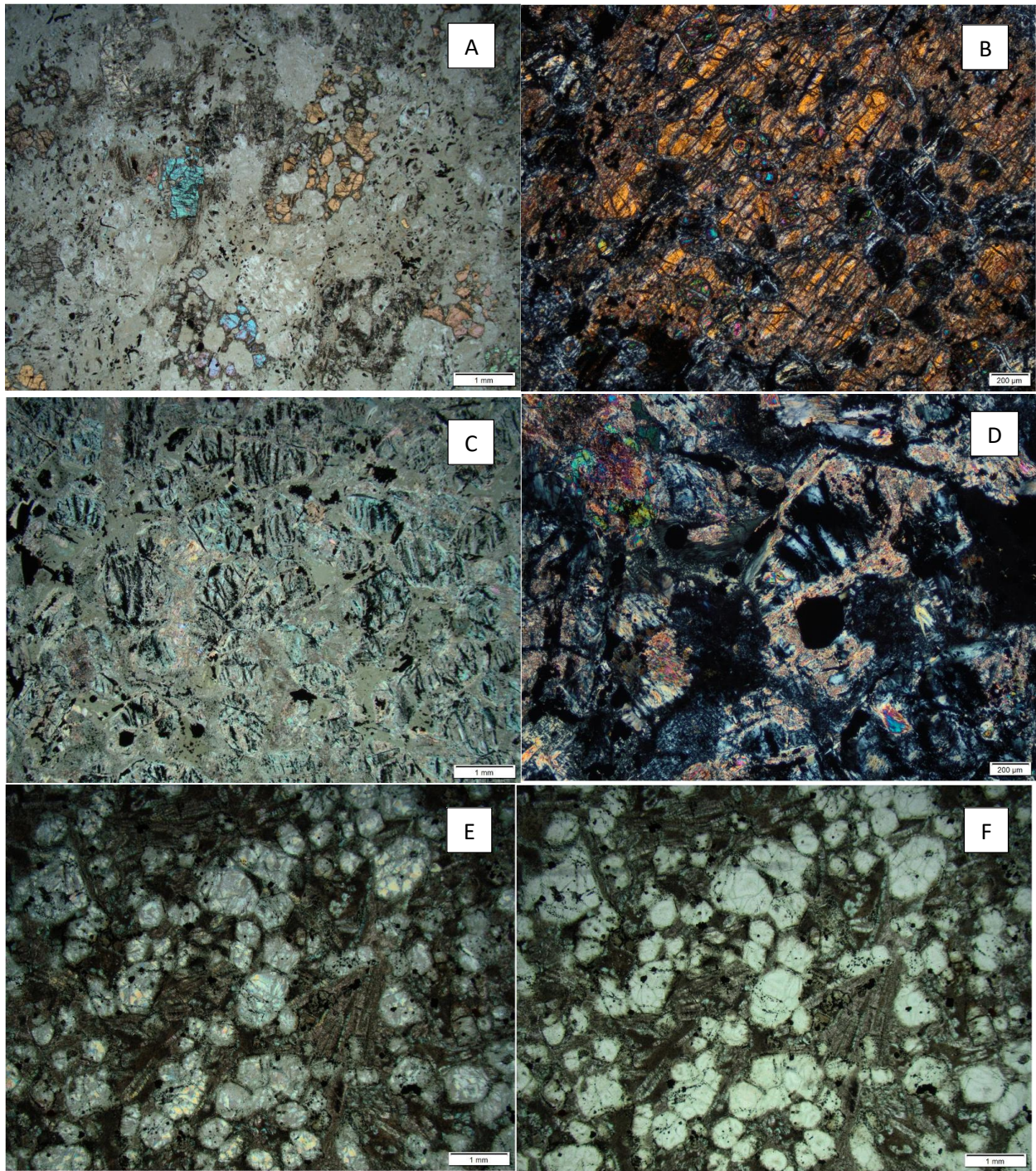
The primary mineralogical make-up of these rocks is > 60% olivine in combination with orthopyroxene and minor chromite (see fig. 5.6A). These minerals occurred in various configurations with each other, resulting in different textures. Olivine occurred both as inclusions

in orthopyroxene oikocrysts (DN4 & SM1: fig. 5.2A & B, respectively) as well as in a granular form (NF5, NF26 & SM6: fig. 5.2C, G, & H, respectively) with crystal sizes ranging from 0.5 mm to 1.5 mm and averaging on 0.8 mm. In addition to the oikocrystic character, orthopyroxene also occurred as intercumulus material in between granular olivine crystals (NF26: fig. 5.2F) and, to a lesser extent, in a granular form. The oikocrysts sizes range from 2 mm to 4.5 mm while those of the granular crystals average around 0.8 mm. While some of these primary textures are preserved, the poikilitic textures in particular, others have been largely disturbed (DN8 & NF11: fig. 5.2I & J, respectively). These rocks are generally finer than those of the Lower division. In addition, the cumulate textures are not as apparent in these rocks.

As in the dunites, the Stolzburg Complex harzburgites have also suffered pervasive alteration. With one exception, where relic olivine inclusions are encased in orthopyroxene oikocrysts (SM1: fig. 5.2B), almost all of the olivine crystals in the harzburgites have been serpentinized. Secondary magnetite, accompanying the serpentinization, occurs as subparallel veinlets transecting serpentine grains (NF5: fig. 5.2C); as speckles of fine particles; and as rims of the serpentine grains. While some of the oikocrysts are well-preserved, orthopyroxene is generally altered to talc, bastite, and chlorite. Some of the partially altered orthopyroxene grains appear dark due to the speckled fine magnetite particles. Replacement of serpentine by talc is common (SM6 & DN8: fig. 5.2H & I, respectively). In addition, talc veinlets can be seen transecting some of the specimen (DN8: fig. 5.2I).

Other peridotites:

In addition to the meta-dunites and meta-harzburgites, few encounters of other rock that were originally constituted by a considerable amount of olivine have been made. Rock types include olivine orthopyroxenites (DN6 and NF7: fig. 5.3A & B, respectively) and lherzolites (NF25: fig. 5.3C & D) which are minor components of the Upper Division (see fig. 5.6A). These rocks have suffered very intense alteration to an extent where all primary minerals have been completely overprinted and original textures have been destroyed. In some cases, however, pseudomorphs after olivine and clinopyroxene retained the original subhedral to anhedral crystal shapes with diameters not exceeding 1 mm. It appears like orthopyroxene only occurred as an intercumulus phase. Olivine was serpentinized; orthopyroxene was altered to talc and chlorite; and clinopyroxene was also replaced by talc. Overprinting of serpentine by talc is not uncommon.



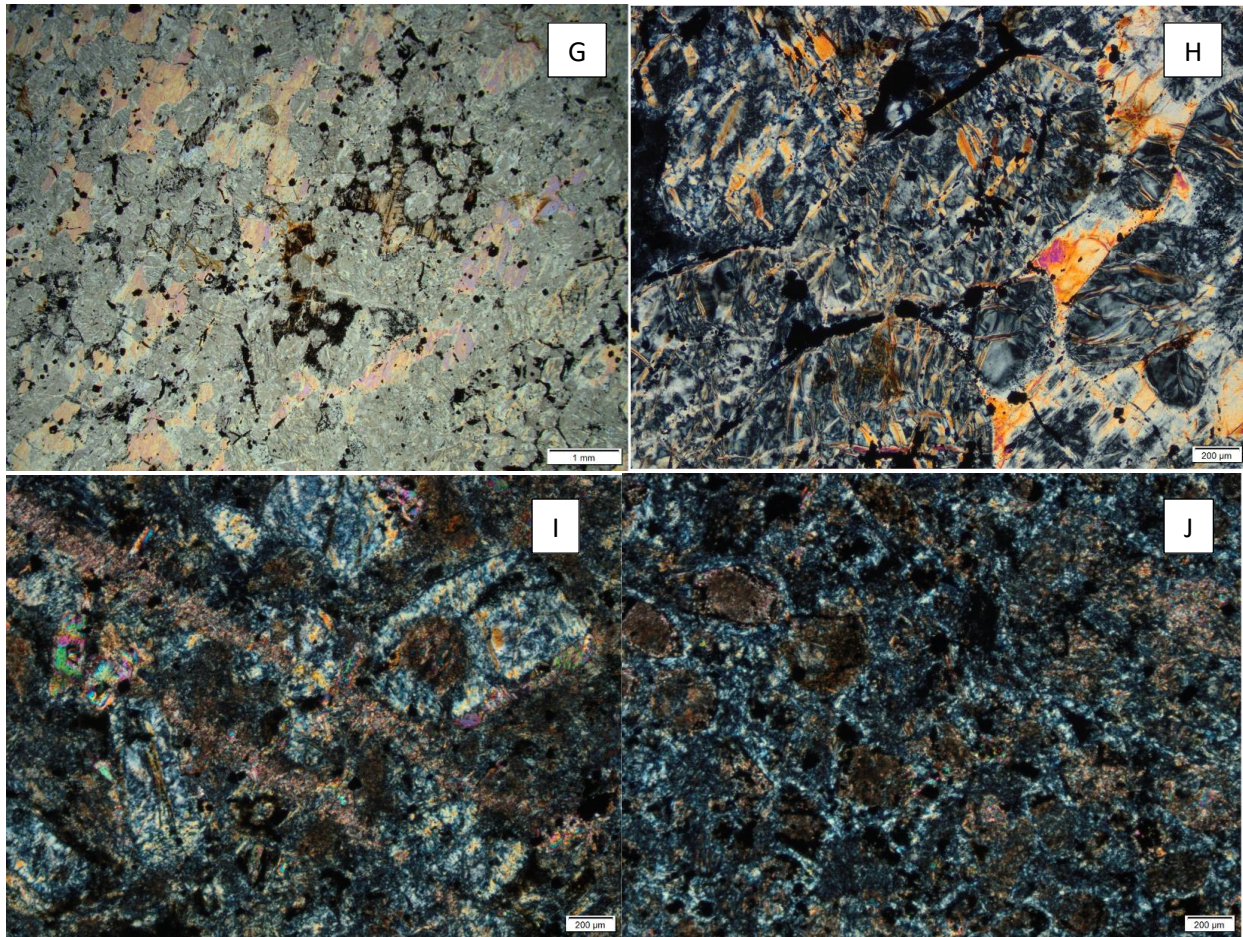


Figure 5.2: Micrographs of Stolzburg Complex meta-harzburgites. (A) DN4 (1.25x; XPL) showing the oikocrystic character of some meta-harzburgites of the Stolzburg Complex in a case where the olivine inclusions have been completely replaced by serpentine. (B) SM1 (4x; XPL) showing partial preservation of olivine inclusions in an oikocrystic orthopyroxene crystal. (C) NF5 (1.25x; XPL) showing magnetite stringers in serpentine grains. (D) NF5 (4x; XPL) showing replacement of serpentine by talc. (E) NF26 (1.25x; XPL) & (F) NF26 (1.25x; PPL) showing cumulus olivine textures and interstitial altered orthopyroxene. (G) SM6 (1.25x; XPL) and (H) SM6 (4x; XPL) showing replacement of serpentine and interstitial material (orthopyroxene?) by talc. (I) DN8 (4x; XPL) displaying intense alteration of a harzburgite sample and talc veins. (J) NF11 (4x; XPL) showing intense alteration of serpentine by harzburgite and replacement of serpentine by talc.

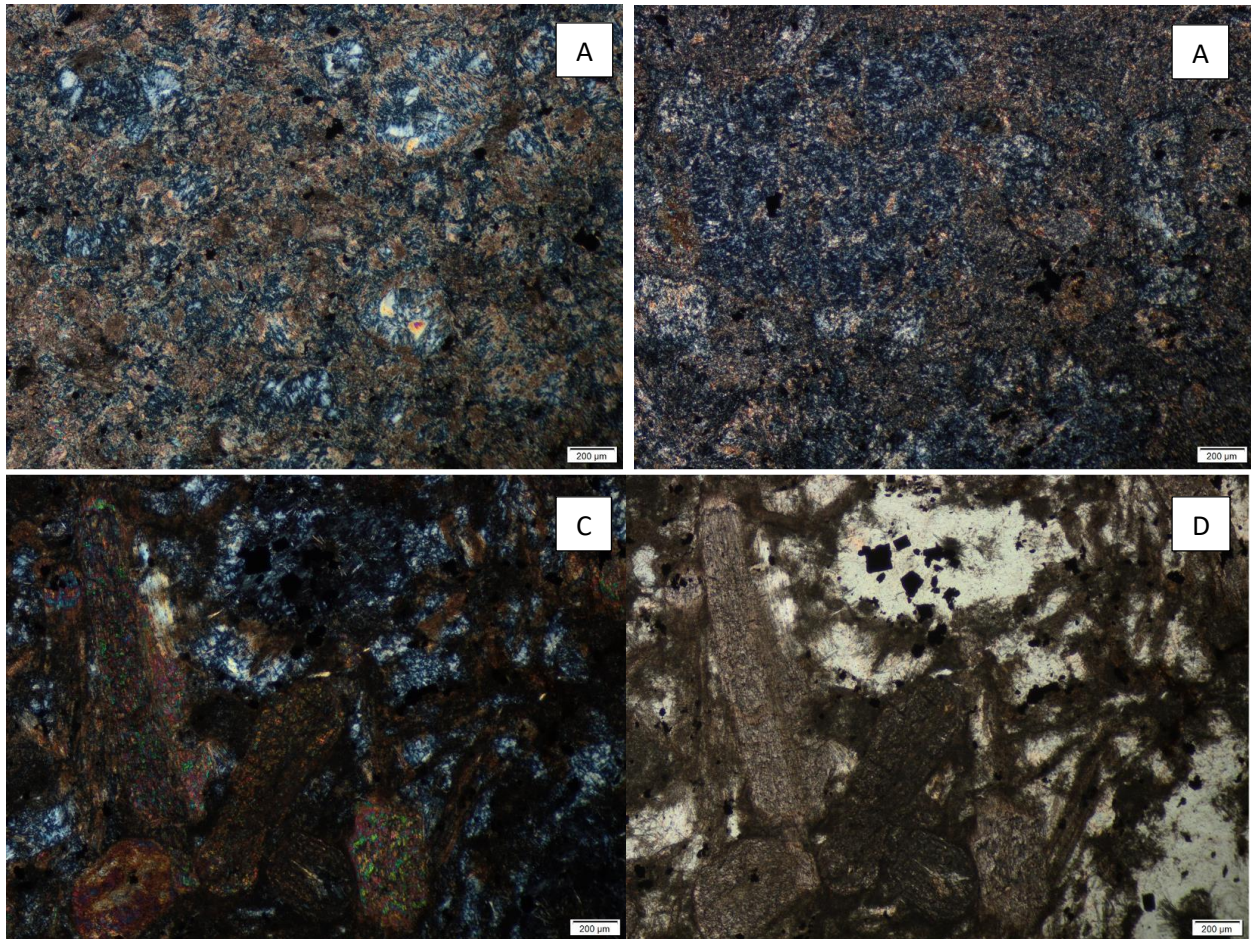


Figure 5.3: *Micrographs of Stolzburg Complex meta-peridotites. (A) DN6 (4x; XPL) and (B) NF7 (4x; XPL) showing intensively altered pyroxene-rich olivine cumulates where primary textures have been destroyed. (C) NF25 (4x; XPL) and (D) NF25 (4x; PPL) portraying an altered lherzolite sample.*

Meta-orthopyroxenites:

Over 80% orthopyroxene together with minor interstitial clinopyroxene and plagioclase constitute the primary make-up of these rocks (see fig. 5.6B). Several samples are essentially monomineralic. Accessory chromite and/ or magnetite may be encountered. Although the orthopyroxenites, in general, have also been subjected to considerable alteration, they are the best-preserved rocks in the Stolzburg Complex. Generally, the orthopyroxene is replaced by talc while the interstitial clinopyroxene is altered to chlorite or actinolite. The degree of alteration varies, with some samples displaying exceptional preservation and showing no significant alteration of the primary minerals (DH61: fig. 5.4A), while others show complete replacement of the orthopyroxene by talc (SB5:

fig. 5.4D). In the early stages of the alteration, incipient replacement of orthopyroxene by talc developed along cleavage and fracture planes as well as along grain boundaries (DH3: fig. 5.4B). The replacement process advanced in this fashion, at some stage, having relic cores as the only remains of the orthopyroxene crystals (SB6: fig. 5.4C). The end product of the alteration is talc pseudomorphs after orthopyroxene grains. Since the alteration progressed through pseudomorphism of orthopyroxene by talc, primary textures are normally preserved even in cases of extreme steatization. However, samples showing destroyed textures were also observed (SB5: fig. 5.4D).

The cumulus nature of the orthopyroxene grains is manifested by the equant to rectangular and subhedral crystal shapes (for both the unaltered and the replaced crystals) as they appear in sample where primary textures have been preserved. The crystal sizes range from 1 mm to 4 mm, with an average of 2 mm. These features result in granular textures.

In addition to the orthopyroxene, some pyroxenite samples consist of a significant amount of intercumulus clinopyroxene, which is now completely altered to chlorite. These samples are termed websterites (fig. 5.6B) and they are uncommon. One sample shows good preservation of primary textures (NF4: fig. 5.4E) while the other one displays total destruction of primary textures (SB10: fig. 5.4F).

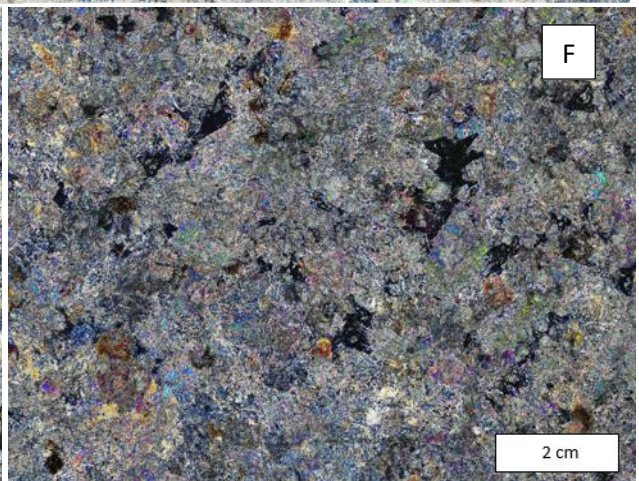
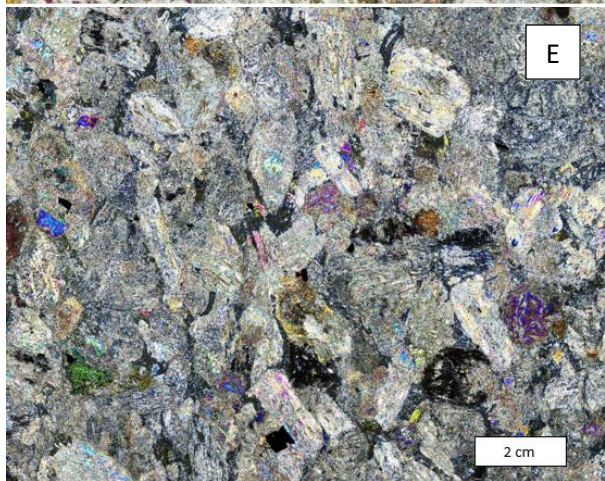
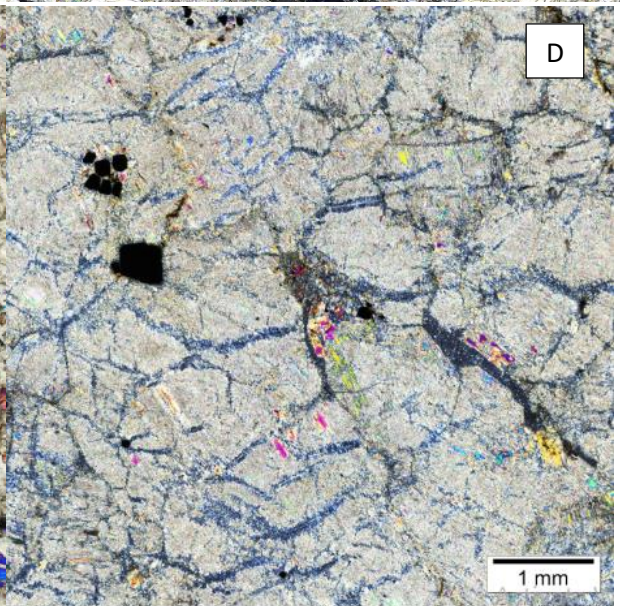
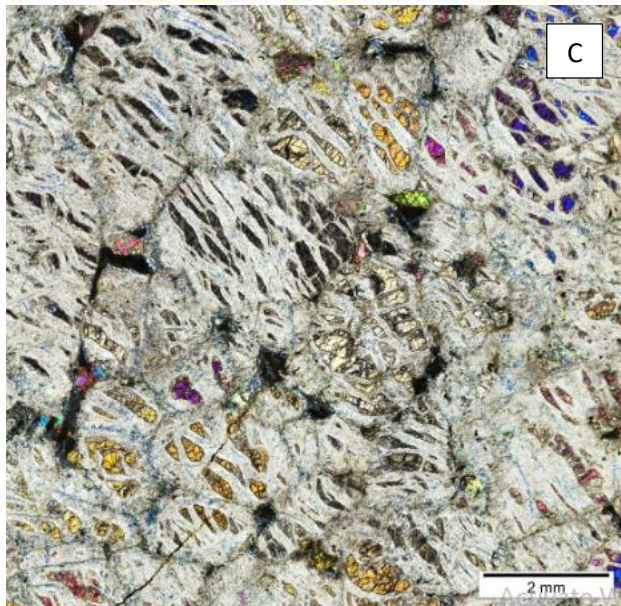
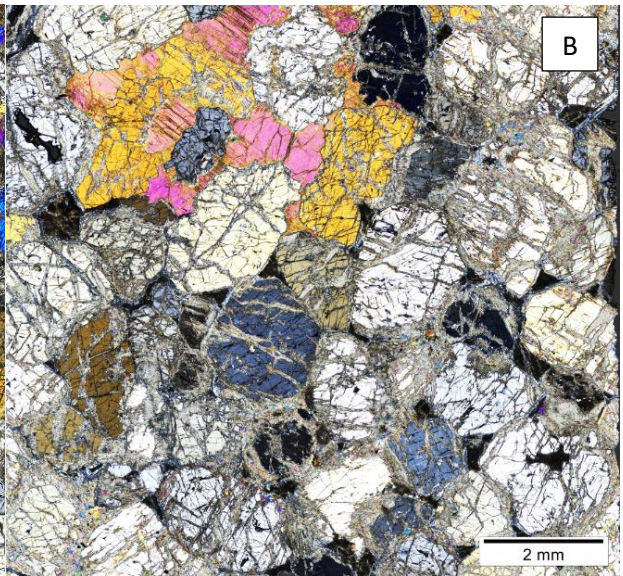
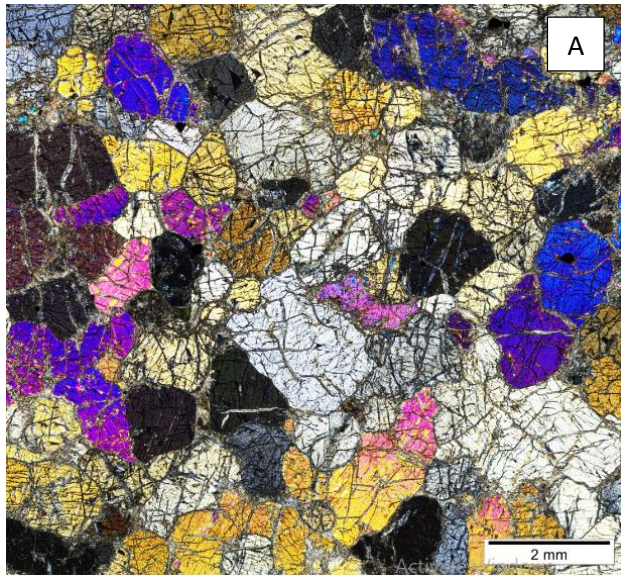
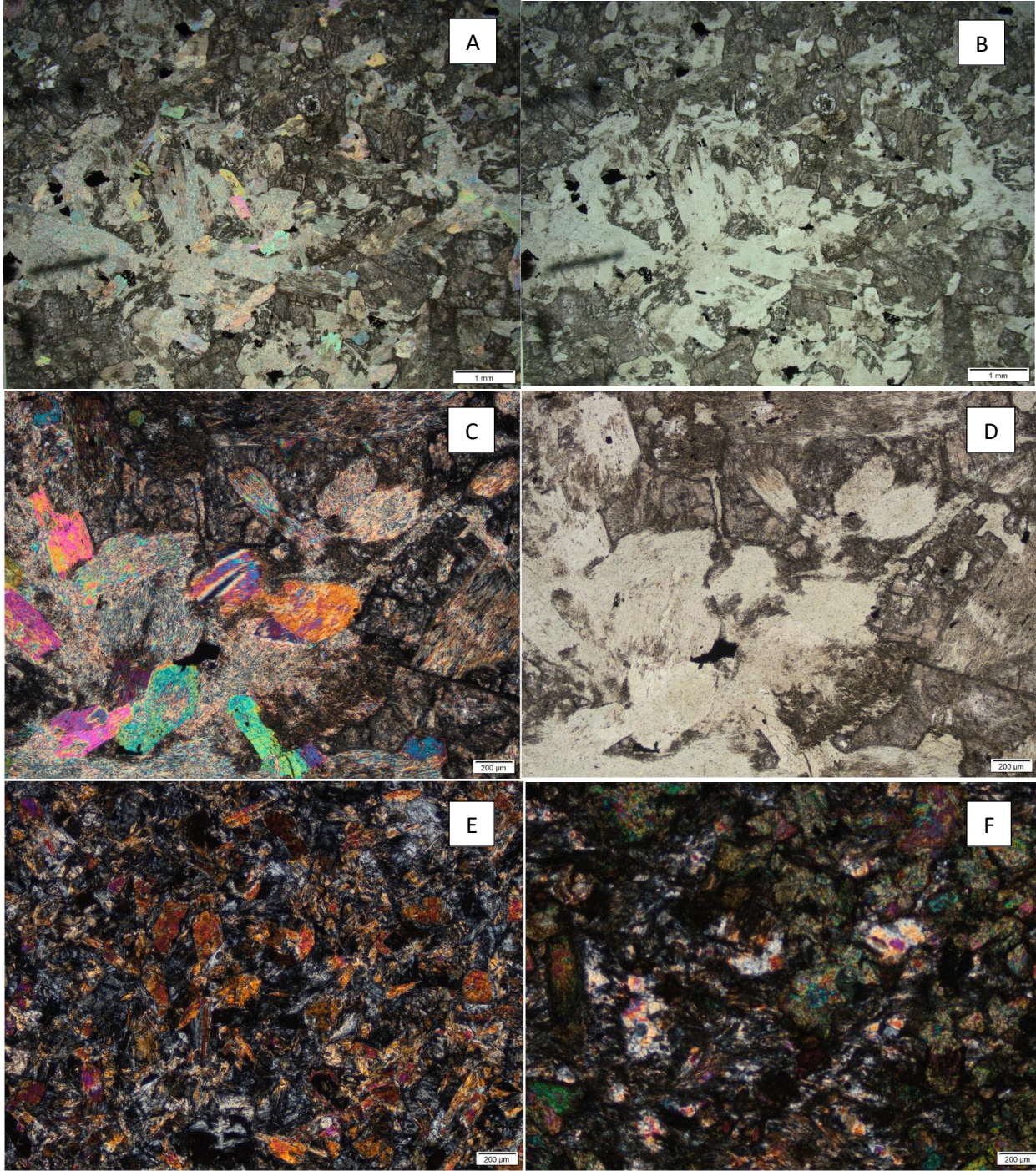


Figure 5.4: *Micrographs of orthopyroxenites of the Stolzberg Complex. (A) DH61 (4x; XPL) showing exceptional preservation of an orthopyroxenite. (B)DH3 (4x; XPL) showing incipient replacement of orthopyroxene crystals by talc along grain fractures. (C) SB6 (4x; XPL) showing advanced replacement of orthopyroxene crystals by talc; only orthopyroxene cores are left behind. Notice that textures are preserved. (D) SB5 (4x; XPL) displaying an orthopyroxene sample that had suffered complete steatization. Textures are extensively destroyed. (E) NF4 (4x; XPL) a websterite sample which has been altered completely. Cumulus orthopyroxene altered to talc while the interstitial clinopyroxene is altered to talc. (F) SB10 (4x; XPL) displaying a websterite sample where textures have been destroyed completely.*

Meta-gabbronorites:

This is the most diverse group of rocks, which consists of varying proportions of plagioclase, clinopyroxene and orthopyroxene together with minor oxides (see fig. 5.6B). The rock types vary from anorthosite, through pyroxenitic anorthosite, to gabbronorites. Primary minerals are barely preserved, with plagioclase being saussuritized to epidote and zoisite and occasionally albitized, while orthopyroxene is mainly steatized and clinopyroxene is uralitized. Alteration of both types of pyroxenes to chlorite is not uncommon. Although primary textures have been significantly disturbed, diversity in mineralogical configurations and structural character is noticeable. The lack of granular and cumulate textures is apparent. These rocks are generally medium- to fine-grained, with grains diameters not exceeding 1.5 mm. Shapes of pseudomorphs are commonly anhedral, except in cases where actinolite after acicular clinopyroxene occur as laths that can go up to 4.5 mm in length (NF10: fig. 5.5H, I, J). The rodingites of the Stolzberg Complex are essentially gabbronoritic rocks that have been subjected to metasomatism by Ca-rich fluids. For this study, the best-preserved samples were selected, so rodingites were intentionally excluded. These rocks are not described here, however, the reader is referred to Anhaeusser (1979) and Rodel (1993) for more information on Stolzberg Complex rodingite occurrences.



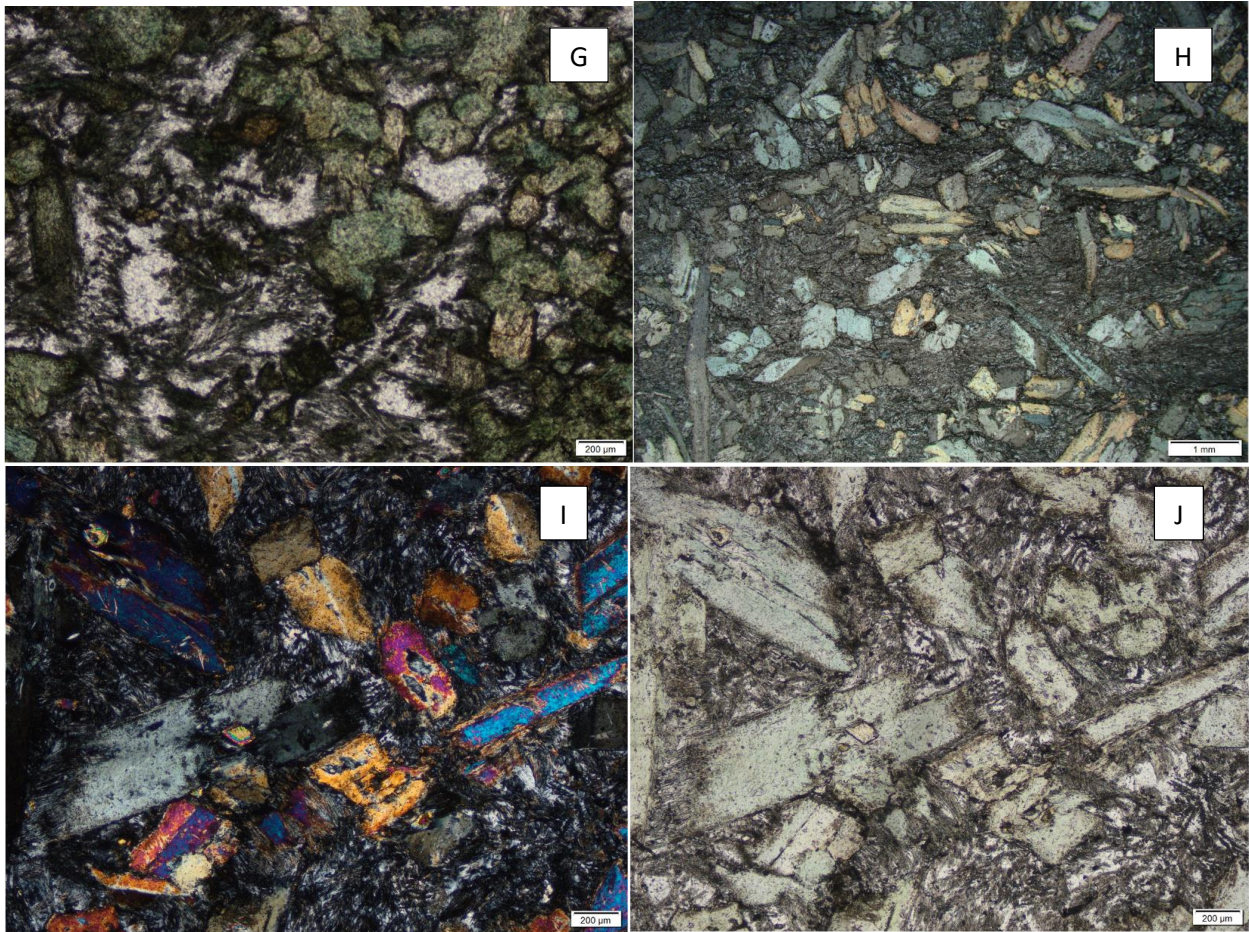


Figure 5.5: Micrographs of gabbronorites of the Stolzburg Complex. (A), (B), (C), and (D), respectively, displaying DH17 (1.25x; XPL), DH17 (1.25x; PPL), DH17 (4x; XPL), and DH17 (4x; XPL). This is an altered gabbronoritic sample with remnants of altered orthopyroxene, talc/actinolite after clinopyroxene, and epidotized plagioclase. (E) DH83 (4x; XPL) showing an epidotized anorthositic gabbronorite. (F) & (G), respectively, displaying GV14 (4x; XPL) and GV14 (4x; XPL). This is another altered anorthositic gabbronorite. (H), (I) and (J), respectively, displaying NF10 (1.25x, XPL), NF10 (4x; XPL), and NF10 (4x; PPL). Acicular altered clinopyroxene crystals are apparent (H). The interstitial plagioclase has been intensively altered.

Table 1: Summary of petrography of the rocks of the Stolzburg Complex. *Ol* = olivine; *Opx* = orthopyroxene; *Cpx* = clinopyroxene; *Plag* = plagioclase.

Rock type	Primary minerals and abundances	Secondary minerals	Alteration type	Textures	Grain size
Dunite	Ol (80-95%) + Opx (5-20%) ± Plag (0-1%) ± chromite	Serpentite+ magnetite ± talc ± iddingsite ± bastite	Serpentinization Steatization Hydration	Granular Cumulate	1 - 4 mm
Harzburgite	Ol (40-60%) + Opx (30-45%) ± Plag (0-8%) ± Cpx (3-13%) ± chromite	Serpentite+ magnetite + talc ± bastite ± chlorite	Serpentinization Steatization Hydration Chloritization	Granular Porphyritic Poikilitic Cumulate	Ol: 0.5 -1.5 mm; Opx: 0.8 mm Opx: 2 - 4.5 mm
Olivine Orthopyroxenite	Ol (20-42%) + Opx (23-60%) ± Plag (11-17%) ± Cpx (0-23%) ± chromite	Serpentite+ magnetite + talc + chlorite	Serpentinization Steatization Chloritization	Textures destroyed	< 1 mm
Orthopyroxenite	Opx (80-93%) ± Cpx (2-12%) ± Plag (3-9%) ± Ol (0-2%) ± chromite	Talc ± chlorite ± actinolite	Steatization Chloritization Uralitization	Granular Cumulate	1 - 4 mm
Websterite	Opx (53-75%) + Cpx (17-27%) ± Plag (7-13%) ± Ol (0-12%) ± chromite	Talc + actinolite + chlorite	Steatization Chloritization Uralitization	Cumulate	2 mm
Gabbronorite	Opx (11-45%) + Cpx (15-47%) + Plag (20-62%) ± Ol (0-6%) ± Ti-oxides	Albite + talc + actinolite + epidote + zoisite + chlorite	Albitization Steatization Uralitization Saussuritization Chloritization	Textures destroyed Acicular pyroxene	< 1.5 mm 2 - 4.5 mm needles

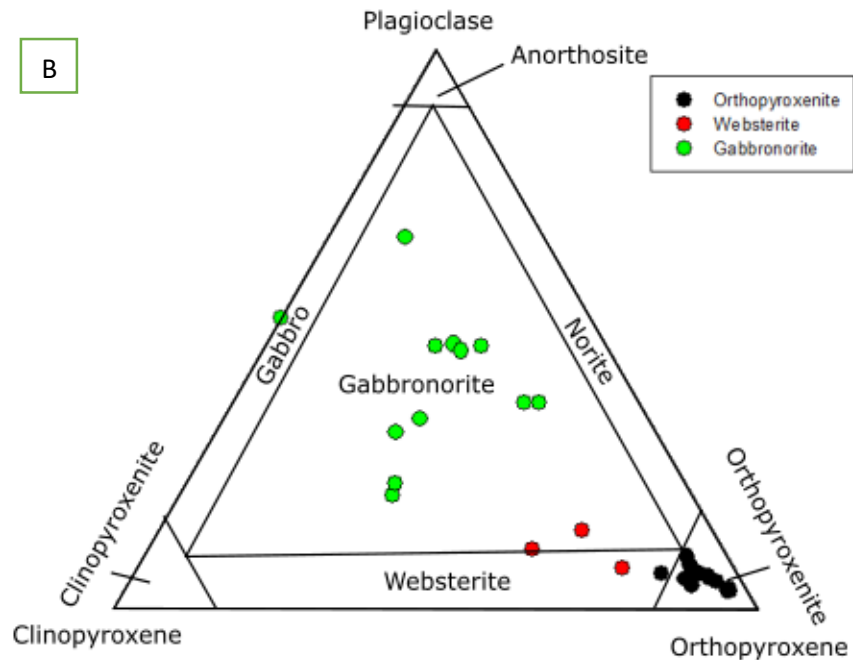
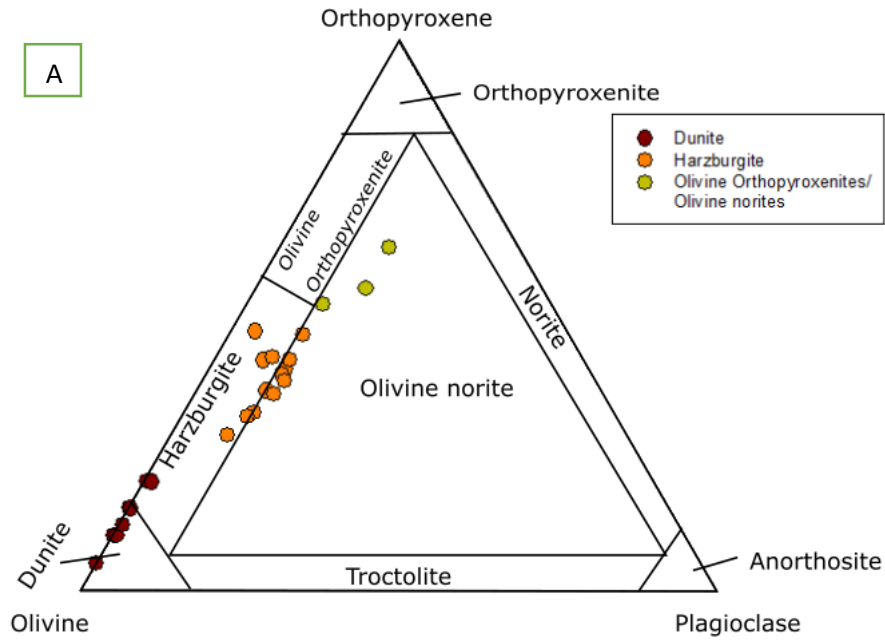


Figure 5.6: Olivine-Orthopyroxene-Plagioclase (A) and Orthopyroxene-Clinopyroxene-Plagioclase (B) classification diagrams of ultramafic-mafic rocks based on estimated modal abundances. Note that the only encountered lherzolite sample is not shown as it can only be correctly presented in the Olivine-Orthopyroxene-Clinopyroxene classification diagram.

7.3. Emplacement mechanism: shallow-level sills vs ponded lavas

In earlier sections of this thesis, it has been demonstrated through reviewing the relationship between the Barberton layered complexes and their surroundings that these bodies most likely represent autochthons, which were developed intimately with the enveloping supracrustal successions. In addition, it was highlighted that these complexes (or at least the Stolzburg Complex) does not display the V-shaped REE pattern which characterized Phanerozoic alpine-type tectonites. On these grounds, it was concluded that the complexes represent autochthons as opposed to allochthons, and were not tectonically emplaced into the Onverwacht Group succession. Following the demonstration that the Barberton layered complexes unlikely represent alpine-type peridotites, the remaining task is to determine whether these complexes formed as shallow-level sills or ponded lavas.

Thompson-Stiegler et al. (2012) and Huber and Byerly (2012), respectively, suggested that the Pioneer and Saw Mill complexes developed largely as repetitively ponded lavas. However, these authors indicated that some of the magmatic units in these complexes may represent sills. Features quoted in support of the ponded lava model includes: (1) the not uncommon occurrence of pyroxene spinifex-textured unit tops, (2) the relatively fine-grained character of some units, and (3) the alleged total absence of cross-cutting relationships between the units. The first two qualities are regarded as evidence for fast cooling under the envisaged extrusive conditions. However, Arndt et al. (2004), through a detailed textural study of a 6 m-thick Dundonald sill in the Kidd-Munro assemblage, Abitibi greenstone belt, Canada, highlighted the remarkable similarities between typical spinifex-textured komatiitic flows and shallow-level sills; these entities are essentially indistinguishable, especially when unit boundaries are obscured. Thus, the first two above-mentioned qualities of the layered units cannot be used as unequivocal evidence in support of the extrusive model. Furthermore, features such as large crystal sizes (reaching 4 cm in diameter), which clearly indicate slow cooling conditions, are common in the Barberton layered complexes (Anhaeusser, 1985, 2001; Robb, 1977; Rodel, 1993; Wuth, 1980; this study). Inch-scale layering, a feature inconsistent with development under fast cooling conditions, in anorthositic gabbro units (generally thought to represent the top of differentiation cycles, therefore cooled the fastest) is also not uncommon (Anhaeusser, 1985, 2001; Rodel, 1993; Viljoen and Viljoen, 1970).

While the alleged absence of cross-cutting relationships amongst the layered units (Thompson-Stiegler et al., 2012; Huber and Byerly, 2012) cannot be used as evidence against the intrusive model, particularly for stratiform intrusions, such features have actually been observed in at least some of the Barberton ultramafic complexes. A harzburgitic dyke has been observed in the Handsup Complex (Phumelele Mashele, 2020: Personal communication). Robb (1977) noted strike-subparallel crosscutting relationships between a basal dunitic layer and an overlying pyroxenitic unit in the Richmond Complex. In the same complexes (namely Pioneer, Saw Mill and Emmenes) where the extrusive model is being championed, instead of well-developed continuous units, Wuth (1980) observed orthopyroxenite pod- or lense-like bodies enclosed in dunitic or harzburgitic units as well as discontinuous lenses or pods of anorthositic gabbro. The lack of shearing in the vicinity of these bodies suggests an igneous origin. Wuth (1980) interpreted these bodies as products of solidified immiscible liquid trapped in a crystallizing dunite or harzburgite layer, or an injected pyroxene-only crystal mush. To some extent, I concur with the latter suggestion (see later). De Wit et al. (1987) also reported possible internal cross-cutting relationships in the Upper Division of the Stolzberg Complex. The presence of such features is supported by the complex layering of the body as depicted in the map of the complex in Anhaeusser (1972).

Of particular interest in the Barberton ultramafic-mafic complexes is the presence of notable sedimentary horizons which are interstratified with the layered igneous units. Units previously interpreted as sheared or slaty ultramafic rocks attributed to intraformation deformation (Anhaeusser, 1969, 1972; Wuth, 1980) have recently been shown to represent ultramafic tuffs (Lowe and Byerly, 1999; Ransom et al., 1999; Thompson-Stiegler et al., 2008, 2010, 2011). Visser (1956) incorrectly interpreted these units as xenoliths of Moodies Group or Fig Tree Group shales, which were trapped in late ultramafic-mafic rocks. The identification of sedimentary structures (such as cross- and convolute-bedding) and microscopic textures in these units left no doubt that they are of sedimentary origin (Lowe and Byerly, 1999; Ransom et al., 1999; Thompson-Stiegler et al., 2008, 2010, 2011). These units were thus interpreted as altered komatiitic tuffs and they were shown to reach thicknesses as great as 50m (Cooper, 2008; de Wit et al., 1987; Huber and Byerly, 2012; Thompson-Stiegler et al., 2012). Due to the weaker rheological properties of these units, intraformational shearing may have been focused in these stratigraphic sections (Lowe and Byerly, 1999), hence they were mistaken for products of shearing by the early workers. The

presence of these sedimentary units serves as additional evidence against the alpine-type peridotite model for the origin of the layered complexes because if these bodies represented fragments of the lithospheric mantle, they would not contain interstratified sedimentary units.

Geochemical studies showed that the layered magmatic units and the interstratified komatiitic tuffs in the Pioneer and Saw Mill complexes are totally unrelated; the magmatic units generally display slight Al-enrichment komatiitic affinities whereas the tuffs are predominantly Al-depleted (Thompson-Stiegler et al., 2008, 2010, 2011). Proponents of the extrusive model for the origin of the Pioneer and Saw Mill complexes suggested that the tuffs represent distal fall deposits (from a source of composition different from the one that is believed to have supplied the envisaged thick komatiitic flows represented by the layered complexes), which accumulated in between episodes of voluminous eruptions (Thompson-Stiegler et al., 2008). However, the discontinuity and, in places, abrupt thicknesses variation of the komatiitic tuff units in the Pioneer and Saw Mill complexes are inconsistent with the proposed accumulation process; such a process is expected to develop continuous layers, which thin out gradually away from the source. Under the envisaged alternating eruption episodes, it is odd that not even one magmatic unit of Al-depleted compositional affinities have been reported in the Barberton complexes. Robin-Popieuel et al. (2012) reported the occurrence of pyroxene spinifex-textured upward protrusions into the overlying tuff units in the Pioneer Complex. These protrusions are reported to have widths of ~5 m wide and lengths of ~10 m. They extend perpendicularly from the magmatic unit into the overlying tuff layers. These features provide unequivocal evidence that the tuff layers are older than the underlying magmatic units, making the latter components sills (see later). Komatiitic tuffs have also been reported in other Barberton layered bodies: (1) Stolzberg Complex (Anhaeusser, 1972: reported as “slaty serpentinites”; de Wit et al., 1987: reported as hornfelsed and brecciated chert units; Tappe and Bolhar, 2018: personal communication); and (2) Mundt’s Concession and Handsup complexes (Anhaeusser, 1969: reported as “slaty serpentinites”). The lack of compelling evidence (such as pillow lavas, flow top erosion and alteration, flow top breccia, etc.) in support of the extrusive origin of the layered units of the Barberton complexes is noteworthy.

In addition to komatiitic tuffs, other sedimentary units have been observed in the Barberton layered bodies. Robb (1977) noted the occurrence of continuous and lenticular, banded iron formation units in the Core Zone Complex where they occur in between dunite and pyroxenite layers or

within individual dunite layers. As a result, he suggested that the complex formed through multiple sill-like injections of magma into the supracrustal rocks of the Barclay Vale Schist Belt. Viljoen and Viljoen (1970) also reported the occurrence of country rock xenoliths in the Ship Hill, Budd and Koedoe complexes. Discontinuous iron formation units occur along the northwestern boundary of the Stolzberg Complex (Anhaeusser, 1972, 1982; de Wit et al., 1987). This intimate relationship between the Barberton complexes and sedimentary units was interpreted as an indication that these bodies were emplaced preferentially along the weaknesses (i.e., along the interfaces between basaltic and sedimentary units) (Viljoen and Viljoen, 1970).

In light of the features highlighted above, it is more likely that the Barberton layered complexes developed as shallow-level stratiform intrusions. However, in contrast to the early intrusive model, which suggests that the complexes developed through periodic replenishment of large magma chambers (Anhaeusser, 1976, 1979, 1985; Jolly, 1977; Naldrett and Turner, 1977; Rodel, 1993), I envisage settings where each of the magmatic units represents separate sills which invaded a pre-existed sedimentary sequence. Such a model was envisaged by Lowe and Byerly (1999) who proposed that the komatiitic tuff sequence provided a relatively weak horizon along which the magma was injected. These workers suggested that the Pioneer Complex is actually made up of several smaller differentiated ultramafic sills which are separated by the komatiitic tuffs.

In the early intrusive model, each magma pulse is thought to have undergone differentiation resulting in a sequence comprised of dunite at the base, overlain, in order, by pyroxene peridotite, pyroxenite, websterite and capped by a gabbroic unit. The next pulses of magma would generate similar sequences, in this way, developing the repetitive cyclic layering that is encountered in most of the Barberton complexes. While this model appears to perfectly explain the cyclic layering and the apparent upward progressive evolution, it cannot explain the relationship between the magmatic units and the intercalated sedimentary horizons as well as cross-cutting relationships between layers thought to represent a single differentiation cycle (i.e., products of one magma pulse). Extensive sedimentary horizons are not restricted between different designated differentiation cycles, instead, they also split magmatic units of supposedly single differentiation cycle.

The occurrence of extensive komatiitic tuff units between peridotite layers and the immediately overlying gabbroic units in the Upper Division of the Stolzberg Complex (Anhaeusser, 1972)

indicates that the gabbroic layers did not form from the same magma batch as the underlying peridotite layer through magmatic evolution. It is more likely that the peridotite layers and the gabbroic layers represent independent magma injections. This suggestion can explain the abrupt plagioclase compositional reversal between a websterite layer and an overlying gabbroic unit (two units believed to be part of a single differentiation cycle) recorded by Viljoen and Viljoen (1970) in the Kaaapmuiden layered complexes. The overlying gabbroic layer likely formed from a new, primitive, mafic magma which was emplaced above the websterite unit which is from a different magma. The contrasting origin for the peridotitic and gabbroic units is further supported by cross-cutting relationship between these two types of magmatic layers as reported by de Wit et al. (1987) in the Upper Division of the Stolzburg Complex; in a case where the gabbroic layer represents a residual melt from the same magma batch that formed the peridotite unit, development of such a feature is inconceivable. The map of the Stolzburg Complex produced by Anhaeusser (1972) shows transgression of a gabbroic unit into the underlying units of the Lower Division (in the vicinity of the GV4 and GV5 samples (see map of the Stolzburg Complex by Anhaeusser, 1971)). Rodel (1993) also reported a 10 cm thick anorthositic dyke (displaying sharp contacts) cutting a pyroxenitic unit in the Rosentuin Complex. In the Pioneer and Saw Mill complexes, gabbroic and peridotitic layers more commonly occur as discrete individual units which, in some places, are completely isolated from each other and from other magmatic units by intervening laterally extensive and thick komatiitic tuffs (maps: Cooper, 2008; Huber and Byerly, 2012; Wuth, 1980). This provides unequivocal evidence that the gabbroic and peridotitic units represent products of different magma injections. Note that the envisaged magma batches are not necessarily isotopically distinct. In this context, the lenticular anorthositic gabbro horizons developed in the Pioneer, Saw Mill and Emmenes complexes can be ascribed to the invasion of previously formed magmatic units by mafic magma. A case where an earlier formed, laterally continuous, anorthositic gabbro layer is invaded and disrupted by late magmatic injections cannot be ruled out.

In the Pioneer and Saw Mill complexes, dunite and pyroxenite layers also commonly occur as discrete individual units separated from each other and other magmatic units by the bounding komatiitic tuffs (see maps in: Cooper, 2008 (figure 5); Huber and Byerly, 2012 (figure 2); Wuth, 1980). This leaves no doubt that the dunitic and pyroxenitic layers developed independently of each other, as opposed to the pyroxenite layers representing residual melts left behind after the extraction of olivine crystals, which accumulated to form the dunites. It is probable that the

repetitive interstratified dunite and orthopyroxene cycles encountered in other Barberton layered bodies developed in a similar manner. This is supported by the cross-cutting relationship between dunite and pyroxenite layers in the Richmond Complex (Robb, 1977). Further support is provided by the presence of banded iron formation horizons which split dunite and pyroxenite layers as well as individual dunite layers in the Core Zone Complex (Robb, 1977). The thick, presumably individual, dunitic and orthopyroxenitic layers noted in the Stolzburg Complex (Anhaeusser, 1972, 2001; de Wit et al., 1987; Rodel, 1993) and other Barberton layered bodies may actually represent multiple stacked sills emplaced adjacent to each other. Dunitic veins (representing solidified dunitic melt) have been reported in the Nordre Bumandsfjord Ultramafic Pluton, Seiland, North Norway (Griffin et al., 2013; Sturt et al., 1980). Under these conditions, the lenticular orthopyroxenite bodies enclosed by dunite or harzburgite layers, in the Pioneer Complex, represent magma injected into earlier formed units (as suggested by Wuth (1980)) or disrupted continuous orthopyroxenite layer by late peridotite sills. Orthopyroxene and harzburgite lenses occur in the Stolzburg Complex, especially along the regional contact between the Lower and Upper Divisions.

While cyclic layering appears to be well-developed, it is very rare to find a cycle which is complete (Anhaeusser, 1985; Viljoen and Viljoen, 1970; Wuth, 1980). This feature was ascribed to incomplete differentiation or faulting by early workers (Wuth, 1980). Viljoen and Viljoen (1970) suggested that the absence of an evolved sequence above the designated upper dunite-peridotite zone, supposedly representing the base of a second pulse of magma with similar composition to the one that formed the lower differentiation cycle, indicates that the residual melt (following extraction of the peridotite) escaped and fed into the supracrustal succession. Intriguingly, it is not necessarily the very top (gabbroic) unit of the sequence that is missing in the so-called differentiation cycles. This feature may be explained in the context of the sheeted-sills complex model, where sills of different compositions are emplaced discretely into a sedimentary sequence and early formed magmatic units. Such a model is reconcilable with the commonly encountered sharp contacts between different magmatic units (Anhaeusser, 2001; Rodel, 1993; Wuth, 1980). If indeed the Barberton layered bodies developed in this manner, it is unlikely that these bodies acted as feeders for the mafic flows in the supracrustal succession of the Onverwacht Group. Instead, if any of the mafic flows are comagmatic with the layered bodies, they were developed from magma that managed to reach the surface without being temporarily staged in shallow-level chambers. This suggestion is reaffirmed later based on geochemistry (section 10.4). If, indeed, this model for

the development of igneous layering in the Barberton complexes is correct, then it has important implications for larger layered bodies like the Bushveld Complex. Sills-sedimentary complexes (where seemingly “stacked” sills invaded a sedimentary sequence) are actually common, such as the Kyak Bay Intrusion, New Quebec (James Mungall, Bolahr: personal communication)

The obvious question that follows concerns the origin of progressively evolved magmas. In this model, I envisage a voluminous ultramafic magma in a staging reservoir continuously undergoing fractional crystallization. The mechanisms involved in the generation of the parental magma are explored later. Episodic tapping of progressively evolved magma from the reservoir led to the development of the Stolzburg Complex (and possibly other Barberton complexes) through emplacement, in this order, of dunitic, orthopyroxenitic, harzburgitic, and lastly gabbro-noritic sills. This potentially explains why Ficq et al. (2018) recorded lower crystallization temperatures in the orthopyroxenites and harzburgites of the Stolzburg Complex while higher temperatures were reported for dunitic units from the counterpart Barberton complexes (Kareem, 2005).

The sheeted-sills model proposed for the Barberton layered bodies, including the Stolzburg Complex, does not preclude the occurrence of limited magmatic differentiation in the individual sills. For example, it is conceivable that the mafic sills underwent differentiation, resulting in more gabbro-noritic bases and anorthositic tops. In a similar way, the orthopyroxenitic sills developed into monomineralic orthopyroxenite bases and websteritic tops; dunitic sills formed monomineralic dunites at the base and orthopyroxene-bearing olivine cumulates at the top; and peridotite sills formed normal harzburgites at the base and clinopyroxene-bearing peridotites at the top.

The proposed sheeted-sills complex model potentially explains the puzzling lack of Ni-Cu-PGE orthomagmatic deposits in the Barberton layered bodies. It is believed that appreciable concentration of these precious metals generally follows extensive magmatic evolution in large bodies of magma. These conditions are not met in the comparatively thin units envisaged in this study. A 20-30 cm thick chromite seam, which extends for several metres was reported to the south of the Sterkspruit asbestos mine in the Lower Division of the Stolzburg Complex (de Wit and Tredoux, 1988). This unit either formed through chromite accumulation from an ultramafic magma or it represents an injected chromium-oxide liquid as suggested by some workers (Mukherjee et al., 2017; Mungall et al., 2016; Voordouw et al., 2009) for the massive chromitite layers of the

Bushveld Complex; the latter suggestion is favoured as it aligns with the emplacement mechanism proposed in the present study.

Other features, encountered in the Barberton complexes, worth discussing include the pinching and swelling of magmatic units (with thicknesses varying from 100 m to 40 m) as well as the total pinching out of some units (Cooper, 2008; Huber and Byerly, 2012; Thompson-Stiegler et al., 2012). While advocates of the extrusive model ascribe these features to irregular palaeotopography or interaction between the floor rocks and the envisaged thick komatiitic flows, these qualities of the magmatic units are not foreign to stratiform intrusions. In addition, Huber and Byerly (2012) noted apparent folding of the intercalated komatiitic layers around magmatic units. In the context of the extrusive model, this feature is ascribed to loading of thick lava flows on unconsolidated tuffaceous sediments (Huber and Byerly, 2012), however, it can also be regarded as the bulging of tuff units in response to forcefully injected magma.

7.4. What do the rodingites represent?

Rodingites in the Stolzberg Complex have been discussed extensively by Anhaeusser (1979) and Rodel (1993). These are essentially rocks that contain significant abundances of calcium-rich minerals (such hydrogrossular, diopside, vesuvianite, zoisite, etc.), which developed during Ca-metasomatism of mafic rocks (Anhaeusser, 1979). Rodingite bodies commonly occur as dykes and irregular pods and lenses in serpentized ultramafic rocks. The protoliths of rodingites are mafic rocks. In the Stolzberg Complex, some of the gabbronoritic units of the Upper Division which are in close contact with the serpentized dunites of the Lower Division have also suffered rodingitization. The stratiform rodingite bodies (gradually) grade up the stratigraphy into the adjacent gabbronoritic layers that were affected by albitization, saussuritization, uralitization, and epidotization.

In the context of the sheeted-sills model presented in this study, I concur with the suggestion of Anhaeusser (1979) that these bodies represent replaced gabbroic rocks through post-solidus Ca-metasomatism (possibly accompanying the serpentization of the dunites). However, here, it is suggested that the replaced gabbroic dykes, pods and lenses represent protrusions (into the ultramafic units) that accompanied the “late” mafic sills, which invaded the early-formed ultramafic units. This is in contrast to the suggestion by Anhaeusser (1979) that the mafic magma

represent a residual liquid following the extraction of the Upper Division peridotites. Interestingly, the lowest unit of the Upper Division is a thick gabbro-noritic layer, which occasionally transgresses into the underlying ultramafic rocks of the Lower Division. These features demonstrate that the mafic units do not represent a residual liquid, which was left behind after the extraction of the peridotites.

8. Assessing the effect of alteration on primary geochemistry

In section 3.5, it was indicated that rocks of the Barberton greenstone belt (both the supracrustal successions as well as the intimately associated layered complexes) were affected by severe alteration, where nearly all primary phases have been transformed into secondary mineral assemblages. The alteration is believed to have occurred very early in the history of development of these rocks, perhaps nearly contemporaneous with magmatism (Cloete, 1994, 1999). The transformation of primary igneous phases (such as olivine, pyroxene and plagioclase) into secondary minerals (such as serpentine, talc, chlorite, actinolite, and epidote) is commonly accompanied by modification of the original geochemistry of the rocks. This is because during the alteration processes (e.g., serpentinization, uralitization, silicification, etc.), some chemical components are added or subtracted, respectively, to and from the protolith by the action of the metasomatizing fluids (Furnes et al., 2012; Grant, 1986, 2005; Hofmann and Harris, 2008). In addition, chemical species may only be redistributed within the affected rock.

The extent to which chemical components may be disturbed depends on the host minerals, the chemistry of the fluids, physical conditions under which alteration occurs, and the fluid/rock ratio (Niu, 2004). Although this is the case, some elements are commonly affected severely by the alteration while others are generally not disturbed or only modified to an insignificant extent (Guice et al., 2019; Lahaye et al., 1995). Chemical species that are more prone to modification are referred to as mobile elements and those that resist change are called immobile elements. Immobile elements, to a significant extent, preserve the primary signatures of the rocks, thus allowing reconstruction of the nature of the magma from which the rocks formed. In mafic-ultramafic rocks, elements that are normally mobilized include large ion lithophiles (such as Cs, Ba, Rb, Sr, Na, K) whereas immobile elements include high field strength elements (Al, Ti, Zr, Hf, Nb, Ta, Y, REE, P) and transitional metals (Ni, Cr, Sc, V, Co) (Condie et al., 1977; Deschamps et al., 2013; Guice et al., 2019; Polat and Hofmann, 2003; Puchel et al., 2013). Elements such as Fe, Pb, U, and Th

may be either mobile or immobile depending on redox conditions during alteration. Elements considered immobile may be mobilized under certain conditions, for instance in the presence of CO₂ –rich fluids (Gruau et al., 1992; Lahaye et al., 1995).

Igneous processes (such as partial melting and fractional crystallization) play significant roles in determining the compositions of igneous rocks. These processes are largely systematic, generating defined relationships between the constituting elements (Guice et al., 2019; Polat and Hofmann, 2003). In contrast to igneous mechanisms, alteration processes are less systematic and thus tend to produce more erratic chemical signatures; mobilized elements get decoupled from the immobile ones (Grant, 2005; Hofmann and Harris, 2008). These contrasting characters between primary and secondary processes, therefore, allow determination of whether or not a particular element has been modified during alteration; immobile elements retain the primary systematic relationship and display good correlation amongst each other (i.e., inter-element ratios are relatively constant, resulting in a linear trend), whereas elements that have been mobilized get decoupled from this regular pattern and exhibit anomalous and deviant signatures (Polat et al., 2009). Although the inter-element ratio between immobile elements may be unaffected, their absolute concentrations are commonly diluted or enriched due to the addition or subtraction of other chemical components, respectively, into and from the protolith (Hofmann and Harris, 2008). Thus, the measured absolute concentrations may not be regarded as primary elemental abundances despite the elements being highly immobile.

The systematic control on chemical elements by igneous processes is governed by a quantity known as the partition coefficient (Rollinson, 1993; White, 2013). Partition coefficients are an indication of the degree to which a particular element would prefer to be incorporated into one phase over another during igneous processes. The greater the quantity for an element, determined for a certain phase, the more the element of interest would prefer to partition into that particular phase. Values of less than unity shows that the element prefers not to be incorporated into the phase of interest but into other available potential hosts and the chemical element is said to be incompatible.

In studies that investigate the effects of alteration on chemical elements, an element that is commonly highly immobile is used as a reference species against which other elements are plotted. For mafic-ultramafic rocks, the element Zr is commonly used as the reference as it is amongst the

most immobile chemical species and it is highly incompatible in mafic minerals, eliminating effects of igneous processes (Furnes et al., 2012, 2013). Any incompatible element that displays a linear trend when plotted against Zr is generally thought to have not been affected by significant disturbance, otherwise it is regarded as being mobilized. However, without the involvement of phases that incorporate Zr (eg., zircon), the degree of correlation also depends on the extent to which the partition coefficients of the element of interest in mafic minerals are similar to that of Zr, such that similar partition coefficients yield best correlations and vice versa (Niu, 2004). For example, the correlation between Zr and Hf will commonly be better than correlation between Zr and Nb. In normalized multi-elements diagrams, samples that have not been affected significantly by element mobility display coherent patterns whereas those that have undergone chemical disturbances exhibit incoherent (“spiky”) patterns (Guice et al., 2019; Schneider et al., 2019). In these diagrams, the mobile elements display significant enrichment or depletion anomalies.

Compatible immobile elements behave in a slightly different way. The composition of these elements in rocks is greatly influenced by the abundance of mineral phases into which these elements are incorporated (Furnes et al., 2012; Schneider et al., 2019). For example, the element Ni is highly compatible in olivine, hence (in the absence of sulphides) its composition in a particular rock is largely controlled by the abundance of olivine (Rollinson, 1993; White, 2013). During fractional crystallization, where olivine is removed from a magma system, the element Ni becomes preferentially depleted in the residual melt, while being enriched in the resultant olivine cumulate rock. As a result, olivine cumulates define a correlation trend that is different from the one that is displayed by olivine-poor rocks. Similarly, during partial melting, if olivine is retained in the residue, the generated melt is initially depleted in Ni, while the residue becomes enriched. Note that, such mechanisms, unlike alteration processes, still generate systematic patterns (Schneider et al., 2019). The difference is that, for immobile incompatible elements, all rocks samples (in the absence of contamination) will plot along a single linear trend, whereas samples will plot along different trends when immobile compatible elements are involved, depending on the abundance of the controlling phases in each sample. Inter-element ratios between incompatible elements cannot be changed by ordinary magmatic processes (other than contamination) while the ratios can be modified in a systematic way when compatible elements are involved. Crustal contamination processes also generate systematic trends, which are commonly divergent from the

trends displayed by uncontaminated samples (i.e., contaminated samples will define a new trend that is distinguishable from the one displayed by the uncontaminated samples).

In this section, the effects of alteration processes on the primary signatures of the Stolzburg Complex rocks are investigated. That is, elements, which were immobile during the alteration of these rocks, will be identified. The established primary signatures will be used later in pursuit of constraining and reconstructing the petrogenesis of the Stolzburg Complex.

The method employed to assess rocks of the Stolzburg Complex for element mobility relies on the fact that the accumulation of olivine and pyroxene, in general, do not modify the ratios between incompatible trace elements (Arndt et al., 1977; Bougault et al., 1979, 1988; Saunders et al., 1988; Szilas et al., 2014). We then expect co-magmatic olivine-pyroxene cumulates to display a single linear trend in correlation diagrams. Any sample that plot off the correlation line either represent an accumulation of a phase other than olivine and pyroxene or disturbance of the primary geochemistry. An additional phase commonly found in olivine-pyroxene cumulates is chromite, but this phase too does not fractionate incompatible trace elements. Plagioclase-rich rocks are observed to also plot along the olivine-pyroxene control line, meaning plagioclase also does not fractionate these elements. Only samples that plot along the correlation lines are regarded as being pristine and are used in the petrogenetic study.

Many element mobility studies that uses Zr as an alteration-independent reference element simply assume that this element is always the most immobile. While this is true in most cases, rare mobilization of Zr can also contribute to the scattering of data points. It is therefore essential to test whether or not the used alteration-independent element was not affected by alteration.

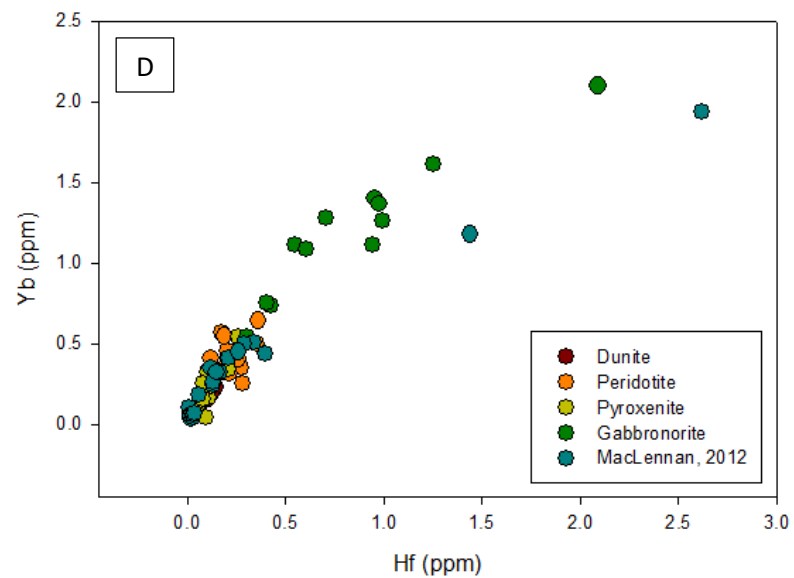
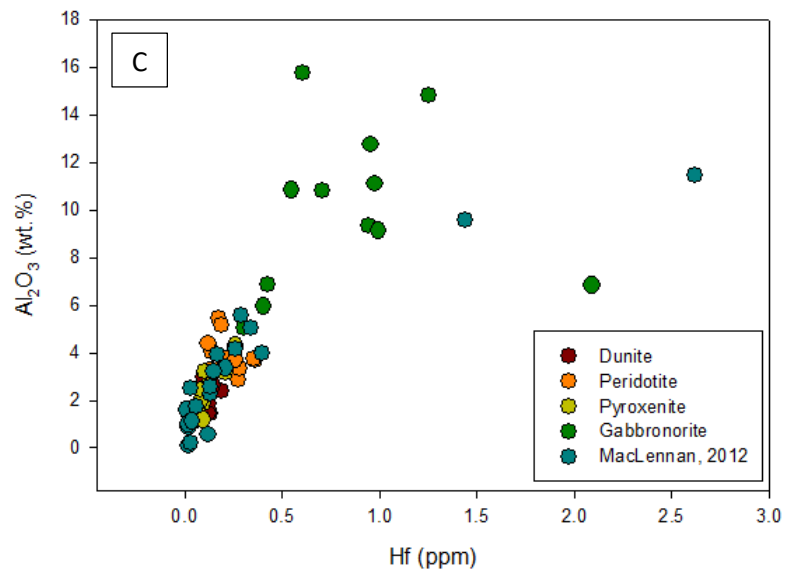
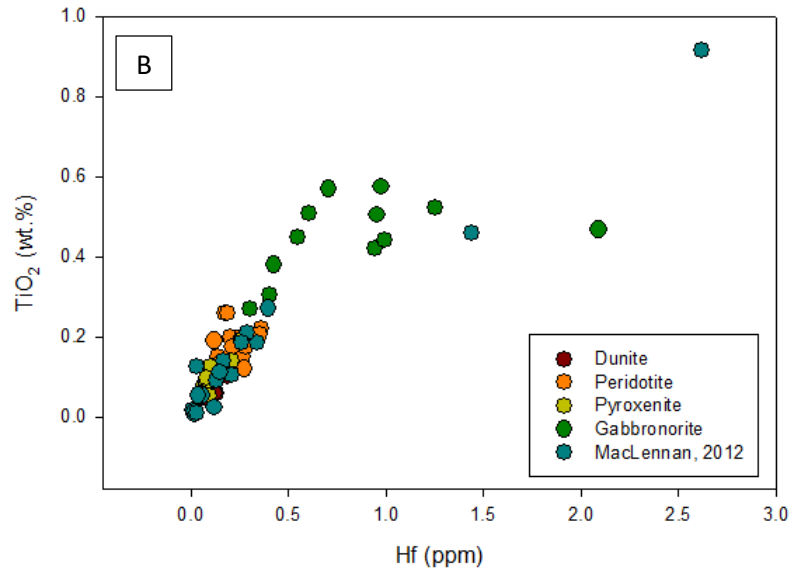
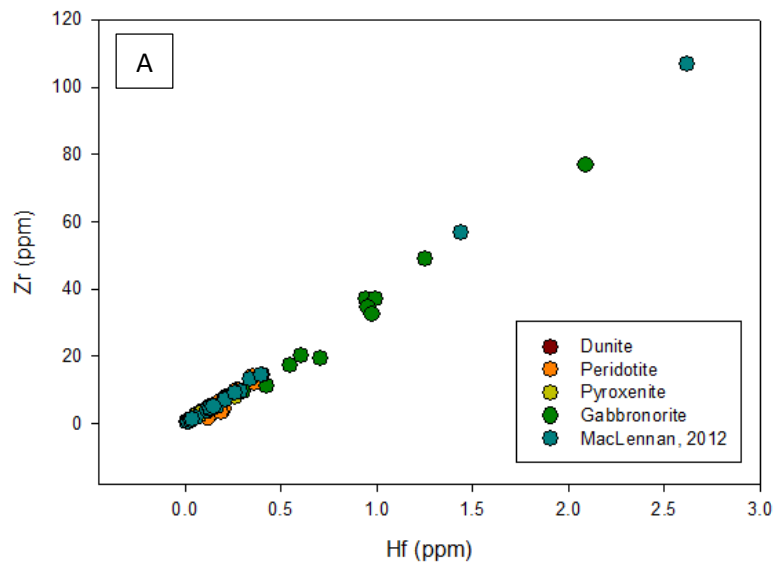
Preliminary investigation in this study showed that Hf consistently yield better correlations than Zr when these elements are plotted against other generally immobile elements (i.e., Ti, Al, Yb, Nb, Ta, Y). Given that Zr and Hf have very similar partition coefficients and therefore cannot be fractionated by ordinary igneous processes, the results suggest that Zr was potentially more affected by the alteration (complexation?) than Hf was. Therefore, Hf was used as the alteration-independent reference element instead of Zr.

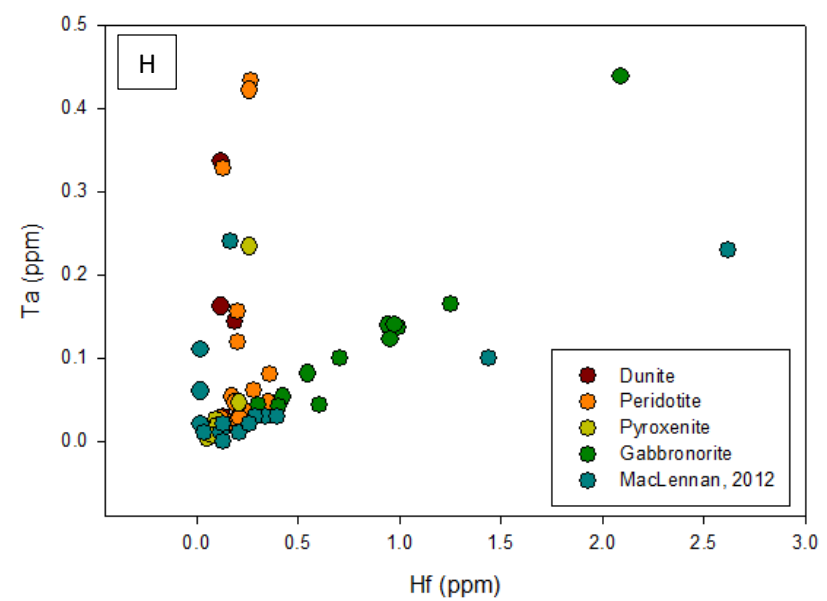
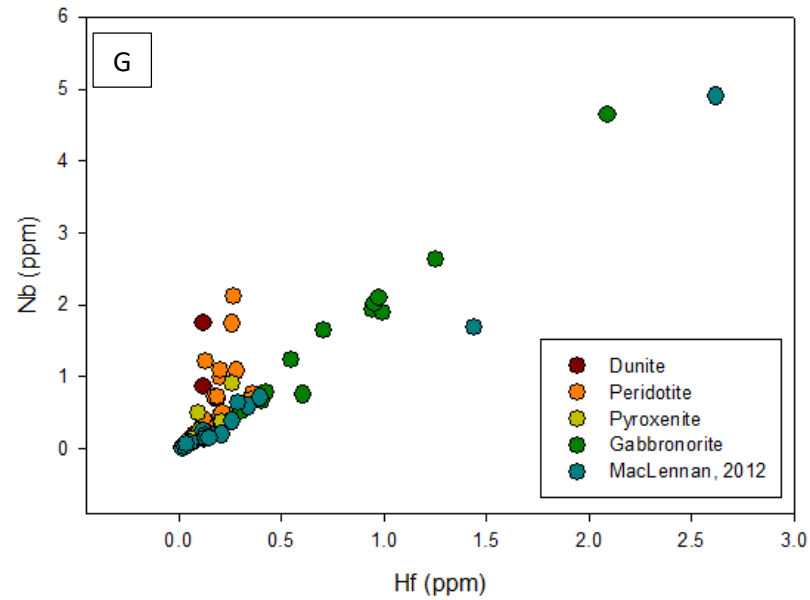
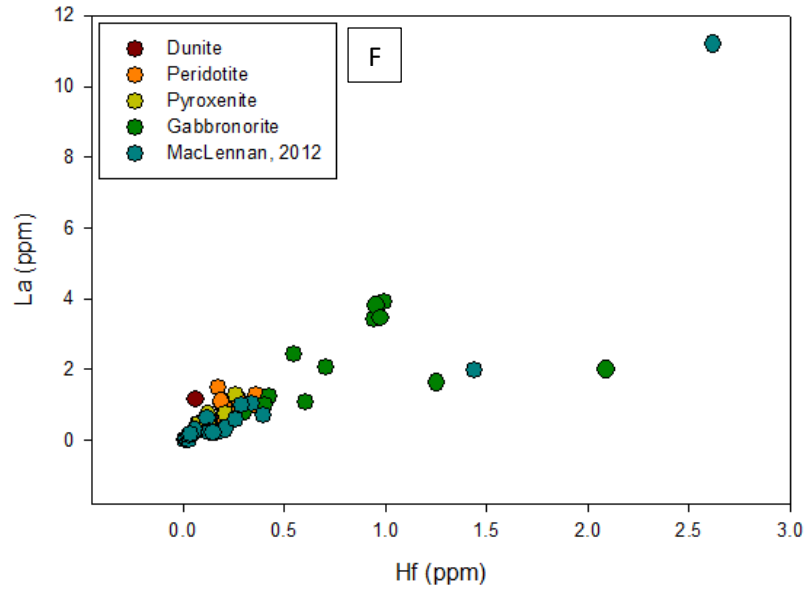
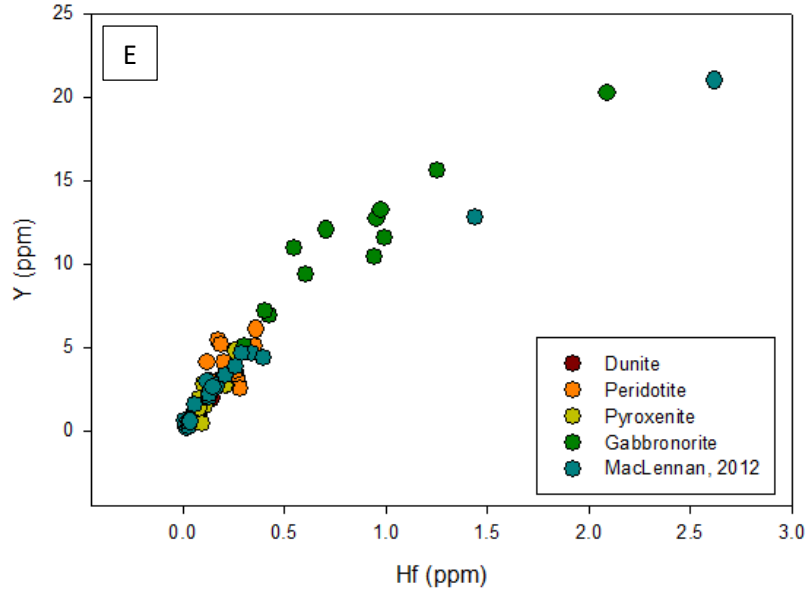
Correlation diagrams are presented in figures 6.1.1 - 6.1.4. As expected, generally immobile elements (Zr, Ti, Al, Y, REE, Nb, Ta, P) display good correlation with Hf (fig. 6.1.1). However,

some samples plot off the displayed linear trends. There are no other discernable trends that are displayed by the samples that plot off the main linear trend (i.e., samples that plot off the correlation line are simply scattered without any order). Thus, this scattering of data points cannot be attributed to igneous processes such as crustal contamination and accumulation of phases other than olivine, pyroxene, chromite and plagioclase (e.g., zircon, apatite, Ti-oxides) as these processes produce systematic trends as well. These erratic geochemical signatures are highly unlikely due to the fractionation of the alteration-independent index (i.e., Hf) from other immobile elements by zircon accumulation, as this phase is typically absent in sub-alkaline ultramafic cumulates, which also plot off the correlation line. Decoupling between Nb and Ta (fig. 6.1.2A & 6.1.7CA) further indicates that the erratic signatures are not due to moderate and low pressure magmatic processes as there is no known such mechanism that fractionate these elements, at least in sub-alkaline magmatic systems (Niu, 2004). Large variations in ratios between immobile incompatible elements (e.g., Nb/Yb, Zr/Nb) could also suggest crystallization of the rocks from very different parental magmas. This is highly unlikely as it would imply that the Stolzburg Complex was fed by magmas derived from multiple and very different sources. If not all, most of the magmatic rocks of the Barberton greenstone belt display similar inter-element ratios. While erratic patterns may, in general, result from analytical error, this is unlikely the case in the present study since abundances of the elements in the rocks of the Stolzburg Complex (table A4) can be reliably measured with precision by ICPMS and measurements of certified reference materials (CRMs) yielded precise result (table A2 & 3), indicating that the instrument was operating well. Moreover, data of the Stolzburg Complex from MacLennan (2012), measured by a different instrument at the University of Cape Town, also display the erratic patterns. Therefore, it is concluded that the generally immobile elements have been disturbed by alteration in samples that plot off the correlation lines. In gabbroic (but not peridotitic and pyroxenitic) cumulates, however, it is more difficult to determine whether elements such as Al, Ti, Zr, P have been mobilized or not, as these may be fractionated by the accumulation of plagioclase, Ti-oxides, zircon, apatite respectively. Nevertheless, such process cannot fractionate the Zr-Hf, Nb-Ta, and Th-U pairs. Thus, divergent Zr/Hf, Nb/Ta, and Th/U ratios are regarded as being affected by element mobility. Although Th and U suffered significant mobilization (as indicated by the noticeable scattering of data points when these elements are plotted against Hf), considerable preservation of these elements is indicated by the excellent correlation displayed when they are plotted against each

other (fig. 6.1.2B). Again, as anticipated, the large ion lithophile trace elements (Rb, Sr, Cs, Ba, Pb) show large ranges for a given value of Hf (fig. 6.1.3). This scattering of data points indicates that these elements were severely affected by alteration. As a result, these elements cannot be used in petrogenetic studies of the Stolzburg Complex rocks.

In contrast to co-variation diagrams using incompatible trace elements, where samples plot along a single linear trend, major and compatible trace elements display multiple linear trends for each group of rocks (i.e., peridotites, pyroxenites, and gabbro-norites). This is because major and compatible trace elements in cumulates are controlled by fractional crystallization, which results in different rock types with systematically variable mineralogical and chemical compositions. In addition to Al_2O_3 , other major elements that produce discernable trends includes MgO and SiO_2 (fig. 6.1.1C and 6.1.4A & B). Although these chemical species are less affected by alteration, some samples display anomalous values, most probably resulting from addition or subtraction of these species during alteration. In contrast, no trends are discernable in plots of CaO , Na_2O , K_2O , MnO , Fe_2O_3 against Hf (fig. 6.1.4C, D, E, F, G). This indicates that these elements were severely mobilized during alteration, as commonly reported. The large spread in abundances of these species over a small range of Hf values is attributed to element mobility (see fig. 6.1.4E & G: orthopyroxenite samples). For compatible trace elements, Cr, Ni, Co, and V display recognizable trends whereas Cu, and Zn show none (fig. 6.1.5). Although samples show a large spread in a plot of Sc against MgO , the expected positive linear trend is visible. In addition, dunite samples also display a large spread in Cr, Ni, and Co values for a given value of MgO . This is probably a result of chromite accumulation in these rocks as these elements are highly compatible in chromite (e.g. Puchtel et al., 2013). Note that Cr_2O_3 values obtained by XRF analysis are used instead of Cr measurements from ICP-MS. This is because Cr content tend to be underestimated in solution-based ICP-MS analysis as chromite is hard to dissolve (Allan Wilson, 2018, personal communication). This chromite effect is indicated by poor correlation between values obtained by XRF and ICP-MS analyses (fig. A1). Samples with low Cr contents (≤ 1000 ppm) (i.e., gabbro-norites) display better correlation as no or limited amount of chromite grains formed in these rocks.





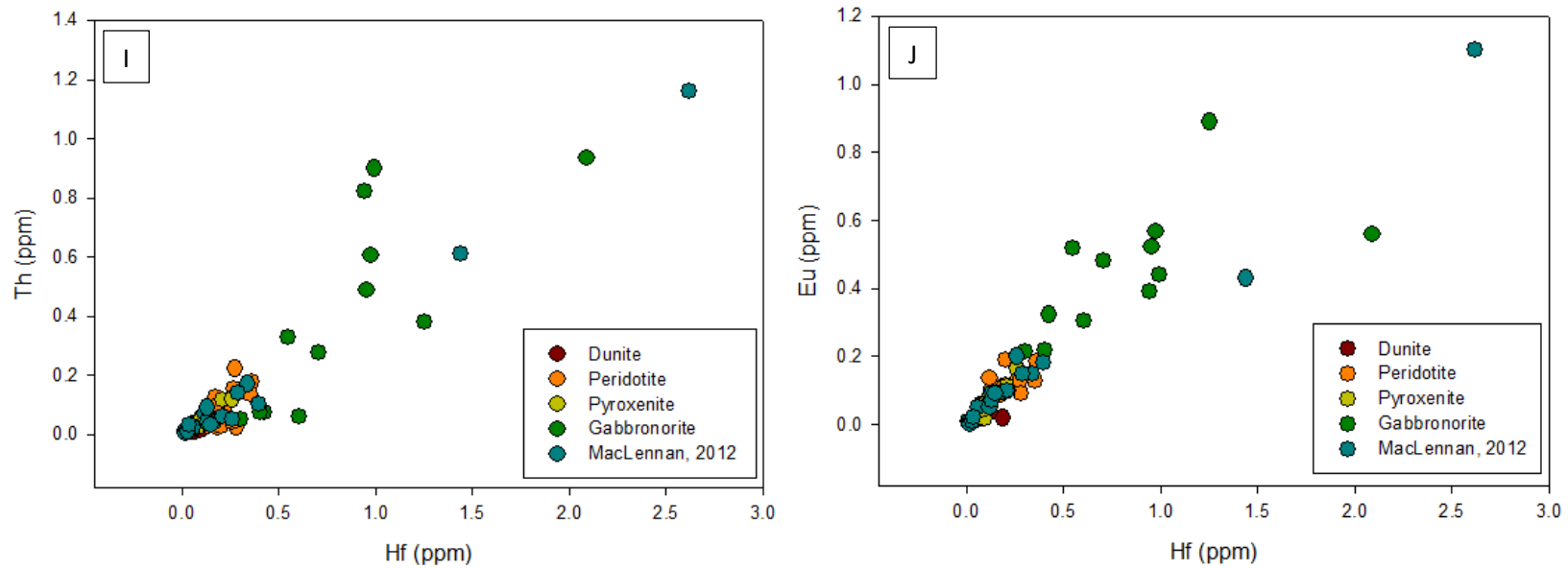


Figure 6.1.1: Plots of generally immobile trace elements (Zr, TiO_2 , Al_2O_3 , Yb, Y, La, Nb, Ta, Eu, Th) against Hf. Maroon, orange, lime, green circles indicate Stolzburg Complex data obtained in this study and the blue circles represent Stolzburg Complex data from MacLennan (2012).

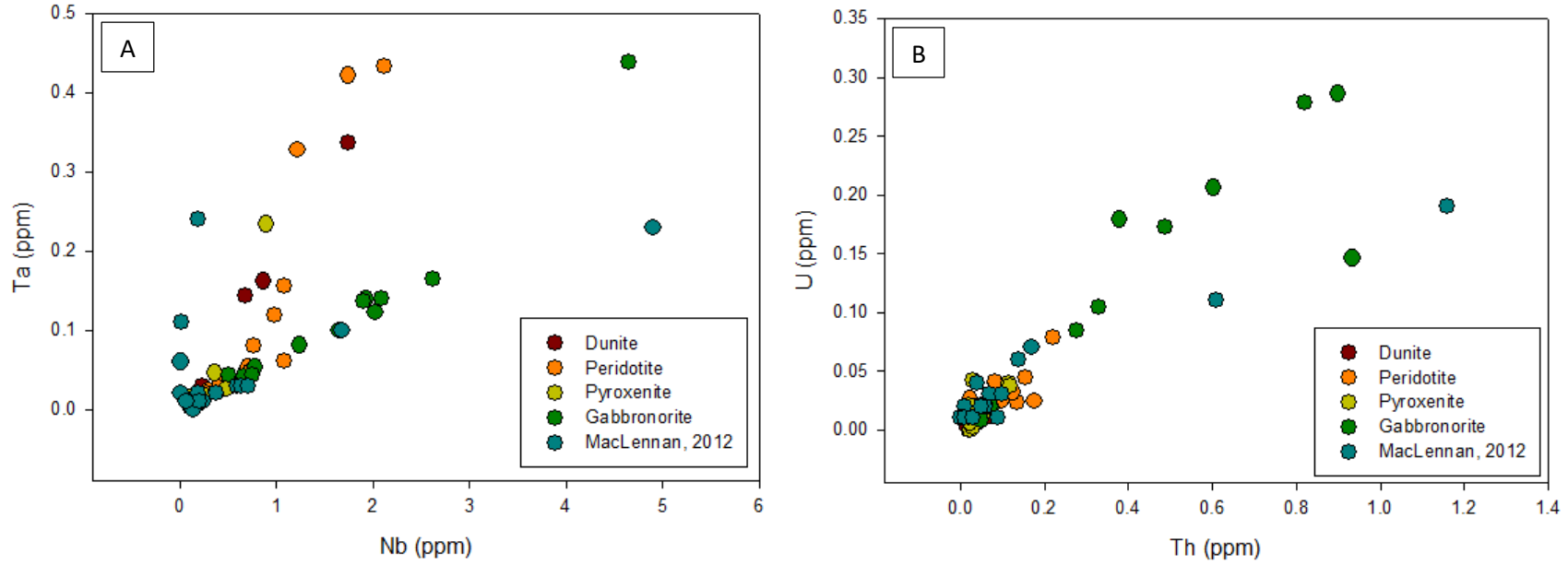
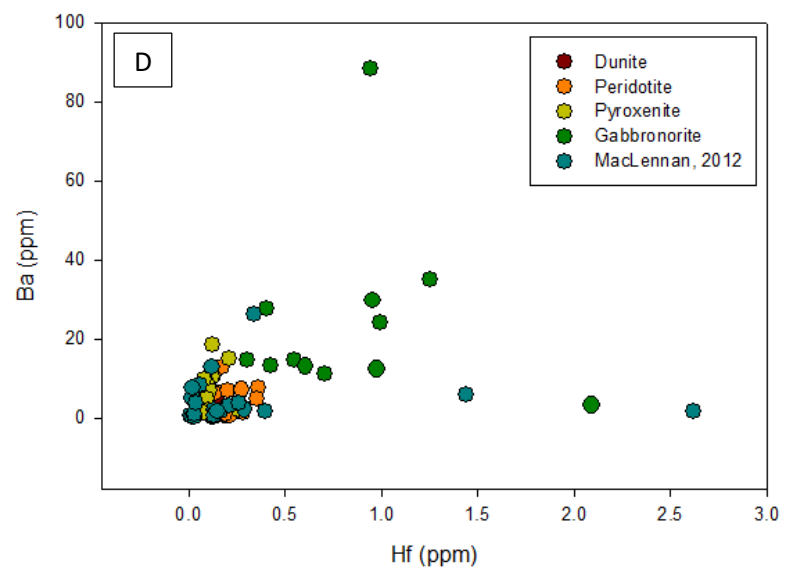
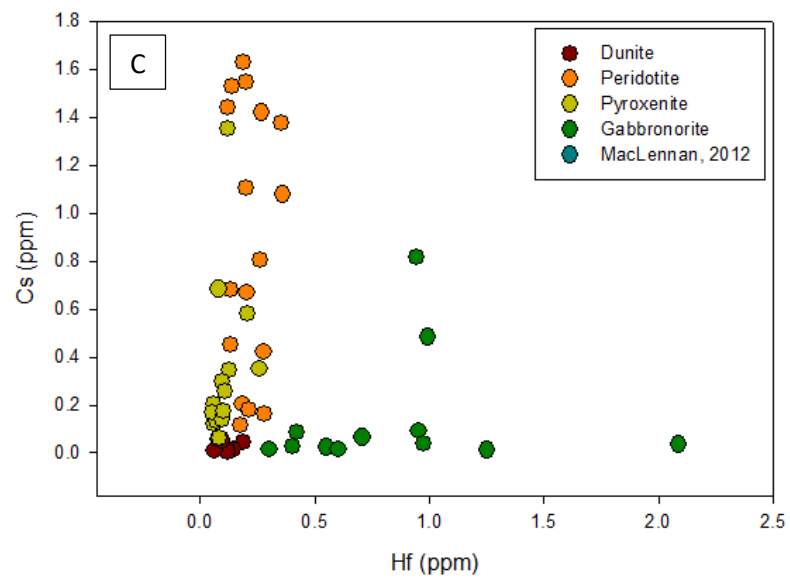
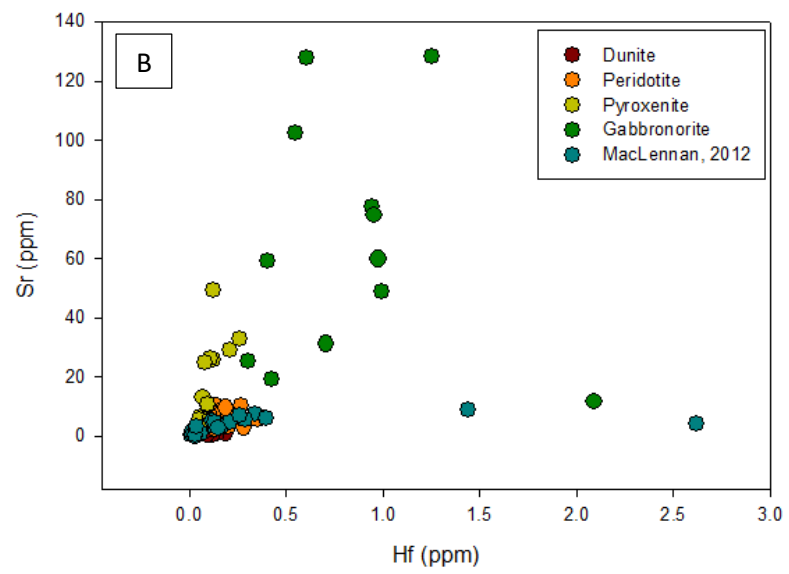
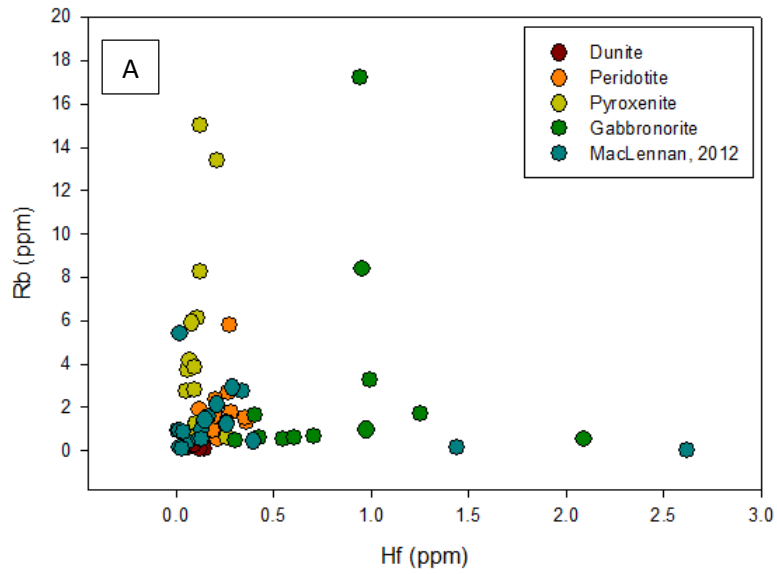


Figure 6.1.2: Correlation diagrams between elements with very similar bulk partition coefficients (i.e., Ta vs Nb and U vs Th). Maroon, orange, lime, green circles indicate Stolzburg Complex data obtained in this study and the blue circles represent Stolzburg Complex data from MacLennan (2012).



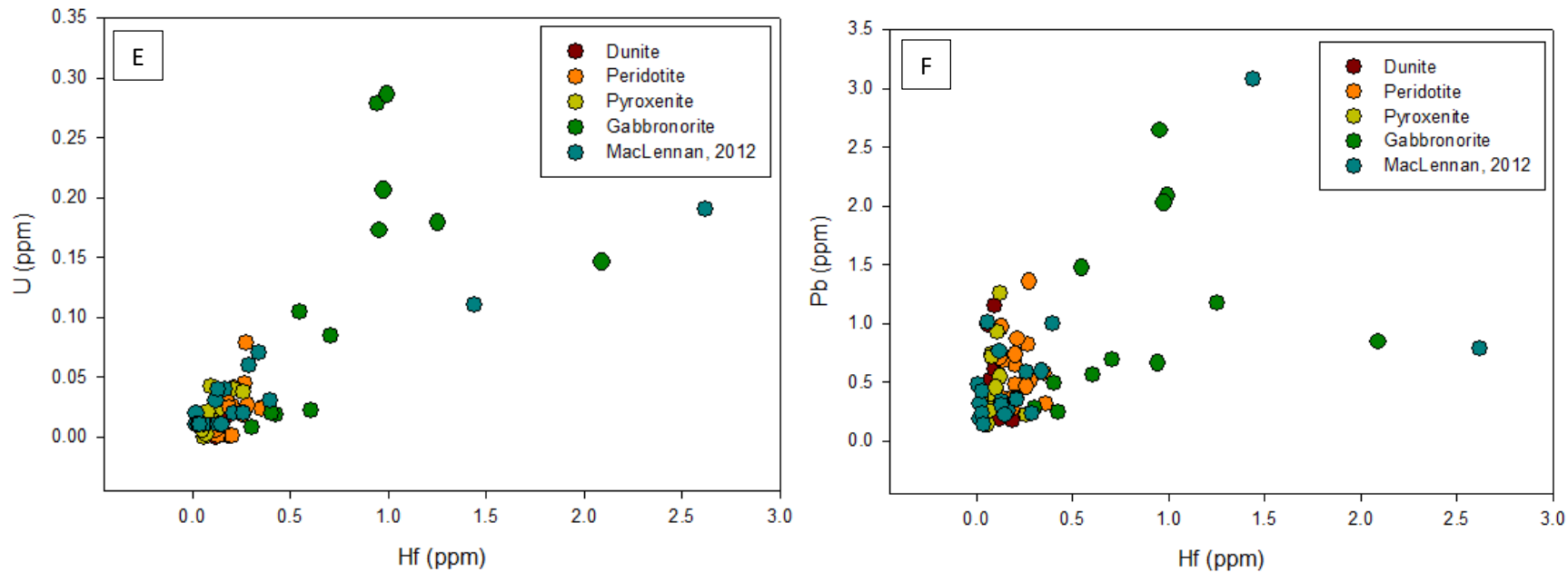
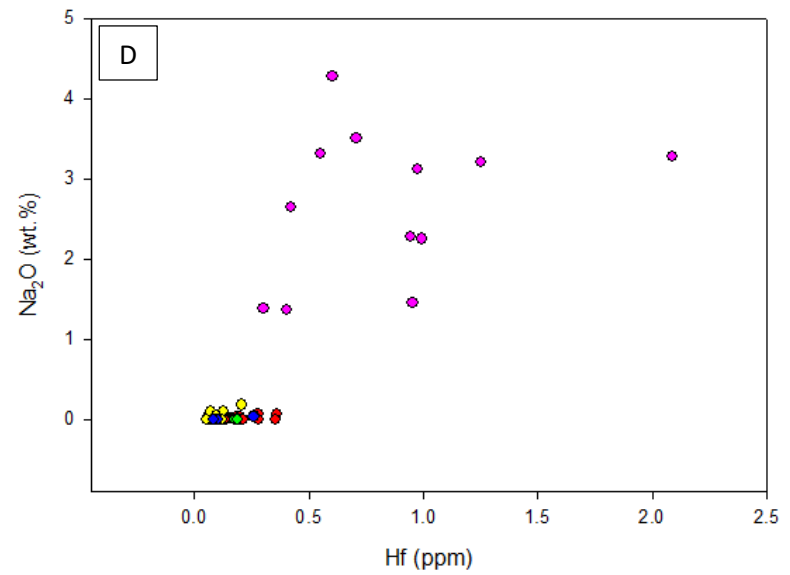
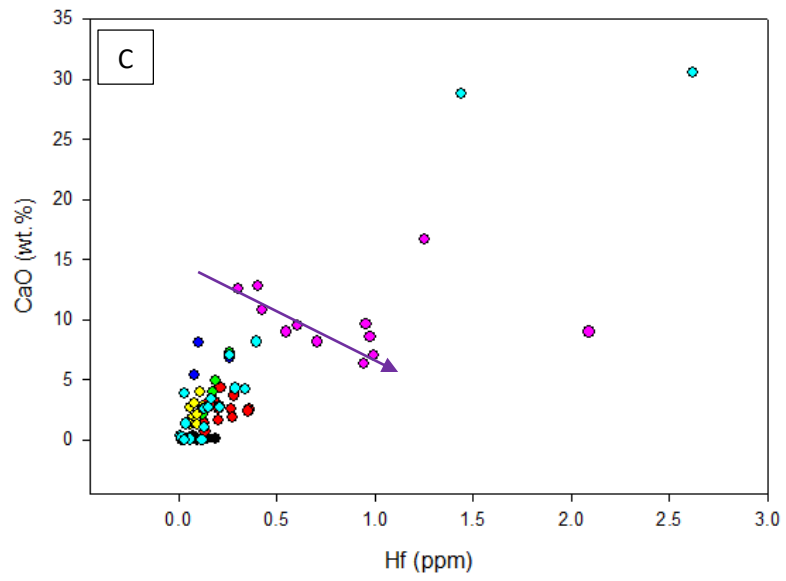
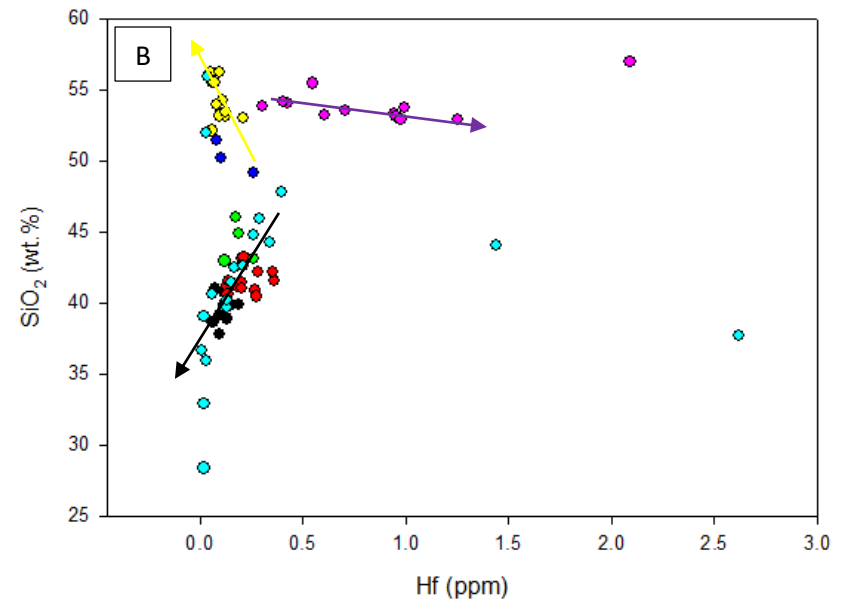
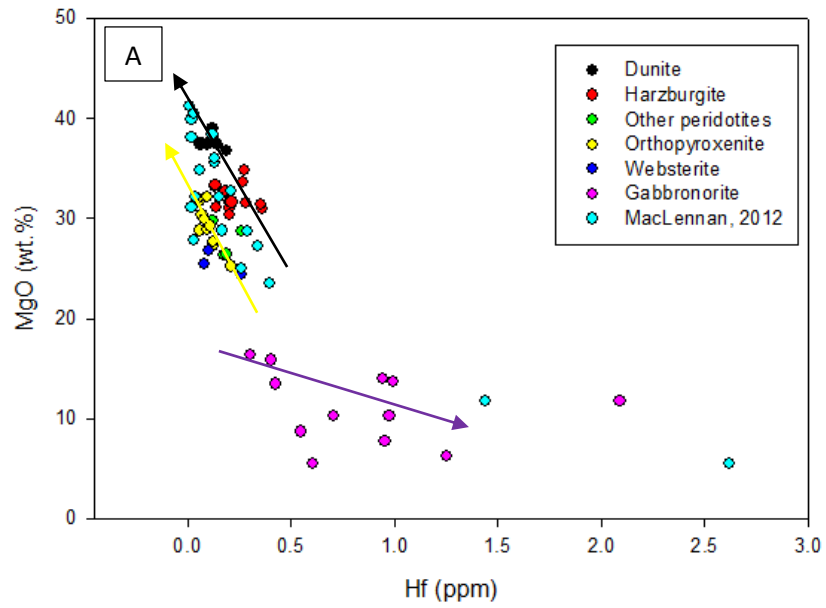


Figure 6.1.3: Plots of generally mobile trace elements (Rb, Sr, Cs, Ba, U, Pb) against Hf. Maroon, orange, lime, green circles indicate Stolzburg Complex data obtained in this study and the blue circles represent Stolzburg Complex data from MacLennan (2012).



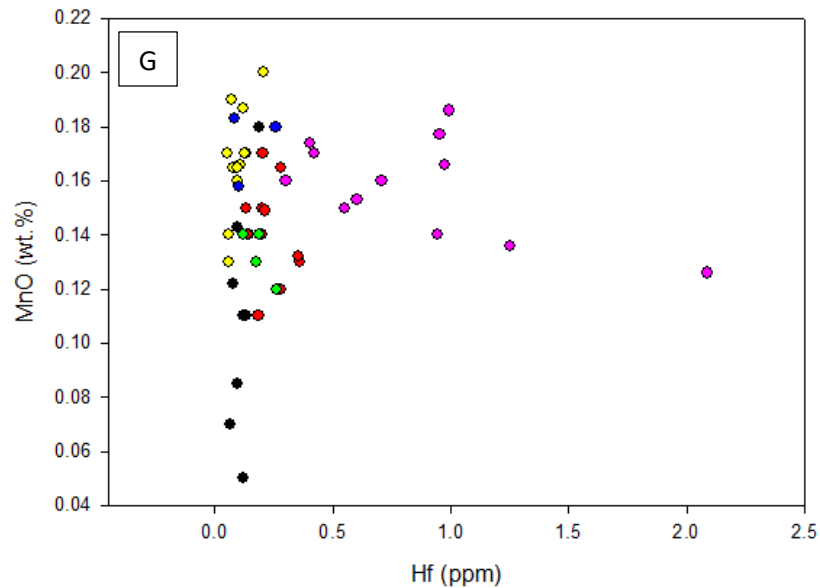
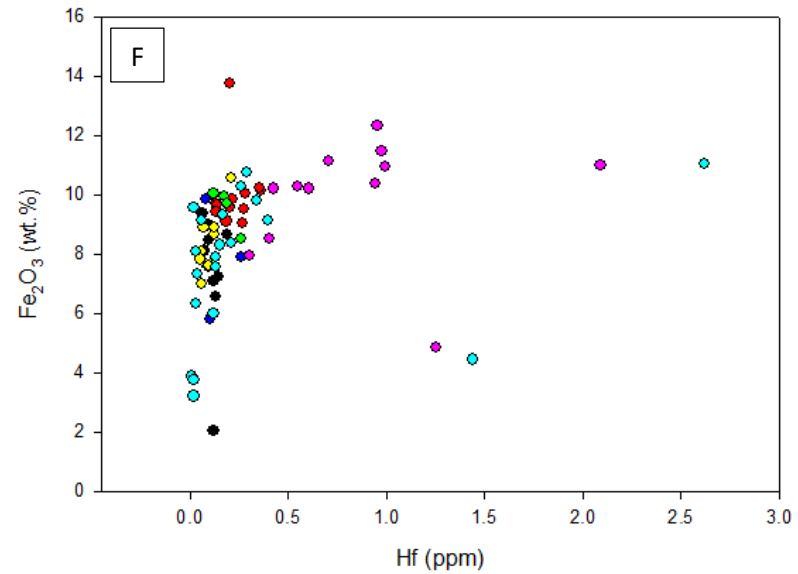
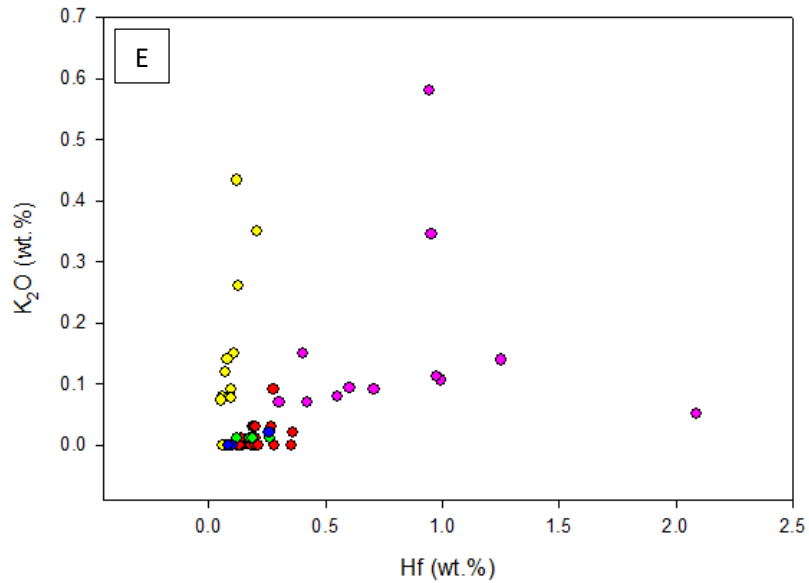
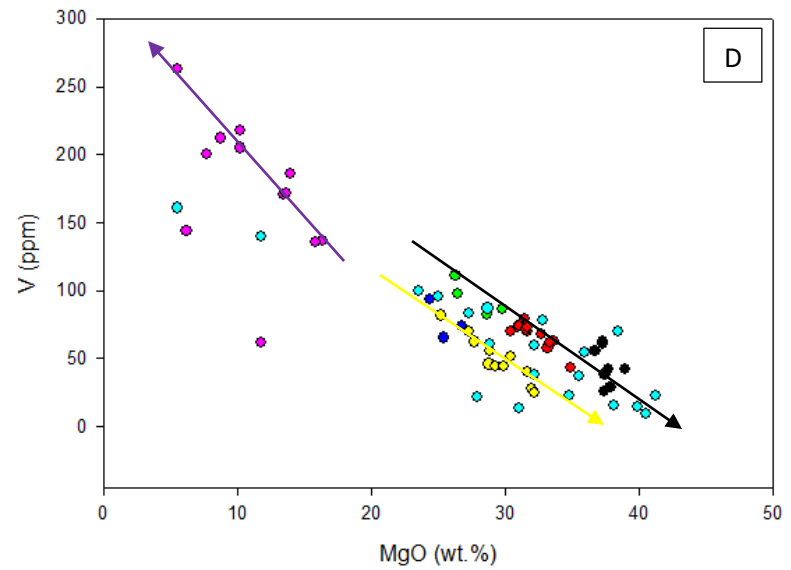
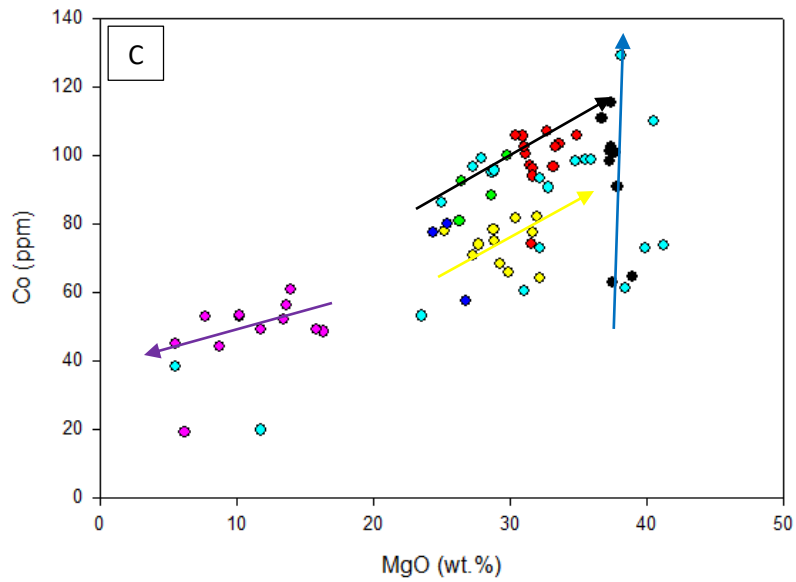
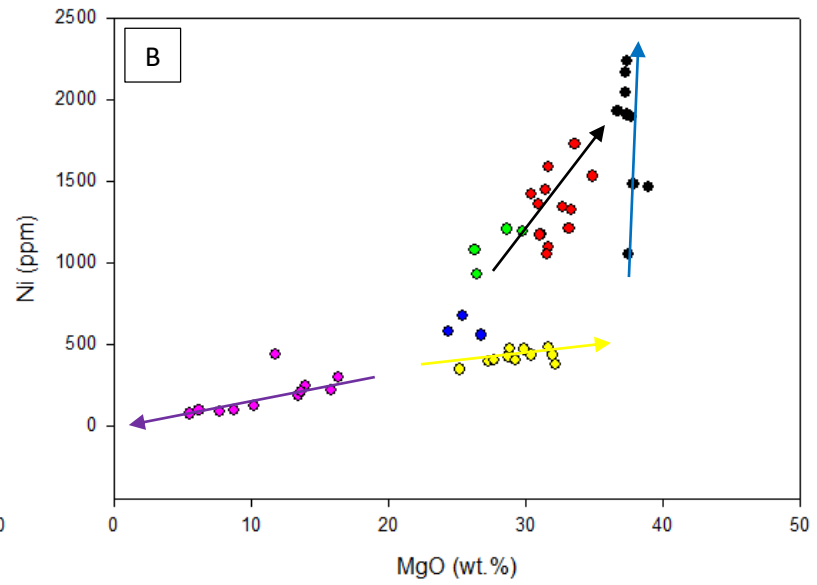
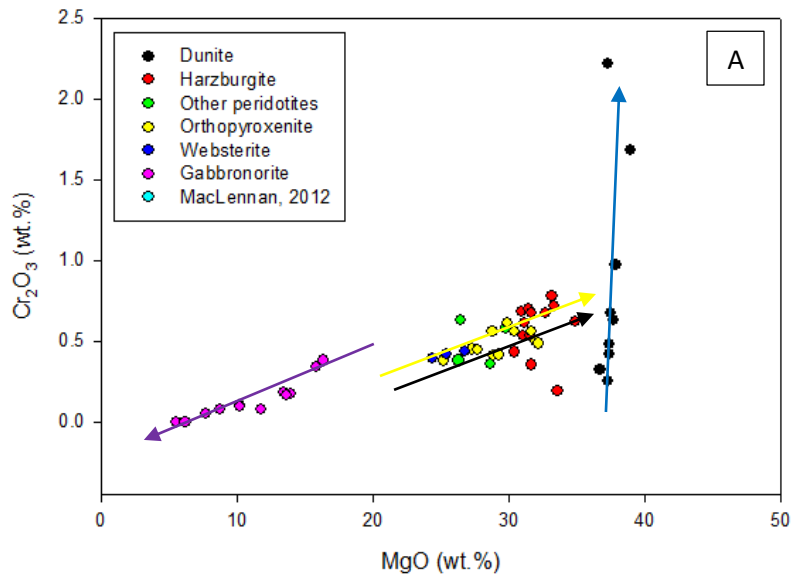
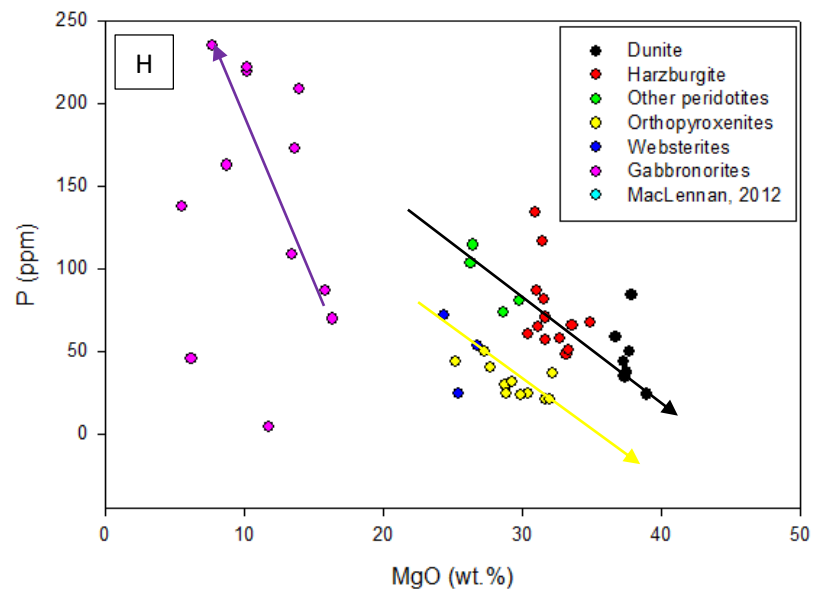
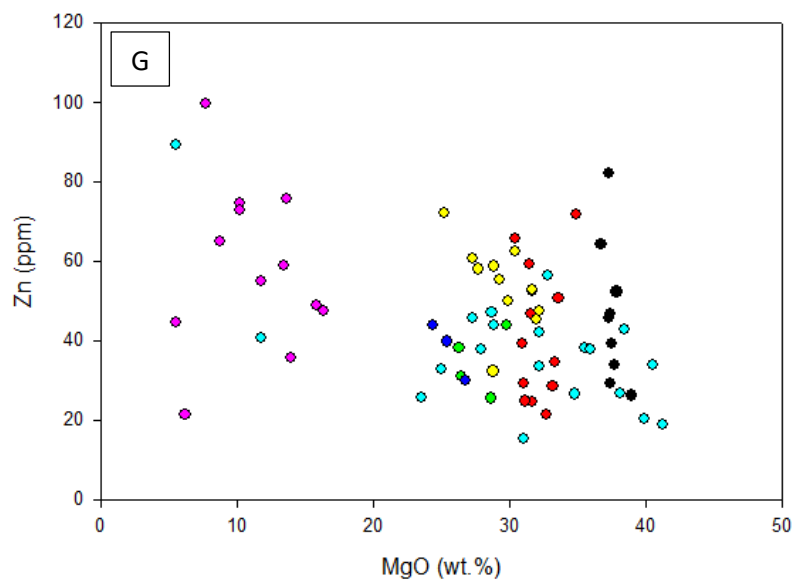
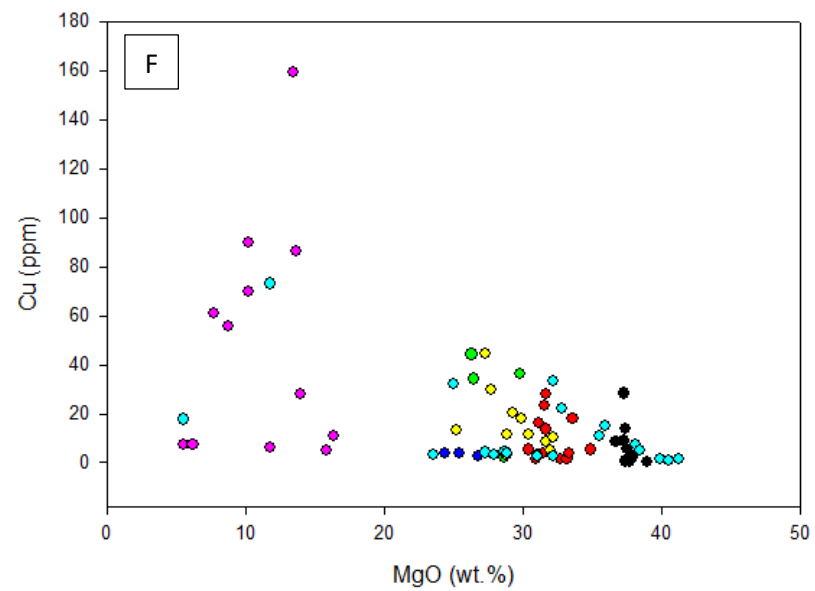
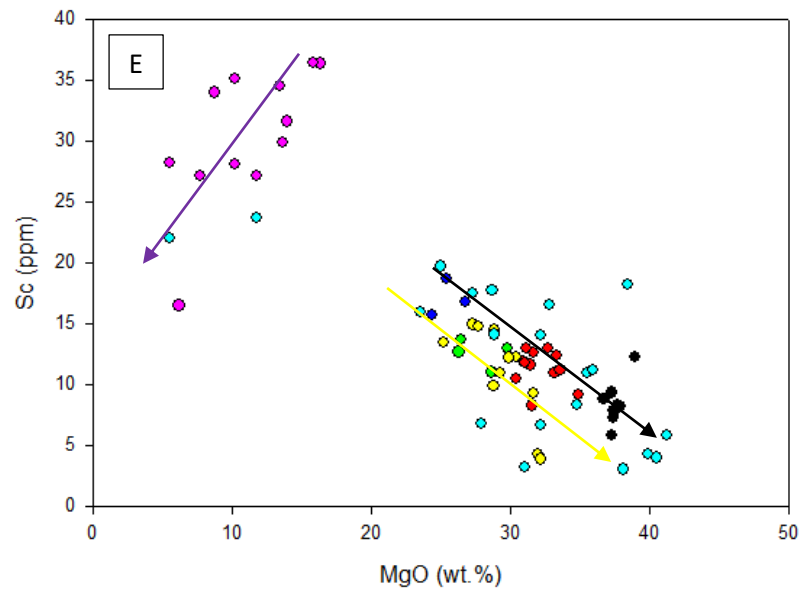


Figure 6.1.4: Plots of major oxides against Hf. Black, red, lime, yellow, royal blue, purple circles, respectively, represents dunite, harzburgite, other peridotite, orthopyroxenite, websterite, and gabbro/norite samples used in this study. Sky blue circles represents Stolzburg Complex data from MacLennan (2012). Black and yellow arrows, respectively, represent olivine and orthopyroxene accumulation (as defined by olivine and orthopyroxene cumulates, respectively) while the purple arrow indicate pyroxene and plagioclase fractionation trend.





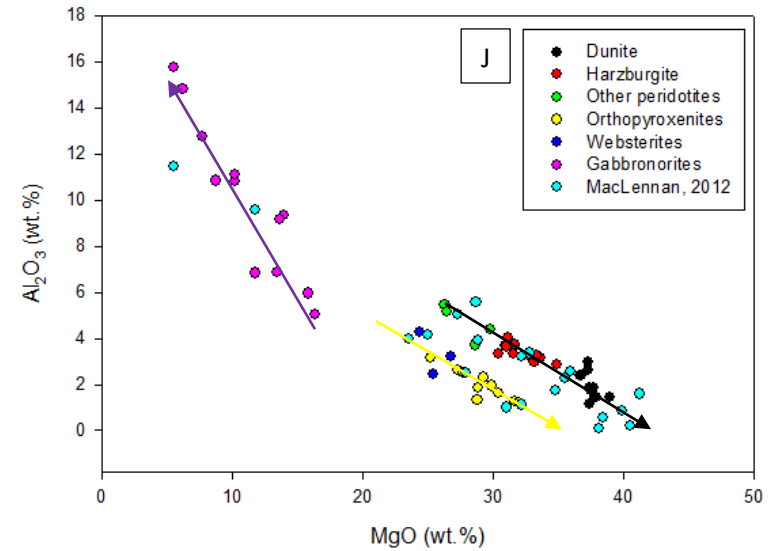
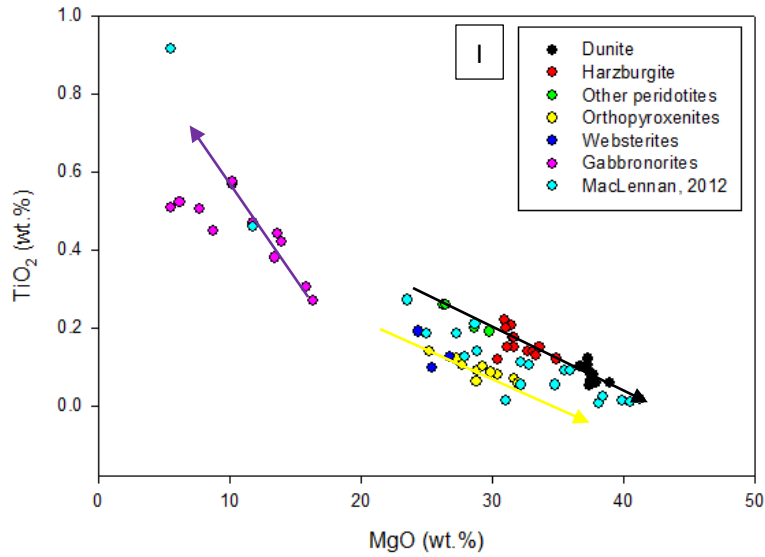


Figure 6.1.5: Plots of compatible trace elements against MgO. Symbols as in figure 6.1.4. Blue arrows represent chromite accumulation.

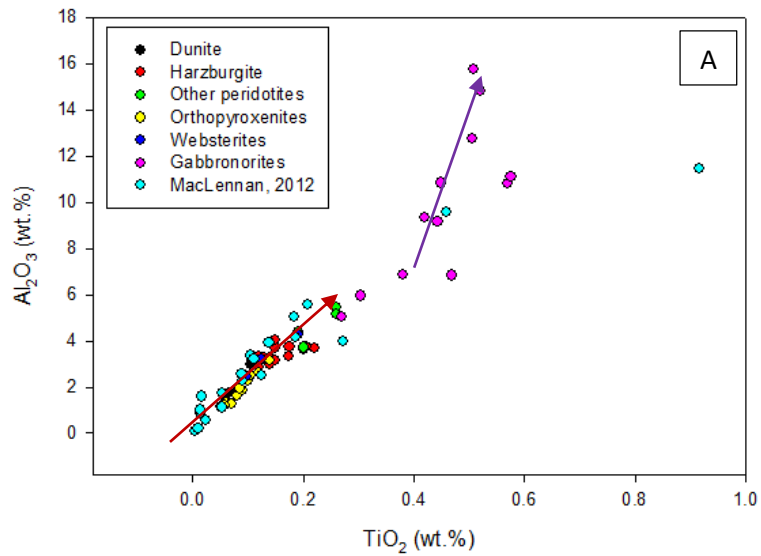


Figure 6.1.6: Plot of Al₂O₃ against TiO₂. Red arrow follows the linear trends defined by both the peridotites and pyroxenites and the purple arrows indicate the trend followed by the gabbroic rocks.

Elements shown above to be minimally affected by alteration allow constraints to be put on the petrogenesis of the Stolzburg Complex. However, the data must be treated with utmost diligence in order to avoid over-interpretation, as the generally immobile elements are shown to be substantially affected by alteration in some samples. Thus, the samples were filtered (see table A5) and only those that display best preservation of primary geochemical signatures were used in the petrogenetic investigation. The method used to filter out samples severely affected by alteration entailed plotting different inter-element ratios (including Nb/Ta, Th/U, La/Hf, Yb/Hf, Y/Hf) against Zr/Hf and rejecting all the samples that plot outside the cluster formed by most samples (fig. 6.1.7A, B, C, D). Since mantle-derived rocks display near-constant Zr/Hf and Nb/Ta ratios of ~ 36 and ~ 17 (Bau, 1996; Green, 1995; Hofmann, 1988; Jochum et al., 1986; Schmidt et al., 2014), respectively, this feature facilitated definition of acceptable cluster regions. Reasonable allowable ranges of 33-39 and 14-20 for Zr/Hf and Nb/Ta ratios, respectively, were assigned. The Th/U ratio in most geological systems was also reported to be near-constant, displaying a very narrow range of 3.7-4.0 (Allègre, 1968; Cumming and Richards, 1975; Tatsumoto, 1978; Manhès et al., 1979). This further assists in the identification of primary compositions (and therefore preserved samples) and an allowable range of 2-5 was set. Samples that plot within the cluster regions are those that display near-constant inter-element ratios, indicating preservation of primary composition. Indeed, samples that survived the filtration process were found to display a consistent and coherent Primitive Mantle (PM)-normalized multi-element pattern (fig. 6.2.1A), which further affirms preservation of primary geochemical signatures. Samples were thereafter grouped in terms of their degree of coherence and conformity to the trace element pattern displayed by the preserved samples; group 1 constituted by the best preserved samples and group 5 mostly comprised of the poorly preserved samples (table A5). In the co-variation diagrams, samples that were observed to plot far off the linear correlation trends were found to belong to group 5 (e.g., fig. 6.1.7C: Nb vs Ta). In addition, samples belonging to group 5 plot far outside the clusters formed by the preserved samples in plots of immobile elements ratios against Zr/Hf (e.g., fig. 6.1.7A: Zr/Hf vs Nb/Ta). These samples display positive Nb and Ta anomalies and subchondritic Nb/Ta ratios of < 10 . Samples that are apparently rodingitized (e.g., HD2, GV6, STLZ-91-7, STLZ-91-8; as indicated by the excessive Ca-enrichment and Si-dilution (fig. 6.1.4C & B, respectively)) display these features and are thus attributed to alteration as opposed to being primary signatures.

Notice that there are no clusters formed by specific rock types (fig. 6.1.7A & B). This further indicates that fractional crystallization of olivine, pyroxene, plagioclase, and chromite does not affect the incompatible element ratios of the parental magmas.

Gabbro-noritic samples display the largest spread in the $\text{Al}_2\text{O}_3/\text{TiO}_2$ ratio, probably due to the fractionation of Al and Ti by plagioclase and Ti-oxides, respectively. However, the olivine-pyroxene cumulates display a narrow range, recording the parental signature (see later). The extreme $\text{Al}_2\text{O}_3/\text{TiO}_2$ values exhibited by three of the group 5 samples are attributed to alteration (rodingitization?); two of these samples display non-chondritic Zr/Hf and Nb/Ta ratios.

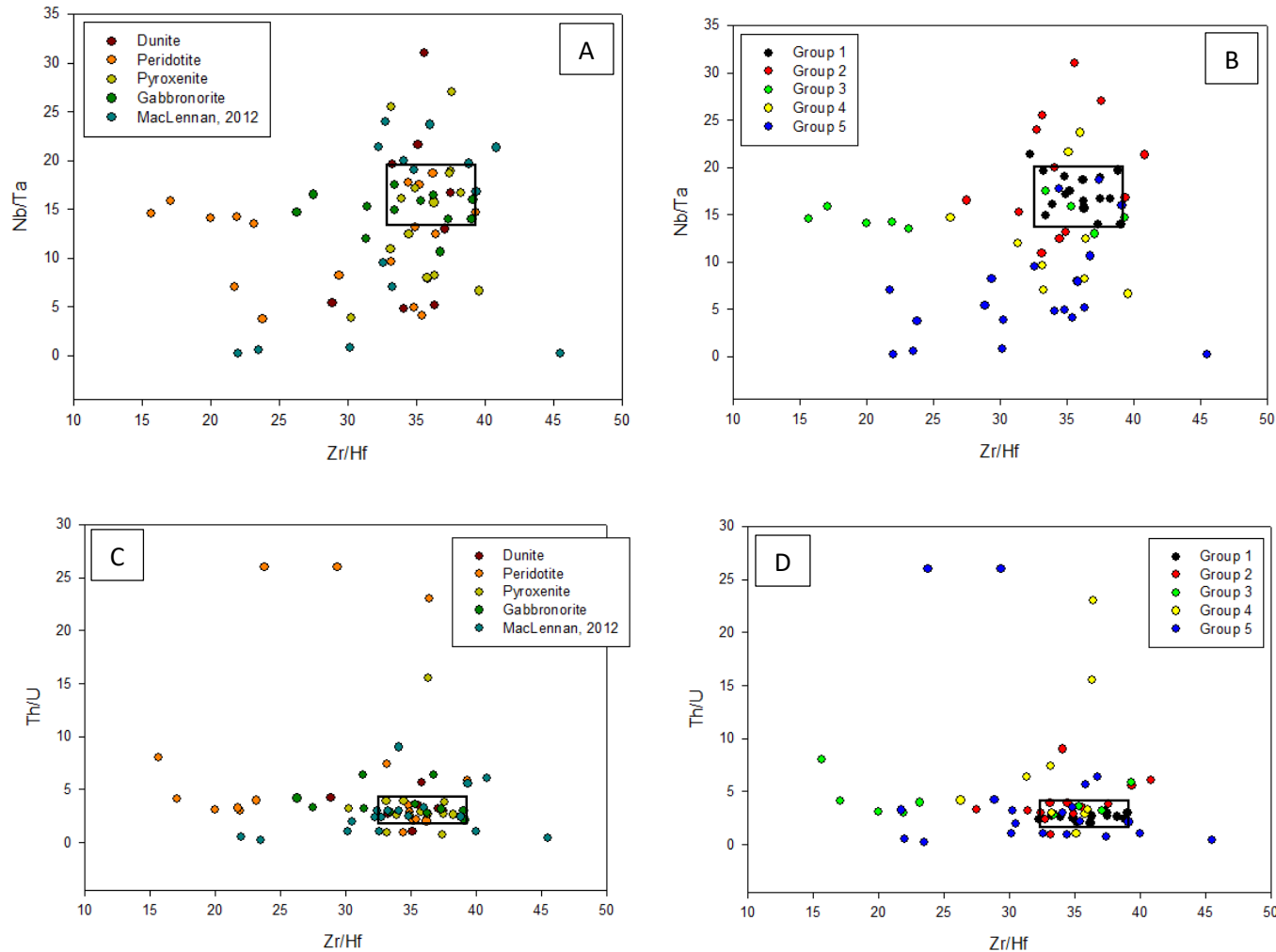


Figure 6.1.7A: Plot of Nb/Ta and Th/U against Zr/Hf showing groupings of the Stolzburg Complex rocks based on degree of preservation of primary geochemistry. The best preserved rocks (group 1; black circles) cluster around the chondritic ratios of ~ 36 , ~ 17 , $\sim 3.7-4$ for Zr/Hf, Nb/Ta, and Th/U, respectively. In contrast, the poorly preserved samples (e.g., group 5; royal blue) plot far off the allowable cluster regions. The rectangles indicate defined ranges of allowable ratios. Diagrams on the left distinguish samples by rock type while the ones on the right represent the same data but distinguished by the defined rock group.

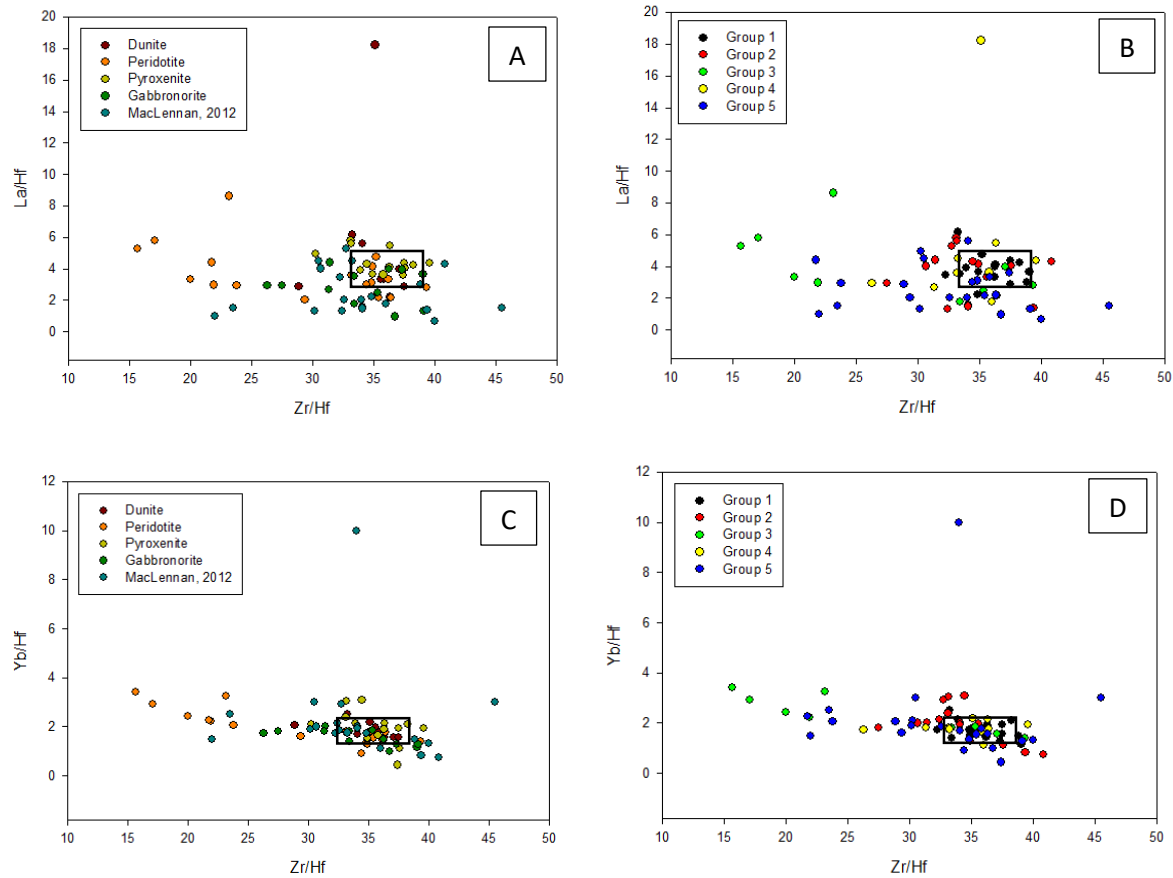


Figure 6.1.7B: Plot of La/Hf and Yb/Hf against Zr/Hf showing groupings of the Stolzburg Complex rocks based on degree of preservation of primary geochemistry. The best preserved rocks (group 1; black circles) cluster around the chondritic ratio of ~ 36 for Zr/Hf . In contrast, poorly preserved samples (e.g., group 5; royal blue) plot far off the allowable cluster regions. The rectangles indicate defined ranges of allowable ratios. Diagrams on the left distinguish samples by rock type while the ones on the right represent the same data but distinguished by the defined rock group.

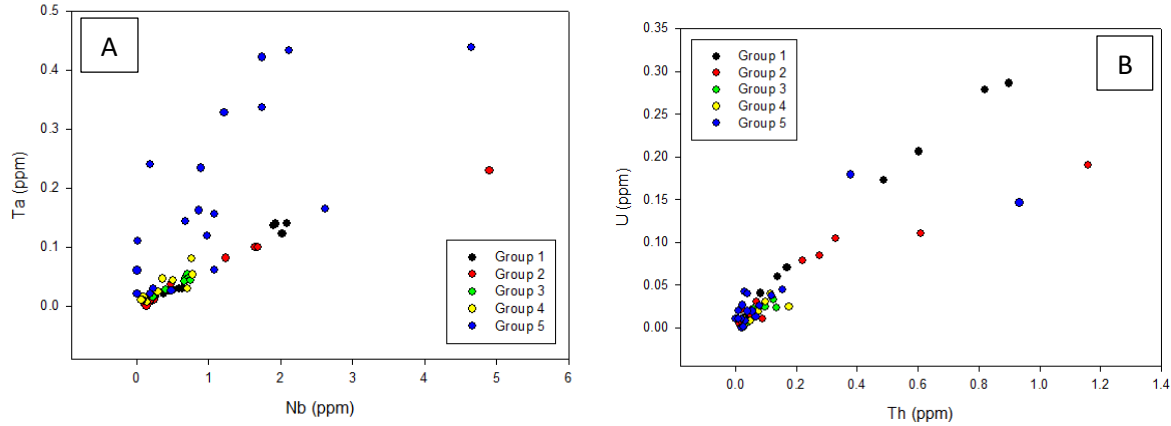


Figure 6.1.7C: Correlation diagrams for Stolzburg Complex data. Plot of Ta against Nb (A). Plot of U against Th (B). Samples are distinguished by the defined rock groups. The least-altered rocks (group 1; black circles) plot along the correlation line while most-altered samples (e.g., group 5; royal blue) plot far off the line.

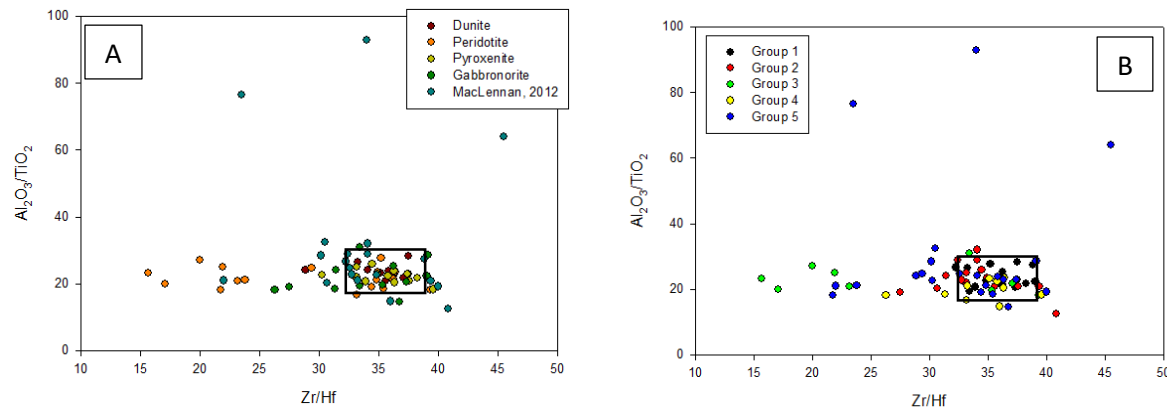


Figure 6.1.7D: Plots of Al_2O_3/TiO_2 against Zr/Hf showing the relationship between the Al_2O_3/TiO_2 ratio and rocks type and degree of primary geochemistry preservation. The least-altered rocks (group 1; black circles) cluster around the chondritic ratio of ~ 36 for Zr/Hf. In contrast, most-altered samples (e.g., group 5; royal blue) plot far off the allowable cluster regions. The rectangles indicate defined ranges of allowable ratios. Diagram on the left distinguish samples by rock type while the one on the right represent the same data but distinguished by the defined rock group.

9. Primary geochemistry

9.1 Major elements

The SiO₂ and MgO contents in peridotites range from 38-43 wt.% and 39-28 wt.%, respectively. In the orthopyroxenites, SiO₂ content ranges from 52-56 wt.% and MgO ranges from 28-32 wt.%. In the gabbronoritic rocks, SiO₂ ranges from 52-57 wt.% and MgO ranges from 5-17 wt. %. Overall, the Al₂O₃/TiO₂ ratio ranges from 17 to 29, with an average of 22, the chondritic value (fig. 6.1.6 & 6.1.7DA). Stolzburg Complex rocks may, therefore, be classified as Al-undepleted ultramafic-mafic rocks.

9.2 Trace elements

Trace elements patterns discussed here are of the least-altered (i.e., best-preserved) samples only (see table A5: group 1). All samples display very similar, if not identical, Primitive Mantle (PM)-normalized incompatible trace elements patterns (fig. 6.2.1A). The samples show consistent LREE enrichment (with an average (La/Nd)_{PM} ratio of 1.38: fig. 6.2.2A), Nb-Ta depletion and generally flat HREE pattern with an average (Gd/Yb)_{PM} ratio of 0.98 (fig. 6.2.2B). Notice that the exhibited (La/Nd)_{PM} ratios are less confined (fig. 6.2.2A) than the (Gd/Yb)_{PM} ratios (fig. 6.2.2B). This is because Gd and Yb is generally less affected by alteration than La and Nd. The flat HREE pattern is consistent with the average Al₂O₃/TiO₂ ratio of 22 for the Stolzburg Complex, further indicating geochemical signatures of Al-undepleted mantle-derived rocks. The degree of incompatible element depletion relative to the primitive mantle ranges between 0.18 and 0.4 in the rocks of the Lower Division (both dunites and orthopyroxenites). Harzburgites also display trace element depletion with compositions that ranges between 0.9 and 0.7 of the PM values. Other ultramafic cumulates (e.g., lherzolites and olivine pyroxenites) display compositions that are in the range of the primitive mantle (i.e., lie about the line sample/PM = 1). Gabbroic rocks show incompatible element enrichment, with compositions that ranges between 2.5 and 3.3 of the PM values.

In addition, PM-normalized U is generally enriched relative to La and Th (see fig. 6.2.1A). There is a lack of Zr-Hf anomalies. Some samples, particularly the gabbronoritic rocks, display negative Ti and P anomalies, while others exhibit no or positive anomalies. This inconsistency suggest that

these anomalies are unlikely a signature of the primary melt(s). Instead, they could be a result of partial disturbance of Ti and P relative to the other incompatible elements or fractionation of Ti-oxides and apatite, respectively, during formation of some of the gabbronorites (see later).

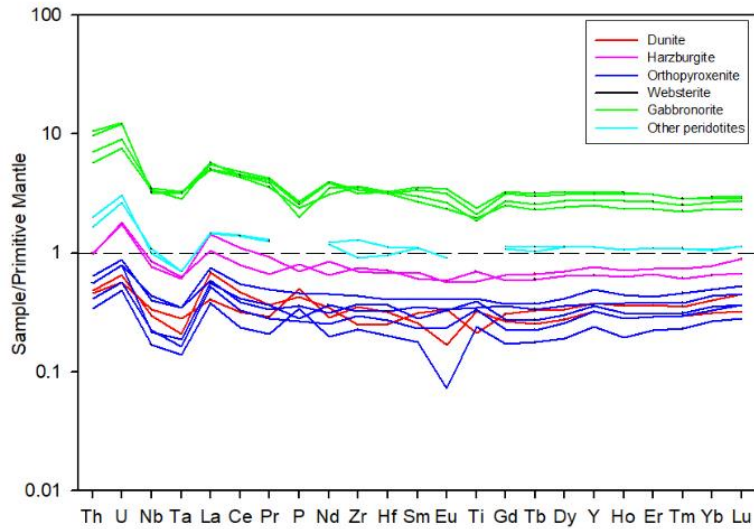


Figure 6.2.1A: *Primitive Mantle – normalized trace element patterns for the best preserved rocks of the Stolzburg Complex (group 1). Red = dunites; pink = harzburgites; cyan = other peridotites; blue = orthopyroxenites; black = websterites; lime green = gabbronorites. Primitive Mantle values are from Palme and O’Neill (2014).*

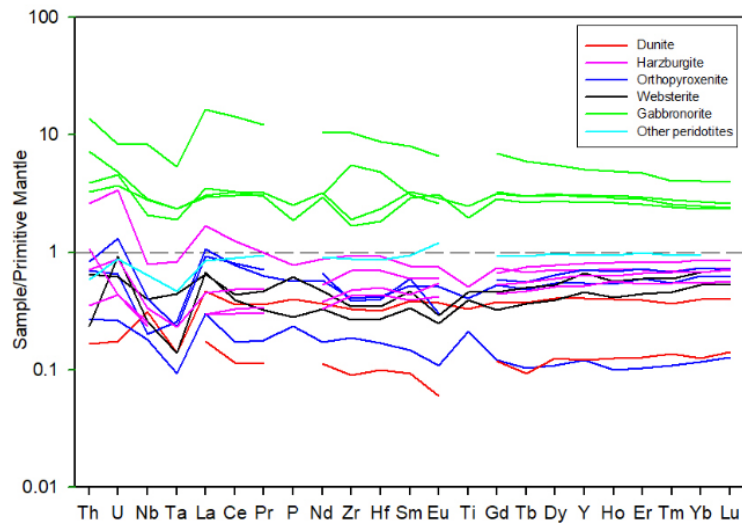


Figure 6.2.1B: *Primitive Mantle – normalized trace element patterns for group 2 rocks of Stolzburg Complex. Red = dunites; pink = harzburgites; cyan = other peridotites; blue = orthopyroxenites; black = websterites; lime green = gabbronorites. Primitive Mantle values are from Palme and O’Neill (2014).*

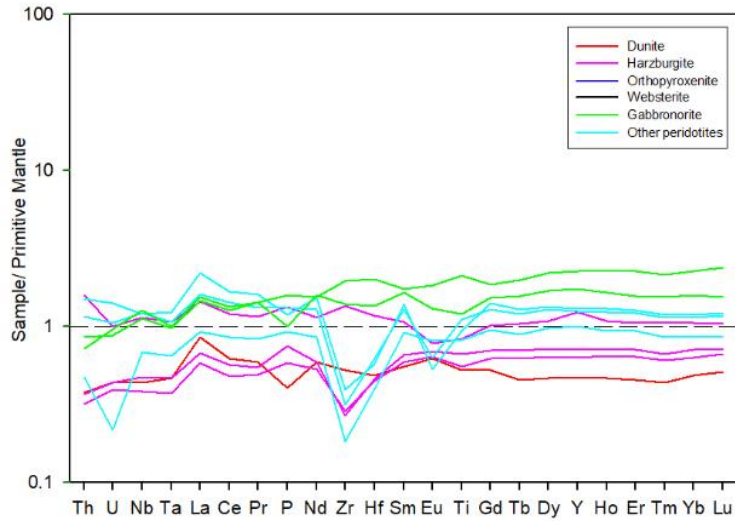


Figure 6.2.1C: *Primitive Mantle – normalized trace element patterns for group 3 rocks of Stolzberg Complex. Red = dunites; pink = harzburgites; cyan = other peridotites; blue = orthopyroxenites; black = websterites; lime green = gabbronorites. Primitive Mantle values are from Palme and O’Neill (2014).*

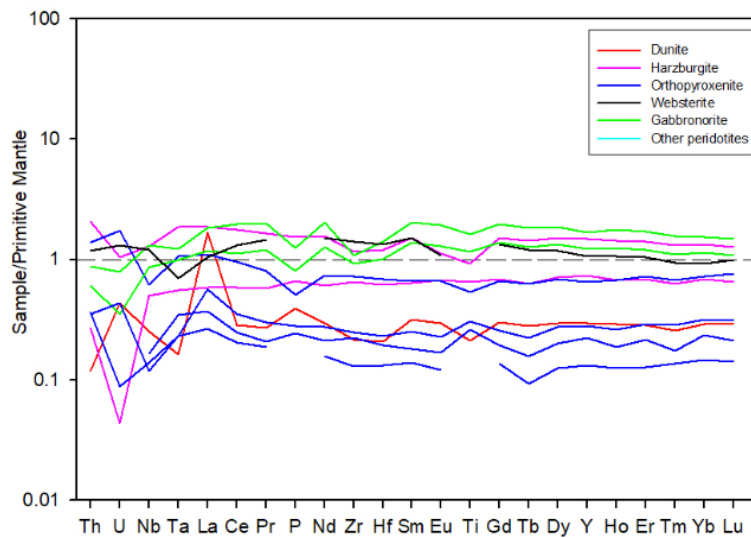


Figure 6.2.1D: *Primitive Mantle – normalized trace element patterns for group 4 rocks of Stolzberg Complex. Red = dunites; pink = harzburgites; cyan = other peridotites; blue = orthopyroxenites; black = websterites; lime green = gabbronorites. Primitive Mantle values are from Palme and O’Neill (2014).*

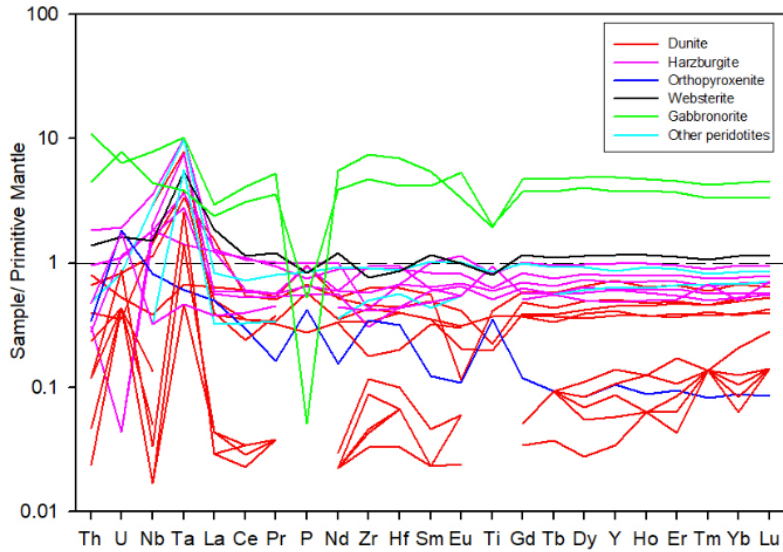


Figure 6.2.1E: *Primitive Mantle – normalized trace element patterns for group 5 rocks of Stolzburg Complex. Red = dunites; pink = harzburgites; cyan = other peridotites; blue = orthopyroxenites; black = websterites; lime green = gabbronorites. Primitive Mantle values are from Palme and O’Neill (2014).*

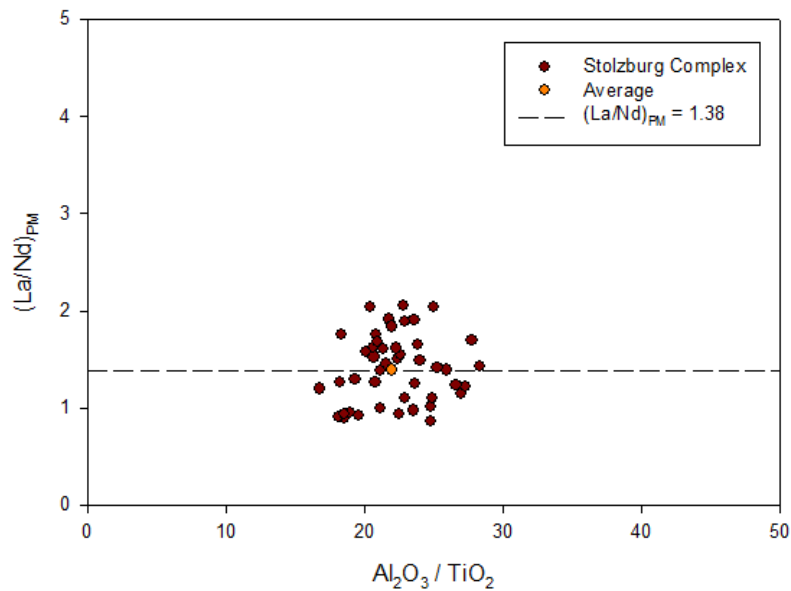


Figure 6.2.2A: *Plot of $(La/Nd)_{PM}$ against Al_2O_3/TiO_2 showing LREE enrichment in rocks of the Stolzburg Complex with an average $(La/Nd)_{PM}$ value of 1.38. Large spread in $(La/Nd)_{PM}$ correspond to partial mobilization of La and Nd. Primitive Mantle values are from Palme and O’Neill (2014).*

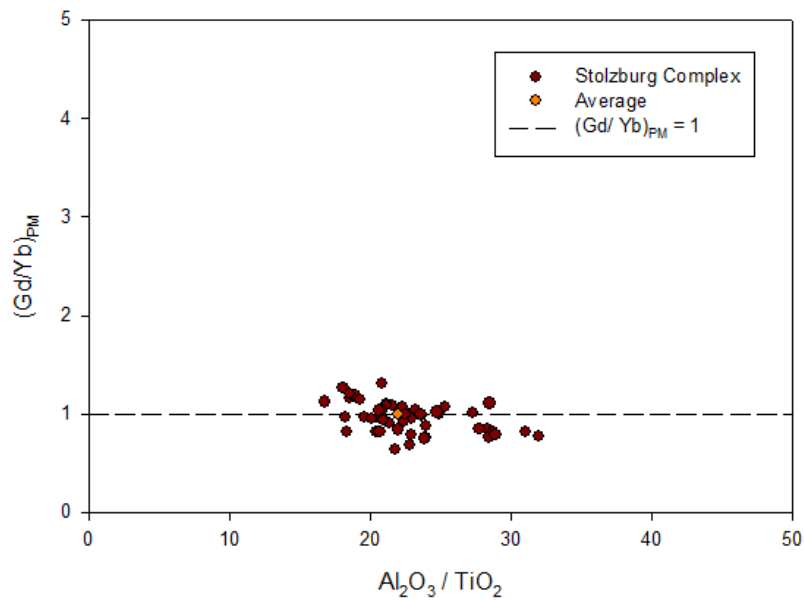


Figure 6.2.2B: Plot of $(Gd/Yb)_{PM}$ against Al_2O_3/TiO_2 showing the flat HREE pattern displayed by rocks of the Stolzberg Complex with an average $(Gd/Yb)_{PM}$ value of 0.98. Primitive mantle values are from Palme and O'Neill (2014).

10. Petrogenesis

10.1. Fractional crystallization

Rocks of the Stolzberg Complex define multiple mineral accumulation vectors resulting mainly from the accumulation of olivine, orthopyroxene, clinopyroxene and plagioclase; olivine and orthopyroxene accumulation trends are defined by dunitic and orthopyroxenitic samples, respectively. The distinct trends displayed by the gabbroic rocks are attributed to interplay between clinopyroxene, orthopyroxene, and plagioclase. In the MgO-Hf space (fig. 6.1.4A), peridotites and pyroxenites display steep, negative, and parallel trends which correspond to the accumulation of olivine and (ortho-)pyroxene, respectively. Clinopyroxene fractionation is suggested by the shallower negative trend followed by the gabbroic rocks. In the SiO_2 -Hf space (fig. 6.1.4B), olivine and orthopyroxene accumulation are, respectively, indicated by the steep positive correlation between SiO_2 and Hf exhibited by the peridotites and a steep negative correlation between SiO_2 and Hf followed by the orthopyroxenites. The gabbroic rocks follows a

shallower negative trend indicating clinopyroxene, orthopyroxene and/or plagioclase fractionation.

Since compatible trace elements have varying partition coefficients in olivine and pyroxene, it is expected that rocks dominated by olivine accumulation display different trends from those that are dominated by pyroxene accumulation. Olivine accumulation is indicated by the steep positive correlation of Ni and Co with MgO as well as the negative correlation of V, Sc, Al, Ti, and P with MgO (fig. 6.1.5) as defined by the peridotites. These trends result from the fact that Ni and Co are highly compatible in olivine, whereas V, Sc, Al, Ti, and P are incompatible in olivine. In contrast, orthopyroxenites and gabbroic rocks define shallower positive correlation trends of Ni and Co with MgO (fig. 6.1.5), respectively, corresponding to orthopyroxene accumulation and clinopyroxene fractionation. While olivine accumulation is not clearly depicted in the Cr₂O₃-MgO space (fig. 6.1.5A), orthopyroxene accumulation and clinopyroxene fractionation are indicated by the positive correlation between Cr₂O₃ and MgO as defined by the orthopyroxenites and gabbroic rocks, respectively. V, Sc, Al, Ti and P are also incompatible in orthopyroxene, hence, the negative correlation between these elements and MgO as defined by the orthopyroxenites. Notice that the trends displayed by peridotites and orthopyroxenes, respectively, corresponding to olivine and orthopyroxene accumulation, are parallel (fig. 6.1.5). This indicates that V, Sc, Al, Ti and P are similarly incompatible in olivine and orthopyroxene, therefore, do not get fractionated by the accumulation of these phases. For a given value of MgO, peridotites display higher concentration of these incompatible elements than the pyroxenites. Interestingly, the Komati Formation samples presented in Figure 2 of Schneider et al. (2019) also display (distinctly separable) parallel trends similar to the ones defined by peridotites and pyroxenites of the Stolzburg Complex. This means that the Komati Formation samples are not just peridotites, some of the samples are pyroxenites. In the Al₂O₃-TiO₂ space (fig. 6.1.6), olivine-pyroxene cumulates (i.e., peridotites and pyroxenites) define a single trend, which further affirms that olivine and orthopyroxene accumulation do not fractionate Al and Ti. It can, therefore, be concluded that olivine-pyroxene cumulates retain the Al₂O₃/TiO₂ ratio of the parental magma. In contrast, gabbroic rocks define a steeper positive trend, corresponding to plagioclase (and Fe-Ti oxides) fractionation. Al is a major component of plagioclase whereas Ti is incompatible in it, meaning plagioclase fractionates Al from Ti. The gabbroic rocks define steeper negative correlation trends of V, Ti, Al, and P with MgO and a positive correlation between Sc and MgO. These trends record the evolution of the residual melt

following the removal of clinopyroxene from the magma. Gabbroic samples that plot off the correlation lines defined by the majority of the gabbroic rocks in the Ti, P- MgO spaces (fig. 6.1.5H, I) may be attributed to Ti-oxide and apatite fractionation, respectively, or disturbance of these elements by secondary processes. In dunites, Ni, Cr, and Co show a large spread over a small range of MgO values (fig. 6.1.5A, B, C), which indicate control on these elements by chromite accumulation.

10.2. Mode of melting

A striking feature of the Barberton layered complexes is the predominance of ultramafic components (~ 80% by volume) over the mafic ones (Anhaeusser, 1985; Menell et al., 1981; Robb, 1977; Viljoen and Viljoen, 1970; Wuth, 1980). Provided that no significant residual magma escaped from the chambers (see Section 7.3 and 10.4), the predominance of ultramafic components suggest that these bodies were developed from an ultramafic parental magma. When rock units were weighted in terms of lithological proportions, the parental magmas for Barberton layered complexes were estimated to have consisted of > 28 wt.% MgO (Anhaeusser, 1985, 2001; Viljoen and Viljoen, 1970; Wuth, 1980) . Additionally, Rodel (1993) obtained a similar parental magma composition for the Stolzberg Complex using analysis of what was interpreted as a chill zone. Ultramafic parental magmas are supported by the high forsterite contents ($Fo > 90$) reported for preserved olivine grains in dunitic units of the Pioneer and Saw Mill complexes (Kareem, 2005; Putchel et al., 2013; Robin-Popieul et al., 2012).

Archaean ultramafic (>28 wt.% MgO) magmas are generally considered to have formed through high degree partial melting (> 30 %) of mantle sources (Herzberg, 1992; Furnes et al., 2012; Robin-Popieul et al., 2012; Wilson, 2003). Currently, the debate on the origin of ultramafic magmas is dominated by the plume model (Arndt et al., 1996, 2008; Blichert-Toft et al., 2015; Hoffmann and Wilson, 2017; Nisbet et al., 1993; Robin-Popieul et al., 2012; Sobolev et al., 2019) and the subduction zone-related hydrous melting model (Allegre, 1982; Furnes et al., 2012, 2013; Grove et al., 1996; Parman et al., 1997). The former model suggest that the magmas were derived from partial melting of “dry” mantle peridotites by an unusually hot mantle plume resulting in a submerged oceanic plateau (Arndt et al., 1996, 2008; Nisbet et al., 1993). The model proposes that

the mantle rock that had undergone partial melting contained insignificant amount of water, so fluids had no role in the melting process. Instead, melting was purely a result of abnormally high temperatures. Most advocates of this model envisage a non-uniformitarian earth in the early Archaean with no plate tectonics. In contrast, another view proposes that the ultramafic magmas were formed by hydrous partial melting in subduction zone settings, possibly under cooler conditions (Allegre, 1982; Grove et al., 1996; Parman et al., 1997). This model suggests fluid-assisted partial melting, where water lowers the solidus of the mantle peridotites, for the origin of the Archaean ultramafic melts. Proponents of this model proposes that plate tectonics was operational in the early Archaean. Puchtel et al. (2013) showed that the ultramafic rocks of the Komati and Weltevren formations contained < 0.75 wt.% water, reinforcing the idea of anhydrous conditions of formation. In contrast, it was suggested, on the basis of the geochemistry of fairly fresh pyroxenes from the Komati Formation, that the Barberton komatiitic magmas contained 3-6 wt.% dissolved water (Grove et al., 1996). More recently, Sobolev et al. (2019) showed that the parental magma to the Sawmill Complex, Weltevreden Formation, had excess water.

The biggest weakness of the hydrous melting model is its failure to explain the super- and sub-chondritic $\text{Al}_2\text{O}_3/\text{TiO}_2$ ratios observed in Al-depleted and Al-enriched komatiites. In the plume model, these geochemical signatures are attributed to the role of garnet during partial melting. Since Al is a major constituent of garnet while Ti is incompatible in it (Rollinson, 1993; White, 2013), during partial melting with garnet in the restite, Al is retained while Ti enters the melt phase (Robin-Popieul et al., 2012), thereby, fractionating Al and Ti. The generated melt will be Al-depleted while the source becomes Al-enriched. Because garnet is only stable under high pressure conditions (depth > 400 km and pressure \sim 13 GPa) (Gruau et al., 1990; Jochum et al., 1991) which are unattainable in the mantle wedge, Al-depleted magmas are generally considered to have formed through high degree partial melting in a deeply-originated mantle plume which eventually reaches the shallow levels of the mantle (Robin-Popieul et al., 2012; Sobolev et al., 2019). Since HREE, Y and Sc are also highly compatible in garnet (Rollinson, 1993; White, 2013), these elements are also comparatively depleted in the Al-depleted magmas. Enroute to the shallow levels of the mantle, the plume crosses the garnet stability field and enters a region where garnet is no longer stable. When this happens, the Al- and HREE-enriched garnet in the restite from the previous melting event, starts undergoing melting, generating an Al-enriched magma with HREE-enriched patterns (Robin-Popieul et al., 2012).

In the absence of garnet in the mantle source, Al and Ti behaves in a similar way and therefore these elements are not fractionated. Partial melting under circumstances where garnet is absent in the residual solid result in a melt with a chondritic $\text{Al}_2\text{O}_3/\text{TiO}_2$ ratio of ~ 22 . In addition, the HREE are not fractionated, thus the generated melts display flat HREE patterns. Since the Stolzburg Complex displays these features, it is therefore concluded that the Stolzburg ultramafic parental magma was generated through high degree partial melting with no garnet in the restite. This suggestion is further supported by the chondritic Zr/Y ratio of the Stolzburg Complex rocks with an average of 2.49 ± 0.42 . Because Y is compatible in garnet and Zr is not, the presence of garnet in the restite results in superchondritic Zr/Y ratios in the generated melt.

The absence of garnet in the restite is generally accepted as an indication of partial melting at shallow levels, particularly in the spinel stability field. However, alternative explanation have been proposed (see later).

10.3. Mantle source characterization

Ratios of elements, particularly those that are highly incompatible, with similar partition coefficients in mantle mineralogy are not expected to be modified by moderate to high degree partial melting nor fractional crystallization under low to moderate pressure conditions (Rollinson, 1993; White, 2013). This is simply because these trace elements enters the melt phase in accordance to their proportions in the source rock, thereby, preserving the inter-element ratios in the source. Similarly, these elements are incorporated in the crystallizing solid phase in accordance to their proportion in the melt during fractional crystallization, again preserving the inter-element ratios in the parental magma. Indeed, ratios between elements with very similar bulk partition coefficients are, with a few exceptions, found to be nearly constant in terrestrial rocks (e.g., Arndt et al., 1977; Bougault et al., 1979, 1988; Saunders et al., 1988; Szilas et al., 2014). Some of these ratios include, but not limited to, Zr/Hf, Nb/Ta, Th/U, $\text{Al}_2\text{O}_3/\text{TiO}_2$, Pr/Nd, and Zr/Nd.

In the presence of exotic solid phases, these inter-element ratios may be modified (e.g., majorite fractionates Al and Ti and perovskite fractionate Zr, Hf, Nb, Ta from REEs). Furthermore, the action of fluids can also fractionate trace elements (such as Ta and La) that behave very similarly in low to moderate pressure magmatic processes. While these elements have very similar bulk

partition coefficients in magmatic systems, their degrees of immobility during secondary processes are significantly different, with Ta being more immobile than La. During dehydration of the subducting slab in convergent margins, it is generally accepted that the less immobile elements such as Th, U, and LREE enter the fluid phase while the highly immobile elements such as Nb, Ta, and Ti are retained in the slab (Furnes et al., 2012; Parman et al., 1997). These fluids rise up and metasomatize the mantle wedge above the slab, leading to a mantle source which is comparatively depleted in highly immobile elements and enriched in less immobile elements. Low degree partial melting of the slab is also believed to have the same effect. When the metasomatized mantle wedge undergoes partial melting, it produces melts which are relatively depleted in highly immobile elements and enriched in the less immobile elements, explaining the LREE, Th and U enrichment and negative Nb-Ta anomalies observed in modern volcanic arc rocks (Elliott et al., 1997).

Assuming high degree partial melting for the generation of the Stolzburg Complex parental magma, provided the magma was ultramafic in composition (see above), it can be concluded that the ratios between trace elements with similar bulk partition coefficients were not modified during melting. Furthermore, since fractional crystallization of olivine, pyroxene and plagioclase does not affect these ratios (except for the Al/Ti ratio, which is affected by fractionation of plagioclase) (see above), the inter-element ratios in the Stolzburg Complex rocks are thus regarded as a representation of ratios in the mantle source. Table 2 presents average inter-element ratios in the Stolzburg Complex. Only samples that plotted tightly along the correlation lines in co-variations diagrams were deemed reasonably preserved and were used to calculate the averages of the inter-element ratios. In order to avoid the effect of apatite, Ti-oxide, and zircon fractionation on P, Ti and Zr-Hf contents, respectively, gabbroic rocks were not included in the calculations of the inter-element ratios as these rocks may contain the mentioned phases. Moreover, gabbroic rocks were excluded in the calculation of the Al_2O_3/TiO_2 ratio because plagioclase and Fe-Ti-oxides fractionation affects this ratio. For comparison, Primitive Mantle and chondritic ratios are included. Primitive mantle and chondritic values are from Palme and O'Neill (2014).

Table 2 shows that the ratios Zr/Hf, Nb/Ta, Pr/Nd, P/Nd, P/Ce, Hf/Sm, Zr/Nd, Ti/Gd, Ti/Zr, Dy/Y, Ho/Y, Yb/Y and Al_2O_3/TiO_2 are in excellent agreement with the Primitive Mantle values and in most cases with chondritic ratios as well. Other inter-element ratios (Th/U, Ti/Eu, Ti/Y, La/Ce) in

the Stolzburg Complex rocks are also comparable with those of the primitive mantle but with slightly higher or lower values. The slightly lower Th/U ratio in the Stolzburg Complex rocks is consistent with the enrichment of U relative to Th observed in the PM-normalized multi-element diagrams (fig. 6.2.1A). This feature is at odds with the Th-U relationship observed in arc rocks or contaminated mantle-derived rocks where Th is commonly enriched than U (Elliott et al., 1997). Similarly, contrast to what is observed in arc and contaminated rocks where Nb is normally more depleted than Ta, in the Stolzburg Complex, Ta is more depleted than Nb. The slightly higher La/Ce ratios also agree with the LREE enrichment observed in the primitive mantle-normalized multi-elements diagrams. The significantly higher (than PM) La/Ta and La/Nb ratios in the Stolzburg Complex rocks are consistent with the LREE-enrichment and Nb-Ta depletion patterns displayed by these rocks.

The lower Ti/Y ratio is probably influenced by the slightly positive Y anomaly observed in some of the Stolzburg Complex rocks. This small positive Y anomaly is unlikely a result of secondary processes as Y is shown not to have been mobilized relative to the HREE by the excellent agreement amongst the samples (i.e., very small standard deviation) in the Dy/Y, Ho/Y, and Yb/Y ratios (fig. 6.1.1D & E). Small positive Y anomalies are not uncommon in mantle-derived rocks of oceanic plateau (e.g., Ontong Java oceanic plateau: Fitton and Godard, (2004)). The obtained Ti/Eu ratio is higher than that of the primitive mantle. The lack of consistent Eu and Ti anomalies in the primitive mantle-normalized spider diagrams argues against Ti enrichment or Eu depletion that could have resulted in this higher ratio. Since data points in a Ti vs Eu variation diagram (not shown) display less coherence than expected, the higher Ti/Eu ratio is likely a result of element mobility and not a primary signature. The effect of alteration processes on the Ti/Eu ratio is also indicated by the very large standard deviation displayed by the samples. Since gabbroic rocks were excluded when calculating this ratio, the large standard deviation is unlikely due to the effects of plagioclase and Ti-oxides fractionations as these phase, respectively, fractionate Eu and Ti.

Table 2: *Inter-element ratios in the Stolzburg Complex rocks. Primitive mantle and chondritic values are from Palme and O'Neill (2014).*

	Stolzburg Complex	PM	Chondrite		Stolzburg Complex	PM	Chondrite
Th/U	3.32 ± 0.44	3.707	3.704	Hf/Sm	0.68 ± 0.11	0.69	0.69
Nb/Ta	15.54 ± 2.17	13.84	18.87	Ti/Eu	8562.61 ± 1881.94	7597.6	7598.16
La/Ta	28.49 ± 12.54	15.89	16.09	Ti/Gd	2228.97 ± 568.48	2160.55	2160.46
La/Nb	1.87 ± 0.53	1.15	0.85	Ti/Zr	125.47 ± 14.70	122.82	123.14
La/Ce	0.50 ± 0.09	0.39	0.39	Ti/Y	283.56 ± 42.78	306.3	306.16
Pr/Nd	0.20 ± 0.01	0.2	0.2	Dy/Y	0.172 ± 0.01	0.175	0.175
P/Nd	65.77 ± 14.12	64.88	2079.38	Ho/Y	0.0375 ± 0.0027	0.0387	0.0387
P/Ce	48.06 ± 13.33	49.63	1590.25	Yb/Y	0.115 ± 0.0088	0.116	0.116
Zr/Nd	7.52 ± 1.30	7.68	7.66	Al ₂ O ₃ /TiO ₂	22.41 ± 2.66	22	22
Zr/Hf	35.56 ± 2.02	34.17	34.08				

Of particular interest in the Stolzburg Complex trace elements patterns are the LREE enrichment and Nb-Ta depletion characters as these features are widely regarded as volcanic arc signatures. The Nb-Ta depletion signatures are common in Archaean greenstone belt mantle-derived rocks (e.g., Guice et al., 2019; Polat et al., 2011) and they are regarded by proponents of the subduction zone model as evidence that the ultramafic magmas were generated through hydrous melting in subduction zone settings (e.g., Furnes et al., 2012; de Wit et al., 2018). However, workers who advance the plume model have presented an alternative explanation for the origin of the high field strength elements (HFSE) anomalies in the Archaean greenstone belts. In the plume model, these anomalies are typically attributed to actions of exotic high pressure phases such as perovskite which are capable of significantly fractionating HFSE from REEs (Blichert-Toft et al., 2015; Gruau et al., 1990; Jochum et al., 1991). The presence of a Nb-Ta depletion signature in the rocks of Archaean greenstone belts such as komatiites of the Komati Formation, which also display Al- and HREE-depletion features (ascribed to partial melting under high pressure conditions), is inconsistent with the origin of these so-called “arc signatures” in subduction zone settings because the envisaged high pressure conditions are not attainable in the mantle wedge. Moreover, the Nb-Ta depletion signature also characterizes the LREE-depleted rocks of the Pioneer and Saw Mill complexes. This is again inconsistent with the origin of these rocks in subduction zone settings because Nb-Ta depletion accompanies LREE enrichment during metasomatism of the mantle wedge, so rocks that display LREE-depletion could not have resulted from such an environment. It is highly unlikely that the Nb-Ta depletion character of the rocks of the Komati Formation and

Pioneer and Saw Mill complexes resulted from crustal contamination as these rocks have been shown not to have endured this process (Chavagnac, 2004; Putchel et al., 2013; Robin-Popieul et al., 2012; Schneider et al., 2019). The Nb-Ta depletion character of the Barberton greenstone belt rocks, including the Stolzberg Complex, likely resulted from geochemical processes which are unfamiliar in present-day geological environments (see later).

10.4. Comparison between the geochemistry of the Stolzberg Complex, the surrounding rocks, and other Barberton layered complexes.

If indeed the layered complexes and the intimately associated lavas are comagmatic, as suggested in the sub-volcanic sill model (see section 3.4.1), they are expected to show similar chemical compositions. Surprisingly, that is not the case at least for the Stolzberg Complex and the Nelshoogte Schist Belt lavas. The Stolzberg Complex parental magma is found to be of the Al-undepleted class whereas the data from Anhaeusser (2001), Rodel (1993) and Conway (1997) shows that the komatiites, komatiitic basalts and tholeiites of the Nelshoogte Schist Belt are of the Al-depleted class (fig. 6.3.1). Because the $\text{Al}_2\text{O}_3/\text{TiO}_2$ ratio cannot be modified by fractional crystallization under low pressure conditions (in shallow level chambers), the difference in this ratio between the Stolzberg Complex rocks and the Nelshoogte Schist Belt lavas provides first order evidence that these two entities are unrelated and were formed by from different magmas. This is consistent with the model proposed in this study (section 7.3) for the development of the Stolzberg Complex where the body is regarded as sheeted sills as opposed to a single large magma chamber which grew through multiple magma injections.

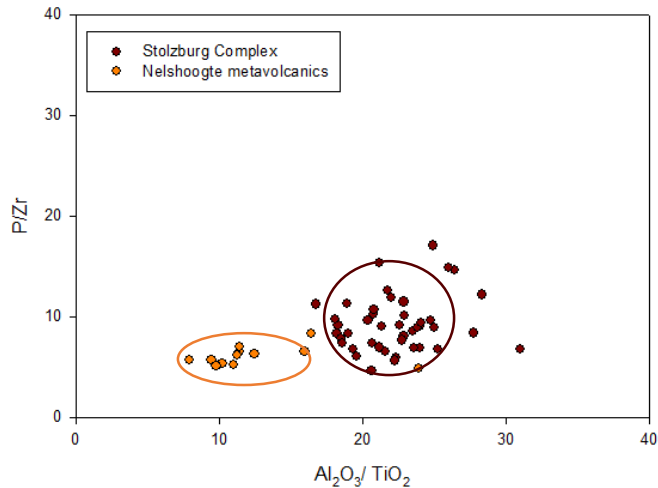


Figure 6.3.1: *Distinction in the Al_2O_3/TiO_2 ratio between the Stolzberg Complex and Nelshoogte greenstones. Stolzberg Complex data from this study and Nelshoogte samples data from Anhaeusser (2001), Conway (1997), and Rodel (1993).*

In contrast to the claim by MacLennan (2012) and de Wit et al. (1987; 2018) that the Lower and Upper Divisions of the Stolzberg Complex are geochemically distinct and therefore unrelated, findings in this study show that these two sections of the complex actually display identical trace element patterns in all aspects (fig. 6.2.1A showing similar PM-normalized multi-element diagrams between the dunites and orthopyroxenites of the Lower division and the harzburgites and gabbro-norites of the Upper division; fig. 6.5.1-6.5.5 illustrating that all rock of the Stolzberg Complex display very similar inter-element ratios). It is therefore concluded that the entire Stolzberg Complex was formed from the same magmatic event as per the sheeted sills model proposed in this study.

The Rosentuin Complex, which is hosted by the tholeiites of the Hooggenoeg Formation in the southern domain of the Barberton greenstone belt, is found to be predominantly of the Al-depleted class (MacLennan, 2012; Rodel, 1993). However, some samples display Al_2O_3/TiO_2 ratios that range between 20 and 22, therefore, belonging to the Al-undepleted class of terrestrial rocks. Again, this clearly indicates that the units that display Al-depletion are not comagmatic with the unit(s) that show no Al-depletion. Using sample descriptions (including stratigraphic column, sample names, and geochemistry) in Rodel (1993), it was possible to decipher that the samples that show no Al-depletion actually belong to an uppermost, 30 m thick, fine-grained peridotite unit

of the Rosentuin Complex. Interestingly, the enclosing tholeiites also belong to the Al-depleted class of rocks. This arrangement could mean that this uppermost peridotite unit is not part of the Rosentuin Complex (i.e., it was formed earlier or later) or it represents a late sill which was emplaced penecontemporaneously with the Rosentuin Complex. The Al-depleted signature of the Rosentuin Complex, in contrast to the Al-undepleted character of the Stolzburg Complex, indicates that these two bodies are not comagmatic. In addition, the Pioneer and Saw Mill complexes hosted by the Oorschot-Weltevreden Schist Belt in the northern domain of the Barberton greenstone belt have been reported to display LREE-depletion, slight HREE-enrichment and slight Al-enrichment (Puchel et al., 2012; Robin-Popieul et al., 2012) in contrast to the Stolzburg Complex which shows chondritic $\text{Al}_2\text{O}_3/\text{TiO}_2$ ratios, LREE-enrichment and flat HREE pattern (see fig. 6.4).

10.5. Evaluation of crustal contamination

Some workers believe that the mantle-derived successions of Archaean greenstone belts were deposited on older felsic basement (Bolhar et al., 2003; Lowe and Byerly, 2007; Schneider et al., 2019). Given the envisaged high emplacement temperatures ($> 1500\text{ }^\circ\text{C}$) of the Archaean ultramafic magmas (Cooper, 2008; Kareem, 2005; Puchtel et al., 2013; Robin-Popieul et al., 2012; Wilson, 2019), it is hard to conceive a scenario where the magmas traversed across the basement without assimilating a significant portion of the felsic crustal material. In fact, modern continental flood basalts which were emplaced at lower temperatures ($1000 - 1200\text{ }^\circ\text{C}$) all show clear features of crustal contamination (Devey and Cox, 1987). The incorporation of continental components in the ultramafic-mafic magmas is accompanied by a drastic increase in abundances of incompatible trace elements (which are enriched in felsic material) in the resultant contaminated magma. Since the abundances of incompatible trace elements are low in ultramafic-mafic magmas, their concentrations and patterns in the resultant magma are controlled by the incorporated felsic components. Continental material, without exception, displays LREE- and Th-U-enrichment, HREE-depletion patterns (thus large $(\text{La}/\text{Yb})_{\text{PM}}$ and $(\text{Gd}/\text{Yb})_{\text{PM}}$ ratios of ~ 7 and $\sim 1.5-2$ respectively; bulk continental crust values from Rudnick and Gao (2014)) and negative Nb-Ta anomalies. In addition, positive Zr-Hf anomalies, negative Ti, P, and Eu anomalies are not uncommon.

Here, the Stolzberg Complex is evaluated for crustal contamination. Although the rocks of this layered body display a LREE-enrichment pattern - characteristic of crustal material, they also show a flat HREE pattern with an average $(\text{Gd}/\text{Yb})_{\text{PM}}$ value of 0.98 ± 0.16 (also see fig. 6.2.2B). Furthermore, the average $(\text{La}/\text{Yb})_{\text{PM}}$ ratio is 2.04 ± 0.61 , which is much lower than the value in continental crust material. These features are preliminary indications that argue against crustal contamination. If the prominent Nb-Ta depletion character displayed by these rocks was transferred from an assimilated crustal material, the $(\text{La}/\text{Yb})_{\text{PM}}$ and $(\text{Gd}/\text{Yb})_{\text{PM}}$ ratios should have been affected as well but there is no indication of that. In fact, the markedly flat HREE pattern exhibited by these rocks strongly argues against any considerable assimilation of crustal material. In the Nb vs La/Yb space (fig. 6.3.2; after Schneider et al., 2019), contaminated mantle-derived rocks are expected to plot at higher Nb and La/Yb values, towards the region of felsic rocks. However, figure 6.3.2 shows that the Stolzberg Complex rocks plot in the same range of values as the Komati Formation, which has been shown to be free of crustal contamination (Chavagnac, 2004; Robin-Popieul et al., 2012; Schneider et al., 2019). Additionally, the Stolzberg Complex extends to lower Nb abundances than the Komati Formation, in contrast to the expected effects of crustal contamination, which would lead to increased incompatible elements concentrations. Moreover, crustal contamination is expected to modify the Nb/Yb and Zr/Nb ratios to higher values but such an effect is not observed in the Stolzberg Complex as these rocks display same range of values as rocks of the Komati and Pioneer complexes (see fig. 6.5.1 & 6.5.4), which have been shown to be free of contamination. The slightly higher Th/Yb ratios correspond to Th enrichment relative to moderately incompatible elements in the Stolzberg Complex. Despite the Th enrichment, the Zr/Th ratio (averaging at 133.86 ± 32.30) is much greater than that of crustal material (~ 20) and it is comparable to the primitive mantle value of ~ 120 . In the Stolzberg Complex, this ratio was likely affected by partial mobilization of Th as indicated earlier. The features discussed above show that the Stolzberg Complex magma was free of crustal contamination. Additional evidence is provided by the lack of consistent and prominent negative Ti, P, and Eu anomalies (which are common signatures of crustal material) in the olivine-pyroxenite cumulates. An alternative explanation for the origin of the negative anomalies in the gabbro-norites was provided earlier, where fractionation of Ti-oxides and apatite is envisaged. Furthermore, there are no prominent and consistent positive Zr-Hf anomalies (not uncommon in continental material) and the rocks are generally depleted in incompatible trace elements.

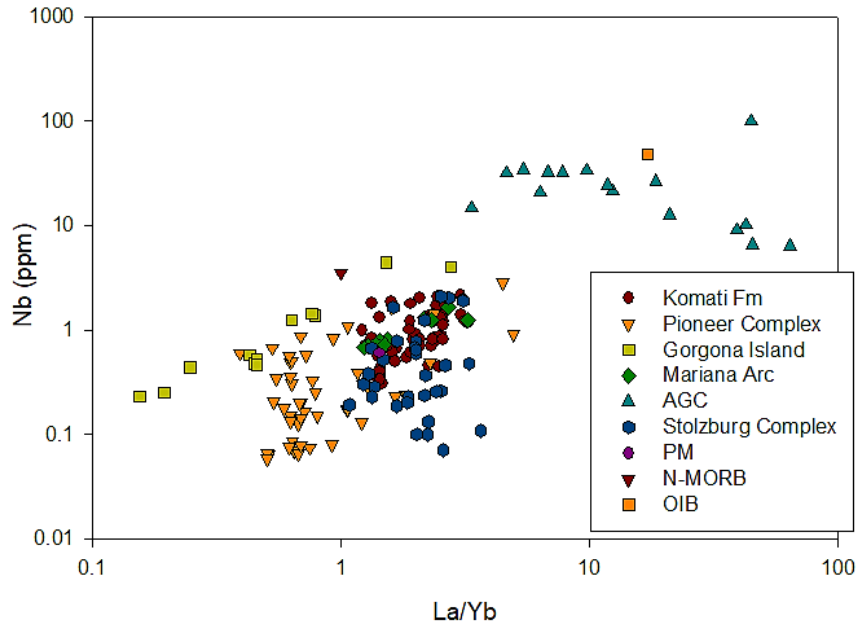


Figure 6.3.2: Plot of Nb against La/Yb demonstrating the lack of crustal contamination signatures in the Stolzberg Complex. *Stolzberg Complex data from this study and MacLennan (2012). Komati Formation data from Chavagnac (2004); Robin-Popieul. (2012) Schneider et al. (2019). Pioneer Complex data from Cooper (2008) and Thompson-Stiegler et al. (2012). Gorgona Island data from Arndt et al. (1997). Mariana Arc data from Elliott et al. (1997). Ancient Gneiss Complex data from Kröner et al. (2013, 2014). Primitive mantle data from Palme and O'Neill (2014). N-MORB data from Hofmann (1988). OIB data from Sun and McDonough (1989).*

The Pioneer Complex could not have experienced crustal contamination as it exhibits LREE depletion and positive ε_{Nd} values (Chavagnac, 2004; Putchel et al., 2013; Robin-Popieul et al., 2012) as opposed to LREE enrichment and negative ε_{Nd} values typical of felsic material. If the crustal contamination-free Pioneer Complex was emplaced in an oceanic setting, the same is expected to have been the case for the (apparently) age-equivalent Stolzberg Complex (Bolhar et al., 2021; Hofmann et al., 2021). Bolhar et al. (2021) reported that over 85% (18 out of 21) of zircon grains extracted from gabbroic rocks of the Stolzberg Complex exhibit mantle-like (i.e., positive) ε_{Hf} values. This serves as additional reaffirmation against crustal contamination.

Schneider et al. (2019) supports the existence of felsic basement over which the oldest ultramafic succession of the Barberton greenstone belt was emplaced. However, these workers suggest that this continental crust was later rifted and led to development of oceanic crust. This suggestion

was influenced by the fact that some Theespruit and Sandspruit formation samples seem to have been contaminated whereas the Komati Formation shows no evidence of crustal contamination. A mantle plume-fed oceanic plateau setting was therefore envisaged by these workers for the origin of the Komati Formation. Since the Stolzberg Complex, together with the Pioneer and Saw Mill complexes, have been shown to be much younger than the Komati Formation (Conolly et al., 2011; Ficq et al., 2018; Puchtel et al., 2013), the lack of crustal contamination features in these layered bodies is consistent with development in oceanic settings in alignment with the model of Schneider et al. (2019). However, in section 5.1, it was reasonably argued, based on geological considerations, that plate tectonics was unlikely operational during the envisaged period. Therefore it is concluded that the Barberton greenstone belt, including the Stolzberg Complex, developed in an oceanic setting without any influence of plate tectonics (i.e., tectonic rifting). This aspect is explored further in the following section. The reported contamination signatures in a few of the samples of the Sandspruit and Theespruit formations (Schneider et al., 2019) were probably influenced by an older and isolated felsic pluton as opposed to a continuous felsic basement.

10.6. Geodynamic setting of the Stolzberg Complex

Many geodynamic environments have been put forth as possible settings for the development of Archaean greenstone belts. Currently, there are two main geodynamic settings being considered: (1) a back-arc spreading centre associated with a subduction zone (Furnes et al., 2012; de Wit et al., 2018) and (2) intraplate oceanic plateau setting connected to a mantle plume (Blichert-Toft et al., 2015; Chavagnac, 2004; Robin-Popieul et al., 2012; Sobolev et al., 2019). However, models that envisage a spreading centre driven by a plume have also gained recognition (Lowe and Byerly, 2007; Schneider et al., 2019).

In section 5.1, aspects of the geodynamic history of the Barberton greenstone belt were discussed based only on physical geology. The notable lack of features that can be regarded as unquestionable vestiges of plate tectonics was highlighted. In this section, the geodynamic setting for the Stolzberg Complex is examined using trace elements geochemistry.

Geochemical tools used to constrain geodynamic settings from which basic magmas were formed include normalized multi-element diagrams as well as tectonic discrimination diagrams. The pros

and cons of each tool are briefly discussed below. Ideally, the two tools should complement each other. Here, it is investigated whether or not the geochemistry of the Stolzberg Complex is consistent with that of at least one of the known modern geodynamic settings. Additionally, it will be examined whether or not the tectonic settings suggested for the Stolzberg Complex by each of the geochemical tools are in agreement.

10.6.1. Normalized multi-element diagrams

Basic magmas generated in different tectonic settings may be distinguished based on patterns of their normalized multi-element diagrams. While the PM-normalized spider diagrams of island arc basaltic rocks characteristically display negative Nb-Ta anomalies, LREE enrichment and flat HREE patterns (Elliott et al., 1997), those of the so-called Normal-MORB are also characterized by a flat HREE pattern but depletion in highly incompatible elements (e.g., Rb, Ba, LREE, Nb, Ta) without Nb-Ta anomalies (Hart, 1971; Kay et al., 1970; Sun et al., 1979; Tarney et al., 1980). Another existing variant of the mid-oceanic ridge basalts, referred to as the Enriched-MORB, displays comparative enrichment in highly incompatible elements but still no Nb-Ta anomalies (Sun et al., 1979; Tarney et al., 1980). While basic magmas contaminated by felsic components typically display negative Nb-Ta anomalies and LREE enrichment patterns, in contrast to island arc basaltic magmas with flat HREE patterns, they display HREE depletion patterns (Devey and Cox, 1987). Back-arc basin basalts (BABBs) are known to exhibit geochemical signatures that range between those of N-MORB and those of island arc basalts (Gill, 1976; Saunders and Tarney, 1979; Saunders and Tarney, 1984). When the mantle source of the BABBs is not influenced by subduction zone-related metasomatism, the generated magmas tend to show geochemical signatures that are more similar to N-MORB. Conversely, the BABBs show affinity to island arcs when metasomatism affected the mantle source. Oceanic plateau basalts (OPBs) predominantly exhibit flat PM-normalized spider diagrams (Kerr et al., 2000). However, variants with LREE depletion or enrichment and/or HREE depletion have been encountered (Kerr et al., 2003). Oceanic island basalts (OIBs) are easily distinguishable from basalts from other tectonic settings by their characteristic positive Nb-Ta and Zr-Hf anomalies and HREE depletion patterns (Weaver, 1991). Moreover, OIBs generally have high concentration of the highly incompatible elements.

The geochemical signatures displayed by the Stolzburg Complex are easily distinguishable from the ones typically exhibited by OIBs as the former show negative Nb-Ta anomalies, no Zr-Hf anomalies and flat HREE patterns, whereas the latter show positive Nb-Ta and Zr-Hf anomalies as well as HREE depletion patterns (fig. 6.4). N-MORB can also be distinguished from Stolzburg Complex rocks as the former display LREE depletion and no Nb-Ta anomalies, while the latter exhibit LREE enrichment and prominent negative Nb-Ta anomalies. Oceanic plateau basaltic rocks notably lack the negative Nb-Ta anomalies displayed by the Stolzburg Complex rocks. The geochemical signatures displayed by the Stolzburg Complex unlikely reflect effects of crustal contamination as it has been demonstrated above (section 10.5) that it is improbable that the parental magma to this body interacted with felsic continental material at least to any significant extent. This leaves island arc and subduction zone metasomatism-influenced back-arc basin settings as the only two potential plate tectonic-based settings for the origin of the Stolzburg Complex. Both these settings exhibit negative Nb-Ta anomalies, LREE enrichment and flat HREE patterns as do rocks of the Stolzburg Complex.

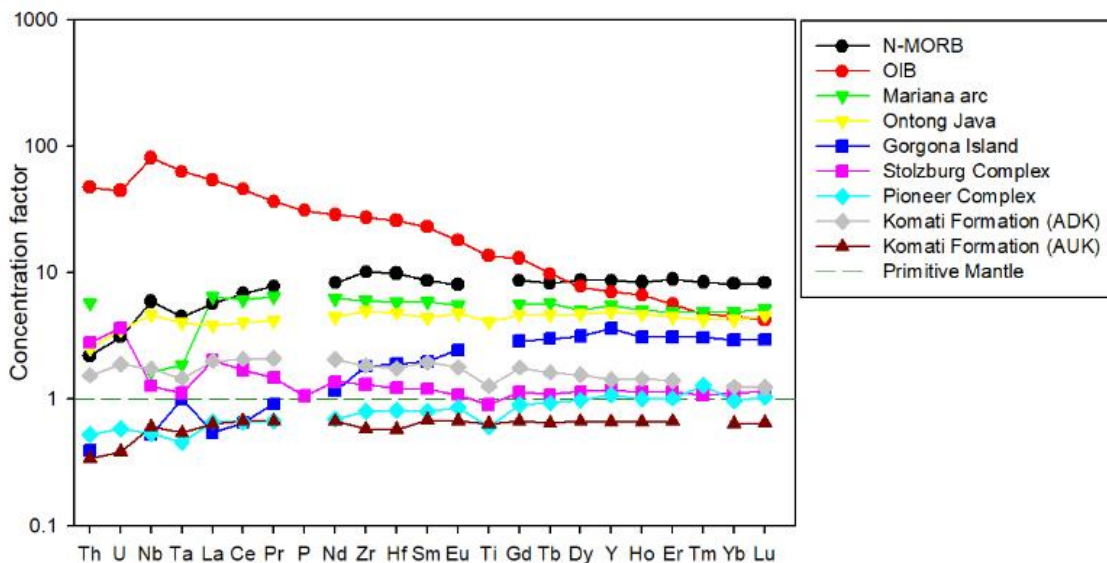


Figure 6.4: PM-normalized diagram comparing incompatible elements patterns of the Stolzburg Complex, Pioneer Complex, Komati Formation, Gorgona Island komatiites; Mariana arc, Ontong Java oceanic plateau, N-MORB, and OIB. Patterns represent calculated averages. Notice the remarkable similarity between the patterns of the Ontong-Java Plateau and Komati Fm (AUK). Stolzburg Complex data from this study and MacLennan (2012). Komati Formation data from

Chavagnac (2004); Robin-Popieul. (2012) Schneider et al. (2019). Pioneer Complex data from Cooper (2008) and Thompson-Stiegler et al. (2012). Gorgona Island data from Arndt et al. (1997) and Révillon et al. (2000). Mariana Arc data from Elliott et al. (1997). Ontong-Java oceanic plateau data from Fitton and Godard, (2004). Primitive mantle data from Palme and O'Neill (2014). N-MORB data from Hoffmann (1988). OIB data from Sun and McDonough, (1989).

10.6.2. Tectonic discrimination diagrams

Following the realization that inter-element ratio in basic rocks from each known modern geodynamic environment are, with some overlaps, generally distinct, diagrams that discriminate rocks based on their trace element geochemistry were constructed (Pearce and Cann, 1971, 1973). This does not come as a surprise as the distinction between incompatible elements ratios in basic rocks from different settings correspond to the contrasting relative abundances of trace elements as observed in normalized multi-element diagrams. The discrimination diagrams are meant to assign basic rocks to specific tectonic environments. Ever since the pioneering diagrams of Pearce and Cann (1971, 1973) were presented, many other discrimination diagrams have been proposed (e.g., Condie, 2005; Fitton et al., 2003). The capabilities and reliabilities of the diagrams differ, with each diagram dedicated to distinguishing suites from selected geodynamic settings.

The reliability of discrimination diagram to correctly fingerprint modern and ancient rocks is a hotly debated topic today. Many researchers have warned against the use of the diagrams as simple tectonic discrimination tools (Condie, 2015; Li et al., 2015; Saccani, 2015). Arguments presented by these workers who question the reliability of these diagrams includes:

- the fact that the diagrams were constructed based on limited and unrepresentative data sets;
- the possibility that distinct mantle domains can be sampled in more than one tectonic setting;
- the fact that varying degrees of partial melting, mixing and contamination can affect incompatible element abundances (and therefore ratios) in the resultant magmas;
- the likelihood that some tectonic settings are not accounted for (e.g., plume-influenced MORB);
- the fact that alteration and metamorphism can affect the trace element concentrations.

Li et al (2015) showed that new global data define new fields that are bigger in size and different in shape from the originally defined fields in various existing discrimination diagrams. Furthermore, these fields overlap heavily. These findings suggest that, unlike the initial belief that compositions of basalts from each tectonic setting display narrowly defined and distinct compositions, basalts from different settings actually cluster together making it impossible to discriminate them. This would mean that incompatible element ratios in basalts from different tectonic settings are not distinguishable, therefore, suggesting that magma sources are not distinctive. If that was the case, the normalized multi-element diagrams of basic rocks from different tectonic settings would not be distinguishable. This is, however, not the case as basalts from different tectonic settings exhibit easily distinguishable normalized multi-element patterns (fig. 6.4).

If distinct mantle domains in the modern Earth are distinguishable on the basis of incompatible elements geochemistry (Pearce, 1983; Pearce and Peate, 1995; Pearce, 2008), the type of mantle source from which a particular suite of basic rocks was derived may be constrained. This is permitted by the fact that incompatible elements geochemistry of mantle sources can be determined from the compositions of their derivative basic rocks (see above). With a significant correlation between mantle sources and tectonic settings, comments can be made on the possible tectonic setting of formation for that particular suite of modern basic rocks. Therefore, incompatible element geochemistry can be useful in constraining, but not ambiguously fingerprinting, tectonic settings (Condie, 2005).

Discrimination diagrams, particularly those that utilize high-field strength elements (HFSE), have been shown to be highly (over 98%) successful in correctly identifying tectonic setting of formation for known modern basalts (Saccani, 2015; Pearce, 2008). The defined fields in these diagrams are in good agreement with the compositions deemed typical for each of the tectonic setting.

The applicability of discrimination diagrams in fingerprinting Archaean greenstones is, however, a very controversial topic. One of the main concerns is around the fact that these diagrams were constructed using modern rocks, which may not be a good representation of Archaean processes. The use of geochemistry of modern tectonic settings to define Archaean geodynamic environments ignores the probability that the Archaean mantle may have been different from the modern mantle

and that some tectonic settings, which may have been unique to the early Earth, may be excluded as they are not represented today. In addition, Archaean basaltic rocks generally possess high Mg contents, indicating higher degrees of partial melting than most modern basalts. Archaean greenstones have also suffered intense alteration and metamorphism, which modified the primary compositions of the rocks.

Since there are very few (if any) Archaean greenstones whose geodynamic settings of formation are not hotly debated, it is not possible to test the reliability of existing discrimination diagrams in correctly fingerprinting Archaean rocks. As a result, the diagrams cannot be used to unambiguously identify tectonic settings of Archaean rocks. However, they can be used to compare the geochemistry typical of modern mantle sources and tectonic settings to that of Archaean greenstones (and their sources). The diagrams are employed for this purpose in this study. Because the geochemistry can be used to assess crustal contamination, this provides a means to constrain whether or not the rocks were formed in continental or oceanic settings. This, combined with the mantle source geochemistry, presents the only currently-available method to constrain the geodynamic settings of Archaean rocks based on geochemistry alone.

Since Archaean rocks have been subjected to intense alteration, modifying the absolute concentrations of the constituent elements, diagrams that utilize absolute abundances are avoided. Diagrams that employ compatible elements are also avoided as rocks of the Stolzberg Complex have been shown to be cumulates (see petrography). The diagrams utilized in this study employ ratios of immobile incompatible elements (including Zr, Hf, Nb, Th, Yb, Y, La).

It was argued in section 10.3 that fractional crystallization from ultramafic-mafic magmas, under low pressure conditions, does not modify the ratios between elements that are incompatible in olivine, pyroxene, and plagioclase. This means that olivine-pyroxene-plagioclase cumulates retains the inter-element ratios of the parental magma from which they were derived. Figure A2 (appendix) demonstrate that mineral accumulation does not modify inter-element ratios. In the diagrams, it can be seen that different cumulates of the Stolzberg Complex are all clustered together but without lithological groupings; the accumulation of olivine, pyroxene, or plagioclase did not shift (relative to the parental signature) the inter-element ratios to neither lower nor higher values. Comparison between figure A2 and figure 6.5.1-6.5.5 further shows that the inter-element ratios of different cumulates of the Stolzberg Complex lie in very restricted fields and that these

samples could not have acquired these ratios from fractional crystallization. I, therefore, conclude that although discrimination diagrams utilized in this study were meant for volcanic rocks, they are equally applicable to olivine-pyroxene-plagioclase cumulates.

The geochemistry of the Stolzberg Complex is compared with that of the spatially and temporally-associated Pioneer Complex as well as that of the Komati Formation (the archetypal ultramafic units of the Barberton greenstone belt). In addition, the rocks of the Stolzberg Complex are compared with the only known Phanerozoic komatiites from the Gorgona Island, a modern oceanic plateau (Ontong Java), a modern island arc (Mariana Arc), average N-MORB and OIB.

Th/Yb vs Nb/Yb

The diagram utilizing Th/Yb vs. Nb/Yb (after Pearce, 2008; fig. 6.5.1) can be helpful in discriminating between arc basalts and MORB-OIB series. The Mariana arc samples, average N-MORB and OIB are correctly identified. Ontong Java Oceanic Plateau plots within the bounds of the MORB-OIB array towards the E-MORB field. This confirms the finding of Pearce (2008), that oceanic plateau (including the Ontong Java and Caribbean-Columbian plateaux) rocks plot entirely within the MORB-OIB array. The Gorgona Island komatiites and picrites plot in the depleted MORB field, which is in agreement with the highly-incompatible elements depletion pattern displayed by these rocks (fig. 6.4).

Samples of the Stolzberg Complex exhibit a diagonal trend, which is steeper than the MORB-OIB array. Samples of the Stolzberg Complex presented in Bolhar et al. (2021) also show this pattern. This trend extends from the upper boundary of the MORB-OIB array into the arc array. Similarly, Komati Formation samples display a diagonal trend that is steeper than the MORB-OIB array. These samples are clustered along the upper boundary of the MORB-OIB array with about half of the samples plotting within the array and the other half plotting above. This feature was noted to be commonly displayed by Archaean greenstones (Pearce, 2008; Smithies et al., 2018), including Barberton greenstones (de Wit et al., 2018). Notice that the Primitive Mantle (PM) also plots above the upper boundary of the MORB-OIB array, in the region where most of the Archaean greenstones are situated. Samples of the Pioneer Complex, which is spatially and temporally associated with the Stolzberg Complex, also plot along the upper boundary of the MORB-OIB array but towards

the depleted MORB field (i.e., Th/Yb and Nb/Yb ratios lower than that of the N-MORB). This is in agreement with the highly-incompatible elements depletion pattern displayed by the Pioneer Complex (fig. 6.4).

Since the Komati Formation samples were not affected by crustal contamination and also display the diagonal trend along the upper boundary of the MORB-OIB array, it can be argued that this geochemical feature is not a result of contamination. In modern tectonic settings, rocks that exhibit diagonal trends that extend from the MORB-OIB array to the arc array are found in back-arc basins (Pearce, 2014).

In a plate tectonic framework, the results of the Th/Yb-Nb/Yb diagram would, therefore, be interpreted as an indication that the Stolzberg Complex, as well as other Archaean greenstones owe their origin to back-arc basin settings. While the back-arc basin is shown to be a possible geodynamic setting in the plate tectonic framework, other non-plate tectonic settings, unique to the Archaean, cannot be ruled out.

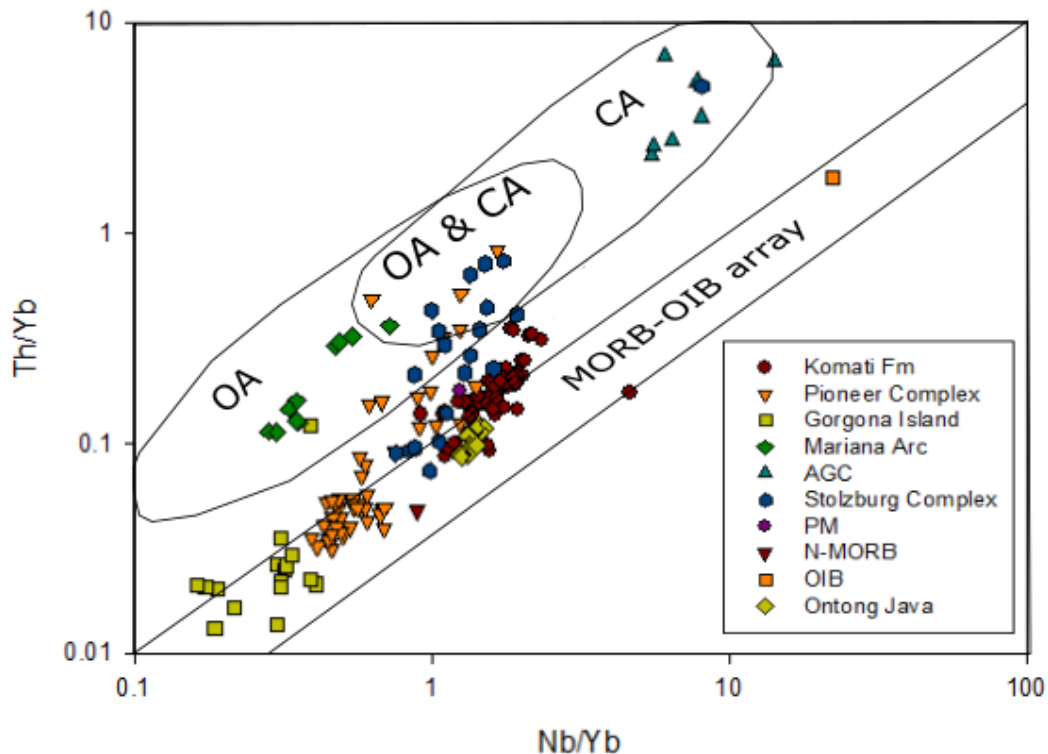


Figure 6.5.1: Th/Yb vs. Nb/Yb tectonic discrimination diagram (after Pearce, 2008). *OC* = oceanic arc and *CA* = continental arc. Stolzberg Complex data from this study and MacLennan (2012).

Komati Formation data from Chavagnac (2004); Robin-Popieul. (2012) Schneider et al. (2019). Pioneer Complex data from Cooper (2008) and Thompson-Stiegler et al. (2012). Gorgona Island data from Arndt et al. (1997) and Révillon et al. (2000). Ontong-Java oceanic plateau data from Fitton and Godard, (2004). Mariana Arc data from Elliott et al. (1997). Ancient Gneiss Complex (possible contaminant) data from Kröner et al. (2013, 2014). Primitive mantle data from Palme and O'Neill (2014). N-MORB data from Hoffmann (1988). OIB data from Sun and McDonough, (1989).

Nb/Th vs La/Nb

The Nb/Th vs La/Nb diagram (after Zhang et al., 2012; fig. 6.5.2) is meant to discriminate between MORB-OIB series from arc affiliated rocks. The Mariana arc samples, average OIB and N-MORB are correctly identified. Ontong Java oceanic plateau samples are confined within the MORB-OIB field.

The Stolzburg Complex samples show a large spread between the arc field and an undefined area outside of the MORB-OIB region. However, these rocks generally plot at lower La/Nb and higher Nb/Th values (indicating smaller Nb negative anomaly and higher enrichment of Th relative to the moderately incompatible elements; also refer to figure 6.4) than the Mariana arc samples. The Komati Formation and Pioneer Complex samples are concentrated at the bottom-right corner of the MORB-OIB region. Similarly, samples from the Gorgona Island plot around the same area. Notice that the PM also plots around the bottom-right corner of the MORB-OIB field.

Although most samples from the Stolzburg Complex plot into the volcanic arc field, several other samples plot above this field at the undefined region situated adjacent to the MORB-OIB field. Some samples of the Komati Formation and Pioneer Complex also plot just outside the MORB-OIB field, adjacent and below the field, with few samples extending into the volcanic arc. This makes it impossible to assign any of the concerned Barberton greenstones to a modern plate tectonic-based geodynamic setting of formation using the Nb/Th-La/Nb discrimination diagram alone.

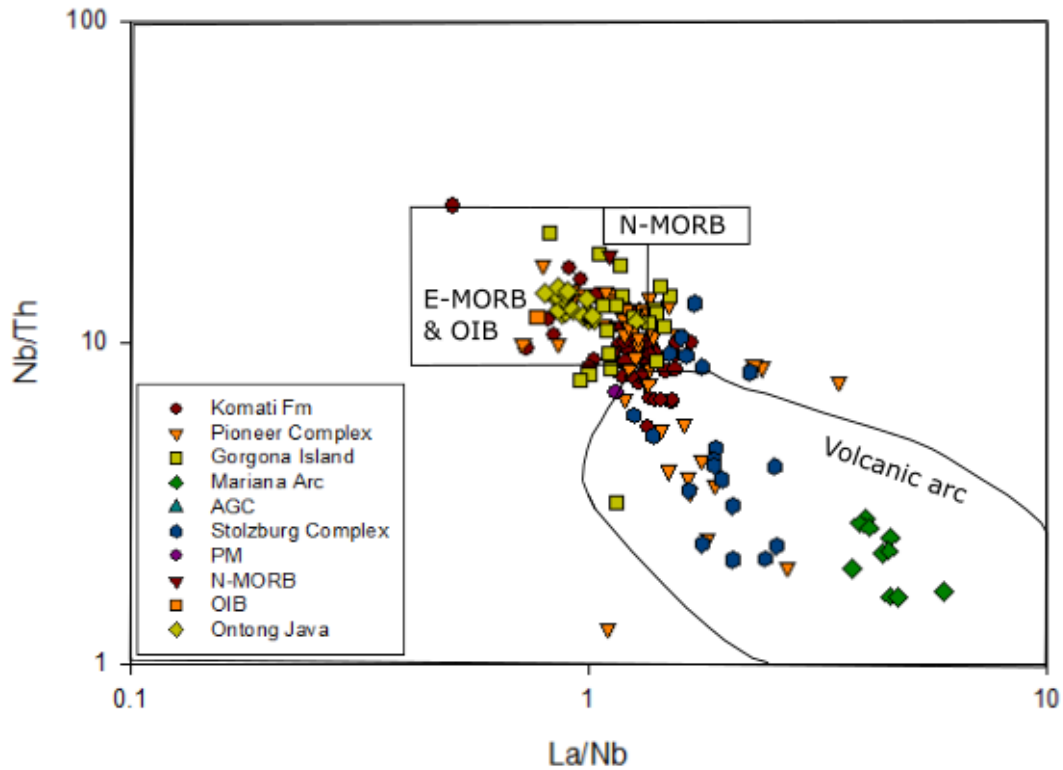


Figure 6.5.2: Nb/Th vs. La/Nb tectonic discrimination diagram (after Zhang et al., 2012). *The same datasets are used as in previous diagrams.*

(Hf/Sm)_{PM} vs (Ta/La)_{PM}

The purpose of the $(\text{Hf}/\text{Sm})_{\text{PM}}$ vs $(\text{Ta}/\text{La})_{\text{PM}}$ diagram (after La Flèche et al., 1998; fig. 6.5.3) is to show the degree of decoupling between incompatible elements (e.g., Hf & Sm and Ta & La) which behave very similar in magmatic systems under moderate pressure conditions. A common process capable of fractionating these elements is subducting slab dehydration, where the less immobile elements (e.g. LREE) enter the fluid phase while the highly immobile HFSE (e.g., Ta and Hf) are retained in the slab. As a result, the fluids become highly enriched in less immobile elements and depleted in the highly immobile elements, leading to subchondritic Hf/Sm and Ta/La ratios. When these fluids metasomatize the mantle wedge, it inherits this geochemical signature, which is in turn inherited by subduction zone-related magmas generated by partial melting of this source. Metasomatism of the mantle wedge by very low degree partial melting of the subducting slab may cause the same effect. Magmas generated from a source unaffected by metasomatism are expected

to display low Ta/La ratios. It is investigated here whether or not the Stolzburg Complex parental magma was derived from a metasomatized mantle wedge.

Although the average $(\text{Ta/La})_{\text{PM}}$ value of ~ 0.67 for the Stolzburg Complex is slightly lower than that of the average N-MORB of 0.78, it is still greater than the Mariana Arc value of 0.30. Actually, most of the Stolzburg Complex samples display values which overlap with those of the N-MORB, Komati Formation (~ 0.86) and Pioneer Complex (~ 0.78). The average was dragged to a lower value by the few samples, which display low $(\text{Ta/La})_{\text{PM}}$ ratios. Figure 6.5.3 demonstrates that most of the Stolzburg Complex samples exhibit $(\text{Ta/La})_{\text{PM}}$ ranges that are the same as those of the Pioneer Complex and Komati Formation. Mariana arc samples markedly display low $(\text{Ta/La})_{\text{PM}}$. It is, therefore, concluded that the Stolzburg Complex magma was unlikely generated from a source similar to the one from which Mariana arc rocks were derived. It may thus be further suggested that the Stolzburg Complex was not derived from a mantle source metasomatized by subduction zone-related fluids. The island arc setting for the origin of the Stolzburg Complex may therefore be preliminarily ruled out.

While samples from the Gorgona Island generally exhibit highly incompatible element depletion patterns, they surprisingly display a positive Ta anomaly (fig. 6.4), hence the high $(\text{Ta/La})_{\text{PM}}$ ratios. This feature may suggest that the source to these rocks was enriched in Ta relative to the other incompatible elements with similar bulk partition coefficients (e.g., La). One way to achieve such chemistry in the source is through retention of Ta (and possibly other HFSE as well) in the source during the preceding melt extraction events. None of the known modern mantle domains and tectonic settings generate melts with such features. Interestingly, the displayed incompatible elements pattern (i.e., LREE depletion and positive HFSE anomalies) is consistent with the inferred geochemistry of the dehydrated subducting slab. If the recorded geochemistry of the Gorgona Island rocks is correct, this could mean that the Gorgona Island komatiites were formed through melting of the peridotitic section of the dehydrated subducting slab. The other similar incompatible elements pattern to that displayed by the rocks from the Gorgona Island is that of the N-MORB, which also exhibits highly-incompatible elements depletion patterns but without the positive Ta anomaly. These findings may suggest that the Gorgona Island magmas were generated in an uncommon setting and/ or conditions, explaining the absence of their analogues in the modern Earth. However, the Stolzburg Complex was clearly derived from a different source as it displays

LREE enrichment and negative Ta anomaly as opposed to the converse displayed by the Gorgona Island rocks.

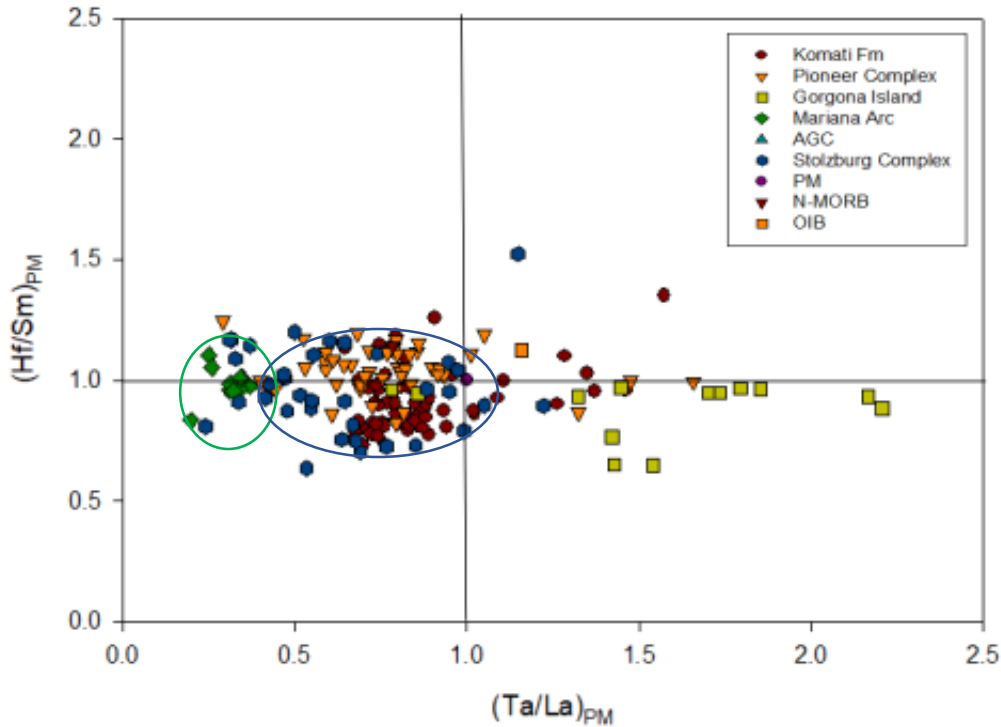


Figure 6.5.3: $(Hf/Sm)_{PM}$ vs $(Ta/La)_{PM}$ tectonic discrimination diagram (after La Flèche et al., 1998). The green oval encloses the cluster region of Mariana arc samples whereas the blue oval encloses cluster region of the Komati Formation, Stolzberg and Pioneer complexes. The same datasets are used as in previous diagrams.

Zr/Nb vs Nb/Th

The Zr/Nb-Nb/Th diagram (after Condie, 2005; fig. 6.5.4), unlike the ones discussed earlier, offers an opportunity to distinguish between oceanic plateau basalts (OPB) and MORB. Samples from the Mariana arc and the Ontong Java oceanic plateau are correctly identified. Likewise, the average N-MORB and OIB are correctly identified.

The Stolzberg Complex samples plot in the overlap region between the ARC and OPB fields as well as in the OPB only field. In contrast, none of the Stolzberg Complex rocks plot in the ARC only region. Since all the samples were obtained from one body and none of the samples plot in

the exclusive ARC field but some samples do plot in the exclusive oceanic plateau field, it is sensible to suggest that the Stolzburg Complex show more affinity to the oceanic plateau setting than to the arc setting. The reason these samples extend into the overlap region is merely because they are enriched in Th (relative to the moderately incompatible elements) and depleted in Nb, leading to low Nb/Th values, which does not necessarily indicate arc affiliation. Notice that the PM also plots in the ARC-OPB overlap region, further demonstrating that low Nb/Th ratios do not necessarily indicate arc affiliation. The Stolzburg Complex rocks clearly show no affiliation to the MORB environment.

Almost all of the Komati Formation samples plot in the OPB only field. For the same range of Nb/Th values, samples from the Pioneer Complex plot at higher Zr/Nb ratios, corresponding to the highly incompatible elements depletion patterns. Samples from the Gorgona Island plot at even higher Zr/Nb values. While few of the Pioneer Complex and Gorgona Island samples plot in the MORB field, most samples are situated in the undefined regions. Although by association (with the Stolzburg Complex and Komati Formation), one could suggest that the Pioneer Complex is also affiliated with oceanic plateau setting, the geochemistry of these rocks appears to be very uncommon in modern tectonic settings (see fig. 4 in Condie (2003)). In fact, such high Zr/Nb values are only known to be exhibited by the peculiar Gorgona Island komatiites and picrites. It thus follows that the Pioneer Complex magma was formed in a geodynamic setting that is incomparable to any of the known tectonic settings today. Since the Stolzburg Complex seems to be spatially and temporally associated with the Pioneer Complex, could this mean that the body was also formed in such an unfamiliar geodynamic setting?

Nb/Y vs Zr/Y

Like the Zr/Nb vs. Nb/Th space, the Nb/Y-Zr/Y space (after Fitton et al., 1997, 2003; fig. 6.5.5) presents an opportunity to discriminate between plume-related (OIB and OPB) and plate margin (MORB and ARC) geodynamic settings. The diagram successfully identifies Ontong Java samples as well as the average N-MORB and OIB. Unfortunately, the diagrams appears to fail to correctly identify the tectonic setting of the Mariana arc samples; as opposed to the arc field, these samples plot in the MORB field. However, this revelation is not very surprising as volcanic arc and N-MORB rocks display similar patterns in terms of Nb, Zr, and Y; both arc and N-MORB rocks are

depleted in Nb relative to the moderately incompatible elements and exhibit flat PM-normalized patterns from Zr to Lu (fig. 6.4). Consequently, the Nb/Y and Zr/Y of arc and MORB rocks may be indistinguishable. Nonetheless, the diagram still managed to successfully distinguish between rocks derived from plate margins and those that were generated in intraplate settings.

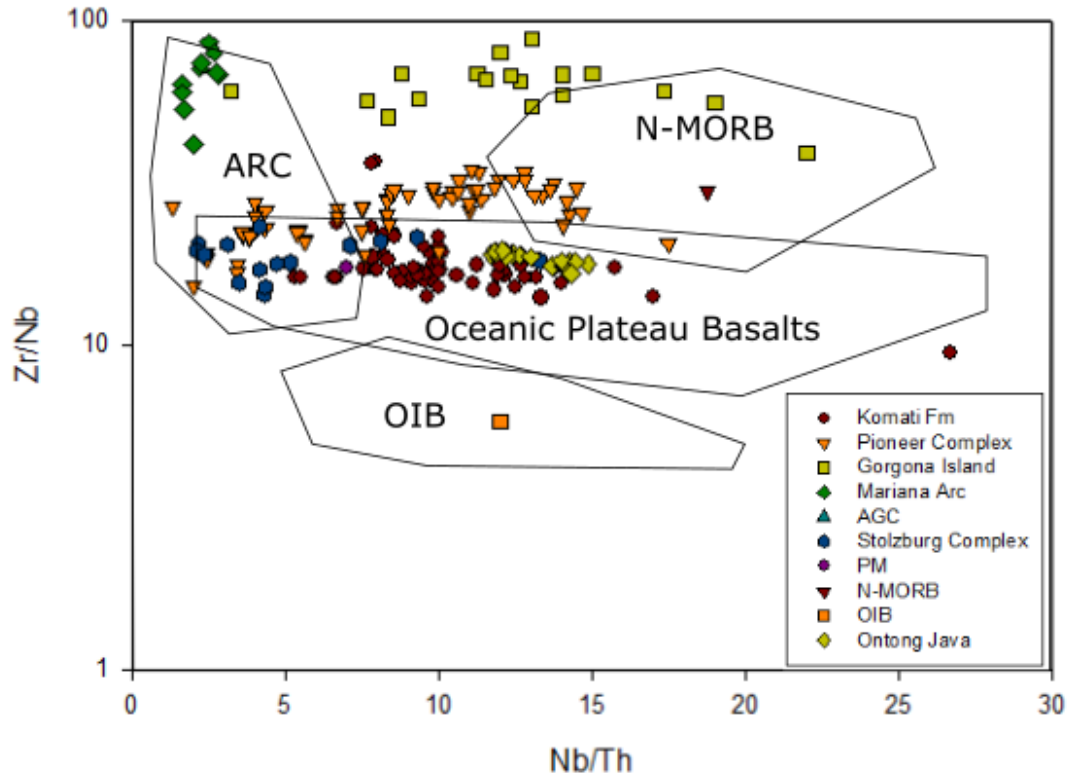


Figure 6.5.4: Zr/Nb vs. Nb/Th tectonic discrimination diagram (after Condie, 2005). *The same datasets are used as in previous diagrams.*

Samples from the Stolzburg Complex exclusively plot in the OPB field, reaffirming the intraplate (oceanic plateau) setting affiliation for this entity as suggested by the Zr/Nb-Nb/Th space. The Komati Formation and Pioneer Complex also plot in the OPB field. Again, the geochemically peculiar rocks of the Gorgona Island show some scattering between the N-MORB field and undefined regions (both plume-related and plume-unrelated). This further indicates that the Gorgona Island komatiites and picrites may have formed under a setting and/or conditions that are

very uncommon (but not necessarily non-existent) in the modern Earth. At this stage, however, effects of alteration and analytical error cannot be ruled out.

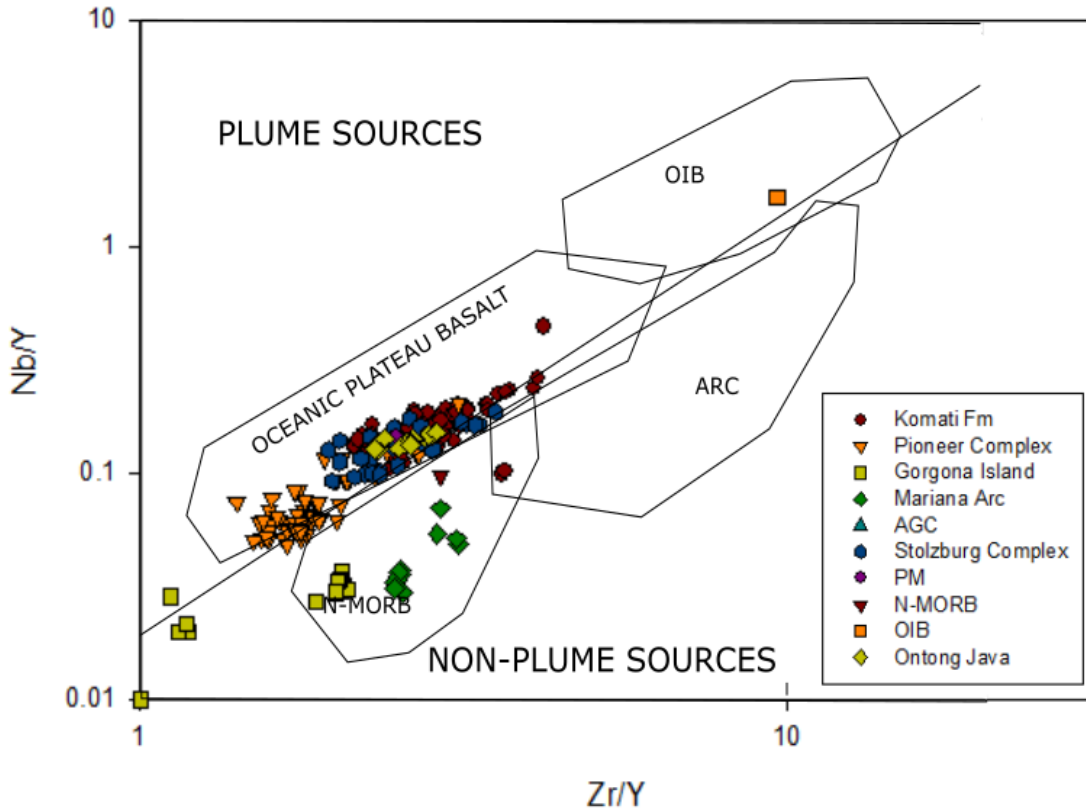


Figure 6.5.5: Nb/Y vs. Zr/Y tectonic discrimination diagram (after Fitton et al., 1997, 2003). *The same datasets are used as in previous diagrams.*

10.6.3. Summary and interpretations

It has been shown that the Stolzburg Complex parental magma was free of crustal contamination, implying that the magma did not traverse across an older, continuous, felsic basement. In turn, this finding may be interpreted as an indication that the Stolzburg Complex was emplaced in an oceanic environment, as opposed to a continental one. However, this conclusion does not preclude the existence of isolated felsic (TTG) plutons at the time and vicinity of emplacement since such plutons are documented; the 3.4 Ga Stolzburg, Theespruit and Doornhoek plutons and the 3.6 Ga

Ancient Gneissic Complexes occur in the south and east of the 3.25-3.26 Ga Stolzberg Complex, respectively.

Assuming that the recorded geochemistry of the Stolzberg Complex is juvenile and pristine (at least in some aspects, such as immobile trace elements), geochemical tools have been applied to this body in an attempt to constrain its geodynamic setting based on geochemistry alone.

The PM-normalized multi-elements pattern of the Stolzberg Complex resembles that of arc rocks. If the PM-normalized diagram alone was to be considered, it would be suggested that the Stolzberg Complex parental magma was derived from a metasomatized mantle wedge in an Archaean subduction zone environment. However, findings from other tools have demonstrated the question to be more complex than that. While the Stolzberg Complex exhibits the negative Nb-Ta anomalies that apparently typify arc rocks, Ta is, however, more depleted than Nb in the former body as opposed to the commonly encountered converse in the latter entity. Furthermore, the Th/Yb-Nb/Yb and Nb/Th-La/Nb discrimination diagrams are consistent with the arc setting (back-arc and volcanic arc, respectively) origin for the Stolzberg Complex, whereas the $(\text{Hf}/\text{Sm})_{\text{PM}}-(\text{Ta}/\text{La})_{\text{PM}}$ diagram argues against the derivation of the Stolzberg Complex parental magma from a fluids-metasomatized mantle source. Moreover, the Zr/Nb-Nb/Th and Zr/Y-Nb/Y diagrams suggest that the parental magma was derived from a source with chemistry similar to that displayed by modern oceanic plateau sources as opposed to a metasomatized mantle wedge. These findings indicate that the geodynamic setting of formation for the Stolzberg Complex cannot be determined on the basis of PM-normalized and discrimination diagrams alone. Perhaps other aspects of Barberton greenstones geology and geochemistry must be considered in order to be able to attain a well-rounded interpretation of the results obtained from incompatible elements geochemistry.

Workers who advance the subduction zone-related settings for the origin of Archaean greenstones commonly quote the presence of negative Nb-Ta anomalies and enrichment in highly incompatible trace elements (e.g., Rb, Sr, Cs, and Ba) in the uncontaminated mantle-derived ultramafic-mafic rocks as definitive evidence for mantle wedge metasomatism (e.g., Parman et al., 1997; Furnes et al., 2012). However, other authors have indicated that these features are not necessarily unique to arc rocks, especially in Archaean rock record (Condie, 2015; Bedard, 2006; Johnson et al., 2016; McCall, 2003; McCuaig et al., 1994; Polat et al., 2011; Xie et al., 1993). Alternative explanations for these geochemical signatures have, therefore, been presented. Enrichment in the highly

incompatible elements (e.g., Rb, Ba, Cs) is ascribed to post-magmatic processes, such as the well-imprinted hydrothermal alteration in Archaean greenstones. Besides crustal contamination, the Nb-Ta depletion patterns have been attributed to high pressure melting conditions where residual exotic phases retain these HFSEs (McCuaig et al., 1994; Xie and Kerrich, 1994). Essentially, these submissions question whether it is even appropriate to interpret the geochemical signatures of Archaean greenstones in the context of modern tectonic settings. Even if the Nb-Ta depletion is not a consequence of subduction zone-related metasomatism, the discrimination diagrams such as the Nb/Th-La/Nb space would still misclassify the rocks as volcanic arc products.

Interestingly, other features of the Barberton greenstone belt are not consistent with the origin of these rocks in the favoured back-arc basin spreading centre setting. For example, the greenstone belt has been shown not to resemble an ophiolite (Dann, 2000; Hamilton, 2008) – a typical product of modern spreading centres. Furthermore, such a setting cannot account for the high pressure melting suggested by the geochemistry (i.e., Al, Y, HREE depletion) of some of the greenstones (e.g., Komati Formation and Nelshoogte belt volcanics). The thick Archaean greenstone sequences are generally considered to have been developed through voluminous mantle-derived magmatism (Brandl et al., 2006; Lowe and Byerly, 2007; Viljoen and Viljoen, 1969a), a feature atypical of modern spreading centre settings (Coffin and Eldholm, 1993). The LREE depleted Pioneer and Saw Mill complexes, which are seemingly spatially and temporally intimate with the Stolzburg Complex, could not have been derived from a metasomatized mantle wedge. Note that the Pioneer Complex also displays a prominent negative Ta anomaly (fig. 6.4), which should not be expected if the magma was derived from a metasomatism-free MORB-like source. Although this unusual geochemistry displayed by the Pioneer Complex cannot be associated with any of the known modern mantle sources, its closest analogue is the MORB composition.

An oceanic plateau setting is the other popular geodynamic environment in which Archaean greenstone belts are envisaged to have originated (Chavagnac, 2004; Kamber, 2015; Schneider et al., 2019; Van Kranendonk et al., 2015). Although such a setting can account for some aspects of the geology and geochemistry of Archaean greenstone sequences, it fails to explain other features. For example, the voluminous magmatism thought to have led to the development of Archaean greenstone sequences can be accounted for as the generally thick oceanic plateaux are associated with the high eruption rates of mantle plumes. Because mantle plumes may originate from deep in

the mantle (up to the mantle-core boundary); the need for extremely high pressure conditions during melting can be explained. Extremely high temperature conditions deep in the mantle may have also promoted high degree partial melting. The generally flat PM-normalized multi-element pattern (commonly characterizing oceanic plateaux) of the Komati Formation have been interpreted as evidence that these rocks were formed in an Archaean oceanic plateau (e.g., Chavagnac, 2004). However, LREE-depleted signatures characterizing the Pioneer Complex are uncommon in plume-derived melts. Moreover, Nb-Ta depletion signatures common in Archaean greenstones (such as the Stolzberg Complex) are not encountered in modern oceanic plateaux. Although the Zr/Nb-Nb/Th and Nb/Y-Zr/Y discrimination diagrams suggest that the Stolzberg Complex and Komati Formation are connected to oceanic plateau settings, the steep diagonal trends exhibited by these rocks in the Th/Yb-Nb/Yb space cannot be explained. Modern oceanic plateau rocks follow the trend of the MORB-OIB array and plot entirely within the array. Bimodal volcanism and interlayering between basic lavas and acidic lavas (e.g., at the top of the Hooggenoeg Formation of the Barberton sequence) occur in the Archaean greenstone belts whereas none of this is encountered in modern oceanic plateau settings. Moreover, Archaean terranes are characterized by dome-and-keel structural patterns, which have never been encountered in modern oceanic plateaux. These features serves as additional evidence against the oceanic plateau setting for the origin of Archaean greenstones.

The fact that not even the two most popular settings for the origin of the Barberton greenstone belt (i.e., oceanic plateau and back-arc basin spreading centre) can satisfactorily explain the geological and geochemical aspects of this entity implies that none of the modern geodynamic environments provide a suitable framework to explain its history and development. Guice et al. (2019) arrived at a similar conclusion. In this regard, the comparable incompatible elements geochemistry between the Barberton (and other) greenstones and modern oceanic plateau rocks may merely indicate derivation from similar less fractionated sources, as opposed to the greenstones being generated in oceanic plateau settings. The suggestion that both these entities were derived from similar least-fractionated sources is supported by the fact that the PM (the unfractionated source) and Archaean greenstones plot in the field of oceanic plateaux in discrimination diagrams (fig. 6.5.1-6.5.5). Furthermore, Stolzberg Complex source characterization revealed that it was very similar to the PM. On the hand, the not-uncommon Nb-Ta depletion patterns in Archaean greenstones, generally associated with arc settings, are likely a consequence of a geochemical

process which was prevalent in the Archaean but no longer common on modern Earth; high degree partial melting under extremely high pressure conditions is one possibility. Such a mechanism is explored further in the following section. When assessing the applicability of geodynamic discrimination diagrams that were constructed on the basis of the geochemistry of modern rocks, Condie (2015) alluded to the possibility that some Archaean/ Hadean geodynamic environments may be unrepresented in the modern Earth.

Gorgona Island, being the only known place where Phanerozoic-age komatiites are found (Echeverría, 1980), serve as the only modern-Earth point of reference for models on the generation of komatiites in the early Earth. Deciphering the setting in which the Gorgona Island komatiites were formed should shed some insights into the kind of environment that Archaean komatiitic magmas were generated. If all komatiitic magmas were generated in the same settings, the variation in chemistries shown by the derivative rocks should reflect differences in source compositions. With some exceptions, the compositions of most Archaean grestones are quite coherent (Condie, 2005; Pearce, 2008).

While the Gorgona Island is generally thought to be a product of melting of a mantle plume (e.g., Arndt et al., 1997; Révillon et al., 2000), the komatiites and picrites of this entity have been found, in the previous section, to exhibit peculiar compositions that cannot be associated with any of the modern geodynamic settings. Although the incompatible elements geochemistry displayed by these rocks cannot be matched with that of any of the modern mantle-derived rocks, its closest analogue is that of MORBs as manifested by the LREE-depletion patterns as well as low Th/Yb and Nb/Yb and high Zr/Nb ratios (fig. 6.4, 6.5.1, & 6.5.4). The peculiar compositions displayed by the Gorgona komatiites are either a consequence of a long-term isolated mantle source with peculiar chemistry or unusual melting processes. Under the extreme pressure-temperature conditions in the mantle, any isolated mantle domain would probably be homogenized. Besides, such compositions have not been reported elsewhere in the modern Earth. It is, therefore, more likely that the peculiar compositions are a result of melting conditions and/ or processes which are not yet realized or understood. Can the same be said about Archaean greenstones? The fact that the Gorgona komatiites are relatively young (~88 Ma; Arndt et al., 1997) and were derived from the modern mantle suggest that the unexplained geochemistry displayed by Archaean greenstones is not necessarily a result of a compositionally different Archaean mantle, but possibly a

consequence of unusual melting mechanism and processes involved in the generation of ultramafic magmas.

10.7. An alternative model for the origin of the Barberton greenstone belt

It is widely accepted that Al-depleted ultramafic melts were generated through high degree partial melting with majoritic garnet in the restite (Gruau et al., 1999a, b). It follows that melting occurred under very high pressure (>13 GPa) since majoritic garnet is only stable in such conditions. Currently, the most popular setting under which such high pressures can be attained is in a plume originating from very deep in the mantle. Anomalously high temperatures, thought to be characteristic of mantle plumes, are believed to be responsible for the high degrees of partial melting. Mantle plumes are also believed to be responsible for voluminous magmatism that develops large igneous provinces such as oceanic plateaux and continental flood basalts (Mahoney, 1987; Coffin and Eldholm, 1993). Although the mantle plume model seemingly explains some of the critical features of Archaean greenstones (i.e., high pressure, high temperature, high degree partial melting, and voluminous magmatism), it has been shown (in the previous section) to be inadequate. This implies that the Archaean Earth must have been shaped by an alternative geodynamic setting that was also characterized by the above-mentioned defining features. One familiar and conceivable candidate is a bolide impact setting. It is well understood that extreme pressure and temperature conditions as well as high degrees of partial melting (up to 100%) are attained at the target site during an impact, potentially also causing large volumes of melts (Vaughan et al., 2013). Bolide impact events, therefore, provide a suitable setting for the formation of Archaean greenstone belts. Interestingly, majoritic garnet was first discovered in a meteorite (Smith and Mason, 1970).

10.7.1. Influx of impactors on Earth in the Archaean

Bolide impact-based models for the origin of Archaean greenstone belts have been proposed before but they are generally overlooked. Part of the reason is that the influx of impactors in the Archaean is underestimated. Because most of the Earth's ancient surface was reworked by plate tectonic processes (as indicated by the paucity of surface rock with early Archaean ages), there is very little record of the Archaean surface processes. It is, therefore, not possible to directly determine the

influx of impactors on Earth in the Archaean. The preserved record of the timing and influx of impactors on the Earth's Moon is, thus, used to estimate the same quantities for the Earth (e.g., Valley et al., 2002). Because the Moon seems to have experienced the last major impact events very early in the Archaean (i.e., ~ 3.8 Ga), at the end of the so-called Late Heavy Bombardment (LHB), the same is thought to have been the case for Earth; it is generally believed that the influx of impactors exponentially declined after the LHB (Neukum et al., 2001; Valley et al., 2002). However, the fact that Earth has a much larger surface area and much stronger gravitational field than its Moon makes one wonder if the preserved records on the Moon are a good representation of what may have happened on Earth. Based on the surface areas and strengths of gravitational fields, it has been proposed that for every large impact event on the Moon, there must have been at least twenty events of a similar size on Earth (Lowe and Byerly, 2018). Another issue is that a record of impactors influx on Earth is biased towards the preserved impact craters on the old continental crust. Currently, there are at least six, young (≤ 2 Ga), large (diameter >100 km) craters that have been identified on the continental crust (Glikson, 2001). Using surface area distribution (40% continental crust and 60% oceanic crust) and the fact that impactors do not preferentially land on any of the crust types, Abbott and Isley (2002) proposed that only 40% of impactors should land on continental crust. This means that at least eight, large impactors must have landed on the (now-recycled) oceanic crust in the last 2 billion years of Earth's history. Assuming that impactors influx declined overtime (on the basis that Earth progressively swept its orbit), it is logical to postulate that many more impactors struck the oceanic crust during the Archaean (i.e., earlier than 2.5 Ga). On these bases, it is, hereby inferred that large impactors struck the Earth's ocean basins frequently in the Archaean. This is supported by the identification of impact events clusters in the Archaean (Lowe and Byerly, 2018). It has been suggested that a tail (continuation after the major/peak event) of accretion of the Earth extended into the Archaean (post 3.7 Ga) (Bottke and Norman, 2017; Bottke et al., 2012; Koike et al., 2020; Marchi et al., 2014; Nesvorný et al., 2017; Morbidelli et al., 2017). Lowe and Byerly (2018) concluded that though the prevailing geodynamic system in the mid-Archaean is not clear, the Earth was still being subjected to frequent, very large asteroid impacts.

10.7.2. Bolide impact-based models for the origin of Archaean greenstone belts

It is widely accepted that bolide impact events shaped the surface of the Earth before ~3.8 Ga but there are debates on when endogenic processes took over. Some workers (e.g., Green, 1972) propose that impact events continued well into the Archaean (at least up to ~3 Ga) to dominate surface processes on Earth. One of the earliest bolide impact-based models was by Green (1972, 1975, 1981). The author regarded the Archaean greenstone sequences as “terrestrial maria”, in comparison to the lunar maria – basaltic plains on the Earth’s Moon which are believed to have been generated by impact-related processes. Similarly, Glikson (1976) proposed that at least some of the Archaean greenstone belts are products of impact-related processes. Frey (1977, 1980) added that the crustal dichotomy on Earth was unlikely a consequence of plate tectonic processes, in fact, it formed before the onset of such processes. The crustal dichotomy is ascribed to impact-related processes in the early Earth. Marchi et al (2014) suggested that the primitive crust was destroyed and replaced by voluminous basaltic volcanism related to impacts events during the LHB. Another model was by Hansen (2015), who proposed an impact-related origin for Archaean cratons. Here, the Archaean granitoid-greenstone terranes are compared with crustal plateaus on Venus, which are believed to have formed as a result of impact-related processes.

10.7.3. Impact-related melt generation mechanism(s)

It is undisputed that shock melting of the target material occurs during a bolide impact event. This process result in voluminous superheated impact melt sheets. In addition to shock melting, a number of authors have postulated other impact-related melting mechanisms. In the model by Green (1972), it is proposed that the voluminous magma is due to unloading and catastrophic diapirism (decompression) of the mantle beneath the impact site. It has also been postulated that the heat deposited onto the mantle at the impact site may lead to steeper geotherms and therefore initiate convection which in turn result in adiabatic melting (Jones et al., 2003). Similarly post-impact melting events have also been proposed (Roberts and Barnouin, 2012; Ubide et al., 2017). More recent description of post-impact melting mechanism(s) is provided by Elkins-Tanton et al.(2004); Elkins-Tanton and Hager (2005); and Jones (2014). These post-impact melting mechanisms have also been linked to the formation of some modern large igneous provinces (Elkins-Tanton et al., 2002; Glikson, 1999; Jones et al, 2002, 2003). Jones et al. (2003) postulated

that the Gorgona komatiites might have resulted from decompression melting following an oceanic impact.

Although post-impact melting is a debated topic, with no unequivocal evidence in support of its occurrence on Earth, such a process is likely feasible, especially in cases where the impactor strikes the generally thinner and high-geothermal gradient oceanic crust (Jones, 2014). Since there is no knowledge relating to the effects of impactors on the mantle beneath the impact site in oceanic settings (Glikson, 1999, 2003; Jones et al., 2003), currently, it is not possible to directly test the post-impact melting mechanism; there is no identified point of reference. Available knowledge is limited and biased towards continental crust-based impact events.

10.7.4. Evidence for the occurrence of impact events in the vicinity of the area now called Barberton

As far as I am concerned, there is no impact-based model specifically presented for the Barberton greenstone belt. However, a number of studies have presented evidence in support of the occurrence of impact events (during the development of the supracrustal sequence) in the vicinity of the area of formation, at least from the mid- to late- Palaeoarchaeon (i.e., 3.4 – 3.2 Ga). Of the evidence presented, the positive identification of impact spherule beds (with distinctive extraterrestrial Cr and Ir isotopic signature) serves as definitive proof that impact events did occur (Lowe and Byerly, 1986, 2018). The oldest known impact spherule bed, named S1 and dated ~3472 Ga, is stratigraphically situated at the upper part of the Hooggenoeg Formation, above the H4 member (Lowe et al., 2003; Lowe and Byerly, 1999). Two other layers, named S2 and S3 and dated ~3260 Ma and ~3243 Ma (Lowe et al., 2003; Lowe and Byerly, 2018), respectively, occur at the base of the Fig Tree Group (Lowe and Byerly, 1999). Other contentious layers (S4-S8) have been reported (Lowe et al., 2014; Hofmann et al., 2006).

Fracturing of the topmost layers of the Onverwacht Group, which was followed by the deposition of the S2 spherule layer, has been attributed to the S2 impact event (Lowe, 2013; Lowe et al., 2014). These fractures were subsequently filled with soft fine sediments, thereby, forming chert dykes. Spherules have been identified in the dykes, indicating flowage of impact-related sediments into the development fractures, presumably following the S2 impact event (Lowe and Byerly,

2018). However, Hofmann and Bolhar (2007) have ascribed the fractures to overpressuring related to hydrothermal processes. The so-called Tsunami conglomerate/breccia (Hofmann et al., 2006), made up of very angular ripped-up chert slabs, at the base of the Fig Tree, may be a result of impact-generated Tsunami.

The geochemically peculiar Bon Accord deposit (which is Ni-rich but sulphide deficient) in Barberton greenstone belt has been interpreted as an oxidized iron meteorite (De Wall, 1978). However, Tredoux et al. (1989) proposed that it is a strongly altered deep mantle fragment within the mantle section of the Archaean Jamestown ophiolite described by de Wit et al. (1987).

In the Barberton greenstone belt, the apparent temporal coincidence between the spherule beds and pulses of ultramafic magmatism may indicate an impact-related origin. In particular, the S2/S3 beds seemingly coincide with the widespread 3.26-3.25 Ga (Bolhar et al., 2021; Connolly et al., 2011; Ficq et al., 2018; Hofmann et al., 2021; Puchel et al., 2014) ultramafic magmatism which led to the development of the layered complexes (e.g. Stolzberg Complex). Some authors have suggested that at least some of the Komati Formation units are sills (see section 10.8, P.129) (eg., Parman et al., 1997), as opposed to lava flows as widely believed. If true, this could mean that the actual age of the Komati Formation is less than the assigned value of 3481 ± 2 Ma (Dann, 2000). The true age may coincide with the 3472 Ma age of the S1 spherule bed. Note that the minimum age of the Komati Formation, constrained by the intruding felsic bodies, is 3467 Ma (Kamo and Davies, 1994).

The apparent systematic sequence of events starting with an impact event are hard to ignore. For example, the S1 event is followed by the 3.45 Ga felsic magmatism (manifested by dacitic volcanism at the top of the Hoogenoeg Formation (H6v unit) as well as the Stolzberg, Theespruit and Doornhoek plutons) and then deposition of sediments (H6c unit). Similarly, the S2 event is followed by widespread 3.2 Ga felsic magmatism (manifested by dacitic volcanism at the base of the Fig Tree Group as well as the Kaap Valley and Nelshoogte plutons) and then the Fig Tree and Moodies groups sedimentation. It is logical to suggest that these cycles were triggered by impact events.

MORB and OIB melts have been shown to display a near-constant $\text{H}_2\text{O}/\text{Ce}$ ratio of $\sim 200 \pm 100$ (Dixon et al., 2002), indicating limited variation in the modern mantle. In contrast, Sobolev et al. (2019) reported notably higher values of ≥ 1000 in melt inclusions trapped in preserved olivine

grains in komatiitic rocks of the (Saw Mill Complex) Weltevreden Schist Belt, Barberton Greenstone Belt. Since the H_2O/Ce ratio cannot be modified by fractional crystallization or partial melting (Michael, 1995), the recorded excess in water over Ce was regarded as the parental melts mantle source character. These authors went on to suggest that the excess water was entrained into the deep-originated mantle plume as it crossed the hydrated transition zone. Since the reconstructed original hydrogen isotopic compositions of the parental melts were found to be considerably depleted in deuterium compared to Archaean and modern mantle compositions, but consistent with that of seawater-altered and partially dehydrated oceanic lithosphere, it is argued that the alleged excess water in the transition zone was accumulated through recycling of oceanic slabs that were transported into the deep mantle through subduction. High H_2O/Ce ratios were also reported in melt inclusions trapped in olivine grains from Abitibi (Sobolev et al., 2016) and Belingwe (Asafoc et al., 2018) greenstone belts, respectively situated in Canada and Zimbabwe, as well as from Gorgona Island komatiites (Gurenko et al., 2016). Allowing time from when the slab was subducted to when the plume-derived melts crystallized, it is suggested that subduction processes were in operation by 3.3 Ga. Earlier in this thesis, an impact-based model for the origin of the komatiitic parental melts was suggested as a viable alternative to the mantle plume- and subduction zone-based models. Such a model may offer an alternative explanation for the origin of the excess of water over Ce in the parental melts, where melting was restricted to the uppermost portion of the mantle; catastrophic mixing of the hydrated oceanic crust with the upper mantle as a result of bolide impacts is one possibility. The impact model could also offer new melting settings under which the variable and anomalously light oxygen isotopic compositions recorded in some Archaean greenstones (e.g., Saw Mill Complex (Byerly et al., 2017) and Stolzberg Complex (Bolhar et al., 2021)) may be explained. These authors, however, present terrestrial interpretations.

The impact model offers a potential explanation for the occurrence of diamonds on the surface of the Earth in the Archaean (i.e., Archaean placer diamonds from the Kaapvaal craton, South Africa) as reported by Smart et al. (2016). In modern Earth, diamonds are transported from deep in the mantle to the shallow depths by alkaline magmatism (e.g., kimberlites). However, such conveyers did not exist before ~ 3 Ga (Tappe et al., 2014). How then did diamonds get to the surface, for them to be incorporated into the sedimentary deposits of the Witwatersrand Supergroup? This remains enigmatic. Smart et al. (2016) indicated that the geochemical signatures of the diamonds are suggestive of a sedimentary carbon source. These authors, however, interpreted this feature as

an involvement of subducted sediment at the site of diamond formation, deep in the mantle. An exogenic model may interpret the diamonds as shock-converted carbonaceous (sedimentary?) material near the surface of the Earth during an impact event.

While rocks in most cratons display greenschist (and localized amphibolite) facies metamorphism, other Archaean terranes (e.g., North Atlantic Craton (Windley and Bridgwater, 1971)) dominantly exhibit high-grade (granulite) metamorphism (Anhaeusser, 2014). Interestingly, granulite terrains known to the geological community are dominantly Archaean (Bohen and Mezger, 1989; Rudnick, 1992; Rudnick and Presper, 1990), indicating that the processes that formed these entities were at optimum in the early Earth. Some workers believe that Archaean granulite terrains are products of continent-continent collisions (Newton and Perkins, 1982), implying that subduction processes were operational then. Since the operation of plate tectonics on Earth in the Archaean is highly controversial, an alternative explanation for the origin of these granulite terrains may be needed. An alternative setting, envisaged in this study, for the formation of Archaean rocks is a bolide impact site. In this framework, the Archaean granulite terrains are thought to be products of impact processes, where the associated high temperature and high transient pressure conditions would have converted near-surface rocks into granulite facies.

10.7.5. Melting conditions for Al-undepleted melts

The absence of garnet in the restite during the generation of Al-undepleted ultramafic melts is widely believed to indicate that partial melting occurred at relatively lower pressure conditions (spinel stability field, specifically), where majoritic garnet was not stable (e.g., Robin-Popieul et al., 2012). However, this suggestion is not consistent with some of the geochemical signatures displayed by Al-undepleted magmatic rocks. For example, melting in the spinel stability field cannot explain the presence of the prominent negative Nb-Ta anomaly exhibited by the Al-undepleted rocks of the Stolzburg Complex. The partition coefficients of REEs, Nb, Ta, Zr, and Hf are uniform in spinel, meaning this phase cannot fractionate these elements (Capobianco and Drake, 1990). Moreover, Lu and Sc are highly compatible than other REEs in spinel (Nagasawa et al., 1980), so it is expected that melts generated with spinel in the restite display complementary depletion (relative to other REEs) of these elements. It is, therefore, unlikely that melting occurred in the spinel stability field.

The source of Al-undepleted melts could not have undergone earlier high pressure partial melting events. Otherwise, the Al/Ti and Zr/Y ratios as well as the HREEs patterns of the source would have been changed to super- or sub-chondritic signatures. In the context of the plume model, this would mean that the source reached shallow depths without undergoing melting and only started melting when it reached the spinel stability field. It is unlikely that not even small degree melts would have been extracted from the source. The paucity of Al-undepleted komatiitic basalts and tholeiites (i.e., lower degree partial melts), at least in the Barberton Greenstone Belt, is noteworthy.

The Nb-Ta depletion patterns commonly encountered in Archaean greenstones are ascribed, by some workers (e.g., McCuig et al., 1994; Xie et al., 1993; Xie and Kerrich., 1994), to the action of high pressure phases (in which Nb and Ta are compatible) in retaining these elements in the restite during partial melting. Mg-Perovskite is one of the high pressure phases thought to be responsible for the Nb-Ta fractionation from REEs (Xie et al., 1993; Xie and Kerrich., 1994). In addition to Nb and Ta, however, Zr and Hf are also compatible in Mg-perovskite (Kato et al., 1988, 1996; Taura et al., 2001; Corgne et al., 2005). This means that Nb-Ta anomalies must be accompanied by Zr-Hf anomalies if the fractionations were a consequence of the action of Mg-perovskite. Since the preserved samples from the Stolzberg Complex display no Zr-Hf anomalies and chondritic Hf/Sm ratios, it may be concluded that Mg-perovskite was not present in the restite during the generation of the parental magma, and is therefore not responsible for the Nb-Ta depletion pattern displayed by these rocks. Similarly, rutile could not have been responsible for the negative Nb-Ta anomalies displayed by the rocks of the Stolzberg Complex as Zr and Hf are also compatible in this phase (Klemme et al., 2005). Lahaye et al. (1995) attributed the negative Nb anomaly in some Archaean greenstones to majorite fractionation. This suggestion is not consistent with the lack of majorite a fingerprint in the form of non-chondritic Al_2O_3/TiO_2 ratios and HREEs patterns in the Stolzberg Complex rocks. It, therefore, seems there is no known high-pressure phase that can explain the negative Nb-Ta anomalies while it remains consistent with the other geochemical signatures of the Stolzberg Complex. Consequently, ascribing the negative Nb-Ta anomalies to high pressure phases in the restite during partial melting remains unsupported at this stage.

There are at least two conceivable ways through which Al-undepleted magmas may be generated under high pressure conditions (i.e., in the stability field of majoritic garnet). One way is through partial melting of a depleted source where olivine and orthopyroxene are the only major phases

present. Under such circumstances, garnet will be negligible or absent in the source and restite as its building components will be lacking. As a result, the generated magma will display chondritic $\text{Al}_2\text{O}_3/\text{TiO}_2$ ratios and HREEs patterns despite melting occurring in the stability field of garnet. The other way involves exhaustively high degree of partial melting of an undepleted source, where garnet is completely consumed (Kerr et al., 1996; Herzburg, 1992). Since there is no garnet retained in the restite, the generated magmas will not show fractionation between Al and Ti and amongst HREEs. The Stolzburg Complex displays LREEs enrichment patterns, suggesting that the parental magma was not derived from a depleted source. If melting occurred under high pressure conditions, it may be inferred that the degree of partial melting was sufficiently high to completely consume garnet, so that none remains in the restite.

Al-undepleted magmas generally have lower abundances of incompatible elements than Al-depleted magmas (Chavagnac, 2004; Robin-Popieul et al., 2012). This may be interpreted as derivation of Al-depleted magmas from a comparatively enriched source or generation of the magma through lower degree of partial melting. Since garnet is retained in the restite during the generation of Al-depleted magmas, it may be deduced that the degree of partial melting in such a case is not exhaustive. Provided that Al-undepleted magmas are generated through exhaustive degrees of partial melting, it may be concluded that the relative enrichment in incompatible elements in Al-depleted magmas is a consequence of a lower degree of partial melting and not necessarily derivation from a more enriched source. Al-enriched komatiites generally exhibit LREEs depletion patterns and low abundances of incompatible elements (Hoffmann and Wilson, 2017; Puchel et al., 2013; Robin-Popieul et al., 2012; Wilson, 2003), indicating derivation from a depleted source. The Al, Y, HREE enrichment and LREE depletion patterns displayed by these rocks is consistent with the generation of these melts through remelting of the garnet-rich residue left behind after the extraction of Al-depleted magmas.

The model presented here for the generation of ultramafic-mafic magmas regards Archaean komatiites and tholeiites as impact melts. During an impact event, the topmost mantle experiences the most extreme pressure and temperature conditions, and as a result, undergoes intense melting and produces Al-undepleted melts. Below this mantle region, at lower shock pressures, Al-depleted melts are produced. Al-depleted komatiitic basalts and tholeiites may be produced at even lower shock pressures and temperatures (i.e., at great depths) where the degree of melting is

consequently lower. The residue left behind after the extraction of Al-depleted magmas may undergo further decompression melting following upliftment at a later stage or may be subjected to shock melting in a successive impact event to produce the Al-enriched magmas. In the same context, the Gorgona komatiites may represent impact melts. The impact melts probably interacted with the ocean water to generate the ultramafic tuffaceous sequences (e.g., Osinski et al., 2019; Ubide et al., 2017) encountered in the Barberton greenstone belt. The same is thought to have occurred in the Sudbury Complex, where basaltic impact melts are thought to have interacted with oceanic water to produce pyroclastic deposits that overly the magmatic body (Grieve et al., 2010). The ultramafic pyroclastic deposits of the Gorgona Island are believed to have formed through interaction between hot, mantle plume-derived melts (Kerr et al., 1996; Storey et al., 1991) or secondary post-impact melts (Jones et al., 2002) with ocean water. Interestingly, the pyroclastic sequences of the Sudbury Complex and Gorgona Island were also invaded by tabular bodies (Kerr et al., 1996; Storey et al., 1991; Ubide et al., 2017).

10.8. Temporal relationship between spatially intimate but compositionally distinct magmatic units

A better understanding of the temporal and petrogenetic relations between the different classes of ultrabasic-basic magmas (i.e., Al-depleted, Al-undepleted, and Al-enriched), encountered in Archaean terranes, has a great potential of shedding light into the mechanism(s) and setting(s) involved during the generation of such magmas. Since these different classes of ultramafic (komatiitic) rocks are normally found in intimate spatial association with each other, current models generally assume contemporaneous generation and emplacement of the magmas. This suggestion may be true in cases where the interstratified distinct magmatic units represent alternating eruptions of magmas of different komatiite types. Conversely, it is unlikely true in cases where one kind of komatiite type may represent early-formed lavas whereas the other type constitutes sills, which later invaded the lavas. It is also possible that an entire formation of magmatic layers may represent a sheeted-sill complex. The conformable nature between the lavas and the sills suggest that the lavas were solid when the sills were emplaced, which suggests a significant emplacement (and possibly generational) time-gap between the spatially-associated yet compositionally distinct magmatic units.

In section 7.3, it was demonstrated that the Stolzburg Complex, together with other Barberton complexes, represent sheeted sill complexes, which developed through magma injection into the early formed country rocks (metavolcanics and komatiitic tuffs). Furthermore, it was shown in section 10.4 that the Nelshoogte metavolcanics and the spatially intimate Stolzburg Complex are not co-magmatic. Although the geochemistry of the komatiitic tuff units found interlayered with the Stolzburg Complex magmatic layers is not known, similar rocks have been shown to be predominantly of the Al-depleted group in the nearby Pioneer and Saw Mill complexes. If these intraformational tuff units in the Stolzburg Complex are also of the Al-depleted type, this could suggest that the tuffs are genetically related to the Al-depleted Nelshoogte metavolcanics, but this remains to be demonstrated. Following the establishment that the Al-depleted Nelshoogte metavolcanics and the Al-undepleted Stolzburg Complex are not co-magmatic despite their intimate spatial association, seeking to understand the temporal relations between these two geological entities becomes necessary. From field relations, it seems plausible that the Nelshoogte volcanism occurred earlier than the Stolzburg Complex magmatism, but it remains to be resolved as to how much earlier. While the Stolzburg Complex has been directly dated only recently, there are no radiometric dates of the Nelshoogte metavolcanics yet. This is a result of difficulties in dating these rocks (i.e., extreme alteration of the rocks, very low concentration of incompatible trace elements (e.g., Nd and Hf), and paucity of suitable dateable phases such as zircons). At this stage, it is therefore difficult to establish the temporal relationship between the Stolzburg Complex and the Nelshoogte metavolcanics with considerable certainty. However, since the intraformational komatiitic tuffs encountered in the Stolzburg Complex and other Barberton complexes are conformable with the magmatic units (sheeted sills), it may be suggested that the sediments were solid during the emplacement of the sills. This, in turn, suggests a considerable time-gap between the depositions of the tuffaceous layers and the emplacement of the sills. Consequently, it may be further suggested that the Al-depleted komatiitic tuffs represent Al-depleted magmas, which were emplaced earlier and followed later by the injection of the Al-undepleted to Al-enriched ultramafic-mafic magmas into the solidified tuffaceous sequence as discrete sills. The komatiitic tuffs were likely formed from the same magma that fed the predominant Al-depleted country rocks such as the Nelshoogte and Oorschot-Weltevreden metavolcanics.

In the Komati and Mendon formations of the Barberton Supergroup, magmatic units of different geochemical types are also interstratified. The lack of direct ages of these interlayered units of different geochemical types makes it impossible to decipher the temporal relations between them. The Komati Formation has been subdivided into two members: a lower member comprised of alternating komatiites and komatiitic basalt units, and an upper member constituted by a stack of pillowed and massive komatiitic basalt units. Since this sequence is generally regarded as a stack of lava flows, it is assumed that the interstratification between these magmatic units of different lithologies and compositions represent alternating periods of compositionally distinct volcanism. Conversely, Parman et al. (1997) proposed, based on a combination of field features and pyroxene geothermobarometry, that at least some of the units represent sills, which solidified at a minimum depth of 6 km. Dann (2000, 2001) and Dann and Grove (2007) highlighted the difficulty in distinguishing between sheet flows and sills. This further complicates the problem of trying to discern the temporal and petrogenetic relationship between the magmatic units in the formation as some of the units that were previously interpreted as flows may be sills. Ultramafic sheeted sill complexes have been identified in the Hooggenoeg and Kromberg formations (Dann and Grove, 2007; de Wit et al., 1987; Viljoen and Viljoen, 1969). One example is the Rosentuin ultramafic intrusion, dated at 3454 Ma (Rodel, 1993), which is hosted by the Hooggenoeg Formation. Geochemical data reported by Rodel (1993) indicate that this body is principally made up magmatic units of the Al-depleted geochemical type but capped by a peridotitic unit of the Al-undepleted geochemical type. Knowing the temporal relationship between these Al-depleted and Al-undepleted lithologies would shed light into the mechanism and setting of melting.

Dann and Grove (2007) also indicate the challenges of differentiating flows from sills in the Mendon Formation. The Mendon Formation is subdivided into several members, which are separated by silicified komatiitic and felsic tuff (now chert) layers. Some of the magmatic units in this formation have been interpreted as sills (Anhaeusser, 1985; Byerly, 1999; Viljoen and Viljoen, 1969). In this formation, there is notable lateral lithological variations and changes in thicknesses of magmatic units. In some cases, distinctive units are absent. These lateral lithological variations have been interpreted by some workers as an indication that the Mendon Formation was emplaced diachronously in multiple isolated sub-basins during rifting (Byerly, 1999; Lowe, 1999a; Lowe and Byerly, 2007; Thompson-Stiegler et al., 2010). In such a model, the lateral facies and thickness variations displayed by both the magmatic and tuffaceous units as well as the complete absence of

some distinctive units are interpreted to be a function of a distance from eruption centres. However, these features may simply be regarded as attributes of sill-sediment complexes, where sheeted sills invaded a sedimentary succession dominated by ultramafic tuffs. Since, as in the Pioneer and Saw Mill complexes, the Mendon Formation is characterized by cyclicity between magmatic units and ultramafic tuffs, it may also be accordingly regarded as a sheeted sill complex. Thus, a large part of the Mendon Formation may constitute sills, and not flows.

Age constraints on the Komati, Hooggenoeg, Kromberg and Mendon formations comes from the bounding and interlayered sedimentary units, and not direct dating of the magmatic units. The reliability of such methods is (in this case) questionable since it has been shown that at least some of the magmatic units previously interpreted as lavas may be sills. This means that the magmatic units, which represent sheeted sills are likely younger than the assigned ages. In addition to the challenges associated with dating Archaean greenstones, the lack of direct ages of these magmatic units is a result of the unrecognized importance of such information in deciphering the development of Archaean greenstone belts. Again, this stems from the assumption that magmatic sequences of Archaean greenstone belts are constituted by lavas, with an unimportant contribution from sheeted sills.

Since the Mendon and Weltevreden formations both underlie the Fig Tree Group, respectively, in the southern and northern domains of the Barberton greenstone belt, there have been attempts to correlate the two sequences (Lowe and Byerly, 1996, 1999). These are the uppermost sections of the Onverwacht Group in the southern and northern domains of the Barberton greenstone belt. Age constraints on the Mendon Formation come from the intercalated felsic tuffaceous units. Based on these dated sedimentary units, the Mendon Formation has been assigned an age ranging between 3298 Ma and 3259 Ma (Byerly et al., 1996). These ages have not yet been confirmed by direct dating of the magmatic units. The only available age of 3310 ± 150 Ma (Chauvel et al., 1987) has a very large error for it to be useful in narrowly constraining the true age of the formation. Since many of the magmatic units that make up the Mendon Formation may well be sills, this sequence may actually constitute a sheeted sills complex, where the magmatic units are younger than the intercalated sedimentary units.

The ages assigned to the Weltevreden Formation comes from direct dating of magmatic units of the Pioneer and Saw Mill complexes. The oldest age obtained in the area is a Sm-Nd isochron age

of 3286 ± 29 Ma determined from the Pioneer Complex (Lahaye et al., 1995). The lower limit of this age is in agreement with the dates obtained from other layered complexes situated in the northern limb of the Barberton greenstone belt. These includes Re-Os isochron ages of 3266 ± 8 Ma (Connolly et al., 2011) and 3263 Ma (Putchel et al., 2014), U-Pb zircon age of 3244 ± 11 Ma (Hofmann et al., 2021) from the Saw Mill Complex; U-Pb zircon age of 3247 ± 2 Ma and U-Pb titanite ages of 3252 ± 16 Ma and 3259 ± 6 Ma from the Stolzburg Complex (Bolhar et al., 2021); and a U-Pb zircon age of 3258 ± 8 Ma from the Mundt's Concession Complex (Hofmann et al., 2021). Because the description of the Weltevreden Formation is biased towards the layered ultramafic-mafic complexes situated in the Oorschot-Weltevreden Schist Belt (i.e., Pioneer and Saw Mill complexes), this succession is believed to be age-correlative only with the upper and presumably younger section of the Mendon Formation (with a minimum age of 3259 Ma; Byerly et al., 1996; Kröner et al., 1991); the lower portion of the Mendon Formation is believed to be older than the Weltevreden Formation (Byerly et al., 1996; Decker et al., 2015; Lowe and Byerly, 1999). There are no ages of the supracrustal rocks of the Onverwacht Group that host the layered ultramafic complexes in the northern domain of the Barberton greenstone belt. In contrast to the correlation presented by previous workers, it is therefore likely that the supracrustal rocks of the Mendon and Weltevreden formations are of the same age. Furthermore, the Weltevreden and Mendon Formation sheeted sills may have formed during the same magmatic event, probably between 3260 Ma and 3250 Ma.

10.9. Coupled origin of Archaean greenstone belts, sub-cratonic lithospheric mantle, and TTG suites

The origins of Archaean greenstone belts, sub-cratonic lithospheric mantle (SCLM) and TTG suites constitute one of the most vigorously debated topics in geology. These are amongst the most enigmatic aspects in geology. The very intimate association between these geological entities leaves little doubt that they may be genetically related. It is unlikely a mere coincidence that the ultradepleted cratonic roots occur beneath areas where high degree partial melts (i.e., komatiites) are found and that TTG plutons occur intimately with Archaean greenstone belts. Together, SCLM, TTG basement and Archaean greenstone belts characterizes cratons.

There are essentially two end-member models that attempt to explain the origins of these geological entities. A mantle plume model regards (1) Archaean greenstone belts as plume-derived melts (e.g., Chavagnac, 2004; Kamber, 2015; Robin-Popieul et al., 2012; Schneider et al., 2019; Sobolev et al., 2019; Van Kranendonk et al., 2015), (2) the TTG plutons as products of partial melting of the base of thick greenstone sequences (Kamber, 2015; Smithies, 2000; Van Kranendonk et al., 2007), (3) and the SCLM as the residual mantle material (left behind after melt extraction) of the superplume (Aulbach, 2011; Kamber, 2015). On the other end, (1) Archaean greenstone belts are thought to have been derived from hydrous melting of a mantle wedge in subduction zone environment (de Wit et al., 2018; Furnes et al., 2012; Parman et al., 2004), (2) the TTG melts are regarded as subducted slab partial melts (Drummond and Defant, 1990), (3) and the SCLM is considered to be accreted subducted oceanic slabs (Helmstaedt and Schulze, 1989; Parman et al., 2004; Stachel and Harris, 2008). To date, these aspects remains highly controversial.

As the model presented in this study for the origin of Archaean greenstone belts falls under neither of the two proposed end-member models, it becomes inevitable to propose alternative model(s) for the origin of the SCLM and TTG melts. In accordance to the meteorite impact-related origin for the Archaean greenstone belts, the SCLM is regarded as the residual mantle left behind after the extraction of high degree partial melts (Herzberg and Rudnick, 2012) during impact events. Correspondingly, the TTG melts are considered to be partial melts of the greenstones, where heat and high pressure were provided by the impact event. Grieve et al. (2006) suggested that some of the Hadean felsic material may have been formed during impact-reworking of mafic precursors. Following documentation of igneous differentiation of the Sudbury impact melt sheet, Latypov et al. (2019) indicated that evolution of Hadean impact melt sheets may have contributed to the formation of an evolved (felsic?) crust. In the present study, cratons are consequently interpreted as accreted regions of closely-spaced Archaean impact sites, which eventually developed into what they are today. The depleted and buoyant upper mantle beneath regions affected by large bolide impacts acted as a rafts, which promoted preservation of the impacted lithosphere (proto-cratons) through resisting subduction.

Evidence presented in support of the subduction and/ or plume models may be reconciled with the impact model proposed in this study. For example, the Archaean Wits diamonds, which display geochemical signatures consistent with the involvement of sedimentary material at the site of

diamond formation, have been regarded as an indication that surficial rocks were being recycled back into the mantle (at least down to a depth of 100 kms) through subduction processes as early as ~ 3.5 Ga (Smart et al., 2016). Since the cratonic roots (the main diamond formation sites in modern Earth (Shirey et al., 2004)) were not yet stable then (Shirey et al., 2004, 2013), these authors suggest that the Wits diamonds formed at an interface between the subducting slab and a mantle wedge. Accordingly, the Kaapvaal SCLM formation is ascribed to oceanic slabs stacking. In the context of the impact model proposed in this study, however, the Wits diamonds are regarded as shock-converted sedimentary carbonaceous material near the surface during an impact event. This interpretation eliminates the need to have subduction processes involved in the generation of the Wits diamonds. Correspondingly, the occurrence of the Wits diamonds may not necessarily be considered as evidence for the operation of subduction processes in the vicinity of the proto-Kaapvaal craton by 3.5 Ga. Another study by Tappe et al. (2011) report the apparent temporal coincidence between mantle eclogites, TTG plutons and SCLM in the North Atlantic Craton (NAC), Greenland, as an indication that these entities are products of subduction processes. Since partial melting of a mafic component in the garnet stability field has been shown to generate TTG melts leaving behind an eclogitic restite (Beard and Lofgren, 1991; Foley et al., 2002; Rapp and Watson, 1995), the reported temporal coincidence between these entities is not surprising. Because the geochemistry (Eu anomalies and non-mantle oxygen stable isotope signatures, respectively indicating the involvement of plagioclase and seawater interaction) of the mantle eclogites suggest a mafic oceanic crust protolith (Jacob, 2004), the eclogites are interpreted as residues of the crust after an extraction of the TTG melts from a subducting slab during the Archaean. However, the same mafic oceanic crust may undergo partial melting in the garnet stability field near the surface during a subsequent impact event. In the Barberton Granitoid-Greenstone Terrane, where two blocks are believed to have collided along the Inyoka-Saddleback Fault System (interpreted as a ~ 3.2 Ga suture zone) (de Ronde and de Wit, 1994; de Ronde and Kamo, 2000; de Wit et al., 1992, 2018; Kröner et al., 1996; Schoene et al., 2008), TTG plutons are situated behind the alleged subduction zone as opposed to the front as it should be expected if the melts were derived from a subducting slab.

The stacked oceanic slab model provides no explanation for the depleted nature of the SCLM. It is unlikely that the peridotitic section of the oceanic crust underwent high degree partial melting during subduction. It is also unlikely that the peridotites were depleted at Mid-Oceanic Ridge

(MOR) spreading centres as such settings cannot account for high pressure and high degree partial melting required for the generation of the Al-depleted komatiitic rocks commonly encountered in Archaean greenstone belts. This is further supported by the notable lack of ophiolitic sequences (which characterizes modern spreading centres-generated oceanic lithospheres) in Archaean greenstone belts. The notable rarity of depleted Archaean greenstones (Condie, 2005) suggests that the sources could not have been already depleted like the sources of modern N-MORBs during melting events. The depleted nature of the SCLM can be easily attributed to high degree partial melting of the upper mantle during impact events. Because highest degree partial melting occurred at the topmost mantle, such a model is in agreement with the reported correlation between increasing depth and decreasing degree of depletion (i.e., Mg#) in the SCLM (Pearson and Wittig, 2014) presented in support of the plume model. Like in the plume model, the impact-based model envisages an “in situ” development of the SCLM.

While TTG plutons are abundant in Archaean cratons, much of the complementary mantle eclogites appears to be missing from the geological record (Jacob, 2004; Schulze, 1989, 1995). It is generally thought that these entities, due to their high densities, may have been foundered and sank into the deeper parts of the mantle as far as the core-mantle boundary (Kamber, 2015; Percival and Pysklywe, 2007). While this suggestion is reasonable, most of these eclogitic components, if formed near the surface during impact events, may have been remelted completely by subsequent impacts. The resultant products would be high Mg and low silica (ultramafic?) melts which would solidify under low pressure conditions. The Al and HREE enriched, LREE depleted, and incompatible elements depleted Comondale komatiites may provide a suitable candidate (Hoffmann and Wilson, 2017; Wilson, 2003, 2019). In this framework, the first appearance of mantle eclogites after ~3 Ga, generally interpreted as the timing of widespread subduction processes (Shirey and Richardson, 2011), may actually correspond to a decline in impact events and thus better preservation.

11. Conclusions

- The Stolzberg Complex (SC) (and other layered bodies in the vicinity of the Barberton Greenstone Belt) represents a sheeted-sill complex, where each magmatic unit formed as a discrete sill, which invaded the early-formed supracrustal succession. The model presented

here contradicts earlier intrusive models that suggested that each complex grew through repetitive magma injection and differentiation in a single chamber.

- The stratigraphy of the Barberton greenstone sequence needs to be reviewed. Some of the units believed to be lava flows may actually be sills.
- The compositions of the Lower and Upper Divisions of the Stolzberg Complex are very similar, suggesting a co-magmatic origin.
- The geochemistry of the Stolzberg Complex is easily distinguishable from that of the surrounding Nelshoogte volcanic sequence, implying that these two entities are not co-magmatic. This finding also argues against an early model that regards the volcanic sequence as a product of magma differentiates that escaped from the Stolzberg Complex chamber.
- The mantle source to the SC magma was not metasomatised by mobile elements-enriched fluids or low degree melts prior to melting. The source appears to have been similar to the Primitive Mantle, except for the LREE enrichment pattern.
- The SC is shown (by, amongst other features, the low $(La/Yb)_{PM} \sim 1.47$ and high $Zr/Th \sim 135$) to be free of crustal contamination, suggesting development in an oceanic setting.
- Not even the two most popular settings for the origin of the Barberton greenstone belt (i.e., oceanic plateau and back-arc basin spreading centre) can satisfactorily explain the geological and geochemical aspects of the SC, implying that none of the modern geodynamic environments provides a suitable framework to explain its history and development.
- Consequently, the geodynamic setting of formation for the Stolzberg Complex remains difficult to be determined on the basis of PM-normalized and discrimination diagrams alone.
- The SC parental magma is proposed to have been generated through very high degree partial melting of an undepleted mantle source, where garnet was completely consumed. It is speculated that an unknown high pressure phase remained in the restite, consequently retaining Nb and Ta in the residual solid.
- The SC parental magma is proposed to have formed during a meteorite impact event. The magma is, therefore, considered to represent an impact melt. Other Archaean greenstones are also regarded as products of impact melts. Accordingly, the sub-cratonic lithospheric

mantle is interpreted as the residual mantle left behind after the extraction of high degree partial melts (i.e., ultramafic magmas) during impact events. Furthermore, the TTG melts are interpreted as partial melts of the greenstones, produced as a result of heating by the impacts. Archaean cratons are regarded as accreted blocks (regions) that experienced closely-spaced impacts.

12. References

- Allégre, C.J., 1968. Comportement des systèmes U-Th-Pb dans le manteau supérieur et modèle d'évolution de ce dernier au cours des temps géologiques. *Earth and Planetary Science Letters*, 5, 261-269.
- Allégre, C.A., 1982. Genesis of Archaean komatiites in a wet ultramafic subducted plate. In: Arndt, N.T. & Nisbet, E.G. (Eds.), *Komatiites*. G. Allen & Unwin, Lond. 495-500.
- Anhaeusser, C.R., 1969a. The stratigraphy, structure, and gold mineralization of the Jamestown and Sheba Hills areas of the Barberton Mountain Land. Unpub. Ph.D. thesis, Univ. Witwatersrand, Johannesburg, 332 pp.
- Anhaeusser, C.R., 1972. The geology of the Jamestown Hills area of the Barberton Mountain Land, South Africa. *Trans. geol. Soc. S. Afr.*, 75 (3): 225-263.
- Anhaeusser, C.R., 1973a. The evolution of the early Precambrian crust of Southern Africa. *Philos. Trans. R. Soc. Lond.* A273, 359–388.
- Anhaeusser, C.R., 1975. The geological evolution of the primitive earth: Evidence from the Barberton Mountain Land. University of the Witwatersrand, EGRU information Circular 98, 22p.
- Anhaeusser, C.R., 1976d. Archaean metallogeny in Southern Africa. *Econ. Geol.* 71, 16–43.
- Anhaeusser, C.R., 1977. Geological and Geochemical Investigations of the Roodekrans ultramafic complex and Surrounding Archaean Volcanic Rocks, Krugersdorp District. *Transactions Geological Society of South Africa* 80, 17–28.
- Anhaeusser, C.R., 1979. Rodingite occurrences in some Archaean ultramafic complexes in the Barberton Mountain Land, South Africa. *Precambrian Research* 8, 49–76.

- Anhaeusser, C.R., 1981. The geology and evolution of the Barberton Mountain Land. In: C.R. Anhaeusser (Editor), Barberton Excursion Guidebook--Archaean Geology of the Barberton Mountain Land. Geological Society of South Africa, Johannesburg, pp. 1- 21.
- Anhaeusser, C.R., 1984. Structural elements of Archaean granite-greenstone terranes as exemplified by the Barberton Mountain Land, Southern Africa. In: Kröner, A., Greiling, R. (Eds.), Precambrian Tectonics Illustrated. E. Schweizerbart'sche Verlagsbuchhandlung, Stuttgart, pp. 57–58.
- Anhaeusser, C.R., 1985. Archaean layered ultramafic complexes in the Barberton Mountain Land, South Africa. In: Ayres, L.D., Thurston, P.C., Card, K.D., Weber, W. (Eds.), Evolution of Supracrustal Sequences. Geological Association of Canada Special Paper 28, pp. 281–301.
- Anhaeusser, C. R., 1986. The geological setting of chrysotile asbestos occurrences in Southern Africa, 359-376. In: Anhaeusser, C. R. and Maske, S. (Editors), Mineral Deposits of Southern Africa, I. Geological Society of South Africa, 1020 pp.
- Anhaeusser, C.R., 1992a. Archaean granite-greenstone relationships on the farm Zandspruit 191-IQ, North Riding area, Johannesburg Dome. S. Afr. J. Geol. 94, 94–101.
- Anhaeusser, C.R., 2001. The anatomy of an extrusive-intrusive Archaean mafic-ultramafic sequence: the Nelshoogte Schist Belt and Stolzberg Layered Ultramafic Complex, Barberton greenstone belt, South Africa. S. Afr. J. Geol. 105, 167–204.
- Anhaeusser C.R., 2004. Palaeoarchaean to Mesoproterozoic (c. 3500-1000 Ma) ultramafic and mafic intrusions of the Kaapvaal Craton and neighbouring metamorphic belts: a review. Economic Geology Research Institute, University of the Witwatersrand, Information Circular 384, 63pp.
- Anhaeusser, C.R., 2006a. Mafic and ultramafic intrusions of the Kaapvaal Craton. In: Johnson, M.R., Anhaeusser, C.R., Thomas, R.J. (Eds.). The Geology of South Africa. Geological Society of South Africa, Johannesburg and Council for Geoscience, Pretoria, pp. 95–134.
- Anhaeusser, C.R., 2006b. A Re-evaluation of Archaean Intracratonic Terrane Boundaries on the Kaapvaal Craton, South Africa: Collisional Suture zones? Geological Society of America, Special Paper 405, 193–210.

- Anhaeusser, C.R., 2010. Magmatic and structural characteristics of the ca. 3440 Ma Theespruit Pluton, Barberton Mountain Land, South Africa. *American Journal of Science*, 310, 1136-1167.
- Anhaeusser, C.R., 2014. Archaean greenstone belts and associated granitic rocks – A review. *Journal of African Earth Sciences* 100, pp. 684–732.
- Anhaeusser, C.R., 2019. The geology and tectonic evolution of the northwest part of the Barberton Greenstone Belt, South Africa: A review. *South African Journal of Geology*; 122 (4): 421–454.
- Anhaeusser, C.R. and Robb, L.J., 1980. Regional and detailed field and geochemical studies of Archaean trondhjemitic gneisses, migmatites and greenstone xenoliths in the southern part of the Barberton Mountain Land, South Africa. *Precambrian Res.*, 11 (3/4): 373-397.
- Anhaeusser, C.R., Mason, R., Viljoen, M.J. and Viljoen, R.P., 1969. A reappraisal of some aspects of Precambrian shield geology. *Geol. Soc. Am. Bull.*, 80: 2175-2200.
- Anhaeusser, C. R., Robb, L. J. and Barton, J. M. Jr., 1983. Mineralogy, petrology and origin of the Boesmanskop syeno-granite complex, Barberton Mountain Land, South Africa. *Spec. Publ. Geol. Soc. S. Afr.*, 9, 169-183.
- Arndt, N. T., Naldrett, A. J. and Pyke, D. R., 1977. Komatiitic and iron-rich tholeiitic lavas of Munro Township, northeast Ontario. *Journal of Petrology*, 18(2), 319-369.
- Arndt, N.J., Albarede, F. and Nisbet, E.G., 1996. Mafic and ultramafic magmatism. In: De Wit, M.J. & Ashwal, L.D. (Eds.), *Greenstone Belts*. Oxford Univ. Press, Oxford, Chapter 3.2.
- Arndt, N.T., Kerr, A.C. and Tarney, J., 1997. Dynamic melting in plume heads: The formation of Gorgona komatiites and basalts. *Earth and Planetary Science Letters* 146, 289–301.
- Arndt, N.T., Leshner, C.M., Houlié, M.G., Lewin, E. and Lacaze, Y., 2004. Intrusion and crystallization of a spinifex-textured komatiite sill in Dundonald Township, Ontario. *Journal of Petrology* 45, 2555–2571.
- Arndt, N.T., Leshner, C.M. and Barnes, S.J., 2008. *Komatiite*. Cambridge University Press, 467 pp.

- Asafov, E.V., Sobolev, A.V., Gurenko, A.A., Arndt, N.T., Batanova, V.G., Portnyagin, M.V., Garbe-Schönberg, D. and Krasheninnikov, S.P., 2018. Belingwe komatiites (2.7 Ga) originate from a plume with moderate water content, as inferred from inclusions in olivine. *Chemical Geology*, 478, pp.39-59.
- Aulbach, S., Stachel, T., Heaman, L. M., Creaser, R. A., and Shirey, S. B., 2011. Formation of cratonic subcontinental lithospheric mantle and complementary komatiite from hybrid plume sources. *Contributions to Mineralogy and Petrology*, 161(6), 947-960.
- Barnes, S.J., Hill, R.E.T. and Gole, M.J., 1988. The Perseverance ultramafic complex, Western Australia: the product of a komatiite lava river. *J Petrol* 29:305–331.
- Bau, M., 1996. Controls on the fractionation of isovalent trace elements in magmatic and aqueous systems: evidence from Y/Ho, Zr/Hf, and lanthanide tetrad effect. *Contributions to Mineralogy and Petrology*, 123(3), pp.323-333.
- Beard, J.S., and Lofgren, G.E., 1991. Dehydration melting and water saturated melting of basaltic and andesitic greenstones and amphibolites at 1, 3 and 6.9 kb. *J. Petrol.* 32, 465–501.
- Bédard, J.H., 2006. A catalytic delamination-driven model for coupled genesis of Archaean crust and sub-continental lithospheric mantle. *Geochim. Cosmochim. Acta* 70, 1188–1214.
- Bédard, J.H., 2012. How many arcs can dance on the head of a plume? A ‘Comment’ on: a critical assessment of Neoproterozoic ‘plume only’ geodynamics: Evidence from the Superior province, by Derek Wyman, *Precambrian Research*, 2012. *Precamb Res.* 229, 189–197.
- Bédard, J.H., 2017. Stagnant lids and mantle overturns: Implications for Archaean tectonics, magmagenesis, crustal growth, mantle evolution, and the start of plate tectonics. *Geoscience Frontiers* 9, 19–49.
- Bédard, J.H., Harris, L. and Thurston, P., 2012. The hunting of the snArc. *Precambrian Research*, 229, 20-48.
- Berger, J.H, Diot, H., Lo, K., Ohnenstetter, D., Féménias, O., Pivin, M., Demaiffe, D., Bernard, A. and Charlier, B., 2013. Petrogenesis of Archaean PGM-bearing chromitites and associated ultramafic-mafic-anorthositic rocks from the Guelb el Azib layered complex (West African craton, Mauritania). *Precambrian Research* 224, 612–628.

- Bleeker, W., 2002. Archaean tectonics: a review, with illustrations from the Slave craton. Geological Society, London, Special Publications 199, 151–181.
- Blichert-Toft, J., Arndt, N.T., Wilson, A. and Coetzee, G., 2015. Hf and Nd isotope systematics of early Archaean komatiites from surface sampling and ICDP drilling in the Barberton Greenstone Belt, South Africa. *Am. Mineral.* 100, 2396–2411.
- Bohlen S.R. and Mezger K., 1989. Origin of granulite terranes and the formation of the lowermost continental crust. *Science* 244, 326–329.
- Bolhar, R., Woodhead, J.D. and Hergt, J.M., 2003. Continental setting inferred for emplacement of the 2.9-2.7 Ga Belingwe Greenstone Belt, Zimbabwe. *Geology* 31, 295–298.
- Bolhar, R., Hofmann, A., Kemp, A.I.S., Whitehouse, M.J., Wind, S. and Kamber, B.S., 2017. Juvenile crust formation in the Zimbabwe Craton deduced from the O-Hf isotopic record of 3.8–3.1 Ga detrital zircons. *Geochimica et Cosmochimica Acta* 215, 432–446.
- Bolhar, R., Tappe, S., Wilson, A. H., Ireland, T., Avila, J. and Anhaeusser, C., 2021. A petrochronology window into near-surface fluid/rock interaction within Archaean ultramafic-mafic crust: Insights from the 3.25 Ga Stolzberg Complex, Barberton Greenstone Belt. *Chemical Geology*, 120130.
- Bottke, W.F. and Norman, M.D., 2017. The late heavy bombardment: *Annual Review of Earth and Planetary Sciences*, v. 45, p. 619–647.
- Bottke, W.F., Vokrouhlický, D., Minton, D., Nesvorný, D., Morbidelli, A., Brasser, R., Simonson, B. and Levison, H.F., 2012, An Archaean heavy bombardment from a destabilized extension of the asteroid belt: *Nature*, v. 485, p. 78–81.
- Bougault, H., Joron, J.L. and Treuil, M., 1979. Alteration, fractional crystallization, partial melting, mantle properties from trace elements in basalts recovered in the North Atlantic. In 2nd Maurice Ewing Symposium (pp. 352-368). AGU.
- Bougault, H., Dmitriev, L., Schilling, J. G., Sobolev, A., Joron, J. L. and Needham, H. D., 1988. Mantle heterogeneity from trace elements: MAR triple junction near 14 N. *Earth and Planetary Science Letters*, 88(1-2), 27-36.
- Brandl, G., Cloete, M. and Anhaeusser, C.R., 2006. Archaean greenstone belts. In: Johnson, M.R., Anhaeusser, C.R., Thomas, R.J. (Eds.), *The Geology of South Africa*.

Geological Society of South Africa, Johannesburg and Council for Geoscience, Pretoria, pp. 5–9.

- Brown, M., 2015. Paleo- to Mesoproterozoic polymetamorphism in the Barberton Granite-Greenstone Belt, South Africa: Constraints from U-Pb monazite and Lu-Hf garnet geochronology on the tectonic processes that shaped the belt: Discussion. *Geological Society of America Bulletin*, 127, 1550–1557.
- Byerly, G.R., Kröner, A., Lowe, D.R., Todt, W. and Walsh, M.M., 1996. Prolonged magmatism and time constraints for sediment deposition in the early Archaean Barberton Greenstone Belt: Evidence from the upper Onverwacht and Fig Tree Groups. *Precambrian Research*, 78, 125-138.
- Capobianco, C. J. and Drake, M. J., 1990. Partitioning of ruthenium, rhodium, and palladium between spinel and silicate melt and implications for platinum group element fractionation trends. *Geochimica et Cosmochimica Acta*, 54(3), 869-874.
- Cawood, P.A., Hawkesworth, C.J., Pisarevsky, S.A., Dhuime, B., Capitanio, F.A. and Nebel, O., 2018. Geological archive of the onset of plate tectonics. In *Philosophical Transactions of the Royal Society A: Mathematical, Physical and Engineering Sciences*, (Royal Society Publishing), p.
- Chabangu, N., 2014. Nickel mineralization in the Jamestown ophiolite, Barberton greenstone belt, South Africa. Unpublished M.Sc. dissertation, Univ. of the Free State, Bloemfontein, South Africa.
- Chauvel, C., Arndt, N. T., Gruau, G. and Hofmann, A. W., 1987. Composition of the Archean mantle: evidence from Nd isotopes: *TERRA Cognita*, v. 7, p. 272.
- Chavagnac, V., 2004. A geochemical and Nd isotopic study of Barberton komatiites (South Africa): Implication for the Archean mantle. *Lithos* 75, 253–281.
- Cloete, T., 1991. Structure and metamorphism of the Komati Formation at Spinifex Stream and Hooggenoeg Formation in the Songimvelo Game Reserve, 123-133. In: Ashwal, L. D., (Editor), *Two Cratons and an Orogen –Excursion Guidebook and Review Articles for a Field Workshop through Selected Archaean Terranes of Swaziland, South Africa and Zimbabwe*. IGCP Project 280, Department of Geology, University of the Witwatersrand, Johannesburg, South Africa, 312 pp.

- Cloete, M., 1995. Komatiite volcanism: evidence for a 3.5 Ga oceanic plateau from the Barberton greenstone belt, South Africa. Abstr. XXI IUGG Gen. Meet. (IAVCEI Comm. Meet.), Boulder, Colorado, 1995, Vol. A, 464-467.
- Cloete, M., 1999. Aspects of volcanism and metamorphism of the Onverwacht Group lavas in the southwestern portion of the Barberton greenstone belt. *Memoir of the Geological Survey of South Africa*, 84, 232 pp.
- Condie, K.C., 1981. Archaean greenstone belts. *Developments in Precambrian Geology*, vol. 3. Elsevier, Amsterdam, 434 pp.
- Condie, K.C., 1981. Archaean greenstone belts. *Developments in Precambrian Geology*, vol. 3. Elsevier, Amsterdam, 434 pp.
- Condie, K.C., 2003. Incompatible element ratios in oceanic basalts and komatiites: tracking deep mantle sources and continental growth rates with time. *Geochem. Geophys. Geosyst.* 4 (1).
- Condie, K.C., 2005. High field strength element ratios in Archean basalts: a window to evolving sources of mantle plumes? *Lithos* 79, 491–504.
- Condie, K.C., 2015. Changing tectonic settings through time: indiscriminate use of geochemical discriminant diagrams. *Precambrian Research*, 266, pp. 587-591.
- Condie, K.C., 2018. A planet in transition: The onset of plate tectonics on Earth between 3 and 2 Ga? *Geoscience Frontiers* 9, 51–60.
- Condie, K.C., and Kröner, A. (2008). When did plate tectonics begin? Evidence from the geologic record. In *Special Paper 440: When Did Plate Tectonics Begin on Planet Earth?*, (Geological Society of America), pp. 281–294.
- Condie, K.C., Viljoen, M.J. and Kable, E.J.D., 1977. Effects of alteration on element distributions in archaean tholeiites from the Barberton greenstone belt, South Africa. *Contributions to Mineralogy and Petrology* 64, 75–89.
- Connolly, B.D., Puchtel, I.S., Walker, R.J., Arevalo, R.J., Piccoli, P.M., Byerly, G.R., Robin-Popieul, C. and Arndt, N.T., 2011. Highly siderophile element systematics of the 3.3 Ga Weltevreden komatiites, South Africa: implications for early Earth history. *Earth and Planetary Science Letters* 311, 253–263.
- Conway, G.P., 1997. The geology and geochemistry of the Sterkspruit intrusion, Barberton Mountain Land, Mpumalanga Province. M.Sc. thesis (unpubl.), Univ. Witwatersrand, Johannesburg, 164 pp.

- Cooper, M.R., 2008. Komatiitic flows of the Pioneer Ultramafic Complex of the 3.3GA Weltevreden Formation, Barberton Greenstone Belt, South Africa: stratigraphy, petrology, and geochemistry. Department of Geology and Geophysics Louisiana State University, Baton Rouge. Master's. 160p.
- Cooper, M.R., Byerly, G.R., Lowe, D.R. and Thompson, M.E., 2005. The Pioneer Ultramafic Complex of the Barberton Greenstone Belt, South Africa. *Eos Transactions AGU Fall Meeting Supplement* 86, 161.
- Corgne, A., Liebske, C., Wood, B. J., Rubie, D. C. and Frost, D. J., 2005. Silicate perovskite-melt partitioning of trace elements and geochemical signature of a deep perovskitic reservoir. *Geochimica et Cosmochimica Acta*, 69(2), 485-496.
- Cumming, G.L. and Richards, J.R., 1975. Ore lead isotope ratios in a continuously changing Earth. *Earth and Planetary Science Letters*, 28(2), 155-171.
- Cutts, K.A., Stevens, G., Hoffmann, J.E., Buick, I.S., Frei, D. and Münker, C., 2014. Paleo- to Mesoarchean polymetamorphism in the Barberton Granite-Greenstone Belt, South Africa: Constraints from U-Pb monazite and Lu-Hf garnet geochronology on the tectonic processes that shaped the belt. *Geological Society of America Bulletin*, 126, 251–270.
- Dann, J. C., 2000. The 3.5 Ga Komati Formation, Barberton greenstone belt, South Africa, Part I: new maps and magmatic architecture. *South African Journal of Geology*, 103, 47-68.
- De Ronde, C.E.J. and De Wit, M.J., 1994. Tectonic history of the Barberton greenstone belt, South Africa; 490 million years of Archaean crustal evolution. *Tectonics* 13, 983–1005.
- De Ronde, C. E. J. and Kamo, S. L., 2000. An Archaean arc-arc collisional event: A short-lived (ca 3 Myr) episode, Weltevreden area, Barberton greenstone belt, South Africa: *Journal of African Earth Sciences*, v. 30, p. 219–248,
- Deschamps, F., Godard, M., Guillot, S. and Hattori, K., 2013. Geochemistry of subduction zone serpentinites: A review. *Lithos* 178, 96–127.
- Devey, C.W. and Cox, K.G., 1987. Relationships between crustal contamination and crystallisation in continental flood basalt magmas with special reference to the Deccan Traps of the Western Ghats, India. *Earth and Planetary Science Letters* 84, 59–68.

- de Waal, S.A., 1978. The nickel deposit at Bon Accord, Barberton, South Africa: A proposed palcometeorite, in Mineralisation in Metamorphic Terraines, Spec. Publ. edited by W. J. Verwoerd, pp. 87-98, Geological Society of South Africa, Johannesburg.
- Dewey, J.F., 2003. Ophiolites and lost oceans: Rifts, ridges, arcs, and/or scrapings?. In Dilek, Y. and Newcomb, S., eds., Ophiolite concept and the evolution of geological thought: Geological Society of America Special Paper 373, p. 153–158.
- de Wit, M. J., 1982. Gliding and overthrust nappe tectonics in the Barberton greenstone belt: *Journal of Structural Geology*, v. 4, p. 117–136
- de Wit, M.J., 1991. Archaean greenstone belt tectonism and basin development: Some insights from the Barberton and Pietersburg greenstone belts, Kaapvaal Craton, South Africa: *Journal of African Earth Sciences*, v. 13, p. 45–63.
- de Wit, M.J., 2004. Archean greenstone belts do contain fragments of ophiolites. In: T.M. Kusky (Editor), *Precambrian Ophiolites and Related Rocks. Developments in Precambrian Geology* 13, 599-614.
- de Wit M.J. and Ashwal, L.D., 1986. Workshop on Tectonic Evolution of Greenstone Belts. Houston, Tex: The Institute, Print.
- de Wit, M.J. and Ashwal, L.D., 1995. Greenstone belts: what are they? *South African Journal of Geology*, Volume 98 Number 4, p. 505 - 520
- de Wit, M.J. and Ashwal, L.D., 1996. *Greenstone Belts. Oxford Monograph on Geology and Geophysics*, vol. 35. Oxford University Press.
- de Wit, M.J. and Tredoux, M., 1988. PGE in the 3.5 Ga Jamestown Ophiolite Complex, Barberton greenstone belt, with implications for PGE distribution in simatic lithosphere. In: Pritchard, H.M., Potts, P.J., Bowels, J.F.W. and Cribb, S.J. (Eds.), *Geoplat 1987*. Elsevier Applied Science, London, 319–342.
- de Wit, M. J., Fripp, R.E.P. and Stanistreet, I.G., 1983. Tectonic and stratigraphic implications of new field observations along the southern part of the Barberton greenstone belt: *Geological Society of South Africa Special Publication* 9, p. 21–29.
- de Wit, M.J., Hart, R.A. and Hart, R.J., 1987. The Jamestown ophiolite complex, Barberton Mountain Land: a section through 3.5 Ga oceanic crust. *J. Afr. Earth Sci.*, 6, 681–730.

- de Wit, M.J., Roering, C., Hart, R.J., Armstrong, R.A., de Ronde, C.E.J., Green, R.W.E., Tredoux, M., Peberdy, E. and Hart, R.A., 1992. Formation of an Archaean continent: *Nature*, v. 357, p. 553–562
- de Wit, M.J., Furnes, H. and Robins, B., 2011. Geology and tectonostratigraphy of the Onverwacht suite, Barberton Greenstone Belt, South Africa. *Precambrian Research* 186, 1-27.
- de Wit, M., Furnes, H., MacLennan, S., Doucouré, M., Schoene, B., Weckmann, U., Martinez, U. and Bowring, S., 2018. Paleoarchean bedrock lithologies across the Makhonjwa Mountains of South Africa and Swaziland linked to geochemical, magnetic and tectonic data reveal early plate tectonic genes flanking subduction margins. *Geoscience Frontiers* 9, 603–665.
- Diener, J.F.A., Stevens, G., Kisters, A.F.M. and Poujol, M., 2005. Metamorphism and exhumation of the basal parts of the Barberton greenstone belt, South Africa: constraining the rates of Mesoarchean tectonism. *Precamb. Res.* 143, 87–112.
- Dixon, J.E., Leist, L., Langmuir, C. and Schilling, J.G., 2002. Recycled dehydrated lithosphere observed in plume-influenced mid-ocean-ridge basalt. *Nature* 420 (6914), 385–389.
- Donaldson, M.J., Leshner, C.M., Groves, D.I. and Gresham, J.J., 1986. Comparison of Archean dunites and komatiites associated with nickel mineralisation in Western Australia: Implications for dunite genesis. *Mineralium Deposita*, 21(4), pp.296-305.
- Elliott, T., Plank, T., Zindler, A., White, W. and Bourdon, B., 1997. Element transport from slab to volcanic front at the Mariana arc. *Journal of Geophysical Research: Solid Earth* 102, 14991–15019.
- Elkins-Tanton, L.T. and Hager, B.H., 2005. Giant meteoroid impacts can cause volcanism: *Earth and Planetary Science Letters*, v. 239, p. 219–232,
- Elkins-Tanton, L.T.E., Van Orman, J.A., Hager, B.H. and Grove, T.L., 2002. Re-examination of the lunar magma ocean cumulate overturn hypothesis: melting or mixing is required. *Earth and Planetary Science Letters*, 196(3-4), 239-249.
- Elkins-Tanton, L.T., Hager, B.H. and Grove, T.L., 2004. Magmatic effects of the late lunar heavy bombardment: *Earth and Planetary Science Letters*, v. 222, p. 17–27,

- Ficq, G., Tappe, S., Bolhar, R., Wilson, A. and Harris, C., 2018. Age and origin of the ultramafic-mafic Stolzberg Complex in the Barberton Greenstone Belt, South Africa. University of Johannesburg, Department of Geology, Bi-Annual Report for the PPM Research Centre, p. 28-29.
- Fitton, J.G. and Godard, M., 2004. Origin and evolution of magmas on the Ontong Java Plateau. In: Fitton, J.G., Mahoney, J.J., Wallace, P.J. and Saunders, A.D., (eds.) Origin and Evolution of the Ontong Java Plateau, Geological Society Special Publication 229, pp. 151–178. London: Geological Society of London.
- Fitton, J.G., Saunders, A.D., Norry, M.J., Hardarson, B.S. and Taylor, R.N., 1997. Thermal and chemical structure of the Iceland plume. *Earth and Planetary Science Letters*, 153(3-4), pp.197-208.
- Fitton, J.G., Saunders, A.D., Kempton, P.D. and Hardarson, B.S., 2003. Does depleted mantle form an intrinsic part of the Iceland plume? *Geochem. Geophys. Geosyst.* 4 (3).
- Foley, S., Tiepolo, M. and Vannucci, R., 2002. Growth of early continental crust controlled by melting of amphibolite in subduction zones. *Nature* 417, 837– 840.
- François, C., Philippot, P., Rey, P. and Rubatto, D., 2014. Burial and exhumation during Archaean sagduction in the East Pilbara granite-greenstone terrane. *Earth and Planetary Science Letters*, volume 396, 235-251p.
- Frey, H., 1977. Origin of the Earth's ocean basins. *Icarus* 32, 235–250.
- Frey, H., 1980. Crustal evolution of the early Earth: the role of major impacts. *Precambrian Res.* 10, 195–216.
- Furnes, H., De Wit, M., Staudigel, H., Rosing, M. and Muehlenbachs, K., 2007. A vestige of earth's oldest ophiolite. *Science* 315, 1704–1707.
- Furnes, H., de Wit, M., Robins, B. and Sandstå, N.R., 2011. Volcanic evolution of the upper Onverwacht suite, Barberton Greenstone Belt, South Africa. *Precambrian Research* 186, 28-50.
- Furnes, H., Robins, B. and de Wit, M.J., 2012. Geochemistry and petrology of lavas in the upper Onverwacht suite, Barberton mountain land, South Africa. *South African Journal of Geology* 115 (2), 171-210.

- Furnes, H., de Wit, M.J. and Robins, B., 2013. A review of new interpretations of the tectonostratigraphy, geochemistry and evolution of the Onverwacht Suite, Barberton Greenstone Belt, South Africa. *Gondwana Research* 23, 403-428.
- Gerya, T., 2014. Precambrian geodynamics: Concepts and models. *Gondwana Research*, 25(2), 442-463.
- Gill, J.B., 1976. Composition and age of Lau Basin and Ridge volcanic rocks: implications for evolution of an interarc basin and remnant arc. *Bull. geol. Soc. Am.* 87, 1384-95.
- Glikson, A.Y., 1976. Early Precambrian mafic-ultramafic volcanic rocks: ancient oceanic crust or relic terrestrial maria? *Geology* 4: 201-205.
- Glikson, A.Y., 1999. Oceanic mega-impacts and crustal evolution: *Geology*, v. 27, p. 387–390.
- Glikson, A.Y., 2003. Comment on "Extraterrestrial influences on mantle plume activity" by DH Abbott and AE Isley-[*Earth Planet. Sci. Lett.* 205 (2002) 53-62]. *Earth and Planetary Science Letters*, 3(215), 425-427.
- Glikson, A.Y., 2014. *The Archaean: Geological and Geochemical Windows into the Early Earth*. Cham; New York: Springer.
- Grant, J.A., 1986. The isocon diagram – a simple solution to Gresens' equation of metasomatic alteration. *Economic Geology*, 81, 1976-1982.
- Grant, J.A., 2005. Isocon analysis: A brief review of the method and applications. *Physics and Chemistry of the Earth*, 30, 997-1004.
- Green, D.H., 1972. Archaean greenstone belts may include terrestrial equivalents of lunar maria? *Earth Planet. Sci. Lett.* 15, 263–270.
- Green, D.H. 1975. Genesis of Archean peridotitic magmas and constraints on Archean geothermal gradients and tectonics. *Geology*, 3(1), 15-18.
- Green, D.H., 1981. Petrogenesis of Archaean ultramafic magmas and implications for Archaean tectonics, in: A. Kroner (Ed.), *Precambrian Plate Tectonics*, Elsevier, Amsterdam, pp. 469-489.
- Green, T.H., 1995. Significance of Nb/Ta as an indicator of geochemical processes in the crust-mantle system. *Chemical geology*, 120(3-4), 347-359.

- Grieve, R.A., Cintala, M.J., Therriault, A.M., Reimold, W.U. and Gibson, R.L., 2006. Large-scale impacts and the evolution of the Earth's crust: The early years. *Special papers-geological society of America*, 405, p.23.
- Grieve, R.A., Ames, D.E., Morgan, J.V. and Artemieva, N., 2010. The evolution of the Onaping Formation at the Sudbury impact structure. *Meteorit. Planet. Sci.* 45, 759–782.
- Griffin, W.L., Sturt, B.A., O'Neill, C.J., Kirkland, C.L. and O'Reilly, S.Y., 2013. Intrusion and contamination of high-temperature dunitic magma: the Nordre Bumandsfjord pluton, Seiland, Arctic Norway, *Contrib. Mineral. Petrol.*, 165, 903–930.
- Grove, T.L., De Wit, M.J., Dann, J.C., 1996. Komatiites from the Komati type section, Barberton South Africa. In: De Wit, M.J., Ashwal, L.D. (Eds.), *Greenstone Belts*, vol. 1. Clarendon Press, Oxford, pp. 438–453.
- Gruau, G., Chauvel, C., Arndt, N.T. and Cornichet, J. 1990. Aluminum depletion in komatiites and garnet fractionation in the early Archean mantle: Hafnium isotopic constraints. *Geochimica et Cosmochimica Acta* 54, 3095–3101.
- Gruau, G., Tourpin, S., Fourcade, S. and Blais, S., 1992. Loss of isotopic (Nd, O) and chemical (REE) memory during metamorphism of komatiites: new evidence from eastern Finland. *Contrib. Mineral. Petrol.*, 112: 66-82.
- Guice, G.L., McDonald, I., Hughes, H.S.R. and Anhaeusser, C. R., 2019. An evaluation of element mobility in the Modderfontein ultramafic complex, Johannesburg: Origin as an Archaean ophiolite fragment or greenstone belt remnant? *Lithos*, 332–333, 99–119.
- Gurenko, A.A., Kamenetsky, V.S. and Kerr, A.C., 2016. Oxygen isotopes and volatile contents of the Gorgona komatiites, Colombia: a confirmation of the deep mantle origin of H₂O. *Earth and Planetary Science Letters*, 454, pp.154-165.
- Hamilton, W.B., 1998. Archean magmatism and deformation were not products of plate tectonics. *Precambrian Research*, 91, 143-179.
- Hamilton, W.B., 2003. An alternative earth: *GSA Today*, v. 13, no. 11, p. 4–12.
- Hansen, V.L., 2015. Impact origin of Archaean cratons. *Lithosphere* 7, 563–578.
- Harris, L.B. and Bédard, J.H., 2014. Crustal evolution and deformation in a non-plate-tectonic Archaean Earth: comparisons with Venus. In *Evolution of Archaean crust and early life* (pp. 215-291). Springer, Dordrecht.

- Harrison, T.M., Schmitt, A.K., McCulloch, M.T. and Lovera, O.M., 2008. Early (≥ 4.5 Ga) formation of terrestrial crust: Lu–Hf, $\delta^{18}\text{O}$, and Ti thermometry results for Hadean zircons.
- Hart, S.R., 1971. K, Rb, Cs, Sr and Ba contents and Sr isotope ratios of ocean floor basalts. *Philosophical Transactions of the Royal Society of London. Series A, Mathematical and Physical Sciences*, 268(1192), 573-587.
- Hastie, A.R., Fitton, J.G., Bromiley, G.D., Butler, I.B. and Odling, N.W.A., 2016. The origin of Earth's first continents and the onset of plate tectonics. *Geology* 44, 855–858.
- Helmstaedt, H. and Schulze, D.J., 1989. Southern African kimberlites and their mantle sample: implications for Archean tectonics and lithosphere evolution. *Kimberlites and related rocks*, 1, 358-368.
- Herzberg, C., 1992. Depth and degree of melting of komatiites. *Journal of Geophysical Research* 97, 4521–4540.
- Herzberg, C. and Rudnick, R., 2012. Formation of cratonic lithosphere: An integrated thermal and petrological model. *Lithos*, 149, pp.4-15.
- Hess, H.H., 1933. The problem of serpentinization and the origin of certain chrysotile asbestos, talc, and soapstone deposits. *Economic Geology*, 28(7):634-657.
- Heubeck, C. and Lowe, D.R., 1994. Late syndepositional deformation and detachment tectonics in the Barberton Greenstone Belt, South Africa. *Tectonics*, 13, 1514-1536.
- Heubeck, C., Engelhardt, J., Byerly, G.R., Zeh, A., Sell, B., Lubert, T. and Lowe, D.R., 2013. Timing of deposition and deformation of the Moodies Group (Barberton Greenstone Belt, South Africa): Very-high-resolution of Archaean surface processes. *Precambrian Research*, 231, 236-262.
- Hickman, A. H. and Van Kranendonk, M., 2012. Early Earth evolution: Evidence from the 3.5-1.8 Ga geological history of the Pilbara region of Western Australia. *Episodes*, 35(1), 283-297.
- Hill, R.E.T., Gole, M.J. and Barnes, S.J., 1989. Olivine adcumulates in the Norseman-Wiluna greenstone belt, Western Australia: implications of the volcanology of komatiites. In *Magmatic sulphides field conference, Zimbabwe*. 5 (pp. 189-206).
- Hoffmann, J.E. and Wilson, A.H., 2017. The origin of highly radiogenic Hf isotope compositions in 3.33 Ga Comondale komatiite lavas (South Africa). *Chemical Geology* 455, 6–21.

- Hofmann, A.W., 1988. Chemical differentiation of the Earth: the relationship between mantle, continental crust, and oceanic crust. *Earth and Planetary Science Letters* 90, 297–314.
- Hofmann, A. and Bolhar, R., 2007. Carbonaceous cherts in the Barberton Greenstone belt and their significance for the study of early life in the Archean record: *Astrobiology*, v. 7, p. 355–388.
- Hofmann, A. and Harris, C., 2008. Silica alteration zones in the Barberton greenstone belt: A window into subseafloor processes 3.5-3.3 Ga ago. *Chemical Geology* 257, 221–239.
- Hofmann, A., Reimold, W.U., Koeberl, C. and Gibson, R.L., 2006. Archean spherule layers in the Barberton Greenstone Belt, South Africa: A discussion of problems related to the impact interpretation. *Special papers-geological society of America*, 405, p.33.
- Hofmann, A., Anhaeusser, C.R. and Li, X.H., 2021. Layered ultramafic complexes of the Barberton Greenstone Belt—age constraints and tectonic implications. *South African Journal of Geology*.
- Huber, M.S. and Byerly, G.R., 2018. Volcanological and petrogenetic characteristics of komatiites of the 3.3 ga saw mill complex, weltevreden formation, Barberton greenstone belt, South Africa. *South African Journal of Geology* 121, 463–486.
- Jacob, D.E., 2004. Nature and origin of eclogite xenoliths from kimberlites: *Lithos*, v. 77, p. 295–316.
- Jochum, K.P., Seufert, H.M., Spettel, B. and Palme, H., 1986. The solar-system abundances of Nb, Ta, and Y, and the relative abundances of refractory lithophile elements in differentiated planetary bodies. *Geochimica et Cosmochimica Acta*, 50(6), 1173-1183.
- Jochum, K.P., Arndt, N.T. and Hofmann, A.W., 1991. Nb-Th-La in komatiites and basalts: constraints on komatiite petrogenesis and mantle evolution. *Earth and Planetary Science Letters* 107, 272–289.
- Johnson, T.E., Brown, M., Kaus, B.J.P. and Vantongeren, J.A., 2014. Delamination and recycling of Archaean crust caused by gravitational instabilities. *Nature Geoscience* 7, 47–52.
- Johnson, T.E., Brown, M., Goodenough, K.M., Clark, C., Kinny, P.D. and White, R.W., 2016. Subduction or sagduction? Ambiguity in constraining the origin of ultramafic-mafic bodies in the Archaean crust of NW Scotland. *Precambrian Res.* 283, 89–105.

- Jolly, W.T., 1977. Relations between Archean lavas and intrusive bodies of the Abitibi greenstone belt, Ontario-Quebec. *Geol. Assoc. Can. Spec. Pap.* 16, 311– 340.
- Jones, A.P., 2014. Impact volcanism and mass extinctions. *Geological Society of America Special Papers*, 505, 369-381.
- Jones, A.P., Price, G.D., Price, N.J., DeCarli, P.S. and Clegg, R.A., 2002. Impact induced melting and the development of large igneous provinces: *Earth and Planetary Science Letters*, v. 202, p. 551–561,
- Jones, A.P., Price, G., DeCarli, P.S., Price, N. and Clegg, R., 2003. Impact decompression melting: A possible trigger for impact induced volcanism and mantle hotspots, in Koeberl, C., and Martínez Ruiz, F., eds., *Impact Markers in the Stratigraphic Record*: Berlin, Springer, p. 91–120.
- Kamber, B.S., 2015. The evolving nature of terrestrial crust from the Hadean, through the Archaean, into the Proterozoic. *Precambrian Research* 258, 48–82.
- Kamo, S.L. and Davis, D.W., 1994. Reassessment of Archean crustal development in the Barberton Mountain Land, South Africa, based on U-Pb dating: *Tectonics*, v. 13, p. 167–192.
- Kareem, K.M., 2005. Komatiites of the Weltevreden Formation, Barberton Greenstone Belt, South Africa: implications for the chemistry and temperature of the Archean mantle. Department of Geology and Geophysics, Louisiana State University, Baton Rouge, LA. Doctor of Philosophy. 227p.
- Kareem, K.M. and Byerly, G.R., 2003. Petrology and geochemistry of 3.3 Ga komatiites; Weltevreden Formation, Barberton Greenstone Belt. *Abstracts of Papers Submitted to the Lunar and Planetary Science Conference* 34.
- Kato, T., Ringwood, A. E. and Irifune, T., 1988. Experimental determination of element partitioning between silicate perovskites, garnets and liquids: Constraints on early differentiation of the mantle. *Earth Planet. Sci. Lett.* 89, 123-145.
- Kato, T., Ohtani, E., Ito, Y. and Onuma, K., 1996. Element partitioning between silicate perovskites and calcic ultrabasic melt. *Physics of the Earth and Planetary Interiors*, 96(2-3), 201-207.
- Kay, R., Hubbard, N.J. and Gast, P.W., 1970. Chemical characteristics and origin of oceanic ridge volcanic rocks¹. *Journal of Geophysical Research*, 75(8), 1585-1613.

- Kerr, A.C., Marriner, G.F., Arndt, N.T., Tarney, J., Nivia, A., Saunders, A.D. and Duncan, R., 1996a. The petrogenesis of komatiites, picrites and basalts from the Isle of Gorgona, Colombia; new field, petrographic and geochemical constraints. *Lithos* 37, 245–260.
- Kerr, A.C., Tarney, J., Marriner, G.F., Nivia, A., Saunders, A.D. and Klaver, G.T., 1996b. The geochemistry and tectonic setting of late Cretaceous Caribbean and Colombian volcanism. *J. South Am. Earth Sci.* 9, 111–120.
- Kerr, A.C., White, R.V. and Saunders, A.D., 2000. LIP reading: Recognizing oceanic plateau in the geological record. *Journal of Petrology* 41: 1041–1056.
- Kerr, A.C., White, R.V., Thompson, P.M., Tarney, J. and Saunders, A.D., 2003. No oceanic plateau—no Caribbean plate? The seminal role of an oceanic plateau in Caribbean plate evolution.
- Kisters, A.F.M. and Anhaeusser, C.R., 1995a. Emplacement features of Archaean TTG plutons along the southern margin of the Barberton greenstone belt, South Africa: *Precambrian Research*, v. 75, p. 1–15.
- Kisters, A.F.M. and Anhaeusser, C.R., 1995b. The structural significance of the Steynsdorp pluton and anticline within the tectonomagmatic framework of the Barberton Mountain Land, South Africa: *South African Journal of Geology*, v. 98, p. 43–51.
- Kisters, A.F.M., Stevens, G., Dziggel, A. and Armstrong, R.A., 2003. Extensional detachment faulting and core-complex formation in the southern Barberton granite-greenstone terrain, South Africa: Evidence for a 3.2 Ga orogenic collapse. *Precambrian Research*, 127, 355–378.
- Kisters, A.F.M., Belcher, R.W., Poujol, M. and Dziggel, A., 2010. Continental growth and convergence-related arc plutonism in the Mesoarchaean: Evidence from the Barberton granitoid-greenstone terrain, South Africa. *Precambrian Research*, 178, 15–26.
- Klemme, S., Prowatke, S., Hametner, K. and Günther, D., 2005. Partitioning of trace elements between rutile and silicate melts: implications for subduction zones. *Geochimica et Cosmochimica Acta*, 69(9), 2361–2371.
- Koike, M., Sano, Y., Takahata, N., Iizuka, T., Ono, H. and Mikouchi, T., 2020. Evidence for early asteroidal collisions prior to 4.15 Ga from basaltic eucrite phosphate U–Pb chronology. *Earth and Planetary Science Letters*, 549, p.116497.

- Kröner, A. and Compston, W., 1988. Ion microprobe ages of zircons from early Archaean granite pebbles and greywacke, Barberton Greenstone Belt, southern Africa. *Precambrian Research*, 38, 367-380.
- Kröner, A., Hegner, E., Wendt, J.I., Byerly, G.R., 1996. The oldest part of the Barberton granitoid-greenstone terrane, South Africa: evidence for crust formation between 3.5 and 3.7 Ga. *Precamb. Res.* 78, 105–124.
- Kröner, A., Hoffmann, J.E., Xie, H., Wu, F., Münker, C., Hegner, E., Wong, J., Wan, Y. and Liu, D., 2013. Generation of early Archaean felsic greenstone volcanic rocks through crustal melting in the Kaapvaal Craton, Southern Africa. *Earth Planet. Sci. Lett.* 381, 188–197.
- Kröner, A., Anhaeusser, C.R., Hoffmann, J.E., Wong, J., Geng, H., Hegner, E., Xie, H., Yang, J. and Liu, D., 2016. Chronology of the oldest supracrustal sequences in the Palaeoarchaean Barberton Greenstone Belt, South Africa and Swaziland. *Precambrian Res.* 279, 123–143.
- La Flèche, M.R., Camire, G., Jenner, G.A., 1998. Geochemistry of post-Acadian, Carboniferous continental intraplate basalts from the Maritimes Basin, Magdalen islands, Quebec, Canada. *Chem. Geol.* 148, 115–136.
- Lahaye, Y., Arndt, N., Byerly, G., Chauvel, C., Fourcade, S. and Gruau, G., 1995. The influence of alteration on the trace-element and Nd isotopic compositions of komatiites. *Chemical Geology* 126, 43–64.
- Latypov, R., Chistyakova, S., Grieve, R. and Huhma, H., 2019. Evidence for igneous differentiation in Sudbury Igneous Complex and impact-driven evolution of terrestrial planet proto-crusts. *Nature communications*, 10(1), pp.1-13.
- Laurent, O., Martin, H., Moyen, J-F. and Doucelance, R., 2014. The diversity and evolution of late-Archaean granitoids: Evidence for the onset of “modern-style” plate tectonics between 3.0 and 2.5 Ga. *Lithos* 205, 208–235.
- Li, C., Arndt, N.T., Tang, Q.Y. and Ripley, E.M., 2015. Trace element indiscriminate diagrams: *Lithos*, v. 232, p. 76–83.
- Lowe, D.R., 1991. Geology of the Barberton Greenstone belt: an overview. In: Ashwal, L. D. (Editor), *Two Cratons and an Orogen –Excursion Guidebook and Review Articles for a Field Workshop through Selected Archaean Terranes of Swaziland, South Africa and*

Zimbabwe. IGCP Project 280, Department of Geology, University of the Witwatersrand, Johannesburg, South Africa, 280, 47-58.

- Lowe, D.R., 1994. Accretionary history of the Archean Barberton Greenstone Belt (3.55-3.22 Ga), Southern Africa. *Geology*, 22, 1099-1102.
- Lowe, D.R., 1999. Geologic evolution of the Barberton Greenstone Belt and vicinity. In: D.R. Lowe and G.R. Byerly (Editors), *Geologic Evolution of the Barberton Greenstone Belt*, South Africa. Geological Society of America Special Paper, 329, 287-312.
- Lowe, D.R., 2013. Crustal fracturing and chert dike formation triggered by large meteorite impacts, ca. 3.260 Ga, Barberton greenstone belt, South Africa. *Geol. Soc. Am. Bull.* 125, 894–912.
- Lowe, D.R. and Byerly, G.R., 1986. Early Archean silicate spherules of probable impact origin, South Africa and Western Australia. *Geology* 14, 83–86.
- Lowe, D.R. and Byerly, G.R., 1999. Stratigraphy of the west-central part of the Barberton Greenstone Belt, South Africa, in Lowe, D.R., and Byerly, *Archean spherule layers in the Barberton Greenstone Belt* 55 G.R., eds., *Geologic Evolution of the Barberton Greenstone Belt*, South Africa: Geological Society of America Special Paper 329, p. 1–36.
- Lowe, D.R. and Byerly, G.R., 2007. An overview of the geology of the Barberton Greenstone Belt and vicinity: Implications for early crustal development. In: M.J. Van Kranendonk, R.H. Smithies and V.C. Bennett (Editors), *Earth's Oldest Rocks*, 1st Edition, *Developments in Precambrian Geology*, Elsevier, 15, 481-526.
- Lowe, D.R. and Byerly, G.R., 2018. The terrestrial record of late heavy bombardment. *New Astronomy Reviews*, 81, 39-61.
- Lowe, D.R., Byerly, G.R., Asaro, F. and Kyte, F.T., 1989. Geological and geochemical record of 3 400-million-year-old terrestrial meteorite impacts: *Science*, v. 245, p. 959–962.
- Lowe, D.R., Byerly, G.R., Kyte, F.T., Shukolyukov, A., Asaro, F. and Krull, A., 2003. Spherule beds 3.47–3.24 billion years old in the Barberton Greenstone Belt, South Africa: A record of large meteorite impacts and their influence on early crustal and biological evolution: *Astrobiology*, v. 3, p. 7–47.
- Lowe, D.R., Byerly, G.R. and Kyte, F.T., 2014. Recently discovered 3.42–3.23 Ga impact layers, Barberton Belt, South Africa: 3.8 Ga detrital zircons, Archean impact history, and tectonic implications. *Geology* 42, 747–750.

- MacLennan, S.A., 2012. Structural, Geophysical and Geochemical Characterisation of a Mesoarchean Paleosuture Zone, Barberton Greenstone Belt, South Africa. Unpublished Thesis. University of Cape Town, 224 pp.
- Mahoney, J.J., 1987. An isotopic survey of Pacific oceanic plateaus: Implications for their nature and origin, in Keating, B.H., Fryer, P., Batiza, R., and Boehlert, G.W., eds., *Seamounts, islands and atolls: American Geophysical Union Monograph 43*, p. 207-220.
- Manhès, G., Allègre, C. J., Dupré, B. and Hamelin, B., 1979. Lead-lead systematics, the “age of the Earth” and the chemical evolution of our planet in a new representation space. *Earth and Planetary Science Letters*, 44(1), 91-104.
- Marchi, S., Bottke, W.F., Elkins-Tanton, L.T., Bierhaus, M., Wuennemann, K., Morbidelli, A. and Kring, D.A., 2014. Widespread mixing and burial of Earth's Hadean crust by asteroid impacts. *Nature* 511, 578–582.
- McCall, G.J.H., 2003. A critique of the analogy between Archaean and Phanerozoic tectonics based on regional mapping of the Mesozoic-Cenozoic plate convergent zone in the Makran, Iran. In *Precambrian Research*, (Elsevier B.V.), pp. 5–17.
- McCuaig, T.C., Kerrich, R. and Xie, Q., 1994. Phosphorus and high field strength element anomalies in Archean high-magnesian magmas as possible indicators of source mineralogy and depth. *Earth Planet. Sci. Lett.* 124, 221–239.
- Menell, R.P., Brewer, T.H., Delve, J.R. and Anhaeusser, C.R., 1981. The Kalkkloof chrysotile asbestos deposit and surrounding area, Barberton Mountain Land. In: Anhaeusser, C.R. and Maske, S. (Eds.), *Mineral Deposits of Southern Africa*, Vol. I. Geol. Soc. S. Afr., 427–435.
- Michael, P.J., 1995. Regionally distinctive sources of depleted MORB - evidence from trace-elements and H₂O. *Earth and Planetary Science Letters* 131 (3-4), 301– 320.
- Minnitt, R.C.A. and Anhaeusser, C.R., 1992. Gravitational and diapiric structural history of the eastern portion of the Archaean Murchison greenstone belt, South Africa: *Journal of African Earth Sciences*, v. 15, p. 429–440.
- Morbidelli, A., Nesvorný, D., Laurenz, V., Marchi, S., Rubie, D.C., Elkins-Tanton, L., Wieczorek, M. and Jacobson, S., 2017. The timeline of the lunar bombardment: Revisited: *Icarus*, v. 305, p. 262– 276.

- Moyer, J-F., Stevens, G., Kisters, A.F.M. and Belcher, R.W., 2006. Record of mid-Archean subduction from metamorphism in the Barberton terrain, South Africa. *Nature* 443, 559-562.
- Mukherjee, R., Latypov, R. and Balakrishna, A., 2017. An intrusive origin of some UG-1 chromitite layers in the Bushveld Igneous Complex, South Africa: Insights from field relationships. *Ore Geology Reviews* 90, 94–109.
- Mungall, J.E., Kamo, S.L. and McQuade, S., 2016. U-Pb geochronology documents out-of-sequence emplacement of ultramafic layers in the Bushveld Igneous Complex of South Africa. *Nature Communications*.
- Nagasawa, H., Schreiber, H.D. and Morris, R.V., 1980. Experimental mineral/liquid partition coefficients of the rare earth elements (REE), Sc and Sr for perovskite, spinel and melilite. *Earth and Planetary Science Letters*, 46(3), 431-437.
- Naldrett, A.J. and Turner, A.R., 1977. The geology and petrogenesis of a greenstone belt and related nickel sulphide mineralisation at Yakabindie, Western Australia. *Precambrian Research*.
- Namur, O., Abily, B., Boudreau, A.E., Blanchette, F., Bush, J.W., Ceuleneer, G., Charlier, B., Donaldson, C.H., Duchesne, J.C., Higgins, M.D. and Morata, D., 2015. Igneous layering in basaltic magma chambers. In *Layered intrusions* (pp. 75-152). Springer, Dordrecht.
- Nédélec, A., Chevrel, M.O., Moyer, J-F., Ganne, J. and Fabre, S., 2012. TTGs in the making: Natural evidence from Inyoni shear zone (Barberton, South Africa). *Lithos*, 153, 25–38.
- Nesvorný, D., Roig, F. and Bottke, W.F., 2017. Modeling the historical flux of planetary impactors: *The Astronomical Journal*, v. 153, 103.
- Neukum, G., Ivanov, B.A. and Hartmann, W.K., 2001. Cratering records in the inner solar system in relation to the lunar reference system. *Chronology and evolution of Mars*, pp.55-86.
- Newton, R.C. and Perkins D., 1982. Thermodynamic calibration of geobarometers based on the assemblages garnet-plagioclase-orthopyroxene (clinopyroxene)-quartz. *American Mineralogist*; 67 (3-4): 203–222.

- Nisbet, E.G., Cheadle, M.J., Arndt, N.J. and Bickle, M.J., 1993. Constraining the potential temperature of the Archaean mantle: a review of the evidence from komatiites. *Lithos* 30, 291–307.
- Niu, Y., 2004. Bulk-rock major and trace element compositions of abyssal peridotites: implications for mantle melting, melt extraction and post-melting processes beneath mid-ocean ridges. *Journal of Petrology*, 45(12), 2423–2458.
- Nutmann, A.P., Friend, C.R.L. and Bennett, V.C., 2002. Evidence for 3650–3600 Ma assembly of the northern end of the Itsaq Gneiss Complex, Greenland: Implication for early Archaean tectonics. *Tectonics* 21, 5-1-5–28.
- O’Neil, J., 2014. Ujaraaluk Unit (Nuvvuagittuq greenstone belt). In *Encyclopedia of Scientific Dating Methods*, (Springer Netherlands), pp. 1–2.
- O’Neill, C., Lenardic, A., Moresi, L., Torsvik, T.H. and Lee, C.T.A., 2007. Episodic Precambrian subduction. *Earth and Planetary Science Letters* 262, 552–562.
- O’Neill, C., Debaille, V. and Griffin, W., 2013. Deep Earth recycling in the Hadean and constraints on surface tectonics. *American Journal of Science* 313, 912–932.
- O’Neill, C., Lenardic, A., Weller, M., Moresi, L., Quenette, S. and Zhang, S., 2016. A window for plate tectonics in terrestrial planet evolution? *Physics of the Earth and Planetary Interiors*, 255, 80–92.
- Osinski, G.R., Grieve, R.A., Hill, P.J., Simpson, S.L., Cockell, C., Christeson, G.L., Ebert, M., Gulick, S., Melosh, H.J., Riller, U. and Tikoo, S.M., 2020. Explosive interaction of impact melt and seawater following the Chicxulub impact event. *Geology*, 48(2), pp.108–112.
- Palme, H. and O’Neill, H., 2014. Cosmochemical Estimates of Mantle Composition. In *Treatise on Geochemistry: Second Edition*, (Elsevier Inc.), pp. 1–39.
- Park, R.G. and Tarney, J., 1987. The Lewisian complex: a typical Precambrian high-gradeterrain? In: Park, R.G., Tarney, J. (Eds.), *Evolution of the Lewisian and Comparable Precambrian High Grade Terrains*. The Geological Society, pp. 13–25.
- Parman, S.W., Dann, J.C., Grove, T.L. and De Wit, M.J., 1997. Emplacement conditions of komatiite magmas from the 3.49 Ga Komati Formation, Barberton greenstone belt, South Africa. *Earth Planet. Sci. Lett.* 150, 303–323.

- Parman, S.W., Grove, T.L., Dann, J.C. and De Wit, M.J., 2004. A subduction origin for komatiites and cratonic lithospheric mantle. *South African Journal of Geology*, 107(1-2), pp.107-118.
- Pearce, J.A., 1983. Role of sub-continental lithosphere in magma genesis at active continental margins. In: HAWKESWORTH, C. J. & NURRY, M. J. (eds) *Continental Basalts and Mantle Xenoliths*, 230-49. Shiva Publishing, Nantwich.
- Pearce, J.A., 2008. Geochemical fingerprinting of oceanic basalts with applications to ophiolite classification and the search for Archean oceanic crust. *Lithos* 100, 14–48.
- Pearce, J.A., 2014. Immobile element fingerprinting of ophiolites. *Elements* 10, 101- 108.
- Pearce, J.A. and Cann, J.R., 1971. Ophiolite origin investigated by discriminant analysis using Ti, Zr and Y. *Earth and Planetary Science Letters* 12: 339-349
- Pearce, J.A. and Cann, J.R., 1973. Tectonic setting of basic volcanic rocks determined using trace element analyses. *Earth and Planetary Science Letters* 19, 290–300.
- Pearce, J. A. and Peate, D.W., 1995. Tectonic implications of the composition of volcanic arc magmas. *Annual Review of Earth and Planetary Sciences* 23, 251–285.
- Pearson, D.G. and Wittig, N., 2014. The formation and evolution of cratonic mantle lithosphere - evidence from mantle xenoliths. In *Treatise on Geochemistry*, ed. KK Turekian, HD Holland, pp. 255–92. New York: Elsevier. 2nd ed.
- Percival, J.A. and Pysklywe, A., 2007. Are Archean lithospheric keels inverted? *Earth and Planetary Science Letters* 254: 393–403.
- Polat, A. and Hofmann, A.W., 2003. Alteration and geochemical patterns in the 3.7-3.8 Ga Isua greenstone belt, West Greenland. In *Precambrian Research*, (Elsevier B.V.), pp. 197–218.
- Polat, A., Appel, P.W.U., Fryer, B., Windley, B., Frei, R., Samson, I.M. and Huang, H., 2009. Trace element systematics of the Neoproterozoic Fiskensæset anorthosite complex and associated meta-volcanic rocks, SW Greenland: Evidence for a magmatic arc origin. *Precambrian Research* 175, 87–115.
- Polat, A., Fryer, B.J., Samson, I.M., Weisener, C., Appel, P.W.U., Frei, R. and Windley, B.F., 2011. Geochemistry of ultramafic rocks and hornblende veins in the Fiskensæset layered anorthosite complex, SW Greenland: Evidence for hydrous upper mantle in the Archaean. *Precambrian Research* 214–215, 124–153.

- Puchtel, I.S., Blichert-Toft, J., Touboul, M., Walker, R.J., Byerly, G.R., Nisbet, E.G. and Anhaeusser, C.R., 2013. Insights into early Earth from Barberton komatiites: evidence from lithophile isotope and trace element systematics. *Geochim. Cosmochim. Acta* 108, 63–90.
- Ransom, B., Byerly, G. and Lowe, D., 1999. Subaqueous to subaerial Archean ultramafic phreatomagmatic volcanism, Kromberg Formation, Barberton Greenstone Belt, South Africa. In: Lowe, D.R. & Byerly, G.R. (eds) *Geologic Evolution of the Barberton Greenstone Belt, South Africa*. Geological Society of America, Special Papers 329, 151-166.
- Rapp, R.P. and Watson, E.B., 1995. Dehydration Melting of Metabasalt at 8–32 kbar: Implications for Continental Growth and Crust-Mantle Recycling. *Journal of Petrology*. 36 (4): 891–931.
- Reimink, J.R., Chacko, T., Carlson, R.W., Shirey, S.B., Liu, J., Stern, R.A., Bauer, A.M., Pearson, D.G. and Heaman, L.M., 2018. Petrogenesis and tectonics of the Acasta Gneiss Complex derived from integrated petrology and ¹⁴²Nd and ¹⁸²W extinct nuclide-geochemistry. *Earth and planetary science letters*, 494, pp.12-22.
- Révillon, S., Hallot, E., Arndt, N.T., Chauvel, C. and Duncan, R.A., 2000. A complex history for the Caribbean Plateau: petrology, geochemistry and geochronology of the Béata Ridge, South Hispaniola. *J. Geol.* 108, 641–661.
- Roberts, J.H. and Barnouin, O.S., 2012. The effect of the Caloris impact on the mantle dynamics and volcanism of Mercury. *Journal of Geophysical Research: Planets*, 117(E2).
- Robin-Popieul, C.C.M., Arndt, N.T., Chauvel, C., Byerly, G.R., Sobolev, A.V. and Wilson, A., 2012. A new model for Barberton komatiites: deep critical melting with high melt retention. *J. Petrol.* 53, 2191–2229.
- Robb, L.J., 1977. The geology and geochemistry of the Archaean granite-greenstone terrane between Nelspruit and Bushbuckridge, Eastern Transvaal. M.Sc. thesis (unpubl.), Univ. Witwatersrand, Johannesburg, 190 pp.
- Rodel, J.E., 1993. The petrography and geochemistry of the Stolzburg and Rosentuin layered ultramafic complexes, Barberton Mountain Land, eastern Transvaal. M.Sc. thesis (unpubl.), Univ. Witwatersrand, Johannesburg, 232 pp.

- Rollinson, H.R.1., 1993. Using geochemical data: evaluation, presentation, interpretation. Harlow, Essex, England: New York: Longman Scientific & Technical.
- Rudnick, R.L., 1992. Xenoliths—samples of the lower continental crust. In *Continental Lower Crust* (eds. D. M. Fountain, R. Arculus, and R. W. Kay), pp. 269–316. Elsevier.
- Rudnick, R.L. and Presper, T., 1990. Geochemistry of intermediate- to high-pressure granulites. In *Granulites and Crustal Evolution* (eds. D. Vielzeuf and P. Vidal), pp. 523–550. Kluwer.
- Rudnick, R.L. and Gao, S., 2014. Composition of the Continental Crust. In *Treatise on Geochemistry: Second Edition*, (Elsevier Inc.), pp. 1–51.
- Sanchez-Garrido, C., Stevens, G., Armstrong, R.A., Moyen, J-F., Martin, H. and Doucelance, R., 2011. Diversity in Earth’s early felsic crust: Paleoproterozoic peraluminous granites of the Barberton Greenstone Belt. *Geology*, 39, 963-966.
- Saccani, E., 2015. A new method of discriminating different types of post-Archean ophiolitic basalts and their tectonic significance using Th-Nb and Ce-Dy-Yb systematics *Geoscience Frontiers*, 6, pp. 481-501.
- Saunders, A.D. and Tarney, J., 1979. The geochemistry of basalts from a back-arc spreading centre in the East Scotia Sea. *Geochimica et Cosmochimica Acta*, 43(4), 555-572.
- Saunders, A.D. and Tarney, J., 1984. Geochemical characteristics of basaltic volcanism within back-arc basins. *Geological Society, London, Special Publications*, 16(1), 59-76.
- Saunders, A. D., Norry, M. J. and Tarney, J., 1988. Origin of MORB and chemically-depleted mantle reservoirs: trace element constraints. *Journal of Petrology*, (1), 415-445.
- Schmidt, K., Bau, M., Hein, J.R. and Koschinsky, A., 2014. Fractionation of the geochemical twins Zr–Hf and Nb–Ta during scavenging from seawater by hydrogenetic ferromanganese crusts. *Geochimica et Cosmochimica Acta*, 140, pp.468-487.
- Schneider, K.P., Hoffmann, J.E., Münker, C., Patyniak, M., Sprung, P., Roerdink, D., Garbe-Schönberg, D. and Kröner, A., 2019. Petrogenetic evolution of metabasalts and metakomatiites of the lower Onverwacht Group, Barberton Greenstone Belt (South Africa). *Chemical Geology*, 511, pp.152-177.

- Schoene, B., De Wit, M.J. and Bowring, S.A., 2008. Mesoarchean assembly and stabilization of the eastern Kaapvaal Craton: A structural thermochronological perspective. *Tectonics*, 27, 1-27.
- Schulze, D.J., 1989. Constraints on the abundance of eclogite in the upper mantle. *Journal of Geophysical Research: Solid Earth*, 94(B4), pp.4205-4212.
- Schulze, D.J., 1995. Low-Ca garnet harzburgites from Kimberley, South Africa: Abundance and bearing on the structure and evolution of the lithosphere. *Journal of Geophysical Research: Solid Earth*, 100(B7), pp.12513-12526.
- Şengör, A.M.C. and Natal'in, B.A., 2004. Phanerozoic analogues of Archaean oceanic basement fragments: Altaid ophiolites and ophiirags. *Developments in Precambrian Geology*, 13, pp.675-726.
- Shirey, S.B. and Richardson, S.H., 2011. Start of the Wilson Cycle at 3 Ga shown by diamonds from subcontinental mantle: *Science*, v. 333, p. 434-436.
- Shirey, S.B., Richardson, S.H. and Harris, J.W., 2004. Integrated models of diamond formation and craton evolution. *Lithos* 77, 923-944.
- Shirey, S.B., Cartigny, P., Frost, D.J., Keshav, S., Nestola, F., Nimis, P., Pearson, D.G., Sobolev, N.V. and Walter, M.J., 2013. Diamonds and the geology of mantle carbon. *Reviews in Mineralogy and Geochemistry*, 75(1), pp.355-421.
- Smart, K.A., Tappe, S., Stern, R.A., Webb, S.J. and Ashwal, L.D., 2016. Early Archaean tectonics and mantle redox recorded in Witwatersrand diamonds. *Nature Geoscience* 9, 255–259.
- Smith, J.V. and Mason, B., 1970. Pyroxene-garnet transformation in Coorara meteorite. *Science*, 168(3933), 832-833.
- Smithies, R.H., 2000. The Archaean tonalite–trondhjemite–granodiorite (TTG) series is not an analogue of Cenozoic adakite. *Earth and Planetary Science Letters*, 182(1), 115-125.
- Smithies, R.H., Ivanic, T.J., Lowrey, J.R., Morris, P.A., Barnes, S.J., Wyche, S. and Lu, Y.J., 2018. Two distinct origins for Archaean greenstone belts. *Earth and Planetary Science Letters*, 487, 106–116.

- Sobolev, A.V., Asafov, E.V., Gurenko, A.A., Arndt, N.T., Batanova, V.G., Portnyagin, M.V., Garbe-Schönberg, D. and Krashennnikov, S.P., 2016. Komatiites reveal a hydrous Archaean deep-mantle reservoir. *Nature*, 531(7596), pp.628-632.
- Sobolev, A.V., Asafov, E.V., Gurenko, A.A., Arndt, N.T., Batanova, V.G., Portnyagin, M.V., Garbe-Schönberg, D., Wilson, A.H. and Byerly, G.R., 2019. Deep hydrous mantle reservoir provides evidence for crustal recycling before 3.3 billion years ago. *Nature* 571, 555–559.
- Sotiriou, P., Polat, A. and Frei, R., 2019. Petrogenesis and geodynamic setting of the Neoproterozoic Haines Gabbroic Complex and Shebandowan greenstone belt, southwestern Superior Province, Ontario, Canada. *Lithos* 324–325, 1–19.
- Stachel, T. and Harris, J.W., 2008. The origin of cratonic diamonds—constraints from mineral inclusions. *Ore Geology Reviews*, 34(1-2), 5-32.
- Stern, R.J., 2005. Evidence from ophiolites, blueschists, and ultrahigh-pressure metamorphic terranes that the modern episode of subduction tectonics began in Neoproterozoic time. *Geology* 33, 557–560.
- Stern, R.J., Gerya, T. and Tackley, P.J., 2017. Stagnant lid tectonics: Perspectives from silicate planets, dwarf planets, large moons, and large asteroids. *Geoscience Frontiers* 9, 103–119.
- Stevens, G., Droop, G.T.R., Armstrong, R.A. and Anhaeusser, C.R., 2002. Amphibolite facies metamorphism in the Schapenburg schist belt: a record of the midcrustal response to 3.23 Ga terrane accretion in the Barberton greenstone belt. *S. Afr. J. Geol.* 105, 271–284.
- Stevens, G. and Moyens, J-F., 2007. Metamorphism in the Barberton granite greenstone terrain: A record of Palaeoarchaeon accretion. In: M.J. Van Kranendonk, R.H. Smithies and V.C. Bennett (Editors), *Earth's Oldest Rocks*, 1st Edition, *Developments in Precambrian Geology*, Elsevier, 15, 669-698.
- Storey, M., Mahoney, J.J., Kroenke, L.W. and Saunders, A.D., 1991. Are oceanic plateaus sites of komatiite formation? *Geology* 19, 376–379.
- Sturt, B.A., Speedyman, D.L. and Griffin, W.L., 1980. The Nordre Bumandsfjord Ultramafic Pluton, Seiland, North Norway. Part 1: Field relations, *Nor. Geol. Undersøkelse Bull.*, 358, 1–30.

- Sun, S.S. and McDonough, W.F., 1989. Chemical and isotopic systematics of oceanic basalts: Implications for mantle composition and processes. *Geological Society Special Publication* 42, 313–345.
- Sun, S.S., Nesbitt, R.W. and Sharaskin, A.Y., 1979. Geochemical characteristics of mid-ocean ridge basalts. *Earth and Planetary Science Letters*, 44(1), 119-138.
- Szilas, K., Van Hinsberg, V.J., Creaser, R.A. and Kisters, A.F., 2014. The geochemical composition of serpentinites in the Mesoarchaeon Tartoq Group, SW Greenland: Harzburgitic cumulates or melt-modified mantle?. *Lithos*, 198, 103-116.
- Szilas, K., van Hinsberg, V., McDonald, I., Næraa, T., Rollinson, H., Adetunji, J. and Bird, D., 2017. Highly refractory Archaean peridotite cumulates: Petrology and geochemistry of the Seqi Ultramafic Complex, SW Greenland. *Geoscience Frontiers* 9, 689–714.
- Tappe, S., Kjarsgaard, B.A., Kurszlaukis, S., Nowell, G.M. and Phillips, D., Petrology and Nd-Hf isotope geochemistry of the Neoproterozoic Amon Kimberlite Sills, Baffin Island (Canada): evidence for deep mantle magmatic activity linked to supercontinent cycles. *J. Petrol.* 55, 2003-2042 (2014).
- Tarney, J., Wood, D.A., Saunders, A.D., Cann, J.R. and Varet, J., 1980. Nature of mantle heterogeneity in the North Atlantic: evidence from deep sea drilling. *Philosophical Transactions of the Royal Society of London. Series A, Mathematical and Physical Sciences*, 297(1431), 179-202.
- Tatsumoto, M., 1978. Isotopic composition of lead in oceanic basalt and its implication to mantle evolution. *Earth and Planetary Science Letters*, 38(1), 63-87.
- Taura, H., Yurimoto, H., Kato, T. and Sueno, S., 2001. Trace element partitioning between silicate perovskites and ultracalcic melt. *Physics of the Earth and Planetary Interiors*, 124(1-2), 25-32.
- Thompson-Stiegler, M.T., Lowe, D.R. and Byerly, G.R., 2008. Abundant pyroclastic komatiitic volcanism in the 3.5 to 3.2 Ga Barberton Greenstone Belt, South Africa. *Geology* 36, 779-782.
- Thompson-Stiegler, M.T., Lowe, D.R. and Byerly, G.R., 2011. Fragmentation and dispersal of komatiitic pyroclasts in the 3.5 to 3.2 Ga Onverwacht Group, Barberton Greenstone Belt, South Africa. *Geological Society of America Bulletin* 123, 1112-1126.

- Thompson-Stiegler, M.T., Cooper, M., Byerly, G.R. and Lowe, D.R., 2012. Geochemistry and petrology of komatiites of the Pioneer Ultramafic Complex of the 3.3 Ga Weltevreden Formation, Barberton greenstone belt, South Africa, *Precambrian Research* 212, 1-12.
- Tomkinson, M.J. and King, V.J., 1991. The tectonics of the Barberton Greenstone Belt: An overview. In: L.D. Ashwal (Editor), *Two Cratons and an Orogen – excursion guide and review articles*. Department of Geology, University of the Witwatersrand, Johannesburg, South Africa, IGCP Project 280, 69-83.
- Toulkeridis, T., Peucker-Ehrenbrink, B., Clauer, N., Kröner, A., Schidlowski, M. and Todt, W., 2010. Pb-Pb age, stable isotope and chemical composition of Archaean magnesite, Barberton Greenstone Belt, South Africa. *Journal of the Geological Society* 167, 943–952.
- Tredoux, M., De Wit, M.J., Hart, R.J., Armstrong, R.A., Lindsay, N.M. and Sellschop, J.P.F., 1989. Platinum group elements in a 3.5 Ga nickel-iron occurrence: possible evidence of a deep mantle origin. *Journal of Geophysical Research* 94, 795–813.
- Turner, S., Rushmer, T., Reagan, M. and Moyon, J-F., 2014. Heading Down Early On; Start of Subduction on Earth." *Geology (boulder)*. 42.2 (2014): 139-142. Print.
- Ubide, T., Guyett, P.C., Kenny, G.G., O'Sullivan, E.M., Ames, D.E., Petrus, J.A., Riggs, N. and Kamber, B.S., 2017. Protracted volcanism after large impacts: Evidence from the Sudbury impact basin. *Journal of Geophysical Research: Planets*, 122(4), pp.701-728.
- Valley, J.W., Peck, W.H., King, E.M. and Wilde, S.A., 2002. A cool early Earth. *Geology*, 30(4), pp.351-354.
- Van Biljon, W., 1964. The chrysotile deposits of the Eastern Transvaal and Swaziland. In Haughton, S., editor, *The geology of some ore deposits in Southern Africa*, pages 625{669}. Geological Society of South Africa.
- van Hunen, J. and van den Berg, A.P., 2007. Plate tectonics on the early Earth: Limitations imposed by strength and buoyancy of subducted lithosphere. *Lithos* 103, 217–235.
- Van Kranendonk, M.J., 2007. Chapter 8.6 Tectonics of Early Earth. *Developments in Precambrian Geology* 15, 1105–1116.
- Van Kranendonk, M.J., 2011. Cool greenstone drips and the role of partial convective overturn in Barberton greenstone belt evolution. *Journal of African Earth Sciences*, 60(5), 346-352.

- Van Kranendonk, M.J., 2021. Gliding and overthrust nappe tectonics of the Barberton Greenstone Belt revisited: A review of deformation styles and processes. *South African Journal of Geology*, 124 (1): 181–210.
- Van Kranendonk, M.J., Collins, W.J., Hickman, A. and Pawley, M.J., 2004. Critical tests of vertical vs. horizontal tectonic models for the Archaean East Pilbara Granite-Greenstone Terrane, Pilbara Craton, Western Australia. In *Precambrian Research*, pp. 173–211.
- Van Kranendonk, M. J., Hugh Smithies, R., Hickman, A. H. and Champion, D. C., 2007. Secular tectonic evolution of Archean continental crust: interplay between horizontal and vertical processes in the formation of the Pilbara Craton, Australia. *Terra Nova*, 19(1), 1-38.
- Van Kranendonk, M.J., Kröner, A., Hegner, E. and Connelly, J., 2008. Age, lithology and structural evolution of the c. 3.53 Ga Theespruit Formation in the Tjakastad area, southwestern Barberton greenstone belt, South Africa, with implications for Archaean tectonics. *Chem. Geol.* 261, 114–138.
- Van Kranendonk, M.J., Kröner, A., Hoffmann, J.E., Nagel, T. and Anhaeusser, C.R., 2014. Just another drip: re-analysis of a proposed Mesoarchaean suture from the Barberton Mountain Land, South Africa. *Precamb. Res.* (accepted – moderate revision required).
- Van Kranendonk, M.J., Smithies, R.H., Griffin, W.L., Huston, D.L., Hickman, A.H., Champion, D.C., Anhaeusser, C.R. and Pirajno, F., 2015. Making it thick: a volcanic plateau origin of Palaeoarchaean continental lithosphere of the Pilbara and Kaapvaal cratons. *Geological Society, London, Special Publications* 389, 83–111.
- Vaughan, W.M., Head, J.W., Wilson, L. and Hess, P.C., 2013. Geology and petrology of enormous volumes of impact melt on the Moon: A case study of the Orientale basin impact melt sea. *Icarus*, 223(2), pp.749-765.
- Viljoen, M.J., 1969a. An introduction to the geology of the Barberton granite-greenstone terrain. *Spec. Publ. Geol. Soc. S. Afr.*, 2, pp.9-28.
- Viljoen, R.P. and Viljoen, M.J., 1970. The geology and geochemistry of the layered ultramafic bodies of the Kaapmuiden area, Barberton Mountain Land. *Geological Society of South Africa, Special Publication*, 1, pp.661-688.
- Visser, D.J.L., 1956. The geology of the Barberton area. *Geological Survey, Special publication*, (15).

- Voordouw, R., Gutzmer, J. and Beukes, N.J., 2009. Intrusive origin for Upper Group (UG1, UG2) stratiform chromitite seams in the Dwars River area, Bushveld Complex, South Africa. *Mineralogy and Petrology* 97, 75–94.
- Wager, L.R. and Brown G.M., 1968. *Layered Igneous Rocks*. Edinburgh Oliver & Boyd pg. 588
- Wang, H., Yang, J.H., Kröner, A., Zhu, Y.S. and Li, R., 2019. Non-subduction origin for 3.2 Ga high-pressure metamorphic rocks in the Barberton granitoid-greenstone terrane, South Africa. *Terra Nova* 31, 373–380.
- Weaver, B.L., 1991. The origin of ocean island basalt end-member compositions: trace element and isotopic constraints *Earth Planet. Sci. Lett.*, 104, pp. 381-397
- White, W.M., 2013. *Geochemistry*. Hoboken, NJ : John Wiley & Sons Inc.,
- Wiemer, D., Schrank, C.E., Murphy, D.T. and Hickman, A.H., 2016. Lithostratigraphy and structure of the early Archaean Doolena Gap greenstone belt, East Pilbara Terrane, Western Australia. *Precambrian Research* 282, 121–138.
- Wiemer, D., Schrank, C.E., Murphy, D.T., Wenham, L. and Allen, C.M., 2018. Earth's oldest stable crust in the Pilbara Craton formed by cyclic gravitational overturns. *Nature Geoscience* 11, 357–361.
- Williams, D.A.C. and Hallberg, J.A., 1973. Archaean layered intrusions of the Eastern Goldfields Region, Western Australia. *Contrib. Miner. Petrol.* 38, 45–70.
- Wilson, A.H., 2003. A new class of silica enriched, highly depleted komatiites in the southern Kaapvaal Craton, South Africa. In *Precambrian Research*, (Elsevier B.V.), pp. 125–141.
- Wilson, A.H., 2019. The Late-Paleoarchean Ultra-Depleted Comondale Komatiites: Earth's Hottest Lavas and Consequences for Eruption. *Journal of Petrology*, 60(8), pp.1575-1620.
- Windley, B.F. and Bridgwater, D., 1971. The evolution of Archaean low- and high-grade terrains. In: Glover, J.E. (Ed.), *Symposium on Archaean Rocks*. Geological Society of Australia Special Publication 3, pp. 33–46.
- Wuth, M., 1980. The geology and mineralization potential of the Oorschot-Weltevreden schist belt southwest of Barberton – eastern Transvaal. M.Sc. thesis (unpubl.), Univ. Witwatersrand, Johannesburg, 185 pp.

- Wyman, D.A., 2013. A critical assessment of Neoproterozoic “plume only” geodynamics: evidence from the Superior Province. *Precambrian Research* 229, 3-19.
- Wyman, D.A., 2017. Do cratons preserve evidence of stagnant lid tectonics? *Geoscience Frontiers* 9, 3–17.
- Xie, Q. and Kerrich, R., 1994. Silicate–perovskite and majorite signature komatiites from the Archean Abitibi greenstone belt; implications for early mantle differentiation and stratification. *J. Geophys. Res.* 99, 15799–15812.
- Xie, Q., Kerrich, R. and Fan, J., 1993. HFSE/REE fractionations recorded in three komatiite-basalt sequences, Archean Abitibi greenstone belt: implications for multiple plume sources and depths. *Geochim. Cosmochim. Acta*, 57:4111-4118.
- Zeh, A., Gerdes, A. and Heubeck, C., 2013. U-Pb and Hf isotope data of detrital zircons from the Barberton Greenstone Belt: Constraints on provenance and Archean crustal evolution. *Journal of the Geological Society*, 170, 215-223.
- Zhang, A., Wang, Y., Fan, W., Zhang, Y. and Yang, J., 2012. Earliest Neoproterozoic (ca. 1.0 Ga) arc–back-arc basin nature along the northern Yunkai Domain of the Cathaysia Block: geochronological and geochemical evidence from the metabasite. *Precambrian Res.* 220, 217–233.

13. Appendices

Table A1: *Modal abundances (%) of primary mineralogy of rocks of the Stolzberg Complex.*

Name	DH78	DN8B	DN8A	NF11	NF17	NF18	NF23	NF24	NF26	SM1	DN4	NF5	NF9
Plagioclase	10	12	12	12	8	10	13	4	11	9	10	9	11
Clinopyroxene	6	2	1	2	0	3	3	0	3	1	8	0	10
Orthopyroxene	30	39	41	39	42	31	37	46	45	28	33	42	32
Olivine	53	46	45	48	50	56	47	48	41	61	48	48	47
Name	GV13	GV14	NF10	DH17	DH83	DH80	GV6	GV12	NF12	NF13	HD2	NF22	
Plagioclase	30	45	46	35	20	22	33	62	36	42	50	45	
Clinopyroxene	39	25	23	15	46	44	34	20	17	17	47	22	
Orthopyroxene	27	25	28	45	33	32	30	11	44	30	0	30	
Olivine	3	0	3	0	0	0	0	6	0	0	0	2	
Name	SB5	DH34	DH61	DH67	DN10	SB6	DH3	DH07	DH8	SS9	SS12		
Plagioclase	4	4	5	7	9	5	6	5	6	3	3		
Clinopyroxene	8	3	4	7	6	5	12	9	6	3	3		
Orthopyroxene	88	92	90	84	81	88	80	84	85	92	93		
Olivine	0	0	0	0	0	0	1	2	0	0	0		
Name	GV1	DH36	NF6	NF20	SM2	SM4	DH65	NF3	SM6				
Plagioclase	0	0	0	0	1	1	0	1					
Clinopyroxene	0	0	0	0	0	0	0	0					
Orthopyroxene	15	10	20	15	10	12	5	20					
Olivine	85	90	80	85	90	88	95	80					
Name	DN6	NF25	GV9	NF7									
Plagioclase	12	11	17	16									
Clinopyroxene	0	23	4	9									
Orthopyroxene	52	23	60	50									
Olivine	36	42	19	25									
Name	NF4	SB3	SB10										
Plagioclase	13	9	7										
Clinopyroxene	19	27	17										
Orthopyroxene	62	53	75										
Olivine	6	11	0										

Table A2: *Certified Reference Materials (CRMs) data from XRF analysis. Meas = measured values; Recom = recommended values.*

CRMs																
wt%	SiO2	Al2O3	Fe2O3	FeO	MnO	MgO	CaO	Na2O	K2O	TiO2	P2O5	Cr2O3	NiO	TOTAL	LOI	
NIM-P	51.67	4.30	1.28	10.34	0.23	25.52	2.65	0.30	0.09	0.20	0.02	3.54	0.07	100.20	-0.23	
NIM-D	38.98	0.30	1.71	13.88	0.22	43.96	0.30	-0.02	0.00	0.02	0.01	0.42	0.26	100.06	-0.51	
W2	53.11	15.68	1.09	8.83	0.17	6.42	10.96	2.20	0.64	1.08	0.13	0.02	0.01	100.33	0.19	
NIM-S	63.76	17.26	0.14	1.13	0.01	0.47	0.66	0.58	15.42	0.05	0.12	0.01	0.00	99.63	0.42	
GSP2	67.64	15.15	0.50	4.01	0.05	0.98	2.13	2.82	5.48	0.67	0.29	0.01	0.00	99.74	0.87	
BCR2	54.84	13.81	1.40	11.30	0.20	3.63	7.21	3.19	1.81	2.28	0.36	0.02	0.00	100.04	0.10	
NIM-N	53.05	16.82	0.90	7.31	0.18	7.56	11.56	2.43	0.25	0.20	0.02	0.01	0.01	100.31	0.04	
NIM-G	76.66	12.28	0.20	1.63	0.02	0.04	0.80	3.33	5.07	0.10	0.01	0.01	0.00	100.17	0.73	
PCC1	44.38	0.73	0.87	7.02	0.12	45.67	0.59	0.00	0.01	0.01	0.01	0.42	0.33	100.15	5.09	
BHVO2	50.07	13.79	1.24	10.08	0.17	7.30	11.49	2.22	0.54	2.76	0.28	0.06	0.02	100.02	-0.48	
AGV2	60.27	17.30	0.68	5.53	0.10	1.82	5.29	4.30	2.92	1.06	0.48	0.01	0.00	99.77	1.80	
G2	69.63	15.52	0.26	2.14	0.04	0.74	1.95	4.13	4.48	0.48	0.14	0.01	0.00	99.52	0.64	
DTS1	40.77	0.24	0.87	7.02	0.12	49.96	0.17	0.01	0.00	0.01	0.01	0.59	0.31	100.07	-0.02	

Table A3: *Certified Reference Materials (CRMs) data from ICP-MS analysis. Meas = measured values; Recom = recommended values.*

	Meas	Meas	Recom	Recom			Meas	Meas	Recom	Recom
	BCR2	BHVO2	BCR2	BHVO2			BCR2	BHVO2	BCR2	BHVO2
P	1554.448	1190.681	1571	1178		P	1505.055	1232.451	1571	1178
Sc	32.132	30.873	32	31		Sc	31.856	31.142	32	31
Ti	12745.39	15945.8	13005	15621		Ti	12420.22	16393.55	13005	15621
V	418.382	325.603	414	329		V	409.49	332.686	414	329
Cr	15.969	290.663	17	285		Cr	14.722	288.432	17	285
Co	37.105	45.404	35.8	47		Co	36.429	46.203	35.8	47
Ni	11.534	116.373	12.7	112		Ni	10.797	114.43	12.7	112
Cu	19.232	143.249	19.4	142		Cu	18.559	148.74	19.4	142
Zn	143.475	109.695	147	107		Zn	139.965	112.664	147	107
Rb	50.165	9.871	49	10.1		Rb	48.885	10.012	49	10.1
Sr	322.677	380.029	321	382		Sr	317.687	386.054	321	382
Y	31.333	22.758	31	23		Y	30.746	23.192	31	23
Zr	184.679	168.505	194	160		Zr	181.666	171.657	194	160
Nb	12.713	16.513	12.8	16.4		Nb	11.647	18.201	12.8	16.4
Cs	1.244	0.104	1.17	0.11		Cs	1.261	0.103	1.17	0.11
Ba	630.403	130.903	641	128.7		Ba	628.316	131.352	641	128.7
La	25.19	15.184	24.5	15.6		La	25.257	15.146	24.5	15.6
Ce	51.146	36.539	50.5	37		Ce	51.144	36.54	50.5	37
Pr	6.343	4.967	6.3	5		Pr	6.436	4.968	6.3	5
Nd	27.511	23.563	27	24		Nd	27.652	23.447	27	24
Sm	6.251	5.846	6.3	5.8		Sm	6.293	5.807	6.3	5.8
Eu	1.916	1.993	1.91	2		Eu	1.933	1.977	1.91	2
Gd	6.48	5.918	6.5	5.9		Gd	6.536	5.868	6.5	5.9
Tb	0.962	0.849	0.95	0.86		Tb	0.972	0.841	0.95	0.86
Dy	5.965	4.929	6	4.9		Dy	6.04	4.868	6	4.9
Ho	1.201	0.909	1.2	0.91		Ho	1.221	0.895	1.2	0.91
Er	3.319	2.287	3.3	2.3		Er	3.35	2.266	3.3	2.3
Tm	0.468	0.295	0.46	0.3		Tm	0.489	0.289	0.46	0.3
Yb	3.308	1.956	3.2	2.02		Yb	3.266	1.934	3.2	2.02
Lu	0.47	0.26	0.47	0.26		Lu	0.475	0.257	0.47	0.26
Hf	4.794	4.284	5	4.1		Hf	4.845	4.235	5	4.1
Ta	0.908	0.824	0.78	0.94		Ta	0.726	1.016	0.78	0.94
Pb	9.532	1.635	10.9	1.4		Pb	10.228	1.498	10.9	1.4
Th	5.697	1.141	5.5	1.18		Th	5.681	1.144	5.5	1.18
U	1.754	0.434	1.73	0.44		U	1.76	0.433	1.73	0.44

Table A4: XRF major elements and quadrupole ICP-MS trace elements data of samples from the Stolzberg Complex. Samples are grouped according to rock rock type, where green = dunites, red = harzburgites; blue = other peridotites; orange = orthopyroxenites; grey = websterites; no colour = gabbro-noritic rocks.

wt%	GV 1	DH 36	NF6	NF 20	SM2	SM4	DH65	NF3	SM6
SiO2	38.90	39.90	39.84	39.88	40.78	38.68	37.78	41.01	39.14
TiO2	0.06	0.10	0.12	0.08	0.06	0.05	0.10	0.07	0.09
Al2O3	1.42	2.40	2.59	1.83	1.44	1.16	2.95	1.72	1.83
Fe2O3	6.55	8.68	7.23	7.10	2.05	9.38	8.50	8.12	8.99
MnO	0.11	0.18	0.14	0.11	0.05	0.07	0.09	0.12	0.14
MgO	37.86	36.72	37.32	37.70	38.95	37.42	37.32	37.49	37.42
CaO	0.06	0.06	0.05	0.05	0.03	0.15	0.00	0.24	0.09
Na2O	0.01	0.00	0.02	0.02	0.07	0.00	0.00	0.00	0.00
K2O	0.00	0.03	0.00	0.00	0.00	0.00	0.00	0.00	0.00
P2O5	0.03	0.02	0.02	0.02	0.02	0.02	0.00	0.00	0.00
Cr2O3	0.97	0.32	0.25	0.63	1.68	0.42	2.22	0.67	0.48
NiO	0.23	0.29	0.30	0.30	0.23	0.34	0.33	0.23	0.28
LOI	13.03	11.58	12.13	12.28	13.87	12.63	11.52	11.19	11.83
Total	99.23	100.28	100.01	100.00	99.23	100.32	100.81	100.86	100.29
ppm	GV1	DH36	NF6	NF20	SM2	SM4	DH65	NF3	SM6
P	83.815	58.323	35.165	50.074	23.895	33.744	43.835	36.966	34.592
Sc	8.165	8.769	9.326	8.3	12.246	7.203	5.841	7.743	7.804
Ti	279.361	523.263	661.971	471.308	250.655	269.551	403.921	267.918	417.439
V	28.935	55.238	60.734	42.126	42.408	25.381	62.176	38.533	38.453
Cr	3243.747	1382.719	1251.168	2387.702	5180.553	1899.346	7882.857	2693.177	3011.079
Co	90.873	110.793	98.317	100.986	64.452	115.455	101.218	62.944	102.488
Ni	1482.295	1929.866	2041.389	1891.788	1463.31	2233.034	2169.723	1048.696	1907.709
Cu	2.313	8.612	28.211	0.527	0.462	0.547	8.728	5.734	13.945
Zn	52.326	64.425	45.734	33.807	26.207	29.333	82.14	39.231	46.859
Rb	0.269	1.37	0.1	0.085	0.074	0.154	1.133	0.251	0.3
Sr	1.012	0.962	0.66	0.395	0.194	0.89	0.576	3.004	1.774
Y	2.088	2.975	1.944	1.699	1.848	1.213	1.326	1.547	1.663
Zr	4.729	6.446	5.413	4.36	3.463	2.213	3.597	2.527	3.383
Nb	0.229	0.684	0.259	1.746	0.864	0.151	0.2	0.176	0.186
Cs	0.006	0.045	0.015	0.013	0.001	0.006	0.052	0.056	0.145
Ba	0.233	1.823	4.697	0.727	0.242	1.392	3.046	1.695	4.978
La	0.439	1.052	0.582	0.263	0.341	1.148	0.276	0.467	0.316
Ce	1.068	0.959	1.089	0.621	0.617	0.498	0.551	0.82	0.633
Pr	0.143	0.136	0.156	0.09	0.086	0.072	0.077	0.097	0.095
Nd	0.69	0.704	0.788	0.471	0.451	0.393	0.38	0.468	0.493
Sm	0.213	0.243	0.239	0.153	0.152	0.138	0.112	0.136	0.166
Eu	0.069	0.019	0.103	0.052	0.034	0.049	0.028	0.056	0.062
Gd	0.282	0.343	0.308	0.218	0.23	0.176	0.155	0.179	0.22
Tb	0.047	0.062	0.049	0.036	0.041	0.03	0.027	0.035	0.04
Dy	0.355	0.473	0.339	0.283	0.306	0.212	0.199	0.242	0.294
Ho	0.076	0.102	0.074	0.059	0.072	0.046	0.045	0.057	0.063
Er	0.23	0.31	0.214	0.183	0.221	0.133	0.135	0.172	0.182
Tm	0.034	0.044	0.032	0.028	0.034	0.019	0.022	0.026	0.027
Yb	0.235	0.319	0.23	0.187	0.248	0.138	0.149	0.191	0.189
Lu	0.037	0.045	0.036	0.028	0.04	0.021	0.023	0.032	0.028
Hf	0.132	0.189	0.146	0.12	0.12	0.063	0.096	0.076	0.095
Ta	0.029	0.143	0.02	0.337	0.162	0.007	0.012	0.009	0.006
Pb	0.319	0.169	0.317	0.238	0.18	0.981	1.147	0.518	0.605
Th	0.068	0.056	0.032	0.021	0.034	0.01	0.039	0.041	0.014
U	0.012	0.019	0.01	0	0.008	0.01	0.013	0.015	0.004

Table A4 (continued)

wt%	DH 78	DN 8B	DN8A	NF 11	NF 17	NF 18	NF23	NF24	NF26	SM1	DN4	NF5	NF9
SiO2	41.13	41.59	42.17	41.51	41.20	40.88	41.56	40.66	43.15	40.46	42.21	41.02	43.22
TiO2	0.14	0.22	0.21	0.15	0.14	0.15	0.15	0.13	0.20	0.12	0.17	0.12	0.18
Al2O3	3.29	3.68	3.75	3.71	2.96	3.17	4.05	3.24	3.65	2.83	3.30	3.30	3.74
Fe2O3	9.12	10.14	10.25	9.64	9.71	9.06	9.66	9.44	9.57	9.53	10.05	13.77	9.84
MnO	0.11	0.13	0.13	0.14	0.17	0.12	0.14	0.15	0.15	0.12	0.17	0.17	0.15
MgO	32.71	30.96	31.46	31.62	33.17	33.59	31.16	33.31	31.04	34.86	31.58	30.39	31.63
CaO	3.13	2.49	2.37	2.50	1.35	2.50	2.91	0.67	2.61	1.82	3.66	1.57	4.28
Na2O	0.02	0.06	0.00	0.00	0.01	0.03	0.00	0.00	0.02	0.06	0.00	0.00	0.00
K2O	0.00	0.02	0.00	0.01	0.00	0.03	0.01	0.00	0.03	0.09	0.00	0.00	0.00
P2O5	0.02	0.04	0.00	0.02	0.02	0.02	0.02	0.02	0.04	0.03	0.00	0.00	0.00
Cr2O3	0.67	0.68	0.70	0.67	0.78	0.19	0.61	0.72	0.53	0.62	0.53	0.43	0.35
NiO	0.21	0.22	0.22	0.19	0.21	0.29	0.18	0.21	0.18	0.24	0.21	0.21	0.23
LOI	9.83	9.82	9.11	9.83	10.46	10.29	9.48	10.92	9.41	9.14	8.97	8.97	6.87
Total	100.36	100.04	100.36	99.98	100.17	100.32	99.93	99.47	100.56	99.92	100.84	99.95	100.48
ppm	DH78	DN8B	DN8A	NF11	NF17	NF18	NF23	NF24	NF26	SM1	DN4	NF5	NF49
P	57.839	133.929	116.587	56.948	48.186	65.383	64.873	50.395	86.324	67.075	81.306	60.31	70.359
Sc	13.003	11.863	11.608	12.622	10.973	11.225	13.013	12.378	11.737	9.119	8.257	10.442	9.249
Ti	817.342	1165.778	1045.371	749.569	643.763	795.981	842.436	703.2	1039.889	643.398	1194.158	720.595	880.733
V	68.288	72.776	79.041	70.126	57.402	62.992	75.176	61.869	73.779	43.622	71.463	69.961	73.247
Cr	805.797	1890.013	4188.196	1637.456	1411.038	668.128	1619.546	1774.669	900.693	1770.765	2474.095	2736.883	2107.273
Co	107.197	105.609	97.108	96.423	96.691	103.22	100.458	102.492	102.529	106.02	74.105	105.896	93.994
Ni	1340.228	1359.223	1445.564	1097.613	1208.972	1727.758	1173.112	1320.648	1169.627	1529.894	1049.272	1417.287	1588.896
Cu	1.338	1.343	3.579	28.042	1.364	17.825	16.219	3.892	3.307	5.268	23.198	5.244	13.487
Zn	21.377	39.239	59.396	24.547	28.623	50.696	24.755	34.681	29.241	71.777	46.818	65.787	52.696
Rb	0.812	1.309	1.532	1.035	0.509	2.696	1.465	0.618	2.348	5.779	1.755	1.566	0.516
Sr	3.188	6.314	5.381	6.351	2.869	10.01	9.973	2.222	5.854	4	2.874	3.169	6.629
Y	3.026	6.082	5.068	2.896	2.496	3.237	2.935	2.592	4.078	2.887	2.481	3.171	2.678
Zr	6.741	11.905	13.953	5.931	3.139	9.399	2.759	2.953	4.37	9.666	9.747	7.183	7.747
Nb	0.299	0.766	0.676	0.979	1.217	2.121	0.282	0.227	1.086	0.472	1.082	0.456	0.503
Cs	0.203	1.078	1.374	1.546	0.452	1.42	1.527	0.681	1.107	0.421	0.161	0.671	0.178
Ba	0.564	7.504	4.735	0.773	10.666	2.318	6.699	6.325	6.795	7.053	1.234	3.064	0.708
La	0.402	1.282	0.99	0.41	0.385	0.835	0.46	0.4	0.883	1.145	0.844	0.971	0.714
Ce	1.018	3.109	2.118	1.025	0.926	1.918	0.994	0.839	1.862	2.186	1.065	1.94	1.392
Pr	0.152	0.434	0.305	0.15	0.143	0.249	0.145	0.13	0.268	0.262	0.15	0.245	0.177
Nd	0.81	2.1	1.534	0.801	0.76	1.188	0.792	0.716	1.353	1.184	0.795	1.127	0.872
Sm	0.28	0.656	0.462	0.277	0.259	0.364	0.284	0.258	0.437	0.333	0.268	0.299	0.265
Eu	0.112	0.186	0.129	0.115	0.108	0.135	0.115	0.106	0.188	0.124	0.09	0.094	0.098
Gd	0.402	0.885	0.594	0.41	0.367	0.484	0.408	0.367	0.588	0.428	0.33	0.383	0.345
Tb	0.067	0.155	0.112	0.07	0.061	0.08	0.075	0.067	0.103	0.073	0.061	0.071	0.064
Dy	0.514	1.091	0.782	0.534	0.463	0.593	0.517	0.461	0.702	0.515	0.418	0.503	0.461
Ho	0.108	0.229	0.173	0.113	0.097	0.125	0.115	0.104	0.157	0.116	0.091	0.113	0.101
Er	0.324	0.66	0.493	0.335	0.288	0.377	0.334	0.299	0.451	0.333	0.255	0.347	0.309
Tm	0.046	0.097	0.078	0.048	0.042	0.055	0.049	0.045	0.066	0.051	0.037	0.054	0.045
Yb	0.327	0.642	0.5	0.325	0.273	0.362	0.337	0.3	0.454	0.35	0.253	0.37	0.31
Lu	0.046	0.089	0.074	0.049	0.04	0.056	0.05	0.047	0.066	0.051	0.039	0.063	0.048
Hf	0.185	0.359	0.355	0.202	0.132	0.27	0.138	0.135	0.201	0.277	0.283	0.204	0.214
Ta	0.024	0.08	0.046	0.119	0.328	0.434	0.02	0.016	0.155	0.036	0.061	0.026	0.027
Pb	0.265	0.317	0.572	0.639	0.966	0.823	0.682	0.359	0.481	1.354	0.516	0.731	0.869
Th	0.023	0.177	0.135	0.026	0.026	0.155	0.031	0.027	0.081	0.222	0.024	0.084	0.083
U	0.001	0.024	0.023	0.001	0.001	0.044	0.01	0.009	0.025	0.078	0.026	0.04	0.041

Table A4 (continued)

wt%	DN 6	NF25	GV 9	NF 7		SB5	DH 34	DH 61	DH 67	DN 10	SB6	DH3	DH7
SiO2	42.97	43.08	46.04	44.93		52.13	55.52	55.50	53.09	53.02	53.17	54.24	53.92
TiO2	0.19	0.20	0.26	0.26		0.06	0.07	0.08	0.12	0.14	0.09	0.10	0.09
Al2O3	4.40	3.70	5.44	5.15		1.33	1.28	1.63	2.64	3.13	1.86	2.29	1.94
Fe2O3	10.06	8.54	9.95	9.72		8.09	7.00	8.92	8.92	10.59	7.57	7.64	7.68
MnO	0.14	0.12	0.13	0.14		0.13	0.14	0.19	0.17	0.20	0.16	0.17	0.17
MgO	29.80	28.67	26.30	26.41		28.81	31.67	30.38	27.32	25.24	28.86	29.25	29.91
CaO	2.12	7.26	3.91	4.89		2.66	1.29	1.76	2.79	2.83	2.08	4.01	3.05
Na2O	0.00	0.04	0.00	0.00		0.00	0.03	0.09	0.10	0.18	0.05	0.00	0.00
K2O	0.01	0.01	0.01	0.01		0.00	0.08	0.12	0.26	0.35	0.09	0.15	0.14
P2O5	0.03	0.03	0.03	0.03		0.00	0.01	0.01	0.02	0.02	0.02	0.00	0.00
Cr2O3	0.58	0.36	0.38	0.63		0.56	0.56	0.56	0.45	0.38	0.41	0.41	0.61
NiO	0.19	0.19	0.18	0.15		0.07	0.07	0.06	0.06	0.05	0.07	0.06	0.07
LOI	9.65	8.12	7.47	7.59		6.23	2.42	0.97	4.14	3.93	5.29	2.47	3.29
Total	100.11	100.31	100.07	99.90		100.07	100.14	100.26	99.82	100.06	99.71	100.79	100.86
ppm	DN6	NF25	GV9	NF7		SB5	DH34	DH61	DH67	DN10	SB6	DH3	DH07
P	80.277	73.158	103.498	114.448		29.447	21.115	24.499	49.459	43.943	24.245	31.129	23.314
Sc	12.985	11.007	12.683	13.727		9.838	9.278	12.306	14.926	13.459	14.446	10.931	12.191
Ti	1033.584	1073.124	1189.098	1408.739		304.894	332.017	389.582	509.171	673.772	439.935	496.569	423.579
V	86.258	82.287	111.216	97.82		45.721	40.262	51.265	70.218	81.713	56.002	44.091	44.339
Cr	1452.538	1866.655	982.709	1500.757		2912.365	2952.189	2567.707	2252.179	2123.64	2454.704	2060.205	2873.329
Co	100.12	88.171	81	92.495		78.461	77.564	81.771	71.017	77.934	74.959	68.207	65.791
Ni	1194.417	1206.157	1076.051	928.522		423.561	481.252	431.042	391.799	344.15	469.592	400.153	467.158
Cu	36.062	2.238	44.117	34.079		3.392	8.487	11.551	44.516	12.98	11.221	20.513	17.789
Zn	43.813	25.519	38.192	31.126		32.304	52.893	62.514	60.858	72.241	58.749	55.248	49.864
Rb	1.886	1.308	0.936	0.934		0.742	3.688	4.187	8.236	13.363	3.841	6.102	5.888
Sr	6.272	6.087	8.59	9.475		2.234	6.364	13.06	25.776	29.027	10.048	26.308	24.593
Y	4.114	3.547	5.389	5.125		0.99	0.919	1.16	2.249	2.704	1.526	1.473	1.33
Zr	1.881	9.281	4.035	3.214		2.331	2.296	2.544	4.173	7.444	3.289	3.839	3.039
Nb	0.406	1.738	0.714	0.728		0.1	0.099	0.082	0.12	0.364	0.129	0.257	0.132
Cs	1.44	0.806	0.112	1.629		0.12	0.202	0.134	0.342	0.582	0.299	0.257	0.683
Ba	0.792	3.325	12.81	0.979		1.33	3.455	5.479	10.316	14.879	8.869	6.783	9.637
La	0.635	0.565	1.499	1.092		0.258	0.252	0.384	0.727	0.751	0.378	0.403	0.353
Ce	1.505	1.264	2.943	2.506		0.409	0.432	0.617	1.349	1.682	0.72	0.676	0.576
Pr	0.221	0.215	0.426	0.35		0.055	0.055	0.08	0.166	0.214	0.097	0.089	0.075
Nd	1.139	1.242	2.049	1.727		0.265	0.282	0.369	0.777	0.983	0.487	0.419	0.337
Sm	0.395	0.443	0.604	0.561		0.077	0.078	0.109	0.225	0.288	0.154	0.122	0.1
Eu	0.135	0.167	0.089	0.105		0.012	0.028	0.038	0.085	0.11	0.056	0.055	0.039
Gd	0.558	0.579	0.818	0.749		0.101	0.114	0.15	0.308	0.386	0.208	0.162	0.132
Tb	0.096	0.1	0.138	0.129		0.019	0.017	0.024	0.052	0.067	0.036	0.029	0.024
Dy	0.705	0.664	0.964	0.933		0.139	0.145	0.2	0.398	0.498	0.261	0.218	0.187
Ho	0.149	0.148	0.209	0.197		0.031	0.03	0.042	0.086	0.108	0.06	0.05	0.045
Er	0.437	0.416	0.597	0.573		0.105	0.1	0.135	0.277	0.336	0.177	0.144	0.135
Tm	0.063	0.06	0.088	0.084		0.017	0.013	0.021	0.04	0.05	0.028	0.023	0.022
Yb	0.409	0.405	0.567	0.546		0.128	0.113	0.15	0.299	0.343	0.206	0.167	0.157
Lu	0.061	0.061	0.086	0.083		0.02	0.015	0.022	0.044	0.054	0.032	0.026	0.026
Hf	0.12	0.262	0.174	0.188		0.061	0.058	0.07	0.126	0.208	0.097	0.11	0.081
Ta	0.028	0.422	0.053	0.046		0.006	0.015	0.01	0.011	0.046	0.008	0.015	0.007
Pb	0.703	0.46	0.337	0.354		0.341	0.143	0.251	0.544	0.362	0.356	0.928	0.736
Th	0.04	0.041	0.127	0.098		0.029	0.024	0.031	0.059	0.117	0.047	0.047	0.035
U	0.005	0.019	0.032	0.024		0.011	0	0.002	0.015	0.04	0.018	0.018	0.013

Table A4 (continued)

wt%	DH8	SS9	SS12	NF4	SB3	SB10	GV 13	GV 14	NF 10	DH 17	DH 83
SiO2	53.43	56.19	56.21	49.19	50.26	51.47	54.05	55.47	53.53	53.35	53.89
TiO2	0.11	0.06	0.05	0.19	0.12	0.10	0.38	0.45	0.57	0.42	0.27
Al2O3	2.50	1.19	1.17	4.29	3.22	2.42	6.87	10.84	10.79	9.35	5.01
Fe2O3	8.91	7.84	7.62	7.90	5.81	9.87	10.22	10.27	11.13	10.39	7.95
MnO	0.19	0.17	0.17	0.18	0.16	0.18	0.17	0.15	0.16	0.14	0.16
MgO	27.73	31.98	32.16	24.41	26.79	25.42	13.45	8.7	10.23	13.94	16.36
CaO	2.50	1.40	1.29	6.75	8.06	5.40	10.73	8.96	8.12	6.27	12.54
Na2O	0.00	0.00	0.00	0.03	0.00	0.00	2.64	3.31	3.51	2.28	1.38
K2O	0.43	0.07	0.08	0.02	0.00	0.00	0.07	0.08	0.09	0.58	0.07
P2O5	0.00	0.00	0.00	0.03	0.00	0.00	0.03	0.05	0.06	0.05	0.03
Cr2O3	0.44	0.50	0.49	0.39	0.44	0.42	0.18	0.08	0.1	0.17	0.38
NiO	0.07	0.07	0.07	0.09	0.09	0.11	0.03	0.01	0.02	0.03	0.04
LOI	4.22	1.28	1.47	6.11	4.81	4.72	1.33	1.7	1.88	2.94	1.68
Total	100.53	100.75	100.77	99.58	99.76	100.11	100.15	100.06	100.17	99.92	99.77
ppm	DH8	SS9	SS12	NF4	SB3	SB10	GV13	GV14	NF10	DH17	DH83
P	39.882	20.566	36.423	71.716	53.236	24.357	108.942	162.686	219.288	208.504	69.601
Sc	14.749	4.313	3.855	15.668	16.803	18.649	34.56	33.991	35.131	31.606	36.371
Ti	518.381	266.438	445.49	1006.816	576.796	495.648	2037.864	2478.436	3112.948	2480.756	1465.094
V	62.186	27.846	24.523	93.554	73.702	65.221	170.449	212.33	217.716	186.09	136.664
Cr	2583.828	2322.232	1675.525	2232.002	2531.272	2597.224	1040.483	456.483	532.615	1050.136	2259.988
Co	73.96	82.209	64.085	77.485	57.35	80.002	52.132	44.217	52.748	60.972	48.531
Ni	399.468	431.307	377.716	575.235	554.39	673.037	184.165	92.25	117.293	245.429	293.973
Cu	29.64	5.139	10.323	3.581	2.571	3.956	159.188	55.738	89.808	27.804	10.655
Zn	58.046	45.383	47.512	43.982	30.032	39.772	58.905	65.145	74.807	35.619	47.382
Rb	14.987	2.752	2.802	0.619	1.265	0.583	0.62	0.55	0.651	17.239	0.468
Sr	49.079	5.481	10.671	32.681	5.061	3.031	18.965	102.312	31.144	77.398	25.173
Y	2.034	0.503	0.436	4.749	2.751	1.88	6.925	10.95	12.046	10.395	5.088
Zr	4.463	1.918	3.593	7.838	3.584	2.721	11.114	17.296	19.475	36.886	9.455
Nb	0.235	0.108	0.486	0.898	0.237	0.153	0.78	1.235	1.649	1.935	0.513
Cs	1.353	0.168	0.138	0.349	0.174	0.059	0.084	0.023	0.064	0.815	0.013
Ba	18.426	3.088	4.712	1.941	1.883	1.274	13.205	14.619	11.038	88.454	14.628
La	0.507	0.205	0.342	1.273	0.446	0.457	1.241	2.415	2.073	3.425	0.803
Ce	0.949	0.303	0.518	2.004	0.76	0.683	3.451	5.755	5.711	7.63	1.977
Pr	0.13	0.047	0.043	0.32	0.123	0.086	0.532	0.799	0.852	0.946	0.319
Nd	0.603	0.23	0.206	1.619	0.63	0.441	2.704	3.928	4.291	4.168	1.688
Sm	0.176	0.063	0.053	0.508	0.201	0.144	0.886	1.25	1.41	1.18	0.597
Eu	0.067	0.018	0.018	0.164	0.048	0.041	0.323	0.519	0.481	0.389	0.213
Gd	0.216	0.071	0.069	0.674	0.27	0.19	1.149	1.665	1.86	1.463	0.803
Tb	0.04	0.011	0.01	0.118	0.054	0.039	0.197	0.282	0.324	0.249	0.136
Dy	0.3	0.079	0.06	0.821	0.383	0.284	1.352	1.976	2.276	1.754	0.967
Ho	0.07	0.016	0.014	0.184	0.09	0.066	0.281	0.419	0.487	0.376	0.2
Er	0.201	0.048	0.044	0.526	0.279	0.206	0.793	1.2	1.376	1.091	0.563
Tm	0.034	0.008	0.006	0.079	0.044	0.034	0.116	0.178	0.206	0.165	0.081
Yb	0.234	0.056	0.042	0.544	0.321	0.25	0.737	1.113	1.281	1.112	0.543
Lu	0.037	0.009	0.006	0.08	0.05	0.037	0.105	0.165	0.183	0.164	0.076
Hf	0.123	0.051	0.096	0.259	0.104	0.082	0.423	0.55	0.708	0.945	0.302
Ta	0.015	0.004	0.026	0.234	0.019	0.006	0.053	0.081	0.1	0.139	0.043
Pb	1.258	0.398	0.386	0.22	0.449	0.713	0.242	1.473	0.693	0.66	0.279
Th	0.054	0.023	0.029	0.118	0.055	0.02	0.075	0.329	0.277	0.82	0.051
U	0.02	0.006	0.042	0.037	0.014	0.021	0.018	0.104	0.084	0.278	0.008

Table A4 (continued)

wt%	DH80	GV6	GV12	NF12	NF13	HD2	NF22
SiO2	54.16	57.01	53.2	53.73	53.15	52.88	52.9
TiO2	0.304	0.468	0.508	0.443	0.505	0.521	0.576
Al2O3	5.942	6.837	15.76	9.138	12.76	14.84	11.12
Fe2O3	8.51	11.02	10.22	10.94	12.34	4.87	11.48
MnO	0.174	0.126	0.153	0.186	0.177	0.136	0.166
MgO	15.85	11.72	5.55	13.65	7.727	6.181	10.21
CaO	12.74	8.951	9.464	7.012	9.609	16.66	8.545
Na2O	1.367	3.286	4.274	2.253	1.452	3.205	3.117
K2O	0.149	0.05	0.094	0.106	0.346	0.139	0.112
P2O5	0	0	0	0	0.064	0	0.059
Cr2O3	0.34	0.073	0	0.165	0.052	0	0.092
NiO	0	0.066	0	0	0	0	0
LOI	0.83	0.55	1.05	2.45	1.8	0.77	1.65
Total	100.368	100.157	100.325	100.073	99.982	100.203	100.027
ppm	DH80	GV6	GV12	NF12	NF13	HD2	NF22
P	86.978	4.418	137.42	172.608	235.42	45.482	221.979
Sc	36.444	27.187	28.227	29.876	27.098	16.479	28.144
Ti	1516.28	2438.288	2674.693	2342.32	2663.909	2510.143	2986.301
V	135.585	61.982	263.021	171.856	200.239	143.584	204.993
Cr	2215.652	482.882	19.881	1065.439	341.764	3	639.059
Co	49.107	49.213	44.808	56.276	52.736	19.242	53.154
Ni	216.333	436.412	71.26	208.376	87.895	95.194	122.674
Cu	4.74	6.252	7.362	86.409	60.696	7.218	69.859
Zn	48.826	55.145	44.676	75.689	99.538	21.329	72.916
Rb	1.631	0.545	0.607	3.252	8.391	1.715	0.957
Sr	59.239	11.582	127.715	48.946	74.646	128.137	59.806
Y	7.205	20.232	9.365	11.598	12.739	15.622	13.213
Zr	14.312	76.734	20.154	37.022	34.58	49.011	32.596
Nb	0.666	4.651	0.752	1.897	2.023	2.626	2.092
Cs	0.024	0.035	0.016	0.482	0.091	0.011	0.037
Ba	27.688	3.24	13.044	24.238	29.678	34.942	12.338
La	1	1.998	1.06	3.906	3.801	1.624	3.447
Ce	2.222	7.251	2.342	7.844	8.357	5.38	7.953
Pr	0.38	1.384	0.38	1.042	1.132	0.944	1.082
Nd	2.12	7.428	2.078	4.725	5.277	5.231	5.231
Sm	0.717	2.375	0.756	1.295	1.469	1.821	1.544
Eu	0.217	0.558	0.304	0.439	0.521	0.89	0.568
Gd	0.895	2.787	1.085	1.597	1.844	2.192	1.921
Tb	0.169	0.505	0.212	0.277	0.319	0.407	0.342
Dy	1.228	3.53	1.597	1.989	2.257	2.892	2.384
Ho	0.263	0.751	0.36	0.435	0.491	0.615	0.512
Er	0.73	2.146	1.06	1.257	1.443	1.724	1.457
Tm	0.114	0.315	0.159	0.185	0.211	0.244	0.209
Yb	0.755	2.1	1.085	1.26	1.402	1.614	1.364
Lu	0.109	0.321	0.168	0.195	0.21	0.236	0.204
Hf	0.405	2.09	0.603	0.991	0.954	1.253	0.976
Ta	0.042	0.439	0.043	0.136	0.123	0.165	0.14
Pb	0.492	0.84	0.559	2.084	2.639	1.176	2.026
Th	0.072	0.934	0.061	0.899	0.488	0.379	0.604
U	0.02	0.146	0.022	0.286	0.173	0.179	0.206

Table A5: Groups of samples from the Stolzburg Complex according to degree of preservation of primary geochemistry.

Group 1	Group 2	Group 3	Group 4	Group 5
DH65	SM6	NF6	SM4	GV1
NF3	SM1	DN8A	DH78	DH36
NF5	DH67	NF23	DN8B	NF20
NF9	SS9	NF24	DH34	SM2
SB5	SB3	DN6	DH61	NF11
SB6	SB10	GV9	DN10	NF17
DH3	GV14	NF7	GV13	NF18
DH7	NF10	DH80	DH83	NF26
DH8		GV12		DN4
DH17				NF25
NF12				SS12
NF13				NF4
				GV6
				HD2

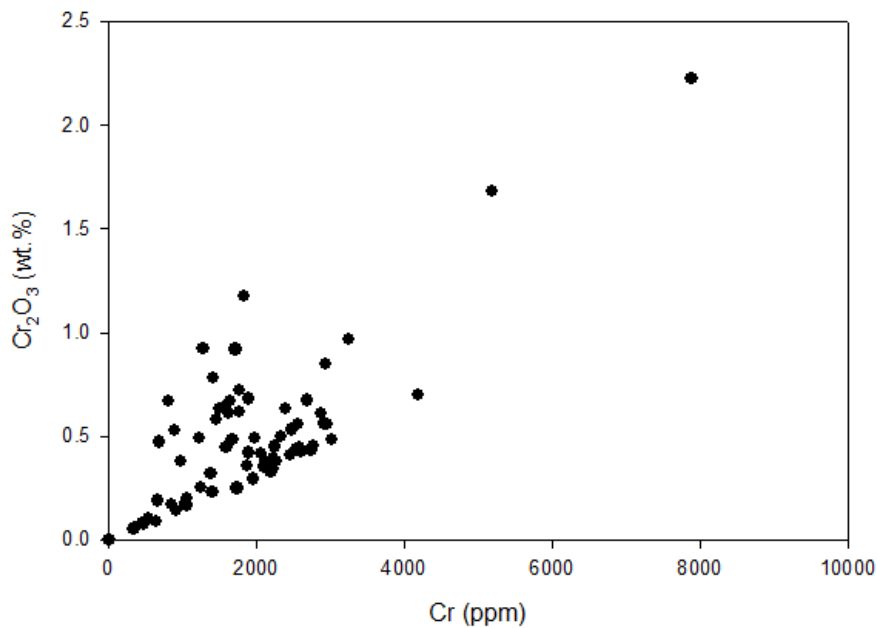
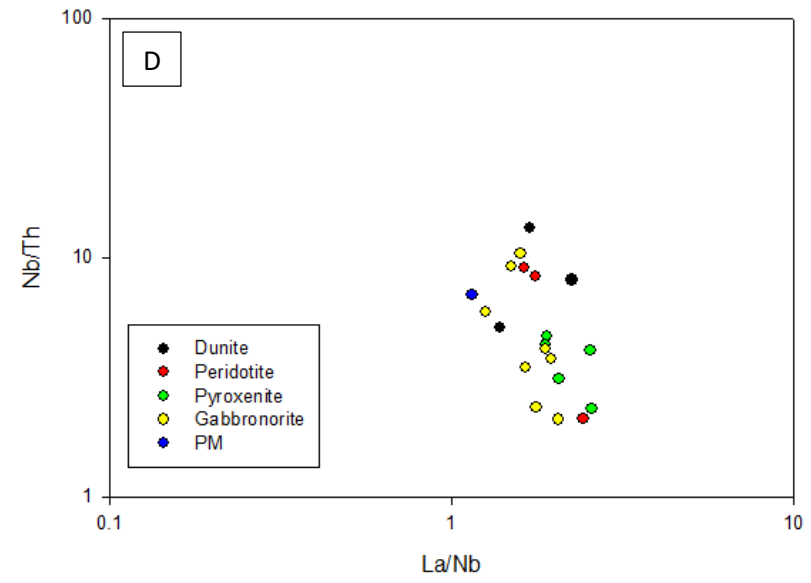
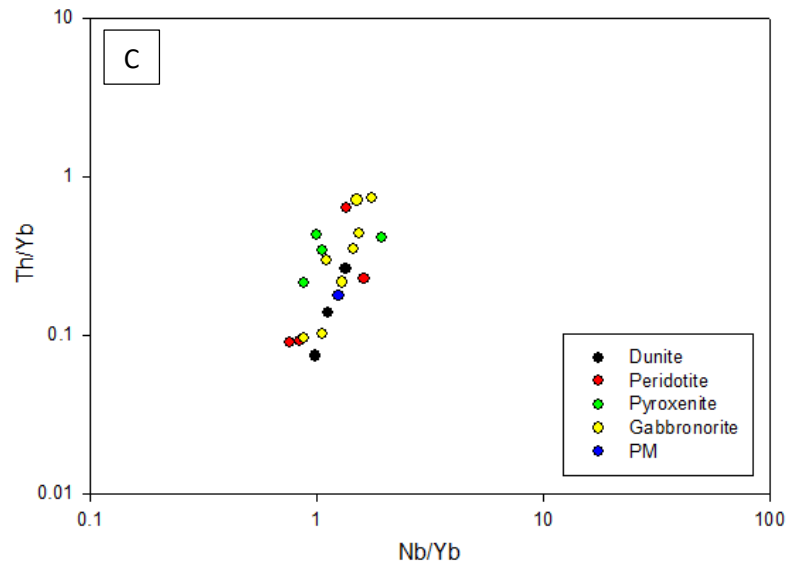
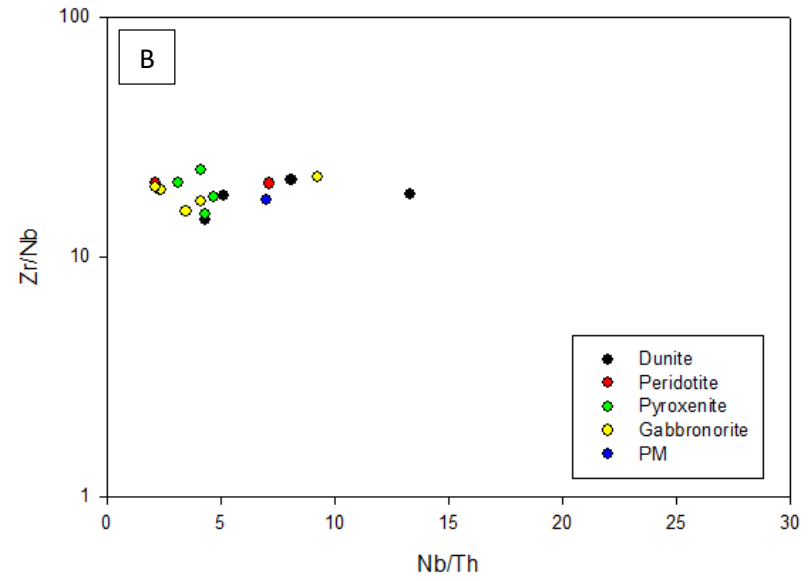
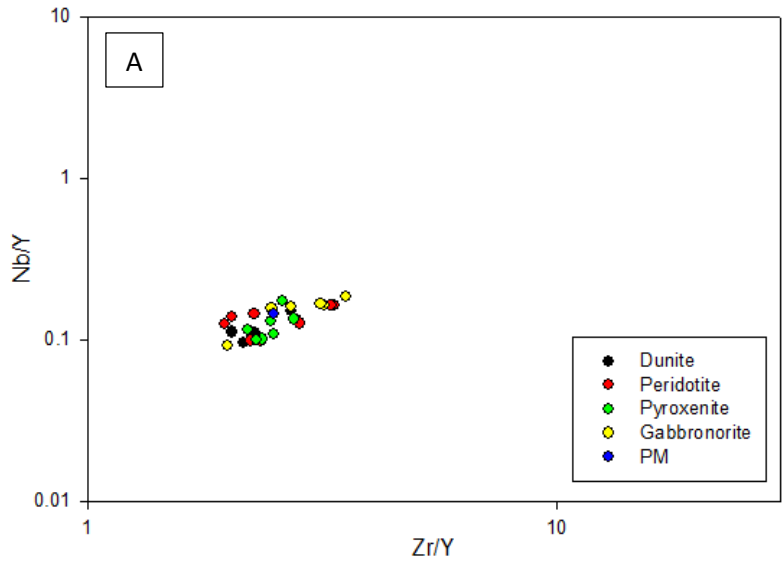


Figure A1: Plot of Cr (ppm) obtained by ICP-MS method against Cr₂O₃ (wt. %) determined by XRF analysis. Scattering of data is a result of poor chromite dissolution in ICP-MS method.



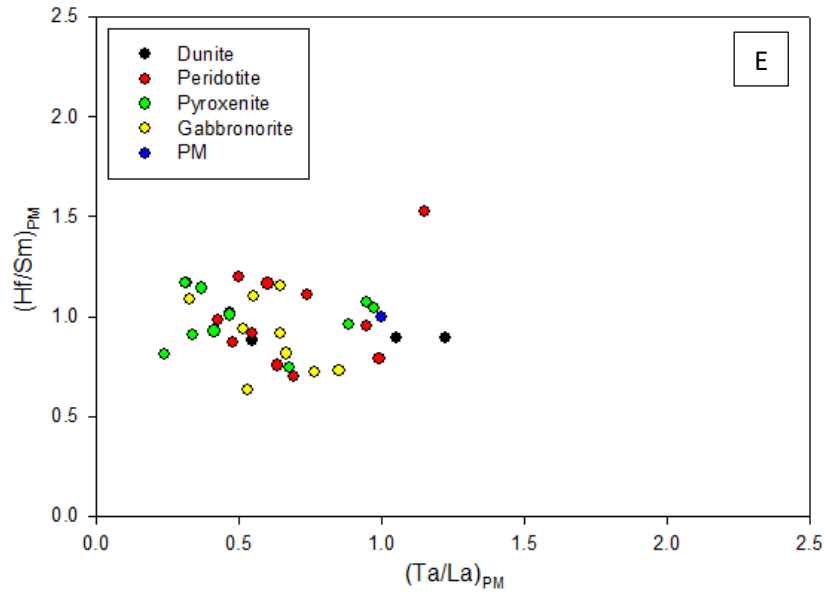


Figure A2: Plots of inter-element ratios of samples from the Stolzburg Complex, where samples are discriminated in terms of lithology.